NATIONAL AERONAUTICS AND SPACE ADMINISTRATION

Space Programs Summary 37-52, Vol. II

The Deep Space Network

For the Period May 1 to June 30, 1968

JET PROPULSION LABORATORY
CALIFORNIA INSTITUTE OF TECHNOLOGY
PASADENA, CALIFORNIA

July 31, 1968

SPACE PROGRAMS SUMMARY 37-52, VOL. II

Prepared Under Contract No. NAS 7-100
National Aeronautics & Space Administration

Preface

The Space Programs Summary is a bimonthly publication that presents a review of engineering and scientific work performed, or managed, by the Jet Propulsion Laboratory for the National Aeronautics and Space Administration during a two-month period. Beginning with the 37-47 series, the Space Programs Summary is composed of four volumes:

Vol. I. *Flight Projects* (Unclassified)

Vol. II. *The Deep Space Network* (Unclassified)

Vol. III. *Supporting Research and Advanced Development* (Unclassified)

Vol. IV. *Flight Projects and Supporting Research and Advanced Development* (Confidential)

Approved by:

W. H. Pickering, *Director*
Jet Propulsion Laboratory

Contents

Contents (contd)

Contents (contd)

I. Introduction

A. Description of the DSN

The Deep Space Network (DSN), established by the NASA Office of Tracking and Data Acquisition under the system management and technical direction of JPL, is responsible for two-way communications with unmanned spacecraft traveling approximately 10,000 mi from earth to interplanetary distances. It supports, or has supported, the following NASA deep space exploration projects: *Ranger, Surveyor, Mariner* Venus 1962, *Mariner* Mars 1964, *Mariner* Venus 67, and *Mariner* Mars 1969 (JPL); *Lunar Orbiter* (Langley Research Center); *Pioneer* (Ames Research Center); and *Apollo* (Manned Spacecraft Center), as backup to the Manned Space Flight Network (MSFN). The DSN is distinct from other NASA networks such as the MSFN, which has primary responsibility for tracking the manned spacecraft of the *Apollo* Project, and the Space Tracking and Data Acquisition Network (STADAN), which tracks earth-orbiting scientific and communications satellites.

The three basic functions performed by the DSN in support of each flight project are as follows:

(1) *Tracking.* Accomplished by radio communication with the spacecraft, tracking provides such metric data as angles, radial velocity, and range (distance from the earth to the spacecraft).

(2) *Data acquisition.* Using the same radio link, the data acquisition function consists of the recovery of information from the spacecraft in the form of telemetry, namely, the engineering measurements recorded by the spacecraft and the scientific data obtained by the onboard instruments.

(3) *Command.* Using the same radio link, the command function involves sending information to the spacecraft to initiate equipment which, for example, operates propulsion systems for changing the trajectory of the spacecraft, changes data transmission rate to earth, or reprograms onboard computers which determine the sequence of spacecraft engineering events.

The DSN can be characterized as a set of the following systems: (1) telemetry, (2) tracking, (3) command, (4) monitoring, (5) simulation, and (6) operations control. Alternately, it can be considered as being comprised of three facilities: the Deep Space Instrumentation Facility (DSIF), the Ground Communications Facility (GCF), and the Space Flight Operations Facility (SFOF).

The DSIF is a worldwide set of deep space stations (DSSs) that provide basic radio communications with spacecraft. These stations and the deep space communications complexes (DSCCs) they comprise are as follows:

Pioneer, Echo, and Mars DSSs (and Venus DSS, described later), comprising the Goldstone DSCC in California; Woomera, Tidbinbilla, and Booroomba[1] DSSs, comprising the Canberra DSCC in Australia; Johannesburg DSS in South Africa; and Robledo, Cebreros, and Rio Cofio[1] DSSs, comprising the Madrid DSCC in Spain. The overseas stations are normally staffed and operated by government agencies of the respective countries, with some assistance from U.S. support personnel.

In addition, the DSIF operates a compatibility test station at Cape Kennedy, which is used for verifying flight-spacecraft/DSN compatibility prior to launch, and a flight-project/tracking and data system interface laboratory at JPL, which is used during the development of the spacecraft to assure a design compatible with the network. A spacecraft guidance and command station on Ascension Island serves to track the spacecraft in the latter part of the launch trajectory while the spacecraft is relatively low in altitude.

To enable continuous radio contact with spacecraft, the stations are located approximately 120 deg apart in longitude; thus, a spacecraft in flight is always within the field-of-view of at least one station, and for several hours each day may be seen by two stations. Furthermore, since most spacecraft on deep space missions travel within 30 deg of the equatorial plane, the stations are located within latitudes of 45 deg north or south of the equator.

Radio contact with a spacecraft usually begins when the spacecraft is on the launch vehicle at Cape Kennedy, and it is maintained throughout the mission. The early part of the trajectory is covered by selected network stations of the Air Force Eastern Test Range (AFETR) and selected stations of the MSFN which are managed by Goddard Space Flight Center. Normally, two-way communications are established between the spacecraft and the DSN within 30 min after spacecraft injection into lunar, interplanetary, or planetary flight. The Cape Kennedy DSS, having supported the preflight compatibility tests, monitors the spacecraft continuously during the launch phase until it passes over the local horizon. The deep space phase begins with acquisition by either the Johannesburg, Woomera, or Tidbinbilla DSS. These stations, with large antennas, low-noise phase-lock receiving systems, and high-power transmitters, provide radio communications to the end of the flight. By international agreement, the radio frequencies assigned for these functions are 2290–2300 MHz for spacecraft-to-earth downlink data transmission and 2110–2120 MHz for earth-to-spacecraft command and uplink data transmission.

To maintain a state-of-the-art capability, research and advanced development work on new components and systems has been conducted continuously at JPL since the establishment of the DSN. To support this work, the Goldstone DSCC has a research and development facility designated the Venus DSS, at which the feasibility of new equipment and techniques to be introduced into the operational network is demonstrated. When a new piece of equipment or new technique has been accepted for integration into the network, it is classed as Goldstone duplicate standard (GSDS), thus standardizing the design and operation of identical items throughout the network.

The GCF, using, in part, facilities of the worldwide NASA Communications Facility (NASCOM, managed and directed by the Goddard Space Flight Center), provides voice, high-speed data, and teletype communications between all stations of the network. Communications between the Goldstone DSCC and the SFOF are provided by a microwave system leased from common carriers. This microwave link has made possible the transmission, in real time, of video data received at the Goldstone DSCC to the SFOF and then to commercial TV systems, as was done during the *Ranger* and *Surveyor* missions.

The SFOF, located at JPL, receives data from all of the tracking stations and processes that information required by the flight project to conduct flight operations. Voice and data channels are distributed throughout the facility, and the following equipment and services are provided: (1) data-processing equipment for the real-time handling and display of tracking and telemetry data; (2) real-time and non-real-time telemetry processing; (3) simulation equipment for flight projects, as well as for network use in training of personnel; (4) monitoring equipment for evaluation of network performance in near-real time; (5) operations control consoles and status and operational display facilities required for the conduct of flight operations; and (6) technical areas for flight project personnel who analyze spacecraft performance, trajectories, and generation of commands, as well as support services required to carry out those functions, such as internal communications by telephone, intercom, public address, closed-circuit TV, documentation, and

[1]Not yet authorized.

reproduction of data packages. The SFOF is equipped to support many spacecraft in flight and those under test in preparation for flight; e.g., over a 24-h period during 1967, as many as eight spacecraft in flight or in operational-readiness tests for flight were supported by the SFOF.

Thus, the DSN simultaneously conducts research and development for support of future flight projects, implements demonstrated capabilities for support of the more immediate flight projects, and provides direct support for the currently active missions, while accommodating differences in the individual projects. In this and future issues of the SPS, Vol. II, the current technical activities of the DSN in these three general categories will be reported under the following subject areas:

Introduction
  Description of the DSN
  Description of DSN Systems

Mission Support
  Introduction
  Interplanetary Flight Projects
  Planetary Flight Projects
  Manned Space Flight Project

Advanced Engineering
  Tracking and Navigational Accuracy Analysis
  Communications System Research
  Tracking and Data Acquisition Elements Research
  Supporting Research and Technology

Development and Implementation
  Space Flight Operations Facility
  Ground Communications Facility
  Deep Space Instrumentation Facility
  DSN Systems and Projects

Operations and Systems Data Analysis
  SFOF Operations
  GCF Operations
  DSIF Operations
  DSN Systems Operations
  DSN Systems Data Analysis

Technical Facilities
  Antennas
  Buildings
  Utilities

In the section entitled "Description of DSN Systems," the status of recent developments for each of the six DSN systems listed above will be described. The more fundamental research carried out in support of the DSN is reported in Vol. III of the SPS, and JPL flight project activities for missions supported by the DSN are reported in Vol. I.

B. Description of DSN Systems

1. Command System, *K. R. Carter and M. L. Yeater*

a. Functions. The DSN command system provides a medium for command generation, transmission to the spacecraft, and verification at appropriate points, as well as for generation of a command master data record (MDR). The commands are generated in the SFOF, transferred to the DSIF by means of the GCF, and transmitted to the spacecraft after handling by the mission-dependent equipment (MDE) at a DSS.

b. System elements. No standard DSN command system configuration exists at the present time. Each flight project uses a different system configuration, and different sets of procedures, MDE at the DSS, and mission-dependent software in the SFOF. A typical configuration is illustrated in Fig. 1.

The subsystems and equipment at the SFOF that are part of, or used by, a typical command system are as follows:

(1) Data-processing subsystem (SPS 37-46, Vol. III, pp. 164–172).

(2) Display subsystem.

(3) Computer input/output subsystem.

Those of the DSIF are:

(1) Transmitter subsystem.

(2) Recording subsystem.

(3) Telemetry and command data-handling (TCD) subsystem (SPS 37-50, Vol. II, pp. 3–14).

(4) Project-supplied MDE.

c. System operation. A command or set of commands is generated by the SFOF IBM 7094 computer and written on magnetic tape, with hard copy printout by the IBM 7040 computer on the IBM 1301 disk and on cards. A set of mission-dependent IBM 7094 user programs is available for each project.

Commands are delivered from the SFOF to a DSS by one, or a combination, of the following methods:

(1) The IBM 7044 computer reads command data from the disk or from cards and formats the data for

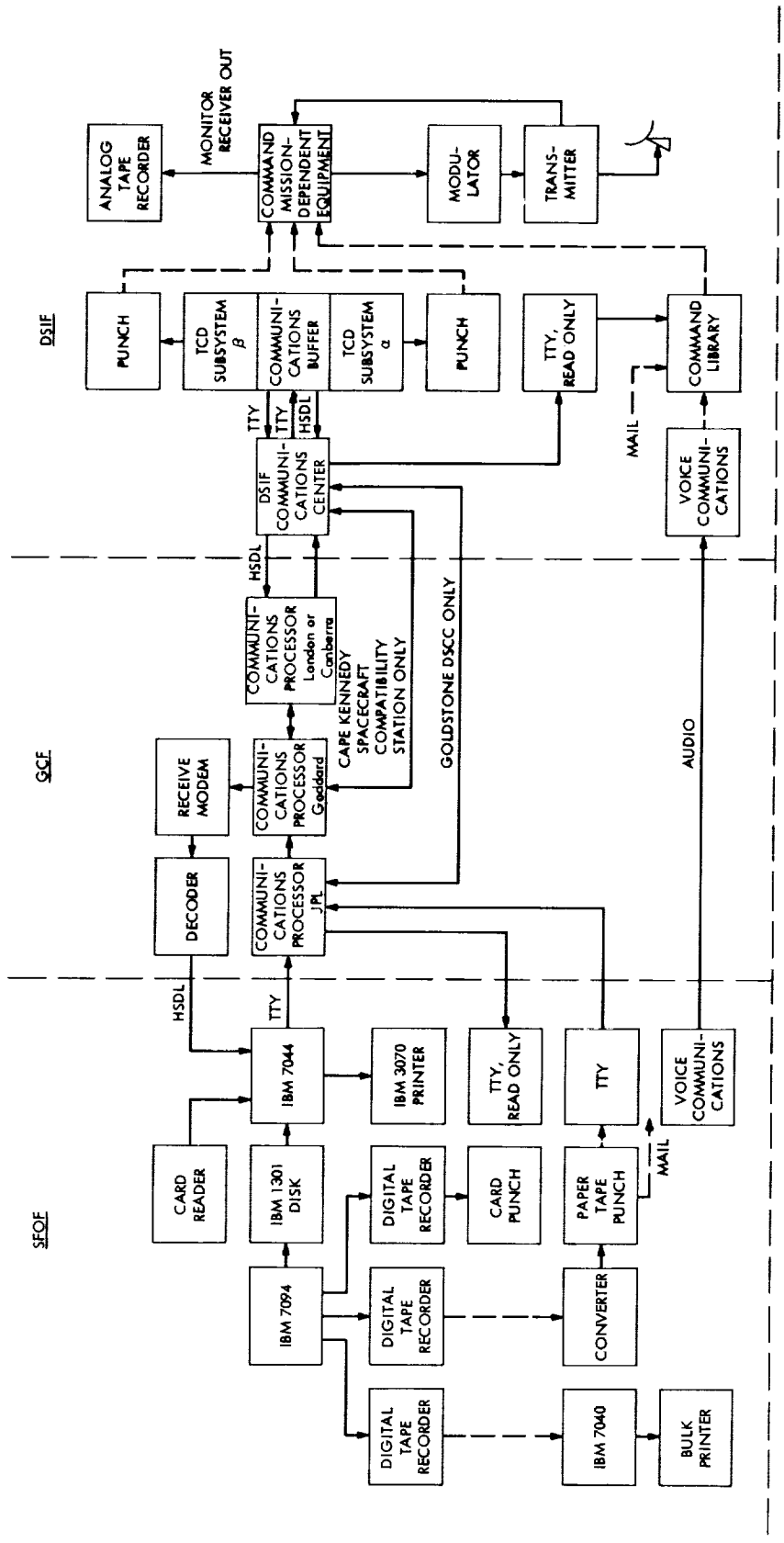

Fig. 1. Typical DSN command system

teletype transmission to the DSS by means of the GCF. The IBM 7044 formatting software is mission-independent.

(2) Command data are converted from IBM 7094 digital magnetic tape to punched paper tape, which is then mailed to the DSS for storage in a command library for later transmission to the spacecraft.

(3) Punched paper tape is read at the SFOF and transmitted by teletype to the DSS.

(4) Commands are transmitted by voice circuits to the MDE operator at the DSS.

(5) Commands are sent by teletype to the DSS TCD subsystem to be punched on paper tape or to be transmitted directly to the MDE by way of the TCD-subsystem/MDE interface. Using the TCD subsystem as part of the command system requires that mission-dependent software have command data-handling capability. The TCD subsystem has a communications buffer for teletype input and a set of MDE hardware interfaces.

After receipt of the commands at the DSS, the MDE provides the modulation signals for transmission to the spacecraft using the DSS transmitter subsystem.

The present command verification procedures are primarily manual operations. At each transfer point, the data are checked for errors and verified. The command data at the DSS MDE is displayed and checked by the MDE command operator. The SFOF is notified of verification using teletype, voice, or high-speed data lines.

Some sets of MDE contain logic for bit-by-bit comparison of the transmitted command with the stored command as it is returned from the RF subsystem. This type of equipment provides a command-inhibit capability (manual or automatic) if an error is detected. Final verification of the transmitted command is obtained using analysis indicators of the spacecraft telemetry stream.

II. Mission Support

A. Introduction

The DSN, as part of the Tracking and Data System (TDS) for a flight project, is normally assigned to support the deep-space phase of each mission. Thus far, responsibility for providing TDS support from liftoff until the end of the mission has been assigned to the JPL Office of Tracking and Data Acquisition. A TDS Manager, appointed by the Office of Tracking and Data Acquisition for each flight project, works with the JPL technical staff at the AFETR to coordinate the support of the AFETR, MSFN, and NASCOM with certain elements of the DSN needed for the near-earth-phase support. A DSN Manager and DSN Project Engineer, together with appropriate personnel from the DSIF, GCF, and SFOF, form a design team for the planning and operational phases of flight support. A typical functional organization chart for operations was shown in Fig. 1, p. 16, in SPS 37-50, Vol. II.

Mission operations design is accomplished in a closely coordinated effort by the Mission Operations System (MOS) and TDS Managers. Mission operations, an activity distinct from the management element MOS, includes: (1) a data system, (2) a software system, and (3) an operations system. The data system includes all earth-based equipment provided by all systems of the flight project for the receipt, handling, transmission, processing, and display of spacecraft data and related data during mission operations. Except for relatively small amounts of mission-dependent equipment supplied by the flight project, all equipment is provided and operated by the DSN. In the near-earth phase, facilities of the AFETR and the MSFN are included. The DSN also operates and maintains the mission-dependent equipment.

The software system includes all computer programs and associated documentation. The mission-independent software is provided as part of the DSN support. The mission-dependent software developed by the flight project is operated and maintained for the project by the DSN.

The operations system includes the personnel, plans, and procedures provided by both the MOS and TDS

which are required for execution of the mission operations. The mission operations design organization is supported by the DSN in the manner shown in Fig. 2, p. 17, in SPS 37-50, Vol. II. The DSN Project Engineer heads a design team composed of project engineers from various elements of the DSIF, GCF, and SFOF. This team is primarily concerned with the data system defined above. The designs of the other systems are the responsibilities of the software system design team and the mission operations design team. The DSN supports these activities through its representative, the DSN Project Engineer.

The mission operations design process which the DSN supports was shown in Fig. 3, p. 18, in SPS 37-50, Vol. II. From the Project Development Plan and the Mission Plan and Requirements are derived the guidelines for operational planning and the project requirements for TDS support. The mission operations design team formulates system-level functional requirements for the data, software, and operations systems. From these requirements, as well as from the TDS support requirements, the DSN design team formulates the DSN configuration to be used in support of the project. It also supports, through the DSN Project Engineer, the activities of the software and mission operations design teams in designing the software and operations systems. The interface definitions are accomplished by working groups from these design teams.

The TDS support required by the project is formulated in the Support Instrumentation Requirements Document (SIRD) and the Project Requirements Document (PRD). The PRD states project requirements for support by the U.S. Department of Defense through the AFETR. The NASA Support Plan (NSP) responds to the SIRD in describing the DSN, NASCOM, and MSFN support.

B. Planetary Flight Projects

1. *Mariner V* Extended Mission Operations Support, D. J. Mudgway

Planning of DSN support for the *Mariner* V Extended Mission Operations (MEMO) Project is essentially complete, and implementation and testing have begun in preparation for the expected reacquisition of the *Mariner* V spacecraft signal about July 22, 1968.

a. Network configuration

DSIF support. The MEMO Project will be supported by the 210-ft-antenna Mars DSS and a combination of 85-ft-antenna DSSs when communication capability allows. The following coverage requirements will be input to the DSN scheduling system:

Interval	Required weekly coverage
July 22–Sept. 22	Seven 4-h passes from the Mars DSS
Sept. 22–Dec. 1	Seven 8-h passes from the Mars DSS and the 85-ft-antenna DSSs, including at least one 8-h pass from the Mars DSS for planetary ranging purposes
Dec. 1–7	Seven 8-h passes from the 85-ft-antenna DSSs (Mars DSS being reconfigured)
Dec. 7–Jan. 1	No coverage available
Jan. 1–22	Seven 4-h passes from the Mars DSS

Figure 1 compares the configurations of the existing ground telemetry system at the Mars DSS and the Robledo DSS (the prime stations) and the newly developed multiple-mission telemetry system at the DSSs committed to the MEMO Project on a "best-effort" basis.

GCF support. The teletype data flow plan, preamble, routing indicators, and channel assignments and the circuit activation procedures for voice, high-speed data, and teletype lines have been supplied to the DSSs. To meet a Project request for real-time display of science data at the Massachusetts Institute of Technology and the Universities of Stanford, Iowa, and Colorado, teletype circuits with terminal machines are being provided.

SFOF support. The communications requirements for the mission support area are defined and include a requirement for a high-speed data switching interface to some special mission-dependent equipment. The installation of equipment in the assigned mission support area is essentially complete. The data processing system input/output devices available to the MEMO Project consist of two IBM 3070 printers, two 30 × 30 plotters, one input/output console, one card reader, and one administrative printer.

The first of two software packages is the original *Mariner* Venus 67 software, designated MOP. Only verification of its operational status is required. This software package will be used at the DSSs equipped with the *Mariner* Venus 67 ground telemetry system and in the SFOF.

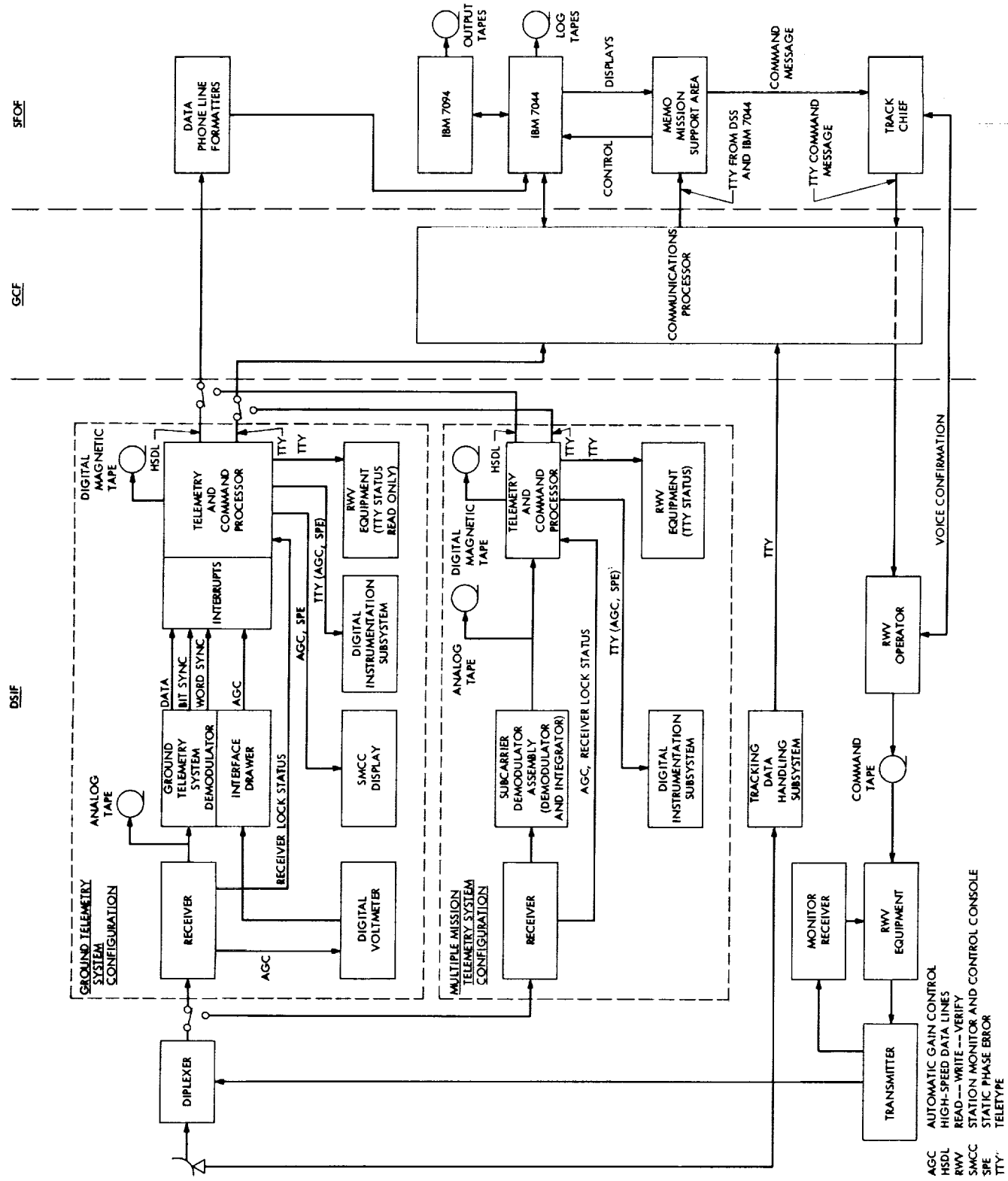

Fig. 1. Network configuration incorporating ground telemetry and multiple-mission telemetry systems

The second software package, designated MOPE, is for use at the DSSs equipped with the multiple-mission telemetry system. The operating features and output formats of the existing MOP program are incorporated in its design; thus, this program is entirely compatible with the existing SFOF software. The functional relationship of the existing MOP and new MOPE programs is shown in Fig. 2.[1]

The hardware to be used in the monitoring area is ready for operation. The following items are included: two selective teletype machines, one IBM 3070 printer, one addressable teletype machine, one Milgo Electronic Corp. printer and one input/output console. Residual plot and print data will be available on a shared basis with the *Pioneer* Project. Real-time monitoring operations will consist of telemetry and tracking data accountability and anomaly detection, telemetry data processing update using reperforated tapes of tracking data, and high-speed-data accountability and anomaly detection. Validation of tracking and telemetry data will be performed as a non-real-time operation.

A new monitoring responsibility is the production of a telemetry master data record (MDR), within 2 to 4 wk of the corresponding station pass, meeting a defined set of criteria. All analog tapes, after return to the SFOF with the corresponding digital telemetry-and-command-processor data tapes, will be used to correct any deficiencies in the original data tapes. After being digitized, the analog tapes will be validated together with the

[1]The implementation plan and related details for the development and testing of these programs was given in Oliver, E. F., *Project MEMO Software Compatibilities*, April 23, 1968 (JPL internal document).

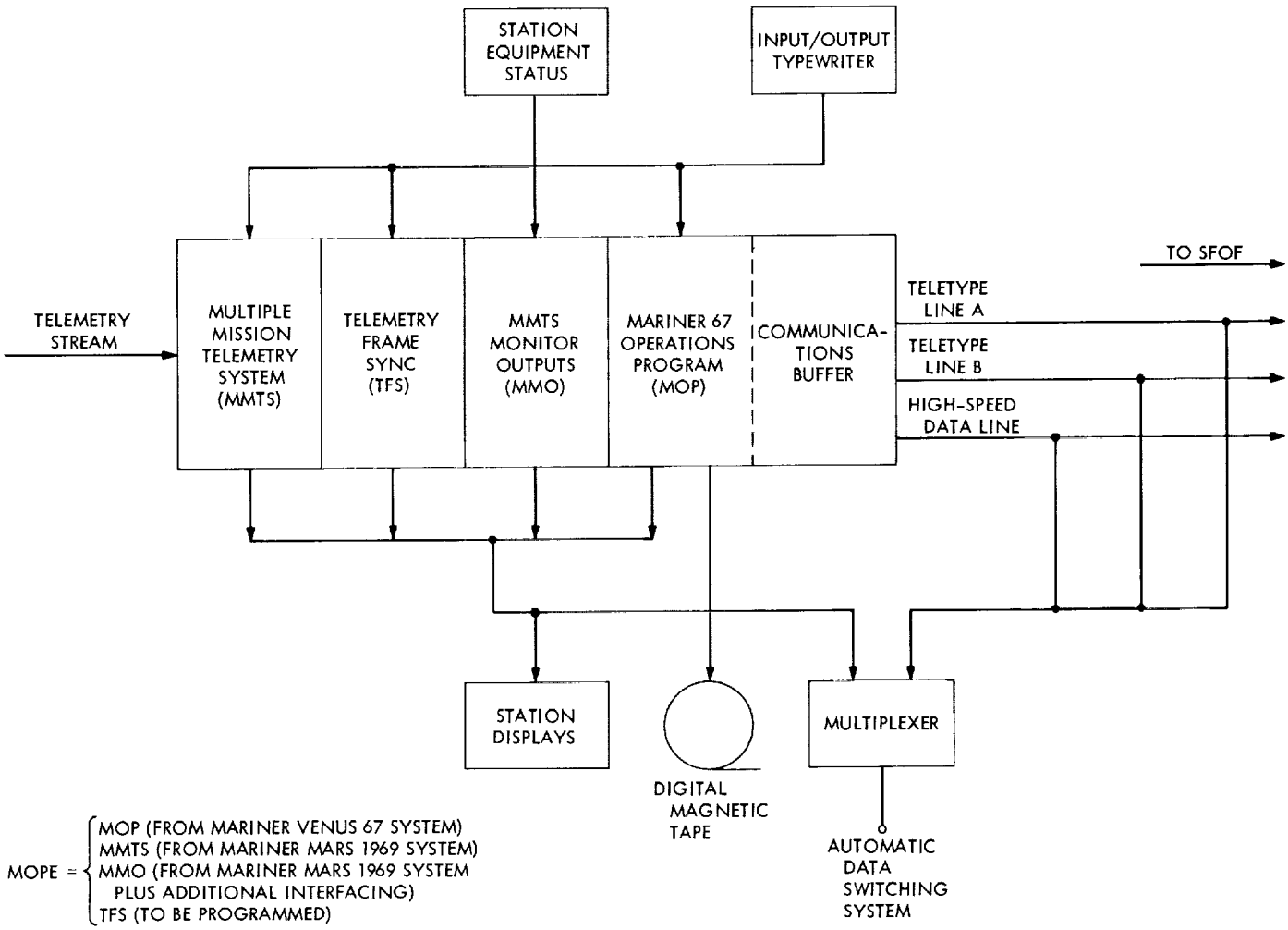

Fig. 2. Functional relationship of MOP and MOPE programs

digital tapes, merged, reformatted (edited), and checked prior to delivery of the master data record to the Project.

b. Validation/readiness testing and operations. Ground telemetry system equipment integration tests and software compatibility tests with MOP programs have been performed at the Mars DSS and the Robledo DSS. In addition, DSIF configuration verification tests and planetary ranging system tests were conducted at the Mars DSS. It is expected that the ranging subsystem will be operational when the spacecraft comes within range of the 210-ft antenna.

Remaining tests include MOPE software integration tests and DSN readiness tests combined with operational verification tests. Every effort was made to make the design of the operations system as close to that of the *Mariner* Mars 1969 operations system as possible to provide some training for the subsequent *Mariner* Mars 1969 missions. Particular attention was devoted to the design of the MEMO command system (Fig. 3).

Beginning in May, several attempts were made to detect the *Mariner V* spacecraft signal using the 210-ft antenna at the Mars DSS and special long-time integration techniques at the Venus DSS. Although these techniques should have made possible the detection of signal levels as low as −190 dBmW, the spacecraft signal was not detected as of June 18. It was concluded that unfavorable polar diagrams due to the spacecraft's attitude precluded the detection of a signal up to that time. However, during the ensuing period, the spacecraft–earth line would be moving rapidly around the spacecraft antenna polar diagrams, and signal levels were expected to increase rapidly. Efforts to detect the signal prior to the scheduled operations on July 22 continued.

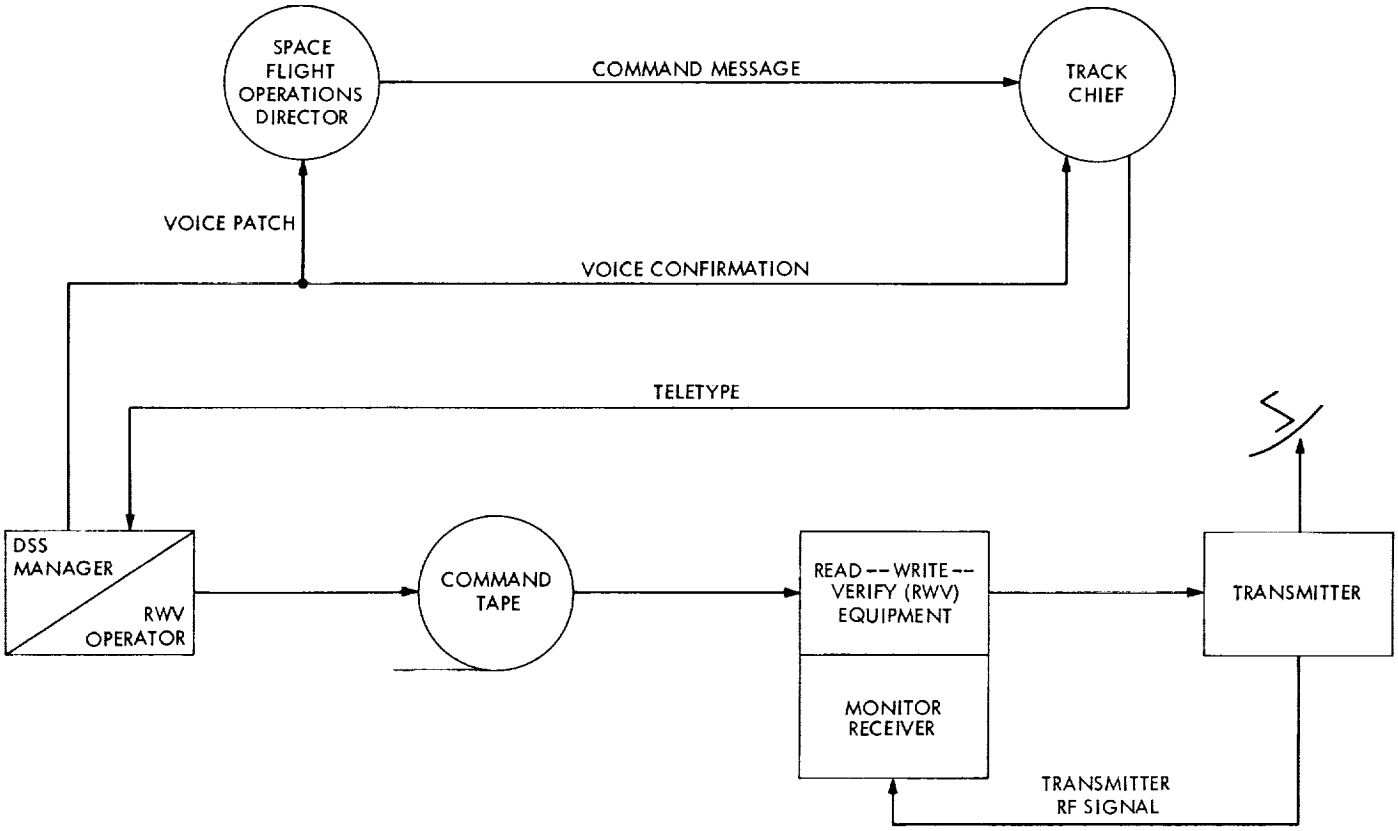

Fig. 3. Command system configuration for MEMO Project

III. Advanced Engineering

A. Tracking and Navigational Accuracy Analysis: DSN Inherent Accuracy Project

1. Introduction, *T. W. Hamilton and D. W. Trask*

The DSN Inherent Accuracy Project was formally established by the DSN Executive Committee in July 1965. The objectives of the project are:

(1) Determination (and verification) of the inherent accuracy of the DSN as a radio navigation instrument for lunar and planetary missions.

(2) Formulation of designs and plans for refining this accuracy to its practical limits.

Achievement of these goals is the joint responsibility of the Telecommunications and Systems Divisions of JPL. To this end, regular monthly meetings are held to coordinate and initiate relevant activities. The project leader and his assistant (from the Systems and Telecommunications Divisions, respectively) report to the DSN Executive Committee, and are authorized to task project members to (1) conduct analyses of proposed experiments, (2) prepare reports on current work, and (3) write descriptions of proposed experiments. The project is further authorized to deal directly with those flight projects using the DSN regarding data-gathering procedures that bear on inherent accuracy.

The various data types and tracking modes provided by the DSIF in support of lunar and planetary missions are discussed in SPS 37-39, Vol. III, pp. 6–8. Technical work directly related to the Inherent Accuracy Project is presented in SPS 37-38, Vol. III, and in subsequent *Deep Space Network* SPS volumes, and is continued in the following subsections of this volume.

Subsections 2, *3*, and *4* discuss results obtained by postflight analysis of tracking data from the *Surveyor*, *Lunar Orbiter* and *Mariner V* missions, respectively. *Subsection 2* covers an intermediate stage of the postflight tracking data analysis for six of the seven *Surveyor* missions. While the DSS locations obtained from the *Surveyor* missions agree well with the combined *Ranger* solutions (SPS 37-43, pp. 18–24), the *Surveyor* values are far more consistent on a flight-to-flight basis than the *Ranger* values were at a corresponding stage in the analysis. This is probably due not only to the improvements made in the DSIF tracking system between the *Ranger* and *Surveyor* series of flights, but also to improvements in both the lunar ephemeris and tropospheric refraction

model, as well as the fact that a heavy reliance was placed on the values of $GM_\oplus$ and $GM_\leftmoon$ (the universal gravitational constants times the mass of the earth and the moon, respectively) as determined from previous missions.

Subsection 3 discusses correlations between the major visible lunar features and systematic variations in the radio tracking data experienced with the *Lunar Orbiter* missions. In SPS 37-51, pp. 28–37, it was demonstrated that the variations in the doppler tracking data from the *Lunar Orbiter* spacecraft are related to the sublunar track of the spacecraft trajectory. This article discusses the correlation of these residuals in a gross sense with major visible features; namely, the maria and the highlands. Data from spacecraft orbits with similar sublunar tracks over the highland area show consistent variations with relatively larger amplitudes than orbit tracks primarily over maria.

An experiment designed to analyze error sources which influence the doppler and ranging systems differently has been previously discussed for the case of *Lunar Orbiter* in SPS 37-44, pp. 28–33, SPS 37-46, pp. 23–38, and SPS 37-48, pp. 4–7. It is envisioned that a calibration technique can be devised to account for the effect of charged particles in the ionosphere and space plasma, providing other error sources (such as the differential variation in the electrical path length through the doppler and ranging systems in the spacecraft transponder and ground tracking station) can be independently removed from the tracking data. However, to date this aspect of the experiment has not been successful using either the *Lunar Orbiter* data previously reported or data from *Mariner V*, which is reported in *Subsection 4*. The *Mariner V* data was obtained using the planetary ranging system, which is an improvement over the ranging system used with *Lunar Orbiter*. At the same time, the *Mariner V* spacecraft was in a far more stable environment than the *Lunar Orbiter*, which at times passed through the lunar shadow. However, differences between range changes obtained by continuously counting the doppler data and those obtained by differencing two range measurements at the ends of this counting interval have been observed which grow to 50 m over a 3-h interval. This is far too large to be accounted for by charged particles or any of the other effects investigated to date.

Subsections 5 and *6* are extensions of previously reported work designed to gain insight into the ability to navigate a distant spacecraft. The first of these continues the analysis reported in SPS 37-51, pp. 37–41, which discusses the effect of target planet gravity on the estimate of navigational accuracy for a deep space probe during the planetary encounter phase. Approximate analytical expressions are presented for the partial derivatives of geocentric range rate of the spacecraft with respect to the *B*-plane encounter parameters. The simplicity of these expressions allows a quick insight into the geometrical properties of the spacecraft range rate prior to the planetary encounter and may be of considerable value for rough calculations of navigational accuracy during the planetary encounter phase.

The accuracy of the continuous minimum variance estimate of the state of a distant space probe determined from a single pass of tracking data was discussed in SPS 37-49, pp. 43–52. *Subsection 6* extends this work for several passes of data, and yields empirical formulas which illustrate the geometrical influences on the accuracy of the estimates. The empirical formulas are accurate for reasonable lateral velocities and are valid up to about ten successive passes of data when the probe is relatively free from planetary gravitational forces and is at an appreciable distance from the sun.

The difficulty in accurately computing the long-term evolution of an orbit of an artificial satellite about a central body and the importance of such calculations were discussed in SPS 37-50, pp. 104–110, and an algorithm for a numerical integration of orbital satellite "lifetime" trajectories was reported. *Subsection 7* describes a computer program (IBM 7094 double-precision Fortran IV) under development which implements this algorithm and briefly discusses the use and output of the program.

2. Deep Space Station Locations and Physical Constants Solutions of Surveyor Missions, S. K. Wong

a. Introduction. This article is concerned with an intermediate stage of the postflight analysis of the tracking data from six of the seven *Surveyor* missions (Refs. 1, 2 and 3). The *Surveyor II* mission was omitted here because of its incomplete flight to the moon. During the *Surveyor* missions, primary tracking support was provided by the Pioneer, Canberra, Johannesburg, and Madrid DSSs.

Some of the error sources which affect this analysis are: (1) the limited numerical computational accuracy of the single-precision orbit determination program (SPODP), (2) discrepancies between the real universe and its model in the SPODP (these include timing errors and polar motion effects; however, the polar changes for the translunar trajectory are insignificant), (3) hardware errors, such as

reference frequency instability and doppler counter error, and (4) ephemeris error.

Timing errors between ephemeris time (ET, used to locate the position of celestial bodies) and universal time (UT.1, determined by the rotation of the earth and used to fix the location of a DSS in space) may affect the orbit determination process by misrepresenting the trajectory of a probe with respect to the earth and other celestial bodies. Differences between UT.1 and Universal Time Coordinated (UTC),[1] must also be reconciled in the orbit determination processes, since the DSN synchronizes with UTC and uses this time as a tag on the data received.

b. Discussion. The parameters estimated in the computations made to determine the best estimate of $GM_\oplus$, GM_ζ (the universal gravitational constant times the mass of the earth and moon, respectively) and station location parameters for the *Surveyor* missions were: the spacecraft position and velocity at an epoch; $GM_\oplus$; GM_ζ; the spacecraft accelerations f_1, f_2 and f_3; the solar radiation constant G; and two components (geocentric radius and longitude) of station location for each tracking station. The spacecraft nongravitational acceleration f_1 is a constant acceleration positive from sun to spacecraft; f_2 is a constant acceleration positive in the direction normal to the sun line with a component in the anti-Canopus direction; f_3 is a constant acceleration in the direction required to complete the right-handed orthogonal system. Only the two-way doppler data were used in the computations.

A priori 1-σ uncertainties of 100 m were used for station location parameters, radius, and longitude. For $GM_\oplus$ and GM_ζ, 1-σ uncertainties of 1.0 and 0.25 km^3/s^2, respectively, were used. These values are approximately three times the 1-σ uncertainties associated with the combined *Ranger* estimates.

In an effort to obtain the best estimate of the solved-for parameters, the solution vector and its associated covariance matrix, were used as *a priori* information for the postmidcourse maneuver data. The method of combining this information is shown in Fig. 1.

$$q_2^* = q_{1,2} + q_m + \Delta q_2^* = \text{best maneuver estimate}$$

where

q_m = nominal inflight maneuver estimate

$q_{1,2} = U(q_1)$

[1]Broadcast by the National Bureau of Standards.

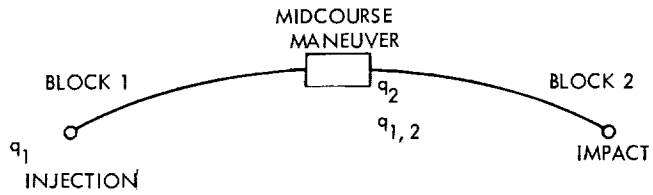

Fig. 1. Method of combining premidcourse and postmidcourse phase

q_2 = solution vector of estimated parameters from block 2 (from midcourse maneuver to impact) data only

$$\Delta q_2^* = (A_2^T W A_2 + \Lambda_{1,2}^{-1})^{-1} [A_2^T W (O_2 - C_2) + \Lambda_{1,2}^{-1}(q_{1,2} - q_2)]$$

and

$$A_2 = \frac{\partial \text{ observable in block 2}}{\partial \text{ estimated parameter}}$$

$O_2 - C_2$ = residuals (i.e., observed data minus calculated data; block 2)

q_1 = solution vector of estimated parameters from block 1 (from injection to midcourse maneuver) data only

U = matrix which maps q_1 to postmidcourse epoch

W = diagonal weighting matrix on observables

$\Lambda_{1,2} = U\Lambda_1 U^T + \Lambda_m$

Λ_m = covariance on maneuver (diagonal purposely set to a very pessimistic value of 100 m/s)

$\Lambda_1 = (A_1^T W A_1 + \tilde{\Lambda}^{-1})^{-1}$
= covariance on estimated parameters from block 1 data only

$\tilde{\Lambda}$ = *a priori* covariance matrix

Spacecraft orbital elements and physical constants estimated from range rate (doppler) data are influenced by tropospheric refraction. The SPODP includes an equation to correct the data for this effect, as follows:

$$\Delta\dot{\rho} = \left(\frac{N_i}{340}\right)\left(\frac{A}{\tau}\right)\left[\frac{1}{(\sin F + B)^{1.4}} - \frac{1}{(\sin G + B)^{1.4}}\right]$$

Table 1. Station locations and parameters (referenced to 1903.0 pole)

Data source	r_s, km	r_s 1-σ standard deviation, m	λ, deg	λ 1-σ standard deviation, m	Geocentric radius, deg	Geocentric latitude, deg
Pioneer DSS						
Mariner II	5206.3357	3.9	243.15058	8.8	6372.0044	35.208035
Mariner IV, cruise	.3404	10.0	067	20.0	.0188	08144
Mariner IV, post-encounter	.3378	37.0	072	40.0	.0161	08151
Pioneer VI, Dec. 1965–June 1966	.3359	9.6	092	10.3	.0286	08030
Goddard land survey, Aug. 1966	.3718	29.0	094	35.0	.0640	08230
Surveyor I, post-touchdown	.3276	2.9	085	23.8	.6446	16317
Surveyor III, in flight	.3408	29.7	100	49.0	−.0230	08192
Surveyor IV, in flight	.3326	41.1	097	49.0	.0129	08192
Surveyor V, in flight	.3256[a]	47.0	092	39.0	.0043	08192
Surveyor VI, in flight	.3337	30.3	091	43.0	.0141	08182
Surveyor VII, in flight	.3359	26.1	086[a]	−36.0	.0164	08184
Tidbinbilla DSS						
Mariner IV, cruise	5205.3478	10.0	148.98136	20.0	6371.6882	−35.219410
Mariner IV, post-encounter	.3480	28.0	134	29.0	.6824	19333
Pioneer VI, Dec. 1965–June 1966	.3384	5.0	151	8.1	.6932	19620
Goddard land survey, Aug. 1966	.2740	52.0	000	61.0	.7030	20750
Surveyor I, post-touchdown	.3474	3.5	130	22.1	.6651	19123
Surveyor III, in flight	.3522	26.5	146[a]	45.0	.6905	19372
Surveyor IV, in flight	.3487	34.8	161	49.0	.6861	19372
Surveyor VI, in flight	.3501	24.6	153	45.0	.6879	19372
Surveyor VII, in flight	.3445	27.1	156	35.0	.6807	19368
Johannesburg DSS						
Combined *Rangers*, LE 3[b]	5742.9315	3.5	27.68572	22.2	6375.5072	−25.739169
Ranger VI, LE 3	.9203	19.7	572	69.3	.4972	9215
Ranger VII, LE 3	.9211	25.5	583	61.3	.4950	9157
Ranger VIII, LE 3	.9372	22.3	548	85.0	.5130	9159
Ranger IX, LE 3	.9626	56.6	580	49.5	.5322	8993
Mariner IV, cruise	.9363	10.0	540	20.0	.5120	9148
Mariner IV, post-encounter	.9365	40.0	557	38.0	.5143	9198
Pioneer VI, Dec. 1965–June 1966	.9332	11.6	569	12.0	.5094	9176
Goddard land survey, Aug. 1966	.9706	39.0	586	43.0	.5410	8990
Surveyor I, in flight	.9380	38.3	578	41.0	.5144	9169
Surveyor III, in flight	.9312	35.0	574	46.2	.5069	9169
Surveyor IV, in flight	.9337	39.3	575	46.8	.5096	9169
Surveyor V, in flight	.9355	44.1	574	31.5	.5116	9169
Surveyor VI, in flight	.9413	25.6	570	43.0	.5180	9169
Surveyor VII, in flight	.9309	32.5	573	36.7	.5062	9165
Robledo DSS						
Lunar Orbiter II, doppler	4862.6067	9.6	355.75115	44.4	6369.9932	40.238566
Lunar Orbiter II, doppler and ranging	.6118	3.4	138	4.0	69.9999	38566
Mariner IV, post-encounter	.6063	14.0	099	24.0	70.0009	38655
Pioneer VI, Dec. 65–June 66	.6059	8.8	103	10.4	70.0060	38715
Surveyor III, in flight	.6054	24.5	126	47.0	70.0046	38701
Surveyor VII, in flight	.6062	27.3	129	39.0	70.0050	38701

[a]This number is questionable because of possible error in the station data.

[b]JPL lunar ephemeris 3 (DE 15); all *Surveyor* in-flight solutions used JPL lunar ephemeris 4 (DE 19).

where

$A = 0.0018958$

$B = 0.06483$

$F = \gamma + (\tau/2)\,\gamma$

$G = \gamma - (\tau/2)\,\gamma$

N_i = index of refraction of station i

γ = elevation angle, deg

τ = doppler averaging time, s

The SPODP "canned" value of N_i is 340 for all stations. However, improved values have been provided (A. S. Liu, SPS 37-50, Vol. II, pp. 93–97) and used for this study. They are:

DSS	N_i
Pioneer	240
Tidbinbilla	310
Johannesburg	240
Robledo	300

The ephemeris used for this study was JPL development ephemeris 19 (DE 19), which has incorporated the updated mass ratios and Eckert's corrections (Ref. 4).

c. Results of station location solutions. The results of these computations are presented in Table 1[2] in an unnatural station coordinate system (geocentric radius, latitude, and longitude) and in a natural coordinate system (r_s, λ, Z), where r_s is the distance off the earth spin axis in the station meridian, λ is the geocentric longitude, and Z is distance along the earth spin axis. Figures 2–9[3] show the station locations obtained for *Surveyor* missions as compared to other various missions. Likewise, Figs. 10–12 indicate results for the relative locations. The first set of figures show that the range of values of the station location parameters obtained from *Surveyor* missions is as shown in Table 2.

If three estimates were omitted from the list (Table 1) the range of station location parameters would be as shown in Table 3.

[2]Values for missions other than *Surveyor* were obtained from Ref. 1.

[3]Terms used in Figs. 2–12: REF. = referenced; DOP. = doppler; CR. = cruise; COMB. = combined; PE = post-encounter; PT = post-touchdown; LE = lunar ephemeris; *LO* = *Lunar Orbiter.*

Table 2. Range of values of station location parameters

DSS	Range of values, m	
	Δr_s	$\Delta\lambda$
Pioneer	15	14
Tidbinbilla	7	15
Johannesburg	10	8
Robledo	0	3

Table 3. Range of values of station location parameters omitting three estimates

DSS	Range of values, m	
	Δr_s	$\Delta\lambda$
Pioneer	8	9
Tidbinbilla	7	8

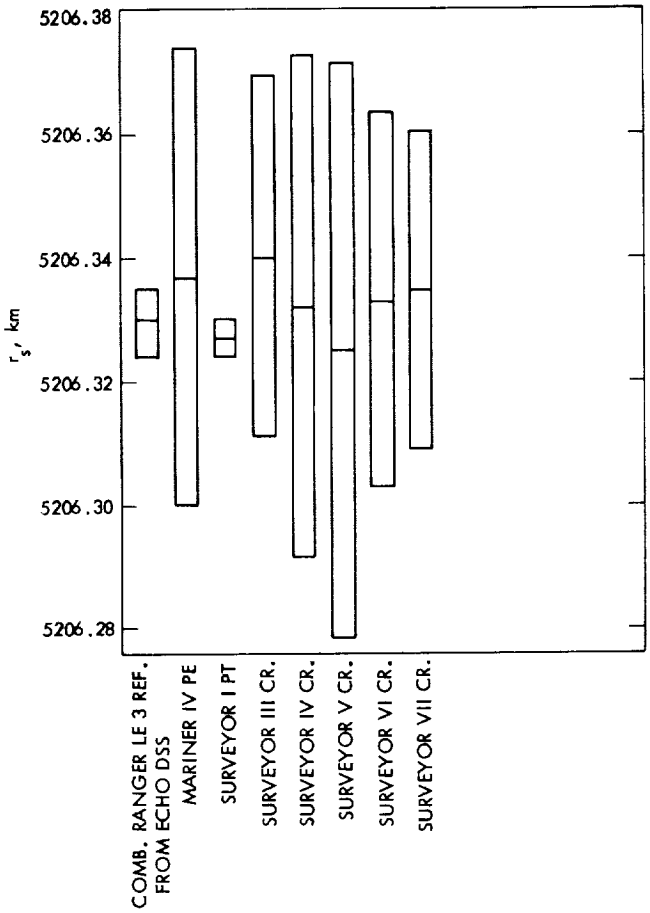

Fig. 2. Distance off spin axis (earth-fixed system, 1903.0 pole, Pioneer DSS)

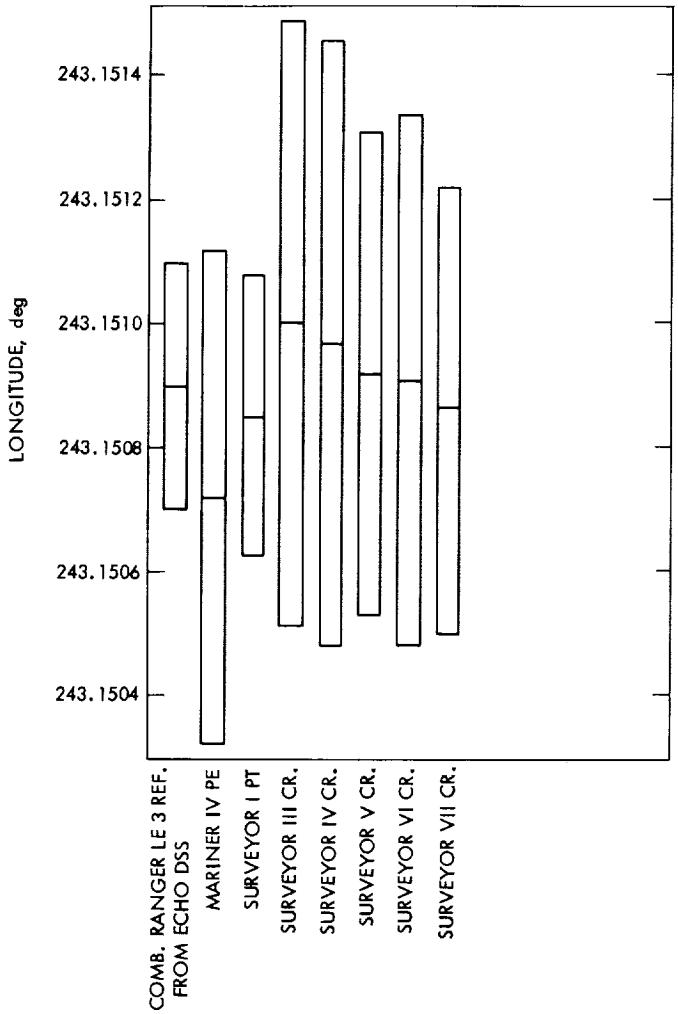

Fig. 3. Geocentric longitude (earth-fixed system, 1903.0 pole, Pioneer DSS)

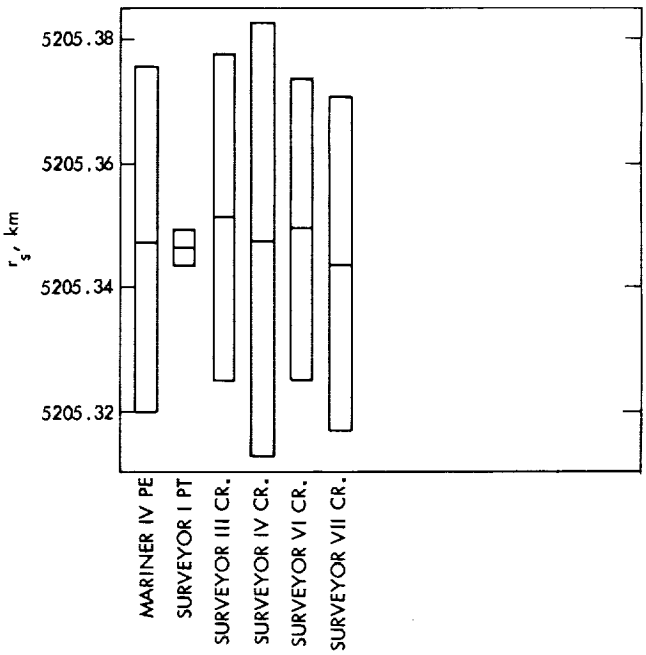

Fig. 4. Distance off spin axis (earth-fixed system, 1903.0 pole, Tidbinbilla DSS)

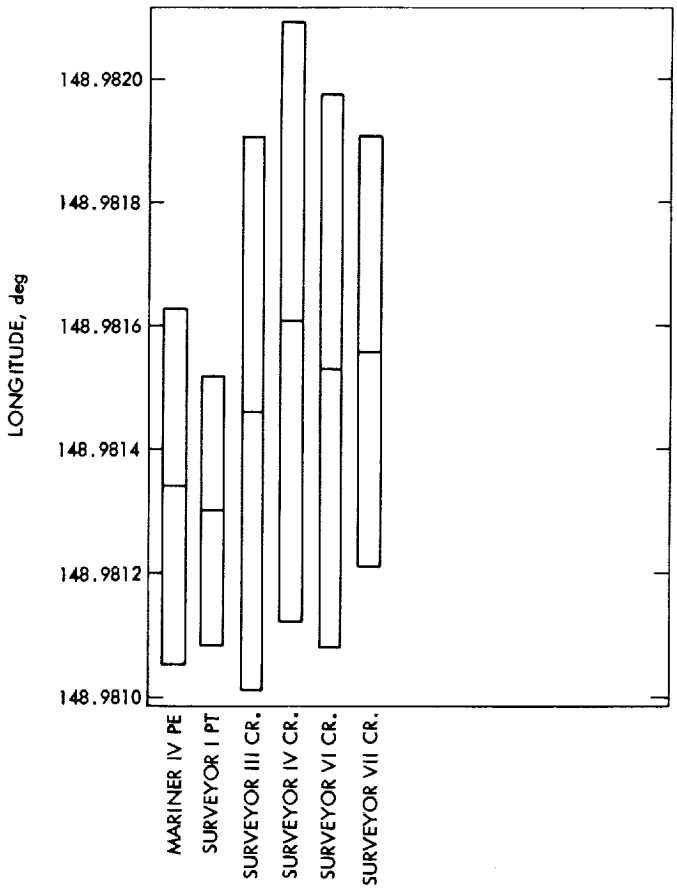

Fig. 5. Geocentric longitude (earth-fixed system, 1903.0 pole, Tidbinbilla DSS)

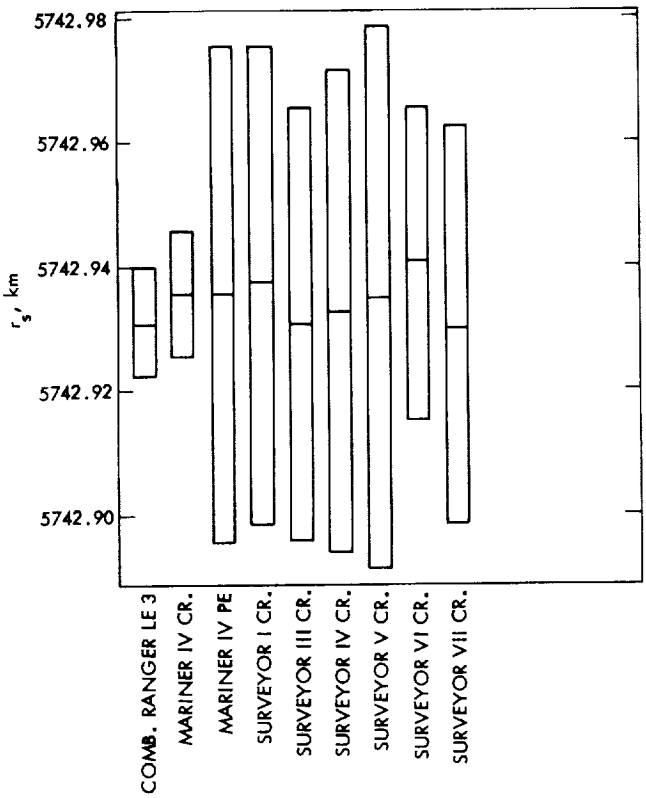

Fig. 6. Distance off spin axis (earth-fixed system, 1903.0 pole, Johannesburg DSS)

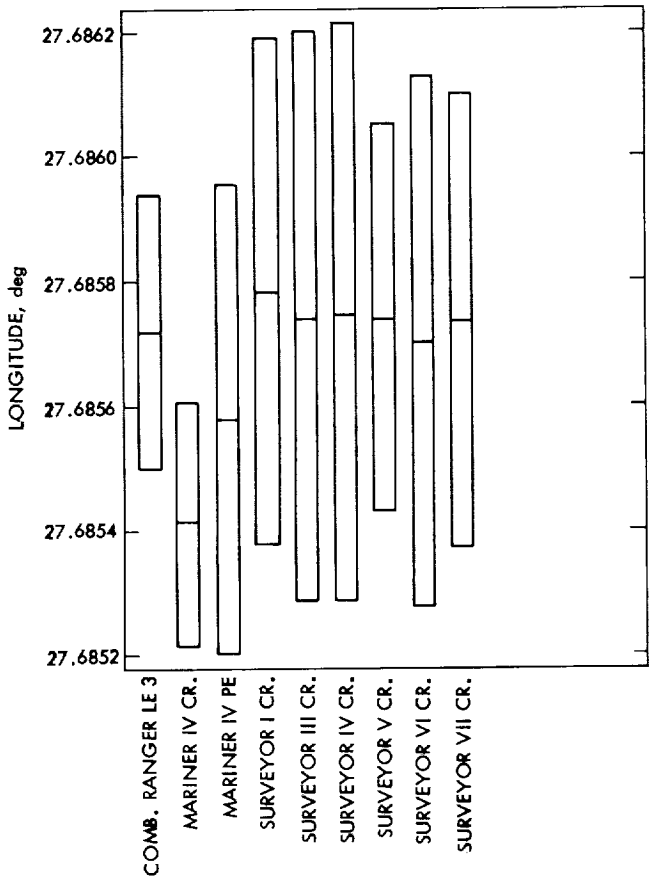

Fig. 7. Geocentric longitude (earth-fixed system, 0903.0 pole, Johannesburg DSS)

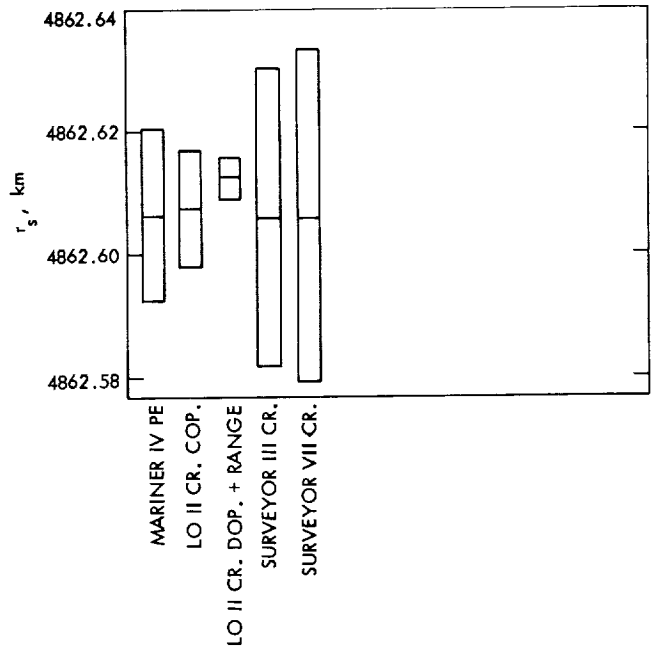

Fig. 8. Distance off spin axis (earth-fixed system, 1903.0 pole, Robledo DSS)

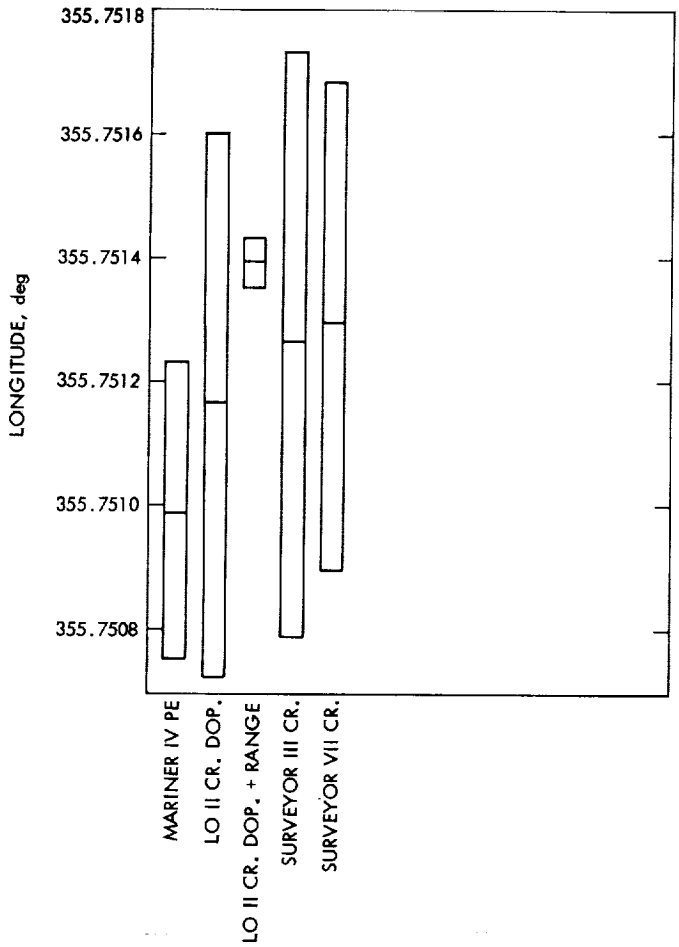

Fig. 9. Geocentric longitude (earth-fixed system, 1903.0 pole, Robledo DSS)

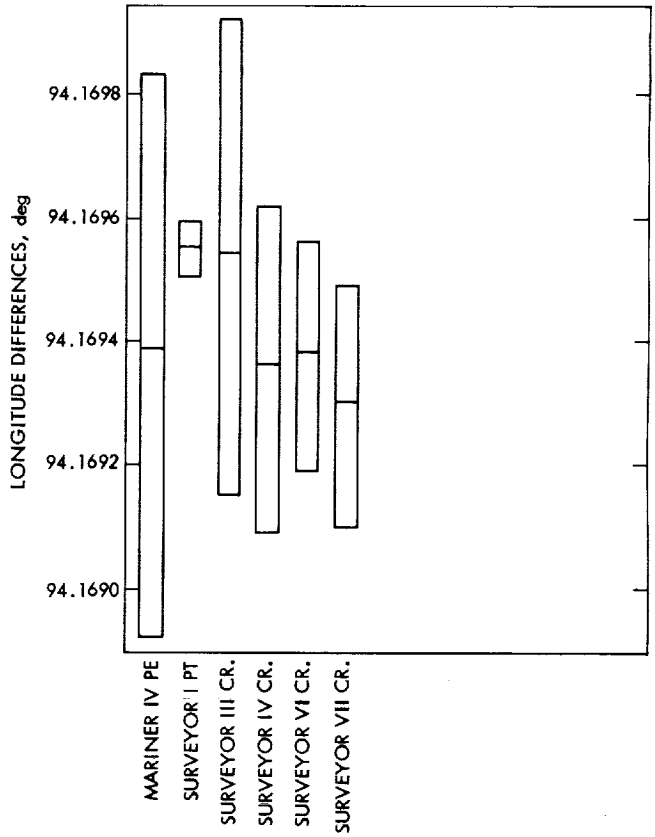

Fig. 10. Geocentric longitude differences (earth-fixed system, 1903.0 pole, Pioneer DSS values minus Tidbinbilla DSS values)

These three estimates are:

(1) r_s for Pioneer DSS; *Surveyor V*.

(2) λ for Pioneer DSS; *Surveyor VII*.

(3) λ for Tidbinbilla DSS; *Surveyor III*.

For this study the obvious biased data or erroneous data had been removed. The observed minus computed residuals indicate possible errors in the Pioneer DSS data for *Surveyor V* and *VII* missions. A more detailed analysis of Pioneer DSS data is required to determine this error. The estimated value of Tidbinbilla DSS geocentric longitude for *Surveyor III* appears to be slightly low when compared to the other *Surveyor* missions. This is probably due to the removal of 7 h of Robledo DSS biased near-moon data between Tidbinbilla and Pioneer DSSs.

The range of values indicates that consistent station locations were obtained from the *Surveyor* missions. The weighted mean of r_s and λ for Pioneer DSS differs only by 4.8 and 4.3 m, respectively, from the combined *Ranger* estimates[4] referenced from Echo DSS. The weighted mean of r_s and λ for Johannesburg DSS also differs by only 4.3 and 2.4 m, respectively, from combined *Ranger* estimates.

d. Results of physical constant solutions. The estimates of $GM_\oplus$ and GM_ζ for the *Surveyor* missions are presented in Table 4. Figures 13 and 14 show how well the $GM_\oplus$ and GM_ζ estimates obtained from the *Surveyor* missions compare to the estimates obtained from other missions. The results indicate that the *Surveyor* missions contribute little information to the GM_ζ estimate, since the 1-σ uncertainty associated with the *Surveyor* GM_ζ estimate decreased from the input *a priori* by only a very small amount. The values obtained for $GM_\oplus$ range from 398601.10 to 398601.27 km^3/s^2. The average $GM_\oplus$ value (398601.16 km^3/s^2) for the *Surveyor* missions is only 0.06 km^3/s^2 from the combined *Rangers* estimate.

[4]Obtained using JPL lunar ephemeris 3.

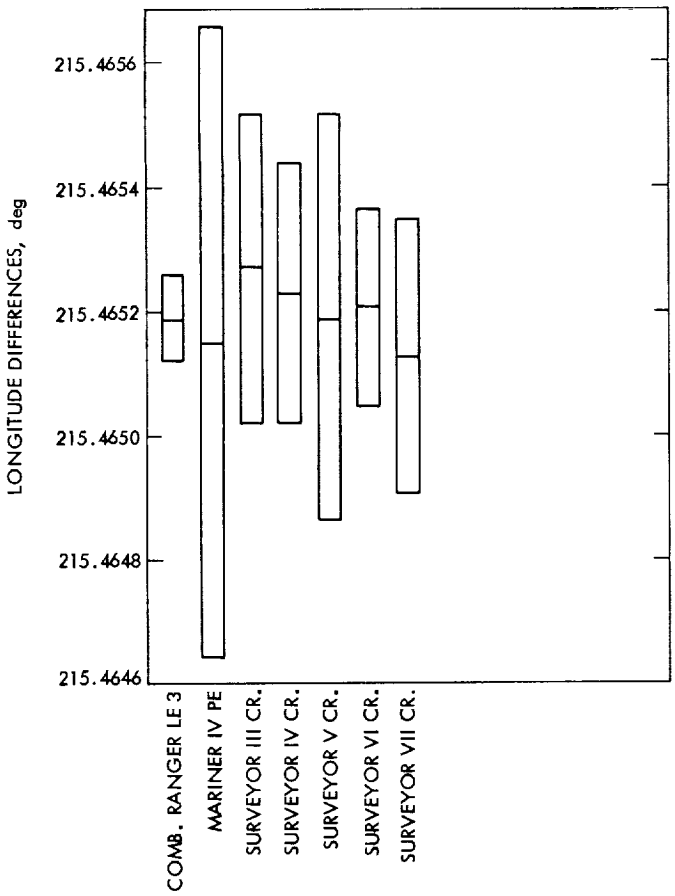

Fig. 11. Geocentric longitude differences (earth-fixed system, 1903.0 pole, Pioneer DSS values minus Johannesburg DSS values)

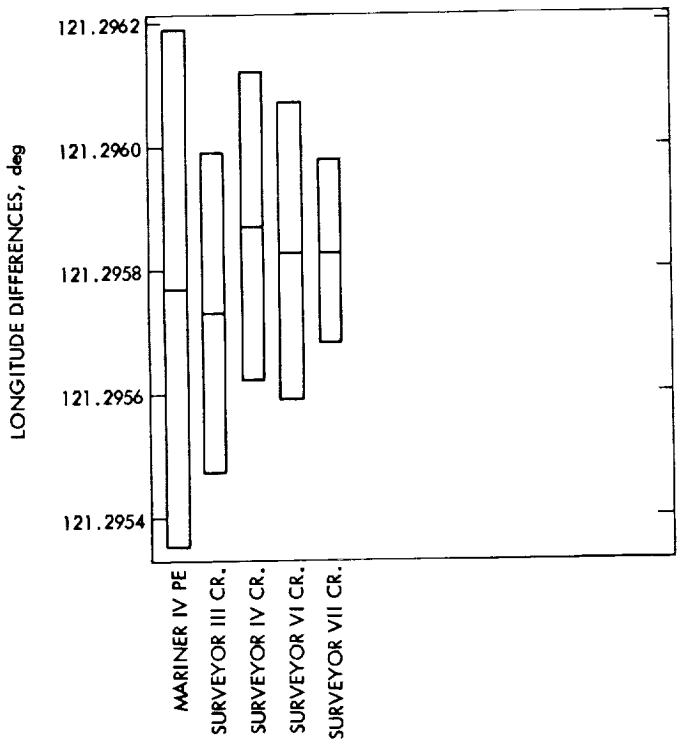

Fig. 12. Geocentric longitude differences (earth-fixed system, 1903.0 pole, Tidbinbilla DSS values minus Johannesburg DSS values)

e. Conclusion. The station locations and physical constants obtained are consistent between *Surveyor* missions and are in agreement with the estimates of other missions. However, some differences are expected between the *Surveyor* estimates and estimates of other missions for the following reasons:

(1) *Surveyor* used an S-band tracking system, whereas missions such as the *Rangers* used an L-band tracking system.

(2) *Surveyor* estimates were computed with a new set of indices of refraction.

(3) Differences in the physical constants used in the trajectory (SPACE) program.

(4) An improved version of the ephemeris was used in *Surveyor* orbit computations.

There are no physical phenomena that justify estimating the spacecraft nongravitational accelerations f_1, f_2, f_3.

Table 4. Physical constants and statistics

Data source	$GM_\oplus$, km^3/s^2	$GM_\oplus$ 1-σ Standard deviation, km^3/s^2	GM_ζ, km^3/s^2	GM_ζ 1-σ Standard deviation, km^3/s^2
Lunar Orbiter II[a] (doppler)	398600.88	2.14	4902.6605	0.29
Lunar Orbiter II[a] (doppler and ranging)	398600.37	0.68	4902.7562	0.13
Combined *Rangers*[b]	398601.22	0.37	4902.6309	0.074
Ranger VI	398600.69	1.13	4902.6576	0.185
Ranger VII	398601.34	1.55	4902.5371	0.167
Ranger VIII	398601.14	0.72	4902.6304	0.119
Ranger IX	398601.42	0.60	4902.7073	0.299
Surveyor I	398601.27	0.78	4902.6492	0.237
Surveyor III	398601.11	0.84	4902.6420	0.246
Surveyor IV	398601.19	0.99	4902.6297	0.247
Surveyor V	398601.10	0.60	4902.6298	0.236
Surveyor VI	398601.11	0.54	4902.6425	0.235
Surveyor VII	398601.11	0.80	4902.6429	0.235

[a] *Lunar Orbiter* values were obtained from SPS 37-48, Vol. II, pp. 12–22.
[b] *Ranger* values were obtained from SPS 37-44, Vol. III, pp. 11–28.

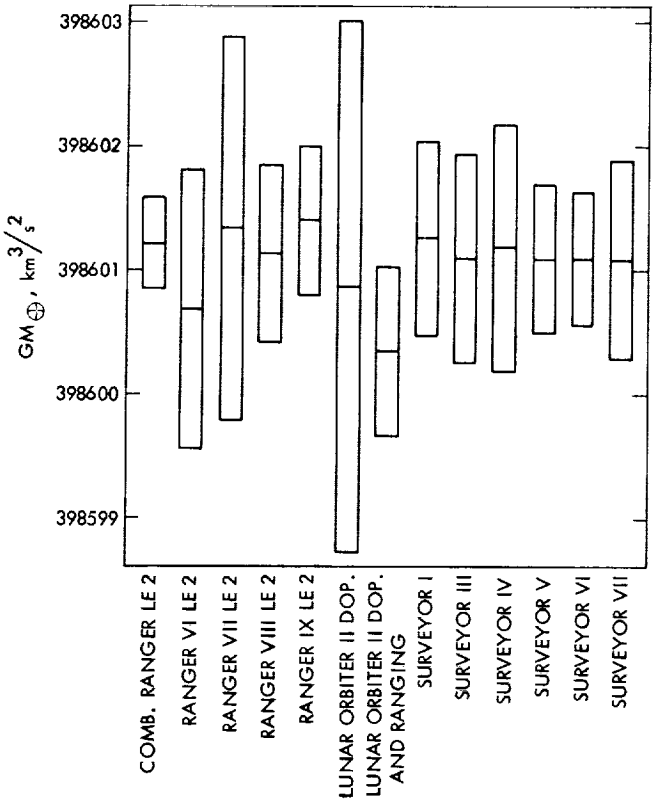

Fig. 13. Comparison of $GM_\oplus$ estimates

However, when these accelerations are estimated, the fit on the near-moon data is significantly improved. This seems to indicate that solving for spacecraft acceleration compensates for the near-moon orbit-determination-program model inadequacies. Efforts are being continued to improve this set of estimates and publish a set of combined *Surveyor* station locations and physical constants.

References

1. Thornton, T. H., Jr., et al., *The Surveyor I and Surveyor II Flight Paths and Their Determination From Tracking Data*, TR 32-1285, Jet Propulsion Laboratory, Pasadena, California (in process).
2. O'Neil, W. J., et al., *The Surveyor III and Surveyor IV Flight Paths and Their Determination From Tracking Data*, TR 32-1292, Jet Propulsion Laboratory, Pasadena, California (in process).
3. Labrum, R. C., et al., *The Surveyor V, Surveyor VI, and Surveyor VII Flight Paths and Their Determination From Tracking Data*, TR 32-1302, Jet Propulsion Laboratory, Pasadena, California (in process).
4. Eckert, W. J., and Smith, H. F., Jr., *Astronomical Papers of the American Ephemeris*, Vol. 19, Pt. II. Nautical Almanac Office, U. S. Naval Observatory, U. S. Government Printing Office, Washington, D. C.

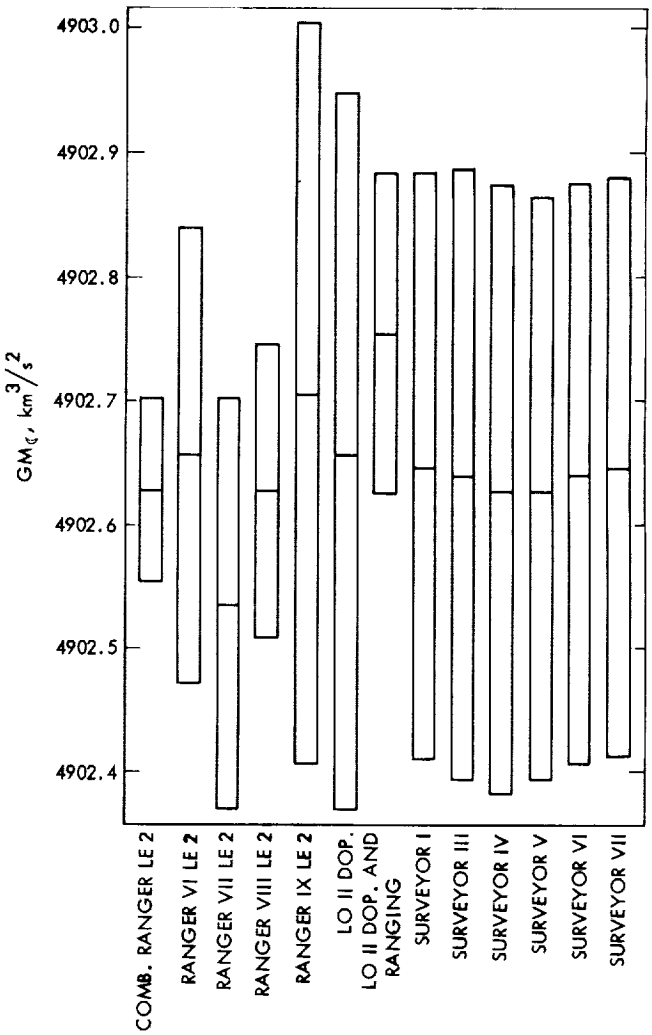

Fig. 14. Comparison of GM_ζ estimates

3. Correlations Between Major Visible Lunar Features and Systematic Variations in Radio-Tracking Data Obtained From *Lunar Orbiter III*,

W. L. Sjogren and P. M. Muller

In SPS 37-51, Vol II, pp. 28–37, it was demonstrated that the variations in the doppler tracking data from the *Lunar Orbiter III* spacecraft are indeed related to the sublunar track of the spacecraft trajectory, and mention was made that there was some correlation between the tracking data and major visible lunar features. These visible features are essentially two gross areas, namely, the maria and the highlands; the maria being Mare Nubium and its adjacent maria and the highlands being the area between zero and 30 deg east longitude and zero and 30 deg south latitude. Data from spacecraft orbits with sublunar tracks over these areas show consistent variations with relatively larger amplitudes than

those of other orbit tracks, primarily those over certain maria.

Such tracks are displayed in Fig. 15 where tracks a and b are over maria and highland, and track c is primarily over maria. The variations in the doppler data for the three different tracks, after differencing with a fit to a theoretical universe model having a triaxial moon, are shown in Fig. 16 (i.e., residual plots). Of course, the amplitude of the residuals is dependent on the altitude h of the spacecraft over the features (proportional to $1/h^2$), but the primary correlation to note is the slope of the residual, for it is the direct measure of the acceleration produced by some mass distribution. A positive slope on

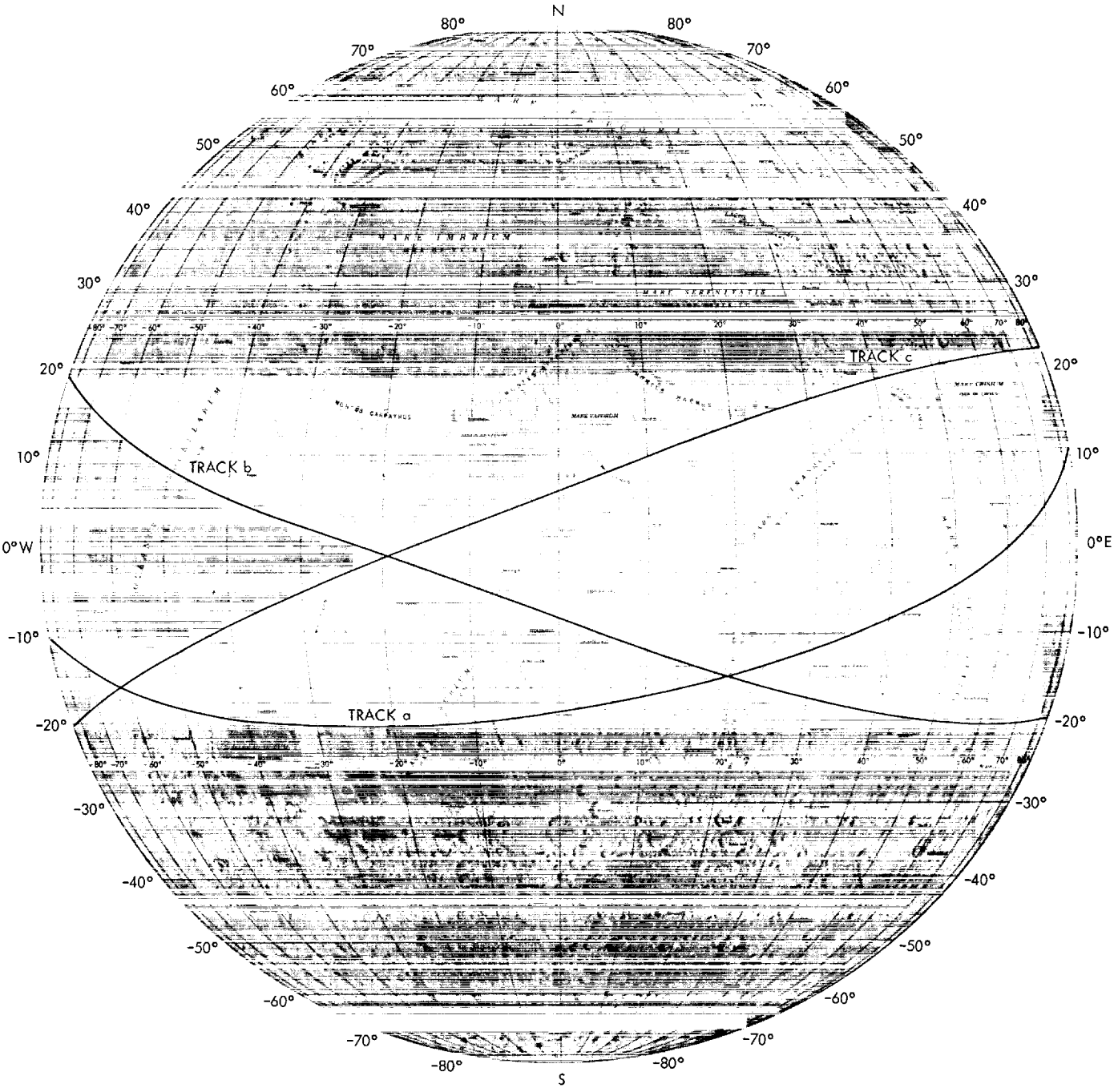

Fig. 15. Lunar map showing *Lunar Orbiter III* orbit tracks

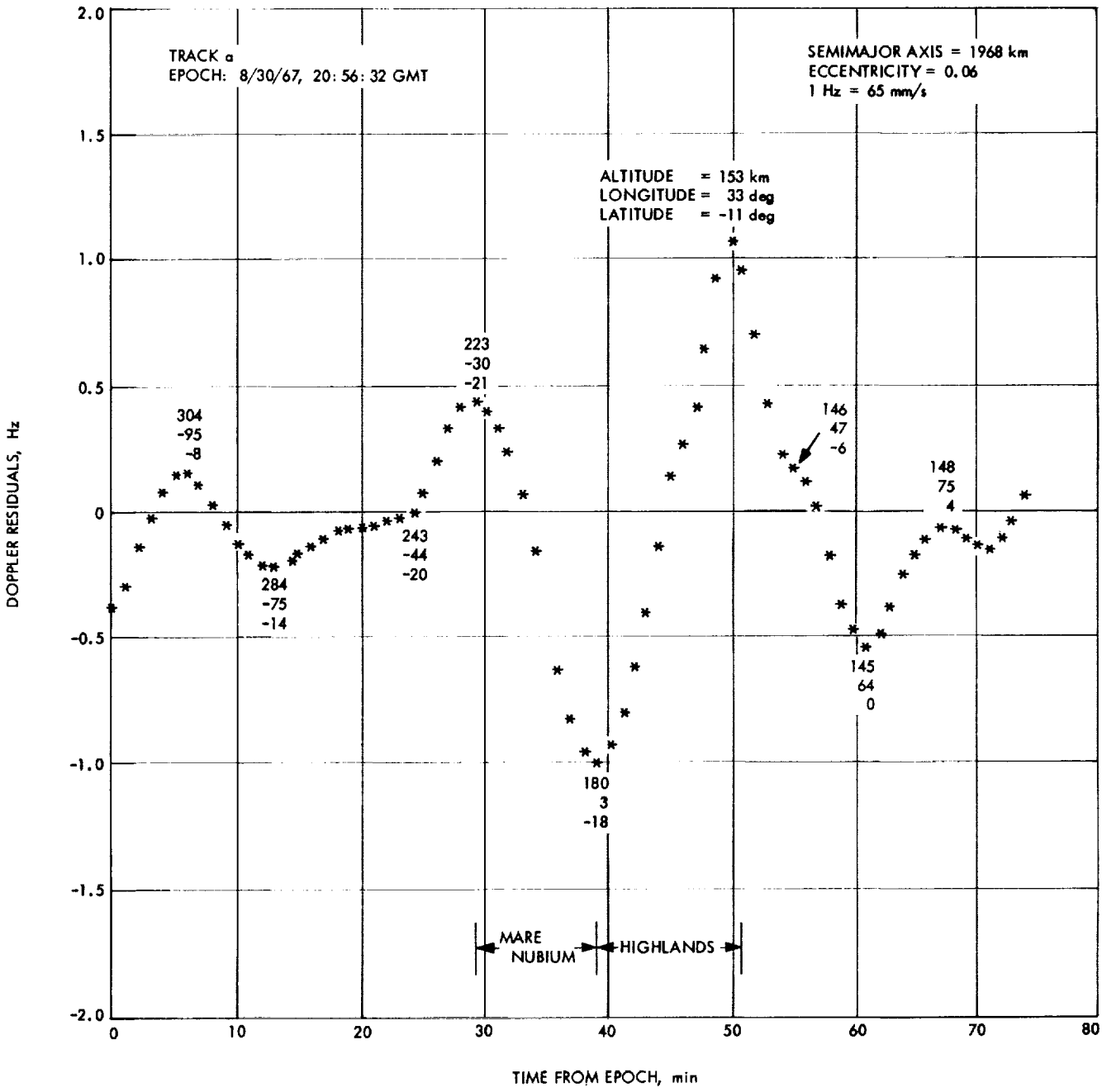

Fig. 16. *Lunar Orbiter III* doppler residuals

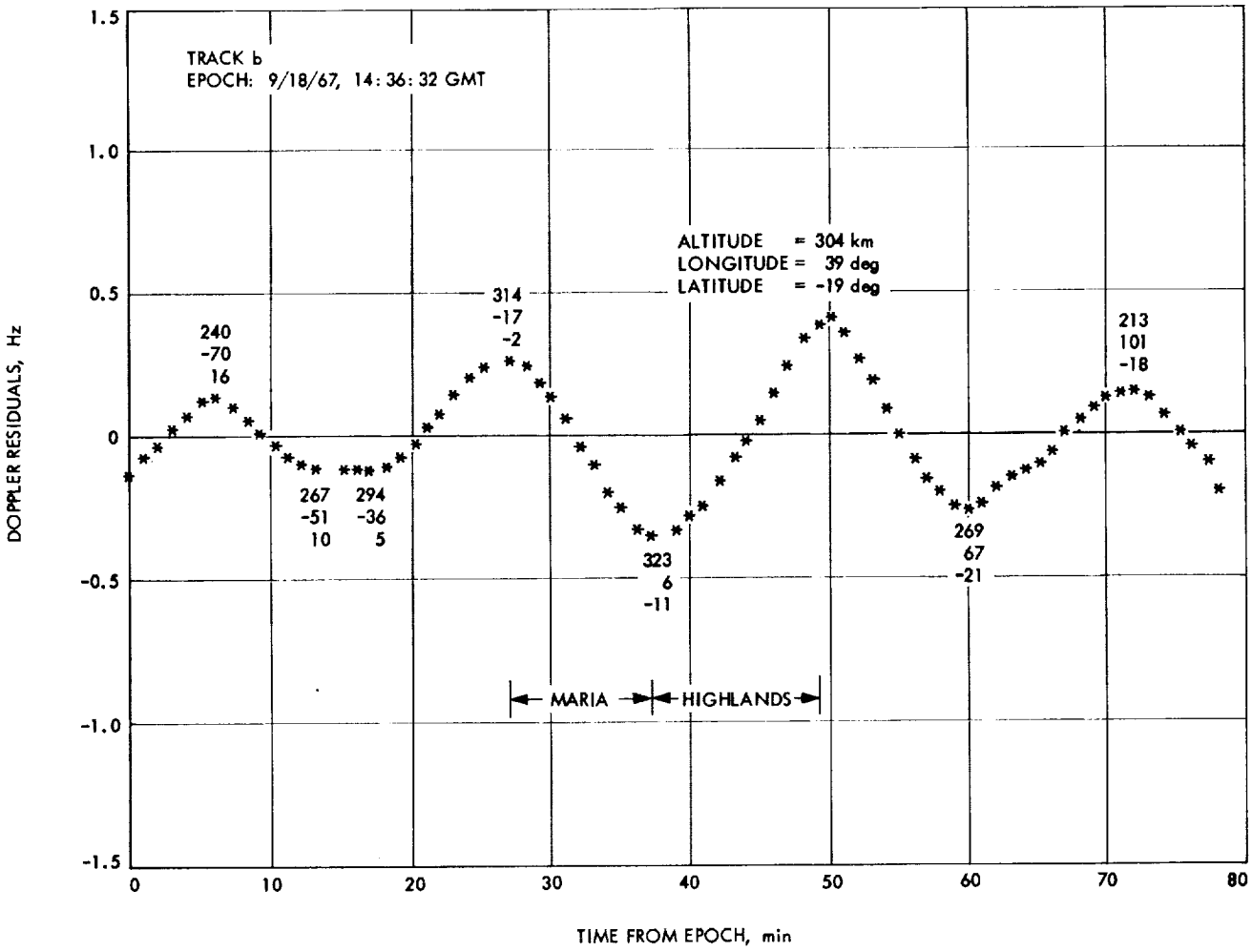

Fig. 16 (contd)

the residuals indicates a positive acceleration. In both Figs. 15 and 16, particularly in the longitudes of the tracks a and b, a definite correlation is apparent between the slopes of the residuals when the spacecraft is passing over a mare (negative) and when it is passing over a highland (positive)—the highlands produce an increase in velocity. These two tracks are representative of many orbits over these areas; all of which display these same characteristics.

If the assumption is made that the disturbing mass causing the positive acceleration in the highland area for tracks a and b (both tracks are rather close in this area) is the same, then an approximation to an effective mass depth can be calculated by the relationship that the acceleration is proportional to $1/h^2$, where h is the altitude of the spacecraft above the mass center. The resulting depth is some 30 km below the mean radius of 1738, and the corresponding mass is approximately 0.5×10^{-6} that of the entire moon.

These are gross features, since even craters like Copernicus are averaged out in each data sample. The data are averaged over 1 min, and in that time the spacecraft has traveled 100–120 km, the entire spread of Copernicus. The features mentioned here cover 600–1000 km. However, in analyzing higher sample rate data (1/10 s), no systematic effects were seen within the noise level of 0.5 mm/s.

Presently data reduction is proceeding on some polar orbits. The initial review of the results shows good correlation between the residuals and the sublunar track. The regions of Mare Imbrium and Mare Serenitatis display high amplitude accelerations, presumably caused by submerged mass distributions. Analysis of the data should give an estimate of this distribution.

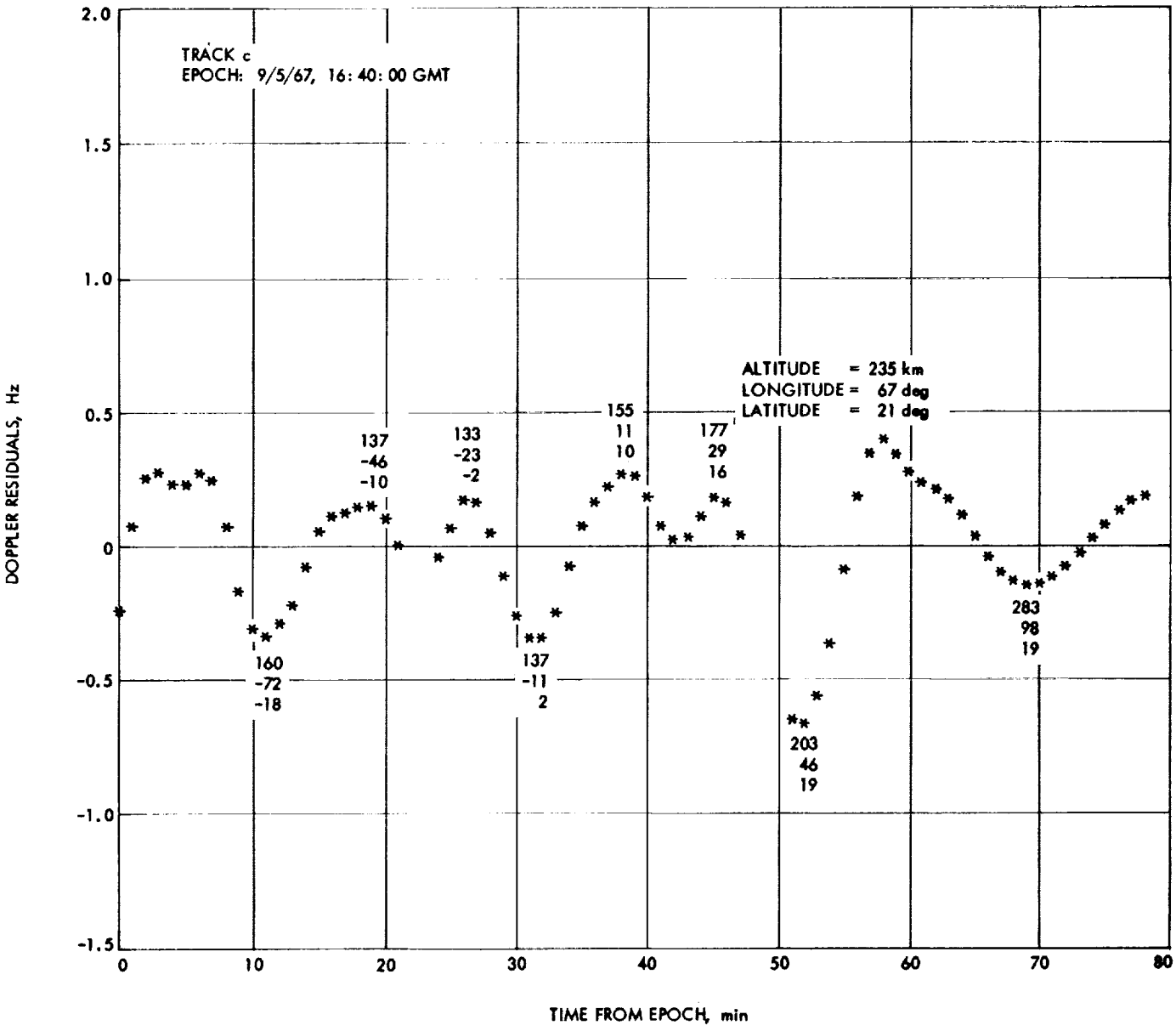
TRACK c
EPOCH: 9/5/67, 16: 40: 00 GMT
ALTITUDE = 235 km
LONGITUDE = 67 deg
LATITUDE = 21 deg
DOPPLER RESIDUALS, Hz
TIME FROM EPOCH, min
2.0
1.5
1.0
0.5
0
-0.5
-1.0
-1.5
0
10
20
30
40
50
60
70
80
160
-72
-18
137
-46
-10
133
-23
-2
137
-11
2
155
11
10
177
29
16
203
46
19
283
98
19

Fig. 16 (contd)

4. *Mariner V* Differenced Range–Integrated Range Rate Experiment, F. B. Winn

a. Introduction. The doppler-ranging calibration experiment was designed to analyze error signatures which influence doppler and ranging systems differently. Under the assumption that the ionospheric charged particle effects constituted the preponderance of error signature, the experiment was to provide the means to measure charged particle effects on the data. Liu (SPS 37-48, Vol. II, pp. 30–37) was the first to attempt to solve this problem, utilizing *Lunar Orbiters II* and *IV* ranging and doppler data sets. The results of that effort are similar to the conclusions of this article. To date, the self-contained calibration inherent to the data pair, ranging and doppler, has been unusable, in that other unknown larger error signatures have contaminated the data samples.

b. Analysis. Mars DSS received tracking data from the *Mariner V* probe at one voltage-controlled oscillator (VCO) setting during each of the following time periods:

Pass	GMT, 1967	
	From day:h:min	To day:h:min
27	191:19:32	191:21:51
39	203:21:02	203:22:54
40	204:19:42	205:01:53

The tracking data types acquired were by research and development planetary ranging units (PRU) (SPS 37-42, Vol. III, pp. 52–56) and coherent two-way doppler (CC3) (Ref. 1).

The net mean difference between PRU and CC3 for consecutive minute intervals throughout the durations of the three passes was computed (SPS 37-44, Vol. III, pp. 28–33) from the following expression

$$\Delta = \{R_t - R_I - (K/f_q)\,[(CC3_t - CC3_I) - 10^6\,(T_t - T_I)]\}\,C$$

where

R_I = octal range converted to decimal at initial time (round-trip range, s)

R_t = octal range converted to decimal at time t (round-trip range, s)

$CC3_I$ = cumulative doppler count at initial time, cycles

$CC3_t$ = cumulative doppler count at time t, cycles

$T_t - T_I$ = time interval of time t minus initial time, s

$$K = \frac{1}{96}\,(240/221)$$

f_q = VCO frequency

C = velocity of light, m/s

The irregular Δ function profiles are depicted in Figs. 17, 18, and 19.[5] The profiles represent the disagreement in range change between the PRU and integrated CC3 data types. The smooth curve is the probe's elevation relative to the Mars DSS astronomical horizon.

c. Charged particle effects. Both data types, PRU and CC3, are affected by the charged particle concentrations characteristic to the space plasma and ionosphere mediums. Electron mediums retard the ranging signal (group velocity) and advance the doppler signal (phase velocity) (Ref. 2). The magnitudes of these influences on the two data types are equal and opposite. The magnitudes of the effects are directly dependent upon the effective number of electrons along the ray path. It was the primary purpose of this experiment to evaluate the charged particle influences, but, as will be shown, other systematic error sources are masking over the sought-after signature.

d. Space plasma. The total electron count to which the data types were subjected can be ascertained. Mean interplanetary medium plasma electron densities at a heliocentric distance of 1 AU were found to be between 5 and 10 electrons/cm^3 by plasma detectors aboard *Pioneers VI* and *VII* (Ref. 3). If 8 electrons/cm^3 is adopted as a mean electron density,[6] the 10^7-km earth-probe distance for pass 40 would produce only a 1.6-m difference between the PRU and CC3 data types.

e. Ionosphere. Ionospheric electron content histories are derived from the Stanford Radio Science Laboratory Applied Technology Satellite Faraday rotation measurements. Figs. 20 and 21 show the ionospheric electron effective total counts for the Mars DSS *Mariner V* subionospheric points.

① Zenith slant range total electron count history.

② Slant range total electron count history for *Mariner V* meridian passage subionospheric point.

[5]Programming by R. N. Wimberly.

[6]*Pioneer VI* plasma detectors measured a mean electron density of less than 10 electrons/cm^3 on Day 204 (private communication from Taylor Howard, Stanford Radioscience Laboratory).

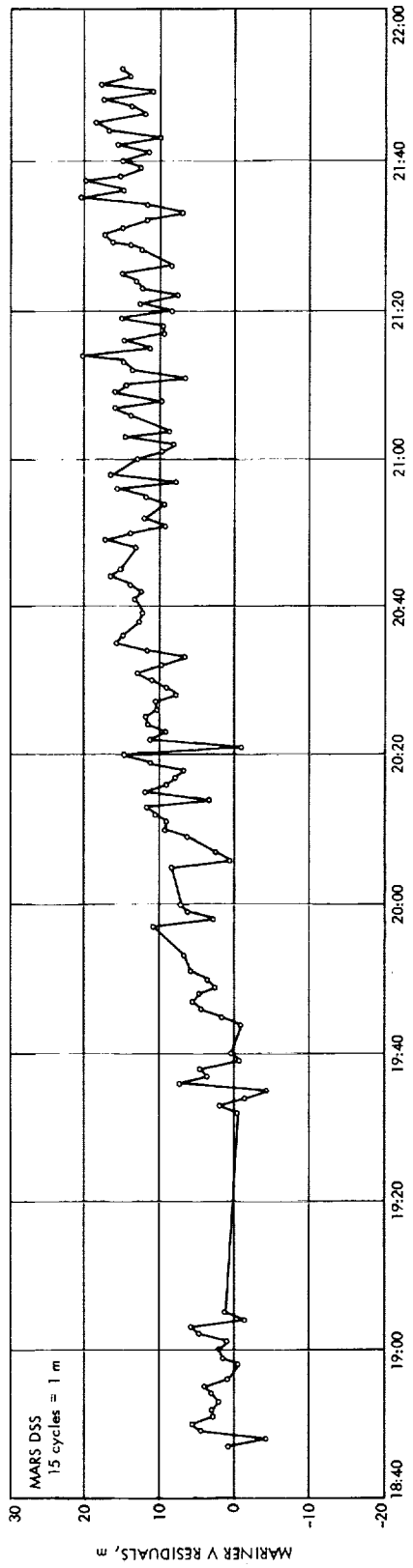

Fig. 17. Pass 27, Day 191, 1967 Δ function profile

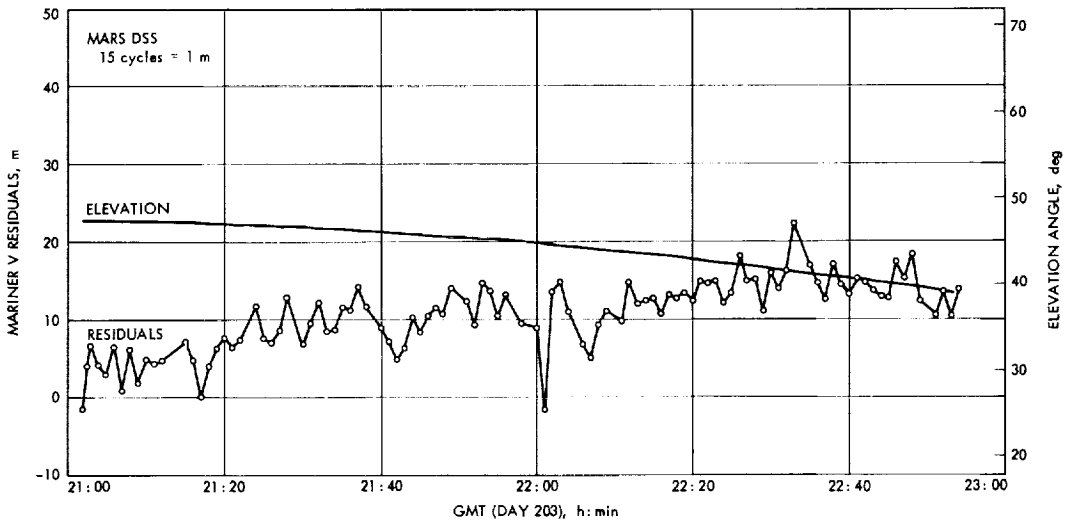

Fig. 18. Pass 39, Day 203, 1967 Δ function profile

③ Slant range total electron count history for the *Mariner V* acquisition subionospheric point.

④ Slant range total electron count history for the *Mariner V* termination subionospheric point.

The broken profile is the ionospheric charged particle influence on the Δ function (10^{17} electron = 1 m). Fig. 21 shows that a 7-m retardation of the ranging code coupled with a 7-m advance of the doppler signal will provide a 14-m maximum magnitude for the pass 40 Δ function. Not only does the maximum magnitude as indicated by the ionospheric study fall far short of the computed differences of the observables, but the ionospheric signature does not resemble the Δ function profile. Similarly, the pass 27 Δ function does not correlate with the ionospheric density profile. Although the ionosphere is known to be a significant influence on the Δ function, it is not the primary influence to which the available data samples were subjected.

f. Mariner V ranging transponder delay. Ranging transponder delay characteristics as functions of temperature, signal-to-noise ratio, and transponder frequency offset have been investigated. The *Mariner V* calibration in conjunction with the known temporal environmental and operational influences on the probe indicates that the spacecraft's hardware did not induce any significant retardation to the ranging code.

g. Temperature-dependent ranging delay. The calibration of temperature influence on the ranging transponder shows a constant 900-ns ranging code delay through the radio subsystem in the temperature range of 50 to 100°F. Figure 22 shows the temperature history of the probe with the near-constant temperatures of passes 27, 39 and 40 indicated. (These temperatures are regarded as fixed for any of the pass intervals.) On the basis of this evidence, transponder temperature variation is excluded as a possible cause of the differenced range–integrated range rate Δ residuals.

h. Ranging transponder delay — frequency-offset-dependent. The Mars DSS has a spin axis distance of 5204 km, and thus the station has a 400-m/s rotation velocity. At S-band frequencies this diurnal rotation velocity amounts to a 7.4-kHz doppler shift for the pass 40 tracking period. The frequency offset-ranging transponder delay calibration (Fig. 23) indicates that the induced transponder delay which corresponds to a frequency offset is only 4.2×10^{-5} m/Hz. Thus, a 7.4-kHz offset will result in a ranging transponder delay of only 0.3 m.

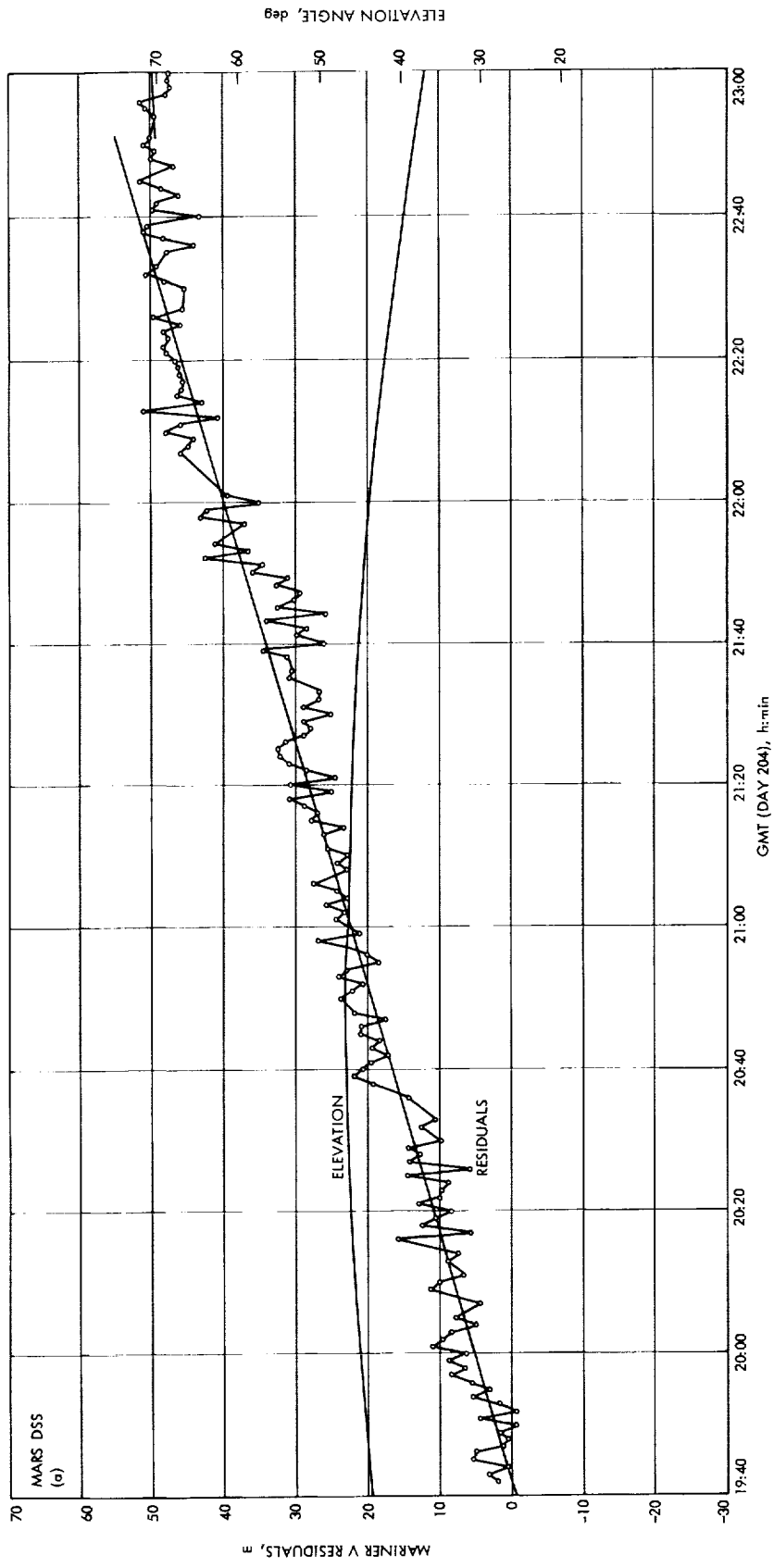

Fig. 19. Pass 40, Day 204–205, 1967 Δ function profile

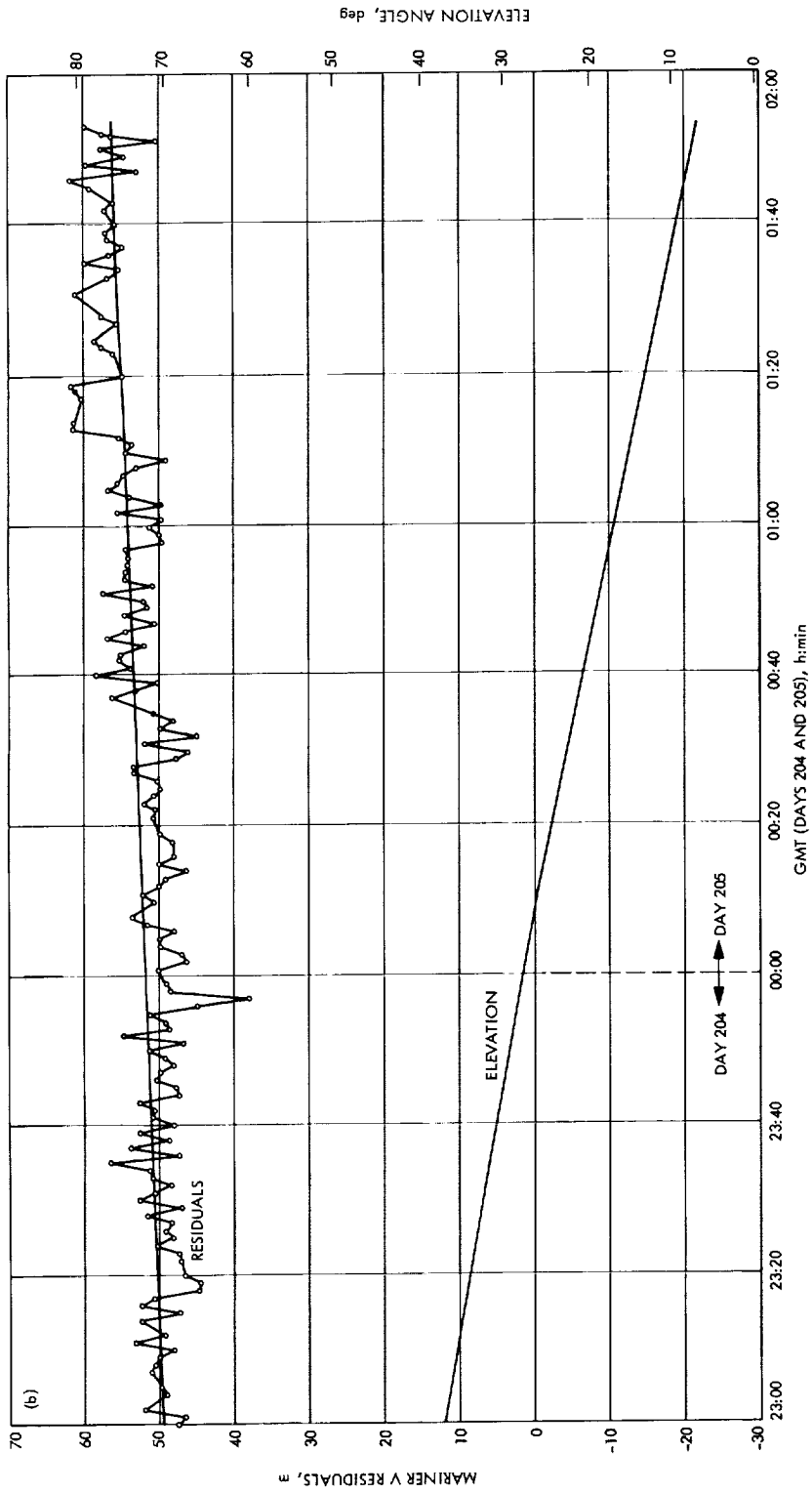
ELEVATION ANGLE, deg
MARINER V RESIDUALS, m
GMT (DAYS 204 AND 205), h:min
RESIDUALS
ELEVATION
DAY 204
DAY 205
(b)

Fig. 19 (contd)

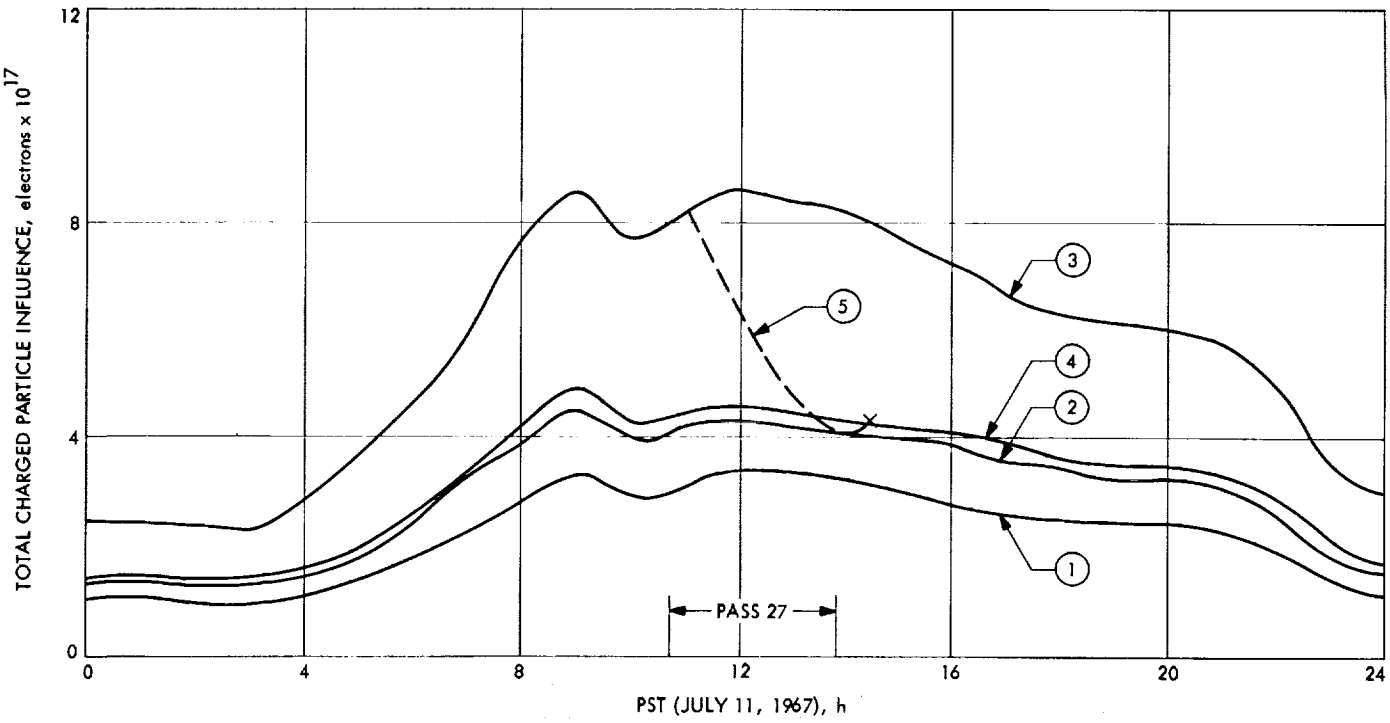

Fig. 20. Ionosphere electron concentration for Mars DSS *Mariner V* subionosphere point (Pass 27, Day 191, 1967)

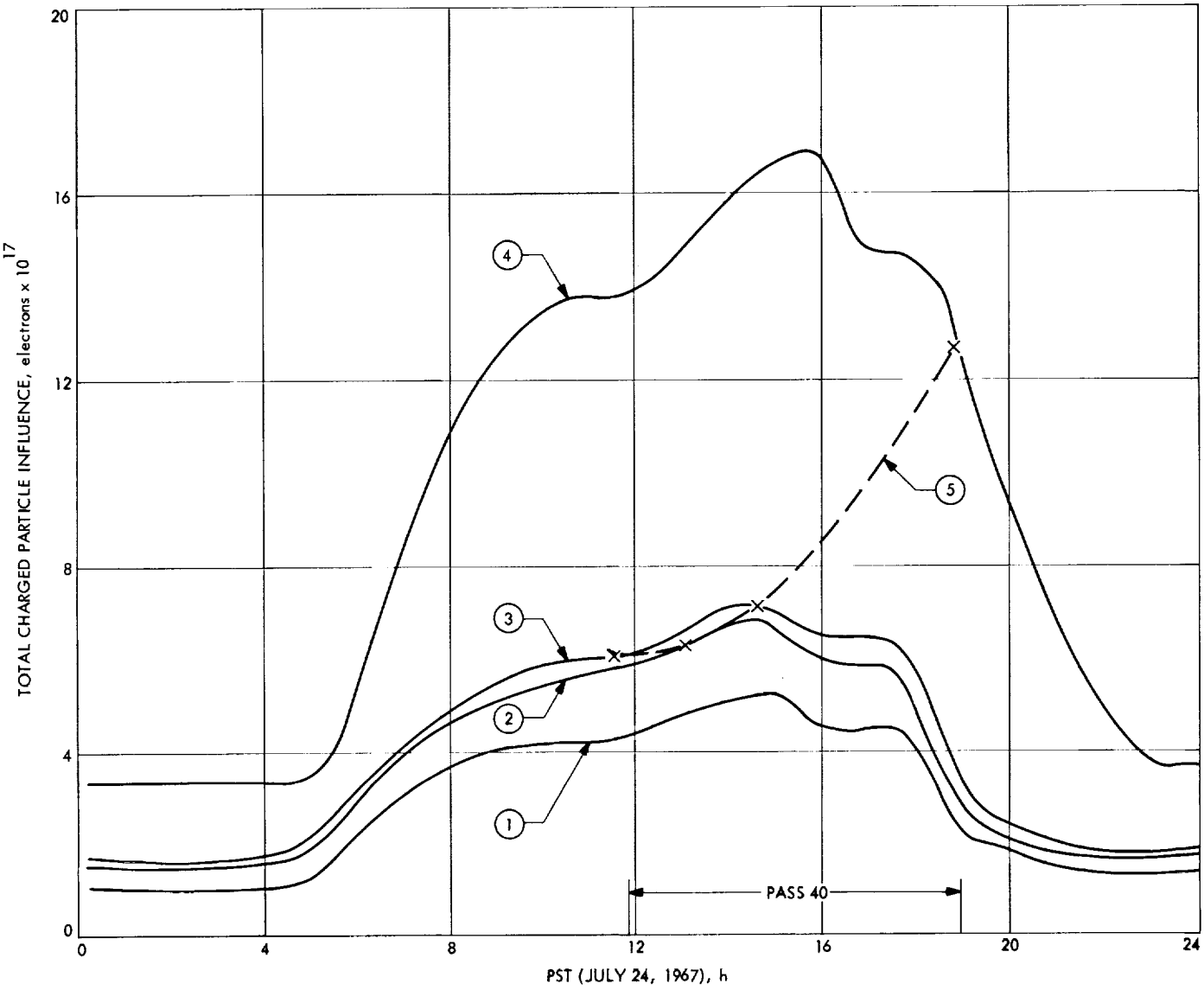

Fig. 21. Ionosphere electron concentration for Mars DSS *Mariner V* subionosphere point (Pass 40, Day 204–205, 1967)

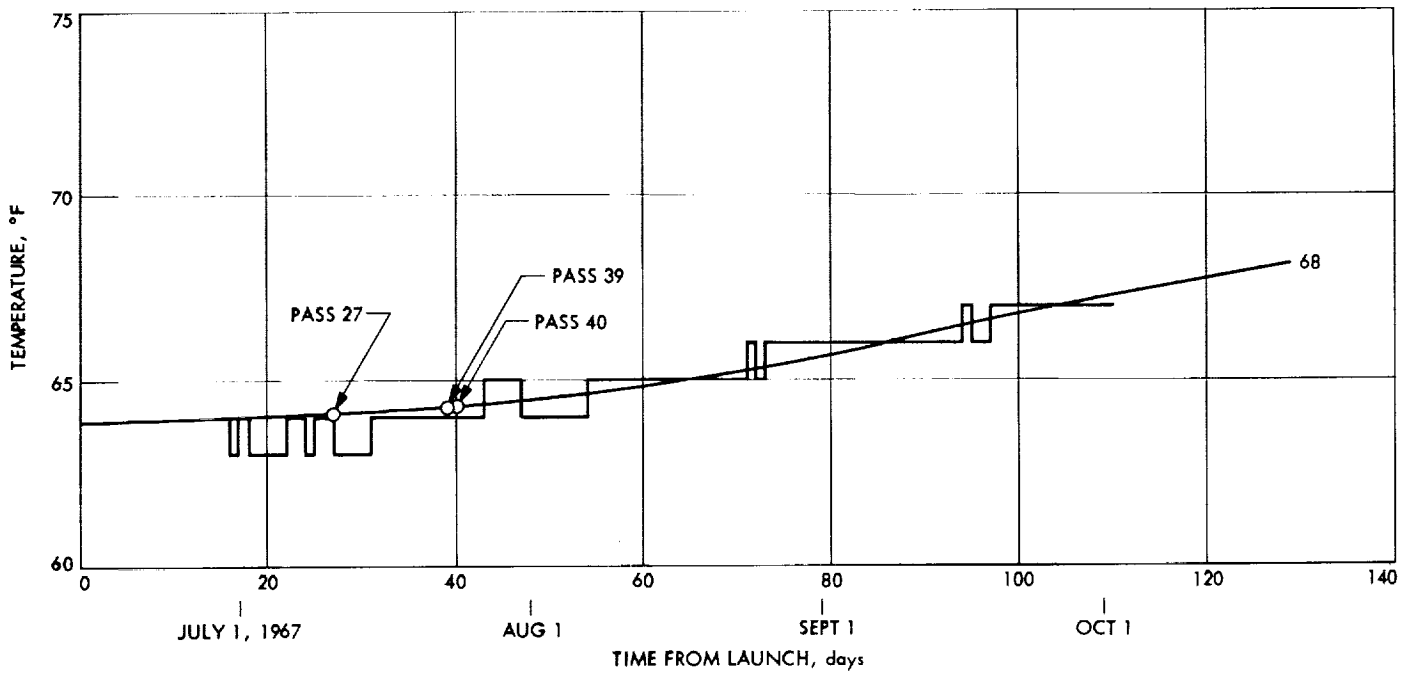

Fig. 22. *Mariner V* temperatures

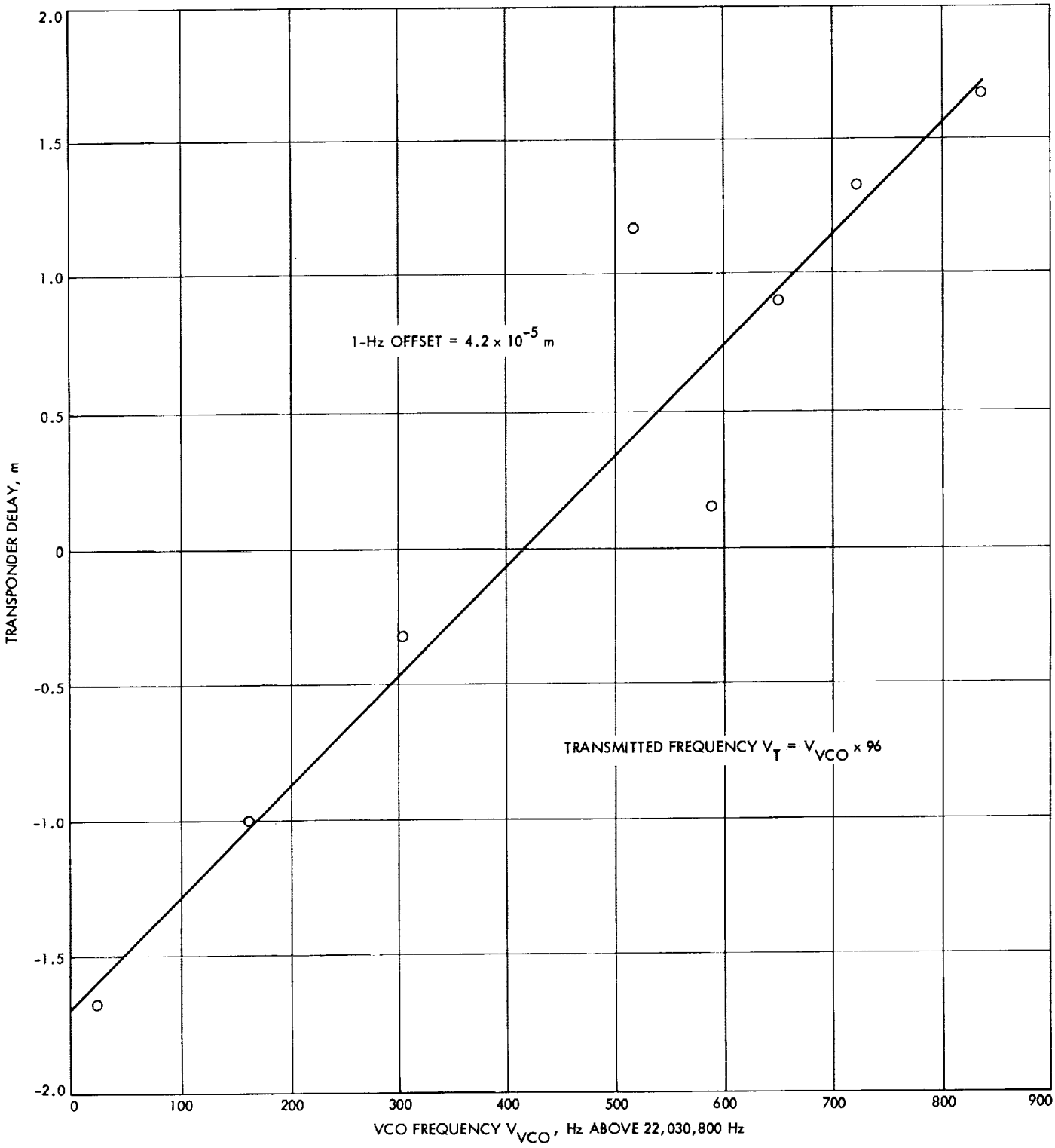

Fig. 23. *Mariner V* ranging transponder delay versus transponder frequency offset (static phase error)

i. Ranging transponder delay — signal-to-noise-dependent. The signal to noise (S/N) level ranging-transponder delay calibration shows an 8.4-ns delay change in the ranging transponder circuit travel time/dBm unit change in the S/N. This linear relationship could produce the Δ function's 48-m bias between the PRU and CC3 data types associated with pass 40 if the S/N varied by 19 dBm; however, telemetry channel data shows the S/N to vary only 0.7 dB between −118.9 and −119.6 dBm. This small variation results from the attitude-control system limit cycle, and can be viewed in Figs. 17, 18, and 19 as small periodic excursions of the Δ function (~2-m amplitude).

j. Conclusion. All efforts to correlate the differenced range–integrated range rate differences with the physical phenomena investigated have failed. The difference function (Δ) profile and magnitude do not correlate with ionospheric charged particle effects, transponder temperature changes, signal-to-noise variation or transponder frequency offset (static phase error). If the medium and transponder are excluded as the primary error signature contributors, then by exclusion the terrestrial hardware system is the indicated source.

An investigation of the research and development planetary ranging system hardware has revealed that some of the system's modules are subject to phase drift.[7] PRU and CC3 data will be collected when *Mariner V* is again within range this fall. Efforts will be made to monitor the phase drift between the research and development planetary ranging system's transmitted and received frequencies; thus it should be possible to calibrate out of the data any system-induced phase drift.

References

1. Lorell, J., Anderson, J. D., Sjogren, W. L., *Characteristics and Format of the Tracking Data to Be Obtained by the NASA Deep Space Instrumentation Facility for Lunar Orbiter*, Technical Memorandum 33-230, Jet Propulsion Laboratory, Pasadena, Calif., June 15, 1965.
2. Stratton, J. A., *Electromagnetic Theory*, McGraw-Hill Book Co., New York, 1941.
3. Koehler, R. L., *Interplanetary Electron Content Measured Between Earth and the Pioneer VI and VII Spacecraft Using Radio Propagation Effects*, Scientific Report 1, Stanford Radio Science Laboratory, Stanford, Calif., May 1967.

[7]Private conversations with R. C. Tausworthe and R. Tappen.

5. An Approximate Solution to the Analytical Partials of the Spacecraft's Geocentric Range Rate During the Pre-encounter Phase of a Planetary Mission,

W. E. Bollman

a. Introduction. The simple analytical expressions for the planet-centered position and velocity vectors of the spacecraft while in the vicinity of the target planet were introduced in SPS 37-51, Vol. II, pp. 37–41. This article will continue the analysis to show approximate analytical expressions for the partial derivatives of geocentric range rate of the spacecraft with respect to the encounter parameters $\mathbf{b}\cdot\hat{T}$, $\mathbf{b}\cdot\hat{R}$, T_e, C_3, $\hat{S}\cdot\hat{T}$, and $\hat{S}\cdot\hat{R}$.

b. Background. The previously mentioned SPS article presented the target-planet-centered position and velocity of the spacecraft to be

$$\mathbf{R}_{s/p} = R_{s/p}\left[\cos\alpha\,\hat{S} + \sin\alpha\cos\theta\,\hat{T} + \sin\alpha\sin\theta\,\hat{R}\right] \tag{1}$$

$$\dot{\mathbf{R}}_{s/p} = \left(V_\infty + \frac{\mu}{bV_\infty}\sin\alpha\right)\hat{S} + \frac{\mu}{bV_\infty}(\cos\alpha - 1)\cos\theta\,\hat{T} + \frac{\mu}{bV_\infty}(\cos\alpha - 1)\sin\theta\,\hat{R} \tag{2}$$

where

$$R_{s/p} = \frac{b^2 V_\infty^2}{\mu\left(1 + \frac{bV_\infty^2}{\mu}\sin\alpha - \cos\alpha\right)} \tag{3}$$

$\hat{S}$ = unit vector along the approach asymptote

$\hat{T}$ = unit vector perpendicular to $\hat{S}$ and parallel to a given reference plane (such as ecliptic) and given by

$$\hat{T} = \frac{\hat{S}\times\hat{P}}{|\hat{S}\times\hat{P}|}$$

where $\hat{P}$ is along north pole of reference plane

$\hat{R} = \hat{S}\times\hat{T}$

α = planet-centered angle from $-S$ to $\mathbf{R}_{s/p}$

b = the miss parameter

V_∞ = the hyperbolic excess speed

μ = the gravitational constant of the planet

θ = the orientation of the trajectory aiming point, measured clockwise from the $\hat{T}$ axis to the miss parameter **b**.

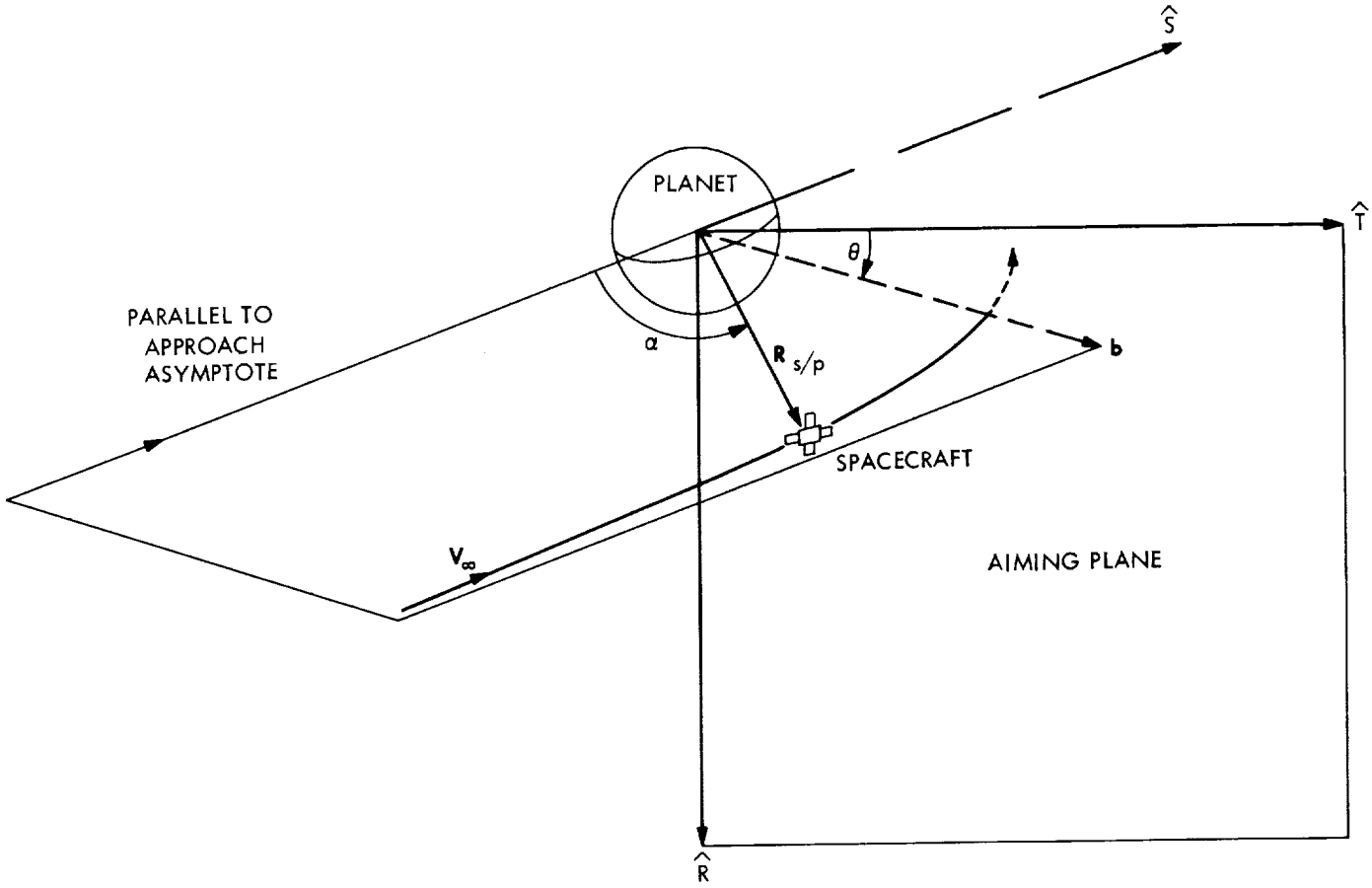

Fig. 24. Hyperbolic encounter parameters

Figure 24 shows a diagram of some of the above parameters.

The angle α, presented in Eqs. (1), (2), and (3) and in Fig. 24, remains a very small angle prior to planet encounter until the spacecraft is within an hour or so of closest approach. This characteristic enables approximate expressions to be easily derived for the partial derivatives of geocentric range rate with respect to the encounter parameters that are accurate during the pre-encounter phase of the mission.

c. Geocentric range rate. The geocentric range rate of the spacecraft during the planetary phase of the mission can be expressed as

$$\dot{r} = (\dot{\mathbf{R}}_p + \dot{\mathbf{R}}_{s/p}) \cdot \hat{r} \tag{4}$$

where

$\mathbf{R}_p$ = the position vector from the center of the earth to the planet

$\mathbf{R}_{s/p}$ = the position vector from the planet to the spacecraft

$\hat{r}$ = the unit vector from the center of the earth to the spacecraft

$\mathbf{r} = r\hat{r} = (\mathbf{R}_p + \mathbf{R}_{s/p})$

Figure 25 shows a graphical explanation of some of the above parameters.

d. Encounter parameters. The encounter parameters to be used in this analysis are as follows:

$\mathbf{b} \cdot \hat{T} = b \cos\theta$

$\mathbf{b} \cdot \hat{R} = b \sin\theta$

T_e = time of closest approach

$C_3 = V_\infty^2$

$\hat{S} \cdot \hat{T}$ = dot product of new perturbed $\hat{S}$ vector with old nominal $\hat{T}$ vector

$\hat{S} \cdot \hat{R}$ = dot product of new perturbed $\hat{S}$ vector with old nominal $\hat{R}$ vector

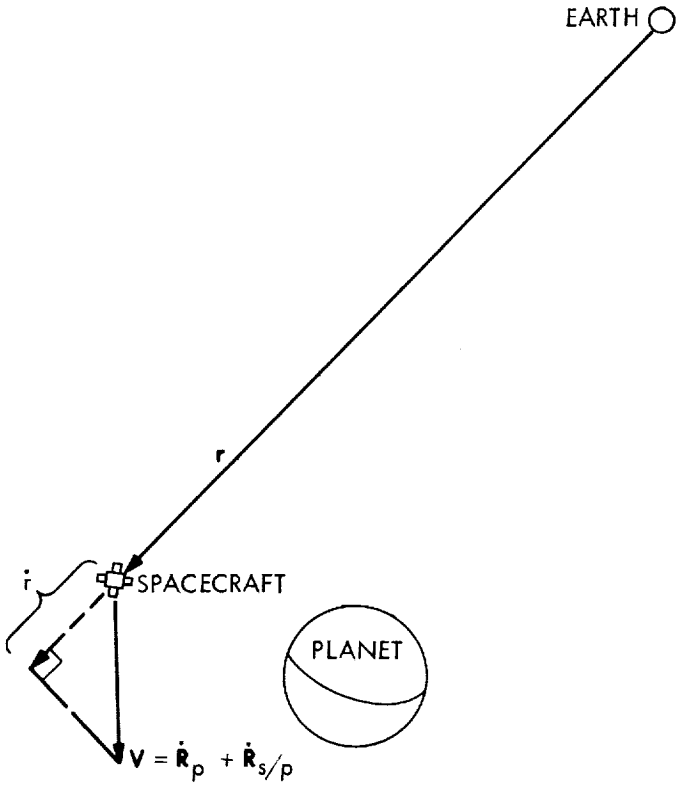

Fig. 25. Geocentric range-rate vectors

e. Partial derivatives. Taking the partial derivative of Eq. (4) with respect to the encounter parameter, e.g., q, yields

$$\frac{\partial \dot{r}}{\partial q} = (\dot{\mathbf{R}}_p + \dot{\mathbf{R}}_{s/p}) \cdot \frac{\partial \hat{r}}{\partial q} + \frac{\partial \dot{\mathbf{R}}_{s/p}}{\partial q} \cdot \hat{r} \tag{5}$$

where

$$q = \mathbf{b} \cdot \hat{T}, \mathbf{b} \cdot \hat{R}, C_3, \text{etc.}$$

The total partial derivative is thus the sum of two expressions. When $q = \mathbf{b} \cdot \hat{T}$ and $\mathbf{b} \cdot \hat{R}$, it is found that the first expression of Eq. (5) is nearly a constant during the pre-encounter phase and usually dominates the second expression until a few hours or a few days before closest approach, depending on the target planet and the approach trajectory, at which time changes of the spacecraft's velocity then become more noticeable from perturbations of the encounter parameters. The velocity of the planet with respect to the earth, $\dot{\mathbf{R}}_p$, does not depend on the encounter parameters and is almost constant during the few-day period when the spacecraft approaches the planet.

The approximate partial derivatives which are valid when the angle α is small are

$$\frac{\partial \dot{r}}{\partial \mathbf{b} \cdot \hat{T}} \approx \frac{1}{r} \left\{ \begin{array}{l} -\dot{\mathbf{R}}_p \cdot \hat{S} + V_\infty)(\hat{r} \cdot \hat{S})(\hat{r} \cdot \hat{T}) \\ +(\dot{\mathbf{R}}_p \cdot \hat{T})[1 - (\hat{r} \cdot \hat{T})^2] \\ -(\dot{\mathbf{R}}_p \cdot \hat{R})(\hat{r} \cdot \hat{T})(\hat{r} \cdot \hat{R}) \end{array} \right\} \tag{6}$$

$$- \frac{\mu(\hat{r} \cdot \hat{T})\alpha^2}{2b^2 V_\infty} + \frac{\mu(\hat{r} \cdot \hat{S}) \cos\theta}{b V_\infty} \left(\frac{\alpha^2}{ae^2} - \frac{b\alpha^3}{a^2 e^2} \right)$$

$$\frac{\partial \dot{r}}{\partial \mathbf{b} \cdot \hat{R}} \approx \frac{1}{r} \left\{ \begin{array}{l} -(\dot{\mathbf{R}}_p \cdot \hat{S} + V_\infty)(\hat{r} \cdot \hat{S})(\hat{r} \cdot \hat{R}) \\ -(\dot{\mathbf{R}}_p \cdot \hat{T})(\hat{r} \cdot \hat{T})(\hat{r} \cdot \hat{R}) \\ +(\dot{\mathbf{R}}_p \cdot \hat{R})[1 - (\hat{r} \cdot \hat{R})^2] \end{array} \right\} \tag{7}$$

$$- \frac{\mu(\hat{r} \cdot \hat{R})\alpha^2}{2b^2 V_\infty} + \frac{\mu(\hat{r} \cdot \hat{S}) \sin\theta}{b V_\infty} \left(\frac{\alpha^2}{ae^2} - \frac{b\alpha^3}{a^2 e^2} \right)$$

$$\frac{\partial \dot{r}}{\partial T_e} \approx \frac{V_\infty}{r} \left\{ \begin{array}{l} -(\dot{\mathbf{R}}_p \cdot \hat{S} + V_\infty)[1 - (\hat{r} \cdot \hat{S})^2] \\ +(\dot{\mathbf{R}}_p \cdot \hat{T})(\hat{r} \cdot \hat{S})(\hat{r} \cdot \hat{T}) \\ +(\dot{\mathbf{R}}_p \cdot \hat{R})(\hat{r} \cdot \hat{S})(\hat{r} \cdot \hat{R}) \end{array} \right\}$$

$$- \frac{\mu(\hat{r} \cdot \hat{S})\alpha^2}{b^2} \tag{8}$$

$$\frac{\partial \dot{r}}{\partial C_3} \approx \frac{(\hat{r} \cdot \hat{S})}{2V_\infty} \tag{9}$$

This expression is related to the partial of V_∞ by

$$\frac{\partial \dot{r}}{\partial V_\infty} = 2V_\infty \frac{\partial \dot{r}}{\partial C_3}$$

$$\frac{\partial \dot{r}}{\partial \hat{S} \cdot \hat{T}} \approx - \frac{R_{s/p}(\dot{\mathbf{R}}_p \cdot \hat{T})}{r} (\hat{r} \cdot \hat{T}) \left(V_\infty + \frac{\mu\alpha}{b V_\infty} \right) \tag{10}$$

$$\frac{\partial \dot{r}}{\partial \hat{S} \cdot \hat{R}} \approx - \frac{R_{s/p}(\dot{\mathbf{R}}_p \cdot \hat{R})}{r} (\hat{r} \cdot \hat{R}) \left(V_\infty + \frac{\mu\alpha}{b V_\infty} \right) \tag{11}$$

The parameter e in Eqs. (6) and (7) is the eccentricity of the spacecraft's hyperbolic trajectory with respect to the planet. Also, as a matter of interest, the partial derivative with respect to the gravitational constant of the planet can be expressed as

$$\frac{\partial \dot{r}}{\partial \mu} = \frac{(\hat{r} \cdot \hat{S})\alpha}{b V_\infty} \tag{12}$$

Other relationships of interest when the angle α is small are

$$R_{s/p} \approx b/\alpha \approx V_\infty t$$

where t is the time before closest approach.

These approximate expressions of the partial derivatives have been checked with the conic program described in the previously mentioned article in SPS 37-51, Vol. II, and are found to agree very well. The accuracy of the expressions becomes degraded near the two ends of the pre-encounter phase: the time period preceding a few days before encounter when the spacecraft's trajectory is primarily heliocentric; and the time period starting at about an hour or so before encounter when the approximation of $\alpha = \sin\alpha$ becomes invalid. Also, the expressions become inaccurate when the miss parameter b is very small.

f. Conclusion. The approximate analytical expressions described may be of considerable value for rough calculations of navigational accuracy during the planetary pre-encounter phase. The simplicity of the expressions may allow a quick insight into the geometrical properties of spacecraft range rate prior to the planetary encounter. A future article will discuss another set of encounter parameters which will allow additional insight into the geometrical properties of both earth-to-spacecraft range and range rate prior to planetary encounter.

6. Continuous Estimation of the State of a Distant Spacecraft During Successive Passes of Data. Part I: Single Tracking Station Results, *J. F. Jordan*

a. Introduction. In SPS 37-49, Vol. II, pp. 43–52, the accuracy of the continuous minimum variance estimate of the state of a distant space probe was observed over a single pass of data. Dependency of the estimation accuracies on the position of the probe and the variance of the noise in the data was noted. Comparisons of the results of Hamilton and Melbourne (SPS 37-39, Vol. III, pp. 18–23) and Curkendall (SPS 37-47, Vol. II, pp. 15–21) were discussed. In particular, the effects of allowing for uncertainty in the lateral velocity of the probe were noted.

In this article the results of SPS 37-49, Vol. II are extended to include the behavior of state estimates during a span of time which may include several passes of data. In particular this presentation is concerned with the time history of the covariance matrix of errors in the state estimates, when the probe is being observed by a single station over successive passes. Comparisons of the results with those from a single pass of data are demonstrated herein.

b. Theoretical development. Consider a tracking station located on the earth's equator observing a distant space probe which is traveling with constant geocentric velocity. The probe state and station location can be specified in the coordinate system illustrated in Fig. 26 with the following definitions:

$$\left.\begin{matrix} x \\ y \\ z \end{matrix}\right\} \text{ geocentric position components of probe}$$

$$\left.\begin{matrix} u = \dot{x} \\ v = \dot{y} \\ w = \dot{z} \end{matrix}\right\} \text{ geocentric velocity components of probe}$$

$$\left.\begin{matrix} x_s \\ y_s \\ z_s \end{matrix}\right\} \text{ geocentric position components of station}$$

$$\left.\begin{matrix} u_s = \dot{x}_s \\ v_s = \dot{y}_s \\ w_s = \dot{z}_s \end{matrix}\right\} \text{ geocentric velocity components of station}$$

It should be noted that the x-axis of the coordinate system extends from the center of the earth through the *a priori* position of the probe at the end of the last completed pass of data, a known direction. The y-axis is perpendicular to the x-axis and lies on the equatorial plane; the z-axis completes the right-handed cartesian coordinate system.

The station position and velocity during the pass can be expressed in terms of geophysical constants by

$$\left.\begin{matrix} x_s = r_s \cos\delta_0 \sin\omega t & u_s = \omega r_s \cos\delta_0 \cos\omega t \\ y_s = -r_s \cos\omega t & v_s = \omega r_s \sin\omega t \\ z_s = -r_s \sin\delta_0 \sin\omega t & w_s = -\omega r_s \sin\delta_0 \cos\omega t \end{matrix}\right\} \quad (1)$$

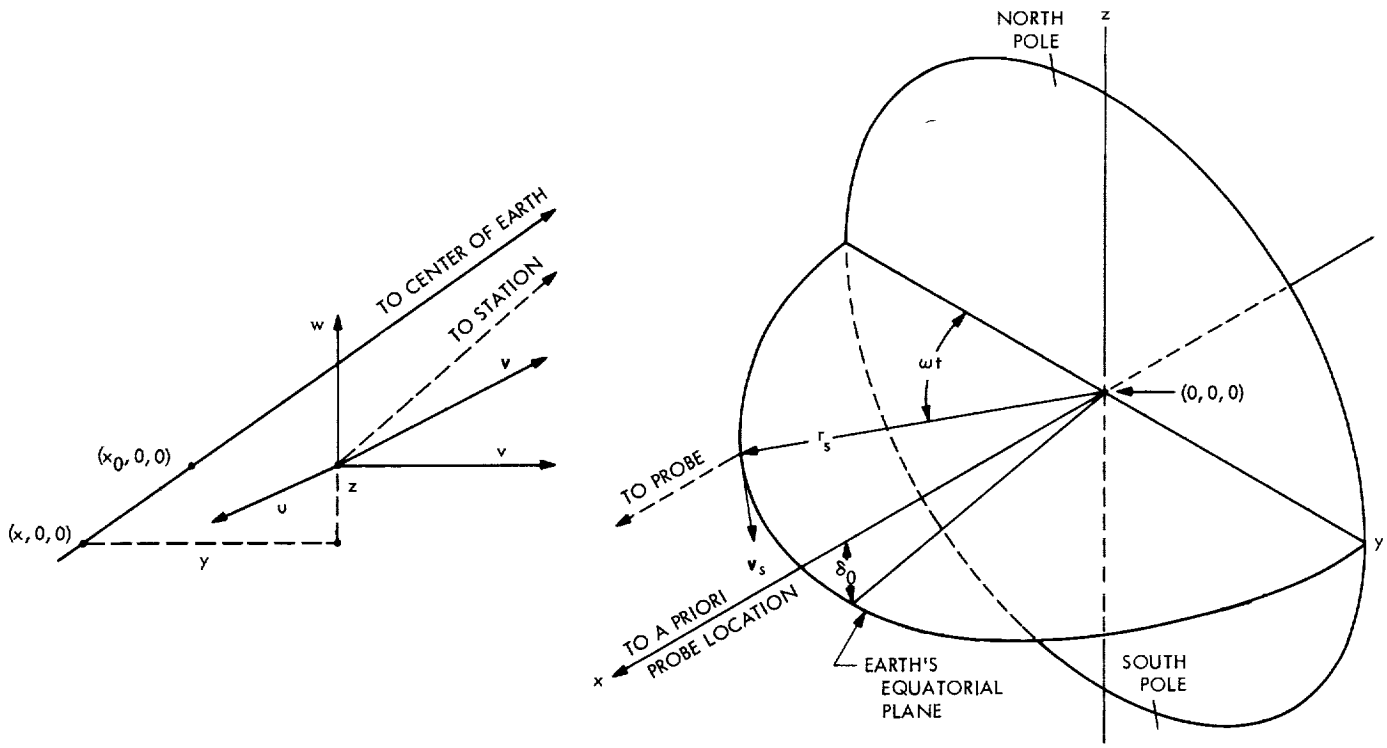

Fig. 26. Problem geometry

where

t = the time measured from the beginning of pass

ω = angular velocity of earth

δ_0 = *a priori* geocentric declination of probe

r_s = equatorial radius of earth

The observational data obtained by the station is counted doppler, or integrated range-rate, contaminated by stationary exponentially correlated noise. Hence, the observable $\phi(t)$ can be expressed as

$$\phi(t) = \int_0^t \dot{\rho}(\tau)\, d\tau + \eta(t) \tag{2}$$

where the station-probe range is related to the probe state by

$$\rho^2 = (x - x_s)^2 + (y - y_s)^2 + (z - z_s)^2 \tag{3}$$

and the additive noise $\eta(t)$ has the following properties:

$$E[\eta(t)] = 0$$

$$E[\eta(t_1)\,\eta(t_2)] = \sigma_\eta^2 \exp(-|t_2 - t_1|/\tau) \tag{4}$$

It should be noted that $\eta(t)$ satisfies the differential equation

$$\dot{\eta}(t) = -\frac{1}{\tau}\eta(t) + W(t) \tag{5}$$

where

$W(t)$ is gaussian white noise possessing the following properties:

$$\left.\begin{aligned} E[W(t)] &= 0 \\ E[W(t_1)\,W(t_2)] &= \frac{2\sigma_\eta^2}{\tau}\,\delta(t_2 - t_1) \end{aligned}\right\} \tag{6}$$

The information content of the data is unchanged if the derivative of the counted doppler is regarded as the observable. This derivative can be written as

$$\dot{\phi}(t) = \dot{\rho}(t) - \frac{1}{\tau}\eta(t) + W(t) \tag{7}$$

Thus the observable can be thought of as the station-probe range-rate contaminated by exponentially correlated noise (which can be estimated) and white noise.

The analytical expression for the station-probe range can be differentiated to obtain the range rate $\dot{\rho}$, i.e.,

$$\dot{\rho} = \frac{x - x_s}{\rho}\frac{d}{dt}(x - x_s) + \frac{y - y_s}{\rho}\frac{d}{dt}(y - y_s) + \frac{z - z_s}{\rho}\frac{d}{dt}(z - z_s) \tag{8}$$

If we let $r = (x^2 + y^2 + z^2)^{1/2}$, and note that ρ is extremely large compared with y, z, x_s, y_s, and z_s, we can approximate ρ in the denominator of the above expression with r, and Eq. (8) can be approximated with the relation

$$\dot{\rho} = u - u_s + \frac{y - y_s}{r}(v - v_s) + \frac{z - z_s}{r}(w - w_s) \tag{9}$$

It can be seen from the partials listed below in Eq. (10) that the primary parameter that can be estimated is the velocity component along the *a priori* earth-probe line u. There is also secondary estimation capability for the lateral velocities v and w, and the lateral positions y and z. The range x cannot be effectively estimated unless the lateral velocity of the probe is large.

The partials of $\dot{\rho}$ with respect to the estimated parameters are listed as follows:

$$\left.\begin{aligned}
&\frac{\partial\dot{\rho}}{\partial u} = 1\\
&\frac{\partial\dot{\rho}}{\partial v} = \frac{y - y_s}{r} = \frac{vt + r_s\cos\omega t}{r}\\
&\frac{\partial\dot{\rho}}{\partial w} = \frac{z - z_s}{r} = \frac{wt + r_s\sin\delta_0\sin\omega t}{r}\\
&\frac{\partial\dot{\rho}}{\partial x} = -\frac{(y - y_s)(v - v_s)}{r^2} - \frac{(z - z_s)(w - w_s)}{r^2}\\
&\frac{\partial\dot{\rho}}{\partial y} = \frac{v - v_s}{r} = \frac{v - \omega r_s\sin\omega t}{r}\\
&\frac{\partial\dot{\rho}}{\partial z} = \frac{w - w_s}{r} = \frac{w + \omega r_s\sin\delta_0\cos\omega t}{r}
\end{aligned}\right\} \tag{10}$$

The accuracy to which the state components of the probe and the exponentially correlated data noise is estimated can be expressed in terms of the covariance matrix of the errors in the estimates. The covariance matrix can be written as

$$\Lambda = E\begin{bmatrix}
(u-\hat{u})^2 & (u-\hat{u})(v-\hat{v}) & \cdot & \cdot & \cdot & \cdot & \cdot\\
(v-\hat{v})(u-\hat{u}) & (v-\hat{v})^2 & \cdot & \cdot & \cdot & \cdot & \cdot\\
\cdot & \cdot & (w-\hat{w})^2 & \cdot & \cdot & \cdot & \cdot\\
\cdot & \cdot & \cdot & (x-\hat{x})^2 & \cdot & \cdot & \cdot\\
\cdot & \cdot & \cdot & \cdot & (y-\hat{y})^2 & \cdot & \cdot\\
\cdot & \cdot & \cdot & \cdot & \cdot & (z-\hat{z})^2 & \cdot\\
\cdot & \cdot & \cdot & \cdot & \cdot & \cdot & (\eta-\hat{\eta})^2
\end{bmatrix} \tag{11}$$

where $\hat{}$ denotes the minimum variance estimate. The square roots of the first six diagonal terms of the covariance matrix are taken as the rms accuracies of the individual state components. These terms can be stated as

$$\left.\begin{aligned}
\sigma_u &= [E[u-u]^2]^{1/2} & \sigma_x &= [E[x-x]^2]^{1/2}\\
\sigma_v &= [E[v-v]^2]^{1/2} & \sigma_y &= [E[y-y]^2]^{1/2}\\
\sigma_w &= [E[w-w]^2]^{1/2} & \sigma_z &= [E[z-z]^2]^{1/2}
\end{aligned}\right\} \tag{12}$$

In the original formulation of the CEP,[8] as reported in SPS 37-48, Vol. II, pp. 23–27, the covariance matrix was obtained as a solution to the following matrix Riccati differential equation

$$\dot{\Lambda} = F\Lambda + \Lambda F^T - \Lambda G\Lambda + H \tag{13}$$

and it was shown in SPS 37-49, Vol. II that the inverse of the covariance matrix $P = \Lambda^{-1}$ obeys the following

[8]CEP = Continuous Estimation Program.

Riccati equation:

$$\dot{P} = -F^T P - PF - PHP + G \tag{14}$$

It can be shown, using Ref. 1, that the elements of F and G can be written in terms of a 6×1 vector of the six partial derivatives in Eq. (10)

$$\left(\frac{\partial \dot{\rho}}{\partial x}\right)$$

as

$$F(7\times 7) = \begin{array}{c} \begin{matrix} 3 & 3 & 1 \end{matrix} \\ \left[\begin{array}{c|c|c} 0 & 0 & 0 \\ \hline I(3\times 3) & 0 & 0 \\ \hline \left(\frac{\partial \dot{\rho}}{\partial x}\right)^T & 0 & 0 \end{array}\right] \begin{matrix} 3 \\ 3 \\ 1 \end{matrix} \end{array} \tag{15}$$

and

$$G(7\times 7) = \frac{\tau}{2\sigma_\eta^2} \begin{array}{c} \begin{matrix} 6 & 1 \end{matrix} \\ \left[\begin{array}{c|c} \left[\frac{\partial \dot{\rho}}{\partial x}\right]\left[\frac{\partial \dot{\rho}}{\partial x}\right]^T & -\frac{1}{\tau}\left(\frac{\partial \dot{\rho}}{\partial x}\right) \\ \hline -\frac{1}{\tau}\left(\frac{\partial \dot{\rho}}{\partial x}\right)^T & \left(\frac{1}{\tau}\right)^2 \end{array}\right] \begin{matrix} 6 \\ 1 \end{matrix} \end{array} \tag{16}$$

Since, in this presentation, no process noise is assumed to occur, the elements of H are zero.

It should be noted that when the space probe is not being tracked, the information matrix of the state, $P'(6 \times 6)$, obeys the following linear differential equation

$$\dot{P}' = -E^T P' - PE \tag{17}$$

where

$$E(6\times 6) = \begin{array}{c} \begin{matrix} 3 & 3 \end{matrix} \\ \left[\begin{array}{c|c} 0 & 0 \\ \hline I(3\times 3) & 0 \end{array}\right] \begin{matrix} 3 \\ 3 \end{matrix} \end{array}$$

c. Accuracy results from successive passes of data. Consider the tracking station described in *Paragraph b* observing a distant spacecraft, and assume that the station completes three successive 12-hour passes of data. The probe is at a distance of 10^8 km from the earth, has a geocentric declination of 20 deg, and is assumed to be traveling more or less directly away from the earth. The *a priori* values of the probe state accuracies are given as

$$\sigma_{u_0} = \sigma_{v_0} = \sigma_{w_0} = 1\,\text{km/s}$$

$$\sigma_{x_0} = \sigma_{y_0} = \sigma_{z_0} = 10^6\,\text{km}$$

which are large enough not to influence the accuracy of the state estimates after the second pass of data is initiated. The standard deviation of the noise in the counted doppler data is taken as 1 m, and the correlation time of the noise is taken as 1000 s, which is of the same order of magnitude as the round-trip light travel time between the earth and the probe. Plots of the time history of the estimation accuracies of the probe state (σ_u, σ_v, σ_w, σ_y, σ_z) are given in Fig. 27. The time span in Fig. 27 includes the first 12-h pass, the 12-h time span when the station is unable to observe the probe (overnight), the second 12-h pass, etc. The total time span is thus 60 h.

The results for pass 1 coincide with those reported in SPS 37-49, Vol. II. It should be noted that at the end of pass 1, high correlations (>0.95) exist between the following sets of state variables: u, w; u, y; u, z; w, y; w, z; and y, z. These high correlations are the result of the similarity of form of the partial derivatives given in Eq. (10) and arise from the natural correlation between the position and velocity along any coordinate. During pass 2 the accuracies of the estimates of all the state variables are seen to improve considerably. The improvement is due primarily to the tracking station's ability to separate the highly correlated variables above by viewing the probe at two different times. After two passes, none of the correlations exceed 0.85. The accuracies improve only slightly during pass 3, due to further filtering of the data noise.

d. Sensitivity of the results to position of the probe. The results of the previous section are given for a probe at a distance of 10^8 km from the earth at a declination of 20 deg. As shown in SPS 37-49, Vol. II, the parameters which are sensitive to the declination are w and z. After the initiation of pass 2, w and z are seen to vary with the factor $1/\sin \delta_0$. The other state variables are not affected by changes in the declination. It should also be noted that the accuracies of lateral state variables v, w, y, and z all vary linearly with the distance of the probe from earth, r.

e. Multiple pass analysis and the sensitivity of the results to the velocity of the probe. If the *a priori* covariance matrix of errors in the state is assumed to be very

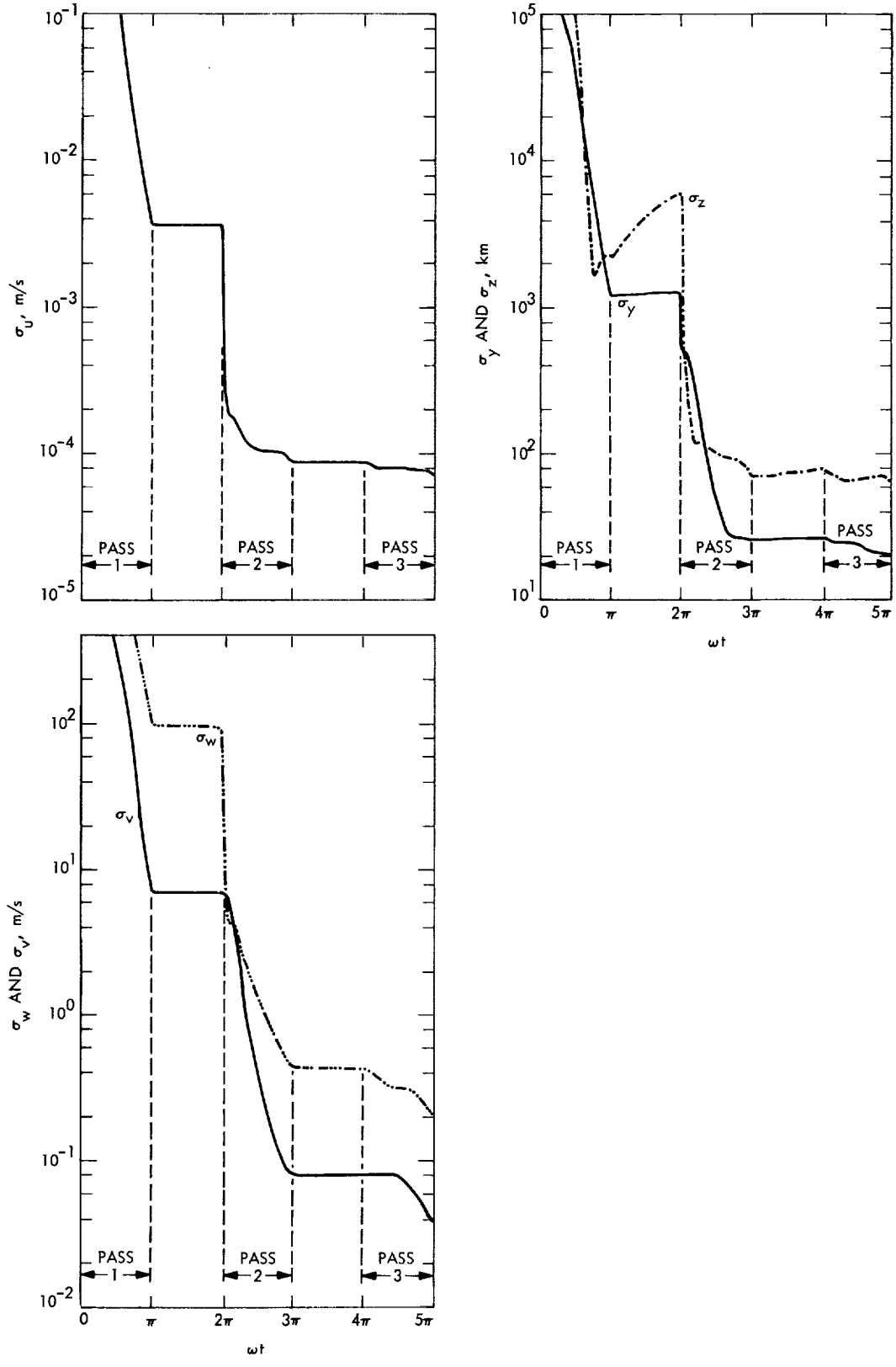

Fig. 27. State uncertainty time histories, three passes of data

large and the noise in the data is assumed to be a stationary random process, then the solution to Eq. (14) can be written at any time t during the first pass of data as

$$P(t) = \Phi(t, t_0) P_0 \Phi(t, t_0)^T + \int_{t_0}^{t} \Phi(t, \tau) G(\tau) \Phi(t, \tau)^T d\tau \tag{18}$$

where

$$P_0 = \begin{array}{c} \begin{matrix} 6 & 1 \end{matrix} \\ \left[\begin{array}{c|c} 0 & 0 \\ \hline 0 & 1/\sigma_\eta^2 \end{array}\right] \end{array} \begin{matrix} 6 \\ 1 \end{matrix} \tag{19}$$

and $\phi(t, t_0)$ is a (7×7) state transition matrix which has the following properties:

$$\begin{aligned} \dot{\Phi}(t, t_0) &= -F^T(t) \Phi(t, t_0) \\ \Phi(t_0, t_0) &= I(7 \times 7) \end{aligned} \tag{20}$$

At the end of a 12-h pass of data ($\omega t = \pi$), the elements of $P'(\pi/\omega)$, the information matrix of the state variables, can be formed from the elements of $P(\pi/\omega)$ by the following relation

$$P'_{ij} = P_{ij} - \frac{P_{i7} P_{j7}}{P_{77}}, \qquad \begin{aligned} i &= 1, \cdots, 6 \\ j &= 1, \cdots, 6 \end{aligned} \tag{21}$$

and the elements of P' can be inverted to yield the elements of the covariance matrix of the probe state $\Lambda'(\pi/\omega)$. The (6×6) information matrix can be mapped forward in time, rotated in space, and combined with the information matrix of the second pass of data to yield the information matrix of two successive passes by the following relation

$$P'\left(\frac{3\pi}{\omega}\right) = \phi A P'\left(\frac{\pi}{\omega}\right) A^T \phi^T + P'\left(\frac{\pi}{\omega}\right) \tag{22}$$

where the elements of ϕ and A are given by

$$\phi(6 \times 6) = \begin{array}{c} \begin{matrix} 3 & 3 \end{matrix} \\ \left[\begin{array}{c|c} I(3 \times 3) & -2\left(\frac{\pi}{\omega}\right) I(3 \times 3) \\ \hline 0 & I(3 \times 3) \end{array}\right] \end{array} \tag{23}$$

$$A(6 \times 6) = \left[\begin{array}{c|c} a(3 \times 3) & 0 \\ \hline 0 & a(3 \times 3) \end{array}\right]$$

$$a(3 \times 3) = \begin{bmatrix} 1 & \frac{2\pi v}{\omega r} & \frac{2\pi w}{\omega r} \\ -\frac{2\pi v}{\omega r} & 1 & 0 \\ -\frac{2\pi w}{\omega r} & 0 & 1 \end{bmatrix}$$

and the elements of $P'(3\pi/\omega)$ are expressed in a coordinate system in which the x-axis passes through the *a priori* position of the probe at the end of the second pass. By generalizing the relation (22) the information matrix of the state variables after N successive passes of data can be found from

$$P'\left[\frac{(2N-1)\pi}{\omega}\right] = \sum_{i=1}^{N} \phi(i) A(i) P'\left(\frac{\pi}{\omega}\right) A(i)^T \phi^T(i) \tag{24}$$

where the element of $\phi(i)$ and $A(i)$ are given by

$$\phi(i) = \begin{array}{c} \begin{matrix} 3 & 3 \end{matrix} \\ \left[\begin{array}{c|c} I(3 \times 3) & -2(i-1)\frac{\pi}{\omega} I(3 \times 3) \\ \hline 0 & I(3 \times 3) \end{array}\right] \end{array} \tag{25}$$

$$A(i) = \left[\begin{array}{c|c} a_i(3 \times 3) & 0 \\ \hline 0 & a_i(3 \times 3) \end{array}\right]$$

$$a_i = \begin{bmatrix} 1 & 2(i-1)\frac{\pi v}{\omega r} & 2(i-1)\frac{\pi w}{\omega r} \\ -2(i-1)\frac{\pi v}{\omega r} & 1 & 0 \\ -2(i-1)\frac{\pi w}{\omega r} & 0 & 1 \end{bmatrix}$$

The information matrix after N completed passes of data can be inverted to yield the covariance matrix of the errors in the state estimates Λ'_N. Figure 28 illustrates the dependency of the state estimate uncertainties on the number of completed passes for various values of v, the velocity along the right ascension direction. Curves

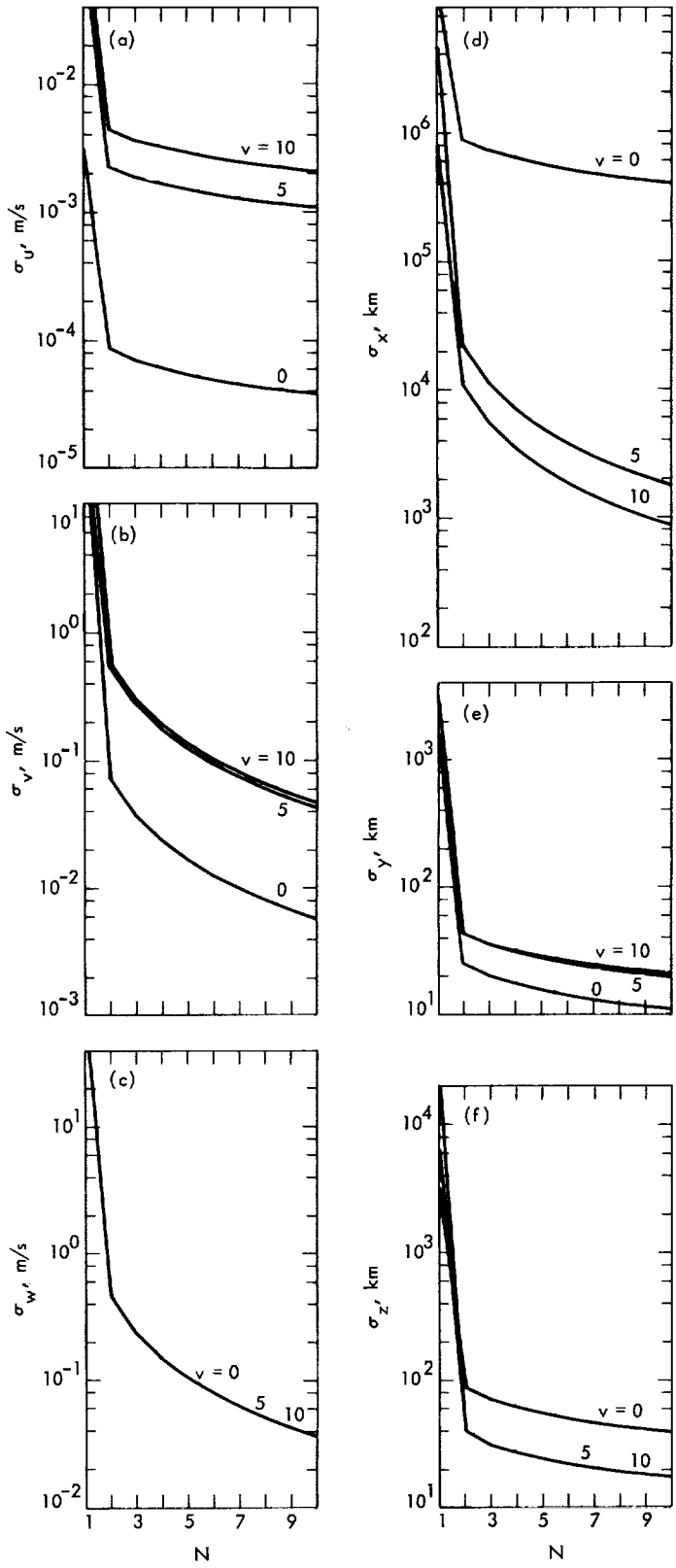

Fig. 28. State uncertainty time histories, ten passes of data: (a) range rate; (b) lateral velocity, right ascension direction; (c) lateral velocity, declination direction; (d) range; (e) lateral position, right ascension direction; (f) lateral position, declination direction

are shown for $v = 0$, 5, and 10 km/s; for these curves, $w = 0$. As seen from the curves, the accuracies of estimates of u, v, and y are degraded when v is nonzero, while the accuracy of w is unchanged, and the accuracy of z is slightly improved. Estimation of the range x is also made possible by a nonzero value of v. It should be noted that considering a nonzero value of w yields a very similar set of curves to those shown.

f. Summary. The results of this article are presented in order to improve insight into the geometrical properties of the accuracies of state estimates of a distant spacecraft. An examination of the figures shown and others from the CEP yields the following empirical formulas, which illustrate the geometrical influences on these accuracies after N completed passes of data ($N \geqq 2$).

$$\sigma_u = \left[\left(\frac{v}{r}\right)^2 \sigma_y^2 + \left(\frac{w}{r}\right)^2 \sigma_z^2\right]^{1/2} \text{m/s}$$

$$\sigma_v = \left[\left(\frac{2}{N}\right)^3\right]^{1/2} (r)\, 0.5 \times 10^{-11} \text{ m/s}$$

$$\sigma_w = \left[\left(\frac{2}{N}\right)^3\right]^{1/2} (r) \frac{1}{\sin \delta_0} 0.2 \times 10^{-11} \text{ m/s}$$

$$\sigma_x = 2\left[\left(\frac{r}{v}\right)^2 \sigma_v^2 + \left(\frac{r}{w}\right)^2 \sigma_w^2\right]^{1/2} \text{m}$$

$$\sigma_y = \left(\frac{2}{N}\right)^{1/2} (r)\, 0.4 \times 10^{-6} \text{ m}$$

$$\sigma_z = \left(\frac{2}{N}\right)^{1/2} (r) \frac{1}{\sin \delta_0} 0.14 \times 10^{-6} \text{ m}$$

where the earth-probe distance r is specified in meters, and the lateral velocities v and w are specified in meters per second. The formulas are accurate for reasonable lateral velocities (between 1 and 25 km/s), and are valid up to about ten successive passes of data. It should be noted that the probe must be relatively free from planetary gravitational forces and be at an appreciable distance from the sun (>1.5 AU). Note that the lateral state variable uncertainties vary linearly with the range of the probe, σ_u is implicitly independent of the range, and σ_x varies as r^2. The effects of lateral velocities are seen in the range-rate and range estimates. σ_u is directly proportional to the lateral velocity, while σ_x is inversely proportional. It should be noted that the entire state information is expressed in terms of the state covariance matrix, and that none of the correlations exceed 0.85.

The empirical formulas given above should approximately represent the accuracy of state estimates of a deep space probe being tracked by a single station over several successive passes of data. The accuracy of state estimates from data from more than one station and the effect of ranging systems on the results will be dealt with in future articles.

Reference

1. Kalman, R. E., *New Methods and Results in Linear Prediction and Filtering Theory*, RIAS TR 61-1. Martin Marietta Corporation, Research Institute for Advanced Studies, Baltimore, Maryland, 1961.

7. A Program for Integrating Lifetime Orbits in Multirevolution Steps, D. Boggs and R. K. Leavitt

a. Introduction. An algorithm for numerical integration of orbital satellite lifetime trajectories was recently reported (SPS 37-50, Vol. II, pp. 104–110). The difficulty in accurately computing the long-term evolution of the orbit of an artificial satellite about its central body and the importance of such calculations was discussed. The main result developed in the earlier report is reviewed here, along with a description of the computer program (IBM 7094 double-precision Fortran IV) under development which implements the algorithm. Program use and output are briefly discussed.

b. Review of algorithm. The algorithm is based on the assumption that many-orbit trajectories can be computed without actually integrating every revolution about the primary. Basically, the change in the Keplerian orbital elements during one revolution is determined by conventional numerical integration. This secular change, in turn, serves as the basis for a multirevolution integration step. The multirevolution integration step then advances the orbital elements m revolutions forward with the result that only one out of m orbits is integrated with a standard stepwise integrator. The solution to the system of nonlinear differential equations describing the motion over a long interval of time reduces then to a two-stage algorithm: an external integration (or extrapolation) with respect to the argument k (the number of revolutions), and an internal integration using standard methods to integrate one revolution.

The multi-orbit trajectory program LEAP (lifetime element advancing program) uses JPL's double precision trajectory program (DPTRAJ)[9] as its internal single-orbit integrator. DPTRAJ is a generalized trajectory integration program which is capable of very accurate single-orbit trajectory computations using a Gauss-Jackson

[9]Warner, M. R., et al., *Double Precision Orbit Determination Program*, June 1967 (JPL internal document).

backward-difference method. Indeed, the existence of DPTRAJ was a prime motivation for this developmental effort. The accuracy of the orbit-skipping technique clearly depends heavily upon the accuracy of this internal single-orbit integrator. An important feature of the approach is that any change in the mathematical/physical model incorporated into the trajectory program DPTRAJ, is automatically incorporated into the lifetime program.

In Fig. 29 the fine grid lines indicate the beginning and ending of successive orbits about a central body, each mark corresponding to a perifocal passage. Thus the interval between two such grids corresponds to one anomalistic period. The distance between the large grid lines corresponds to the multirevolution integration step size m (in terms of integral numbers of orbits); in this case $m=5$. $\mathbf{a}_{nm} = (a_1, a_2, a_3, a_4, a_5, a_6)$ is the orbital element state vector at the nth large integration step, and $\mathbf{a}_{(n+1)m}$ is the state one large step later. The increment $\Delta\mathbf{a}$ in the elements over one orbit, is the forward difference

$$\Delta\mathbf{a}_{nm} = \mathbf{f}_{nm} \equiv \mathbf{a}_{nm+1} - \mathbf{a}_{nm} \tag{1}$$

This increment is assumed to be computed by DPTRAJ over one revolution at the completion of each m-revolution step. Thus it is calculated for the orbit immediately following each large grid.

Assume now that $\mathbf{a}_{nm}$, $\Delta\mathbf{a}_{nm}$, and the increments at large grids preceding the nm grid are known. Further, assume that it is desired to extrapolate this information r orbits forward (or backward) to obtain the state at the $nm + r$ grid, $\mathbf{a}_{nm+r}$, with r any positive or negative integer or zero. The Nth order backward difference formula derived for this purpose is

$$\mathbf{a}_{nm+r} = \sum_{s=-1}^{N} e_s^{m,r} \nabla^{*s} \mathbf{f}_{nm} \tag{2}$$

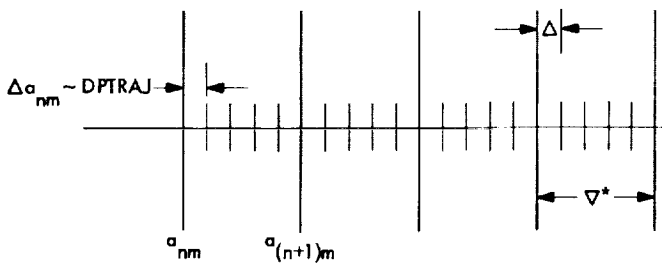

Fig. 29. Schematic of multirevolution integration step

where

$$e_s^{m,r} = \frac{r(r+m)(r+2m)\cdots(r+sm)}{m^s(s+1)!} - \sum_{\beta=2}^{s+2} \frac{(1+m)(1+2m)\cdots[1+(\beta-1)m]}{m^{\beta-1}\beta!} e_{s+1-\beta}^{m,r} \tag{3}$$

for

$$s \neq -1, \qquad e_{-1}^{m,r} = m$$

The asterisked backward differences in Eq. (2) are defined over the large grid width, so that

$$\nabla^* \mathbf{f}_{nm} = \nabla^*(\Delta\mathbf{a}_{nm}) = \Delta\mathbf{a}_{nm} - \Delta\mathbf{a}_{(n-1)m} \tag{4}$$

The explicit formulation for the difference coefficients in Eq. (3) is valid for all integral values of the indices m and r.

The use of the difference equation, Eq. (2), by LEAP is fully described in the previous report. Its use is the core of each of the following basic operations performed by the program:

(1) Initialization of integration (starting procedure).

(2) Integration in one of three modes, *predict only* (P), *predict–pseudocorrect* (P–PC), and *full predict–correct* (P–C).

(3) Calculation of current trajectory time.

(4) Interpolation.

c. Use of program. The necessary data inputs to LEAP are essentially just those necessary to run DPTRAJ. Only five additional inputs are required:

(1) m (orbit-skipping index).

(2) N (order of external integration).

(3) Integration mode (P, P–PC, or P–C).

(4) Output frequency h (output every h orbits).

(5) Total number of orbits to be integrated.

There is no upper limit to the values of m, but the magnitude of the perturbations for a particular orbiter case and the order of integration N used will dictate a sensible range of values for m. In practice, m may range between 1 and 100 revolutions. Core availability constrains the

range of the integration order to $1 \leq N \leq 15$; an optimum value for this parameter should be about 10. While compromises in numerical accuracy and efficiency between m and N are obvious, no practical rule yielding optimum values of these parameters (for a particular orbit case) has yet been determined. Experience with various types of orbital trajectories may furnish such a rule.

The integration mode used should normally be *predict–pseudo correct* (P–PC). The important difference in the modes is that DPTRAJ integrates one orbit per multirevolution step in the P and P–PC modes, but must integrate twice per step in the P–C mode. The expense of a DPTRAJ integration (well over 90% of the total computer time required for a multirevolution step), and the relatively small gain in accuracy by the use of P–C over P–PC, should limit the use of the P–C mode.

Printed output appears once every h orbits (starting with the first), and consists of the five osculating Kepler elements, a, e, i, Ω, ω, the current trajectory time in Ephemeris Time, and the orbit number k. The sixth element, T, is zero, since periapsis is the reference point. The reference coordinate plane for the elements is the mean earth equator of 1950.0, the coordinate system used by DPTRAJ in the single-orbit integration. Other standard two-body orbital parameters, such as c_1 and c_3, will be available. The capability to plot individual orbital elements versus the revolution number k will also be available as a user option.

Restrictions in the use of LEAP are:

(1) The increments in the orbital elements over one revolution, $\Delta\mathbf{a}$, must be sufficiently "smooth" functions of the revolution number k so that the functions $f(\mathbf{a}, k) = \Delta\mathbf{a}$ can be adequately represented by polynomials of fixed degree over a substantial range of values of k. This corresponds physically to the assumption that the perturbing forces vary smoothly and slowly from orbit to orbit. Thus, the technique may not adequately account for perturbing forces which are not near-periodic with respect to the orbital period of the probe. Such a perturbing force would be that due to tesseral harmonic gravitational terms associated with a nonspherical central body with a rotational period not small compared to the orbital period of the probe.

(2) The initial conditions input to the program must correspond to an elliptical orbit.

(3) The starting procedure for the multirevolution integration is a compromise between machine time efficiency and numerical precision. The resulting number of single orbits, J, computed by DPTRAJ (in P–PC mode) during this starting process is equal to $Ns + 1$, where s is the smallest integer such that $2^{s-1} \geq m$. Thus for the case $N = 10$, $m = 100$, we have $J = 81$.

(4) The interpolation procedure allows the computation of the state vector at grid points intermediate to the large grids. Interpolation is *not* valid for computing the state at time points between the fine grids (i.e., at any point on the orbit other than periapsis) since the functions $\mathbf{f}_{nm} = \Delta\mathbf{a}_{nm}$ are not defined between fine grid points.

(5) The computer time required for a given case depends heavily on the choice of m and N, and of course, on the total number of revolutions integrated.

B. Communications System Research

1. Ranging With Sequential Components, *R. M. Goldstein*

a. Introduction. The JPL ranging system is being redesigned with the goal of extending its capability to weaker thresholds without lowering its present high level of accuracy. Simplicity of design is also considered an important goal.

Sequential components allow the full ranging power to be available for each step of the search. Power does not have to be shared among the components. A further advantage is freedom from combinatorial restrictions; i.e., the component lengths need not be relatively prime. Square waves (sequences of length 2) have been chosen for all of the components.

b. Method. This system has been designed so that the RF carrier loop provides the entire tracking function. The receiver coder is geared to the received RF so that the coder necessarily runs at the same rate as the received code. The time of flight measurement is then made open loop.

Figure 30 is a functional block diagram of the system. Here f_c, a submultiple of the transmitted frequency, is the clock for the transmitter coder. The RF doppler is multiplied by a fixed ratio to provide the proper frequency for the code doppler.

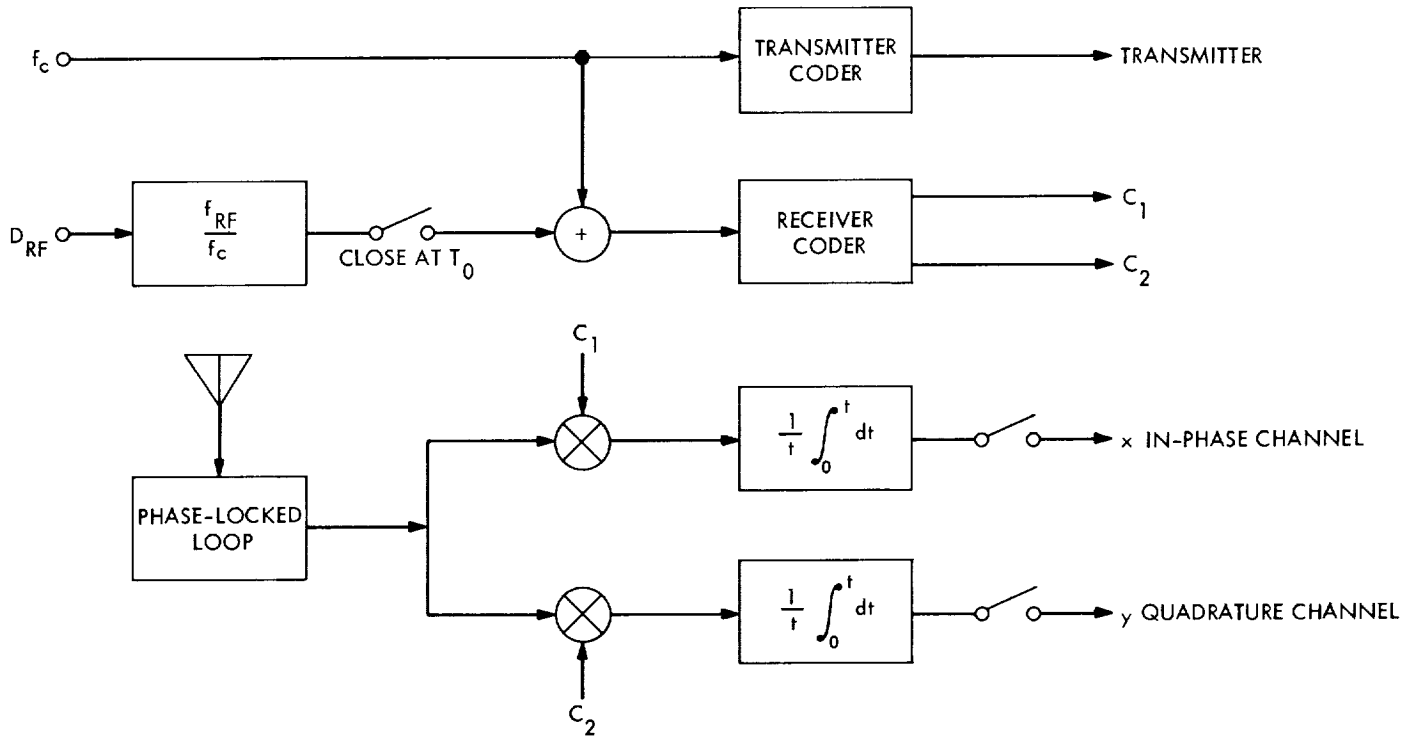

Fig. 30. Functional block diagram of the ranging system

The system operates as follows: With the doppler switch open, the two coders are synchronized. At time t_0 the switch is closed. Thereafter, the timing between the receiver coder and the received code remains fixed. This time difference (measured at leisure) represents the time-of-flight (TOF)[10] of the signal at t_0.

The two receiver channels serve to measure the phase between the received square wave and the receiver coder square wave. This technique parallels closely the optimum phase estimator for a sine wave signal. After t seconds, the integrator outputs x and y are sampled. Figure 31 is a graph of the dependence of x and y on the time difference τ. It is easily shown that

$$\tau = \frac{y}{x+y}\frac{T}{2} \tag{1}$$

where T is the bit period, and (x, y) has been assumed in the first quadrant. A similar formula holds for each quadrant.

[10]TOF at t_0 is ambiguous unless one specifies whether it pertains to the wave arriving at t_0 or to the one leaving. Conventionally, we use the former, or "backward looking," TOF.

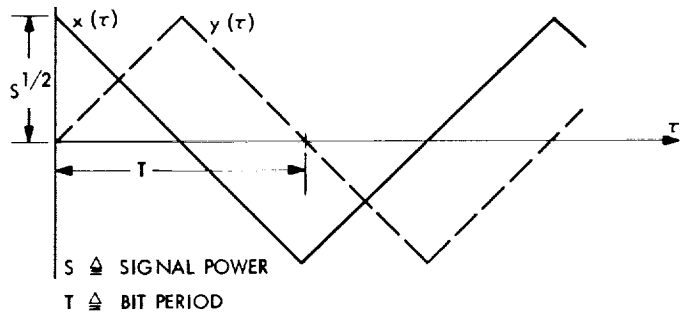

Fig. 31. Integrator outputs plotted as a function of the transmitter coder–receiver coder time difference

There is, of course, an ambiguity in the measurement. Since the first (and shortest) component length is 2 μs, an unknown multiple of 2 μs must be added to the TOF. To resolve this, the receiver coder is switched to the next slower square wave (the transmitter coder having been so switched one TOF previously). This procedure is iterated; each time the integrator outputs (x_i, y_i) are used to remove part of the previous ambiguity. The process terminates when the *a priori* knowledge removes the balance of the ambiguity.

c. Accuracy. In the discussion so far, noise has not been considered. The integrator outputs are only estimates of

the noise-free case, and

$$\hat{x} = x + n$$

$$\hat{y} = y + m$$

where n and m are independent zero mean gaussian variates of variance

$$\sigma_n^2 = \sigma_m^2 = N_0/2t \tag{2}$$

where N_0 is the one-sided noise density, and t is the integration time.

We use the simple approximation

$$\sigma^2 = \left(\frac{\partial \tau}{\partial \hat{x}}\right)^2 \sigma_{\hat{x}}^2 + \left(\frac{\partial \tau}{\partial \hat{y}}\right)^2 \sigma_{\hat{y}}^2$$

evaluated at $\hat{x} = x$, $\hat{y} = y$ and Eq. (1) to find that the variance of the estimate

$$\hat{\tau} = \frac{\hat{y}}{\hat{x} + \hat{y}} \frac{T}{2}$$

of τ is approximately

$$\sigma^2 = T^2 N_0/8st \tag{3}$$

where s is the power in the ranging signal.

d. Component periods. We now consider the following problem: Should the integration time t be long so that fewer square waves with widely spaced periods need be examined; or should many square waves be examined so that t may be short?

The uncertainty of the time measurement, σ_i, at each step need only be small enough to remove the ambiguity of all of the preceding steps (which equals the previous bit time T_{i-1}).

$$k\sigma_i = T_{i-1} \tag{4}$$

The factor k provides a margin, or confidence level. Using Eqs. (3) and (4), we have

$$T_i \left(\frac{a}{t_i}\right)^{1/2} = T_{i-1}$$

and

$$T_{i+1} \left(\frac{a}{t_{i+1}}\right)^{1/2} \left(\frac{a}{t_i}\right)^{1/2} = T_{i-1}$$

$$\vdots$$

$$T_n \left(\frac{a^n}{t_1 t_2 \cdots t_n}\right)^{1/2} = T_0 \tag{5}$$

where $a = k^2 N_0/8s$.

Thus after n steps the uncertainty has been reduced by the factor

$$(t_1 t_2 \cdots t_n/a^n)^{1/2} \tag{6}$$

The total time required for these n steps is

$$t_1 + t_2 + \cdots + t_n \tag{7}$$

Using the Lagrange multiplier technique to maximize Eq. (6) while holding Eq. (7) constant, for fixed n one easily finds that all of the t_i must be equal. Then the advantage becomes

$$(t^n/a^n)^{1/2} \tag{8}$$

and the penalty becomes

$$nt \tag{9}$$

Again, the Lagrangian technique of maximizing Eq. (8) while holding Eq. (9) constant (assuming n a continuous variable), shows that

$$t/a = e$$

Since the ratio of successive periods, from Eq. (5), is $(t/a)^{1/2}$ we see that the ratio

$$T_n/T_{n-1} = e^{1/2} = 1.65 \cdots \tag{10}$$

We choose the convenient nearby integer 2. Hence each of the sequential components of this system has twice the period of the previous one.

e. Probability of error. As we have seen, the first highest speed component serves to measure the time delay with the most precision. Each successive component then removes half of the ambiguities left by all of the previous components. We next consider the probability of making an error in any of the components 2 through n. Any such error would invalidate the entire TOF measurement.

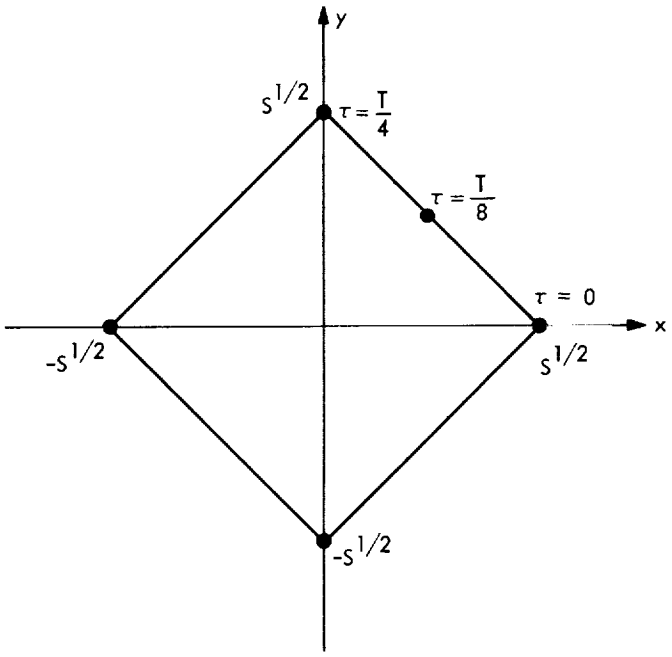

Fig. 32. Integrator outputs plotted against each other, with time difference as a parameter

Figure 32 shows the integrator outputs x and y plotted against each other, with τ as a parameter, in the noise-free case. If the previous measurements happen to give $\tau = 0 +$ (multiple of $T/2$), the current measurement need only distinguish between the two points $(s^{1/2}, 0)$ and $(-s^{1/2}, 0)$. The answer will be correct if, and only if, $x > 0$. This will happen with probability

$$p\,(\text{correct}) = \frac{1}{\pi^{1/2}} \int_{-\infty}^{(st/N_0)^{1/2}} e^{-z^2}\,dz \qquad (11)$$

The same result applies if the previous measurements had shown that $\tau = T/4$, $T/2$ or $3T/4 +$ (multiple of $T/2$). However, if $\tau = T/8 +$ (multiple of $T/2$), the current measurement must distinguish between the closer points $(s^{1/2}/2, s^{1/2}/2)$ and $(-s^{1/2}/2, -s^{1/2}/2)$.

One can see from Fig. 32 that the answer will be correct whenever $y > -x$. The probability of this event is

$$p\,(\text{correct}) = \frac{1}{\pi^{1/2}} \int_{-\infty}^{(st/2N_0)^{1/2}} e^{-z^2}\,dz \qquad (12)$$

A comparison with Eq. (11) shows a 3-dB loss in this case. In order to avoid this loss, the receiver coder is shifted by the amount measured with the first component. Thereafter τ will always equal $0 +$ (multiple of $T/2$). The probability of at least one error is then

$$p_e = 1 - p\,(\text{correct})^{n-1}$$

where n is the total number of components.

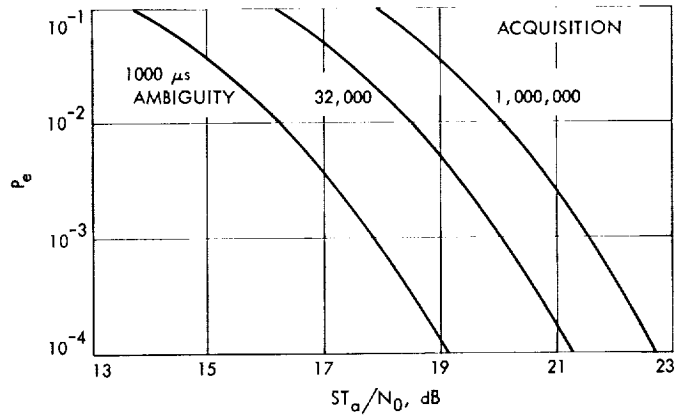

Fig. 33. Probability of an error in resolving the code ambiguities

Figure 33 is a graph of the probability of error as a function of the total acquisition energy-to-noise-density ratio. The final component period (hence the final ambiguity time) is taken as a parameter.

f. Conclusions. We have described a ranging system which uses sequential square wave components. The shortest has a period of 2 μs and each successive component has double the period of the preceding one. The entire tracking function is performed by the RF carrier loop, leaving the time delay measurements to be done open loop. Formulas have been given for the precision of the delay measurement as well as the probability of erroneously resolving any of the ambiguities.

As an example, suppose it were desired to range *Mariner V* at encounter with this system. Suppose that 25 min were available to range to ±15 m with 1 sec of ambiguity and 0.0001 probability of error. Then with $S/N_0 = 0.206$, the first component would require 1 min, and components 2 through 19 would require a total of 15 min. The round trip time was 9 min. The actual S/N_0 was 101, a margin of 27 dB.

2. Ephemeris-Controlled Oscillator Analysis, K. D. Schreder

a. Introduction. An ephemeris-controlled oscillator (ECO) is a sampled-data phase control system in which the output phase is controlled by the input phase. The

input phase is derived from an ephemeris computer program (RADAR 7 and RADAR 7 PHASE) which determines the change in round-trip light time at given times for any celestial body.

The ECO can be used as a programmed assist oscillator to a voltage-controlled oscillator (VCO) in a phase-locked loop receiver, or as the phase controller for an exciter system. In the assist mode, the ECO will track the ephemeris, and the VCO will track any remaining phase variations. Some experiments in which ECOs can be used to improve the results and/or operations of a phase-coherent communication system are the following:

(1) An ECO receiver system can coherently track a spacecraft, planet, or celestial body with an average phase error of zero. Therefore the receiver can maintain a tight phase lock during an entire pass.

(2) Phase-coherent switching from one spacecraft to another spacecraft separated in frequency in a two-way ECO communication link can be accomplished with only one VCO. (This concept has been demonstrated for two spacecraft in SPS 37-49, Vol. III, pp. 67–82.)

(3) Higher precision in ranging can be achieved, because the phase error between the actual ephemeris and the calculated ephemeris is directly obtained.

(4) The phase within a communication link between a spacecraft or planet probe and a ground system can be simulated using an ECO ground transmitter–receiver system. This phase simulation uses the ECO's capability to produce any predicted phase profile.

b. System configuration. A block diagram of the physical elements which comprise the ECO is shown in Fig. 34. A general description of each block is given to clarify the operation of the system.

Physical system. The input phase $\theta(t)$ and the continuous output phase are sampled at the same discrete times. The digital computer forms the difference between the input phase and the current output phase at the sample time. The computer mathematically multiplies the phase error by a compensation equation which ensures finite settling time. This differencing and multiplication operation in the computer causes a time delay following the sampling instant. This delay is taken into account when analyzing the stability of the sampled-data phase control loop.

The digital-to-analog (D/A) convertor changes the digital command from the computer to an analog voltage. The circuit which performs this function is a zero-order hold circuit.

The error signal from the D/A convertor drives an integrating operational amplifier. The output of the integrator is the control voltage for the VCO. The bandwidth of the integrator is smaller than the dynamic bandwidth of the VCO control voltage input. Therefore, the VCO will track the voltage from the integrator exactly.

Included within the VCO block is a frequency synthesizer. This unit allows the initial frequency at the output to be placed anywhere within the frequency range of the frequency synthesizer. The derivative of the VCO output phase (Ref. 1) is

$$\frac{d\hat{\theta}(t)}{dt} = \omega_0 + Ke(t)$$

where ω_0 is the output frequency, and $e(t)$ is the control voltage. The rate of change of the input control voltage is determined by the digital computer.

The VCO output frequency is continuously monitored by the counter. The output of the counter at any time t is the phase change of the VCO from the initial starting time

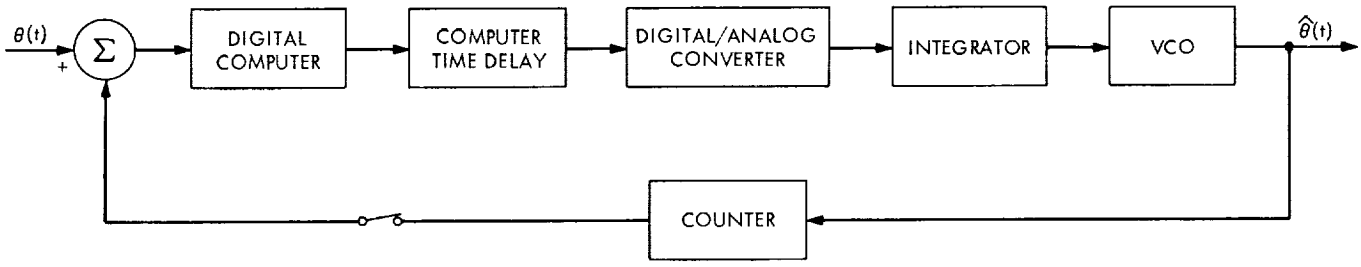

Fig. 34. Ephemeris-controlled oscillator block diagram

of the counter t_0 to the sampled time, t. The instantaneous output phase of the VCO can be expressed as follows:

$$\hat{\theta}_{\text{VCO}}(t) = \omega_0 t + \phi(t) + \phi_0$$

where ω_0 is the output frequency, $\phi(t)$ is the phase change due to the changes in the control voltage, and ϕ_0 is the starting phase. The change in phase for any interval of time is

$$\begin{aligned}\Delta\hat{\theta}_{\text{VCO}}(t - t_0) &= \hat{\theta}_{\text{VCO}}(t) - \hat{\theta}_{\text{VCO}}(t_0) \\ &= \omega_0(t - t_0) + \phi(t)\end{aligned}$$

Therefore, the output of the counter is the change in phase of the VCO from the starting time to the present.

System equations. The block diagram in Fig. 34 can be separated into two sections, namely, a discrete section and a continuous section. The discrete section consists of the digital computer, the sampler, and the summer. The continuous section is the D/A convertor, the integrator, the VCO, and the counter. A functional block diagram for the ECO is shown in Fig. 35.

The open-loop gain, excluding the computer compensation equation

$$\begin{aligned}G_0(s) &= (e^{-\tau s})\frac{1 - e^{-Ts}}{s}\frac{K_1}{s}\frac{K_2}{s}, \\ &= G_0'(s)\, e^{-\tau s}\end{aligned}$$

where $G_0'(s)$ is the open-loop gain of the continuous section, K_1 is the integrator gain, K_2 is the VCO gain, T is the sample period, and τ is the computer time delay. The Laplace transform equation must be changed to a z-transform equation before a solution can be given. The z-transform of $G_0(s)$ can be obtained from the modified z-transform on the open-loop gain $G_0'(s)$ (Refs. 2–4).

Before the z-transform equation of $G_0(s)$ can be stated, the modified z-transform of $G_0'(s)$ must be obtained.

$$Z\{G_0'(s)\} = Z\{G_1(s)[1 - e^{-Ts}]\} \tag{1}$$

where

$$G_1(s) = \frac{K_1 K_2}{s^3}$$

and from Ref. 5:

$$Z\{G(s)\, e^{-nsT}\} = z^{-n} Z\{G(s)\} \tag{2}$$

Substituting Eq. (2) into Eq. (1), the following is obtained:

$$Z\{G_0'(s)\} = (1 - z^{-1}) Z\{G_1(s)\}$$

For the modified z-transform equation of $G_1(s)$ (Ref. 2) where the delay operator m is

$$m = T - \tau$$

and τ is constrained such that $0 \leq \tau \leq T$, is

$$Z\{G_1(s)\} = \frac{K_1 K_2 T^2}{2}\left[\frac{m^2}{z-1} + \frac{2m+1}{(z-1)^2} + \frac{2}{(z-1)^3}\right]$$

If the sample period is normalized to 1, i.e., $T = 1$, then the modified z-transform equation of $G_0(s)$ is

$$\begin{aligned}G_0(z, 1 - \tau) &= Z\{G_0'(s)\, e^{-\tau s}\} \\ &= \frac{K_1 K_2}{2z}\left[\frac{(1-\tau)^2 z^2 - (2\tau^2 - 2\tau - 1)z + \tau^2}{(z-1)^2}\right]\end{aligned} \tag{3}$$

Therefore the open-loop transfer response is

$$G_0(z) = G_0(z, 1 - \tau)\frac{H(z)}{L(z)} \tag{4}$$

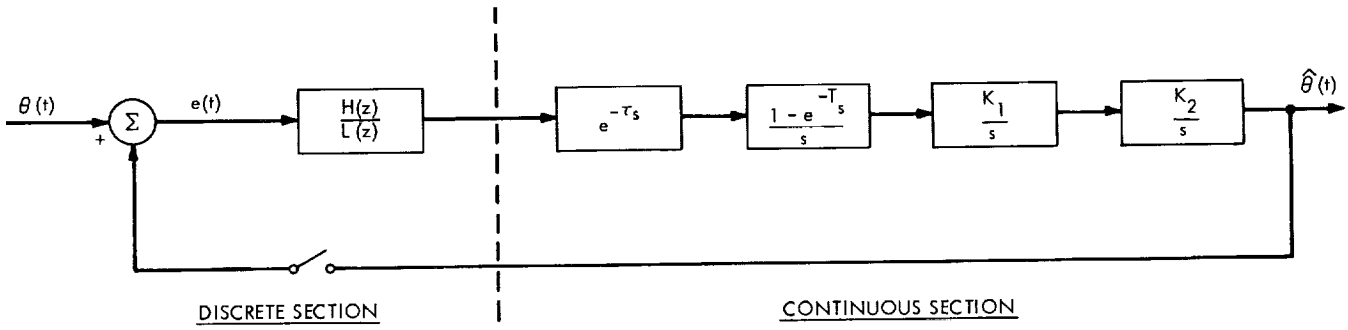

Fig. 35. Functional ephemeris-controlled oscillator block diagram

And the closed-loop transfer response (Ref. 3) for the ECO system is

$$\frac{\hat{\theta}(z)}{\theta(z)} = \frac{G_0(z)}{1 + G_0(z)}$$

$$= \frac{H(z)\,G_0(z, 1-\tau)}{L(z) + H(z)\,G_0(z, 1-\tau)} \tag{5}$$

The characteristic equation for the ECO system is

$$L(z) + H(z)\,G_0(z, 1-\tau) = 0$$

or

$$L(z)\,[2z(z-1)^2] + H(z)\,[K_1K_2\,\{(1-\tau)^2 z^2 - (2\tau^2 - 2\tau - 1)\,z + \tau^2\}] = 0 \tag{6}$$

c. System analysis. The system will be analyzed for two considerations: stability and settling time. The system must be physically realizable with finite settling time and zero steady-state error for an input which could be either a constant, first derivative, or second derivative of phase.

Constraints. The constraints placed upon the system have the following meaning for the system parameters:

(1) Physically Realizable. For a closed-loop system to be physically realizable implies that the degree of the denominator polynomial of the open-loop transfer response is larger than the degree of the numerator polynomial. Therefore from Eq. (4) the degree of the polynomial of $H(z)$ must be less than, or equal to, the degree of the polynomial of $L(z)$.

(2) Zero Steady-State Error. For an input function that is either phase, frequency, or the derivative of frequency, the zero steady-state error constraint implies that the system must be at least a type 3 system (Ref. 6). For a type 3 system there must be three roots of the open-loop transfer function $G_0(z)$ at $z = 1$. Therefore $L(z)$ must have a zero at $z = 1$.

(3) Finite Settling Time. A system has finite settling time if a transient in the output produced by a change in the input converges to zero in a finite time. This is referred to as *deadbeat response* (Ref. 2). A necessary condition for finite settling time response is that the roots of the characteristic equation (Eq. 6) coincide at the origin. Therefore, all the coefficients of the characteristic equation polynomial are set to zero except the highest degree coefficient.

It is assumed that the minimum form for the polynomials for $H(z)$ and $L(z)$ are

$$H(z) = z(nz^2 + pz + r)$$

$$L(z) = (z-1)\left[\frac{1}{2}(z^2 + sz + t)\right] \tag{7}$$

This above assumption will be shown to be true when the coefficients of $H(z)$ and $L(z)$ are calculated. Substituting Eqs. (7) and (8) into Eq. (6) gives

$$z\{z^5 + (s - 3 + K_3n\alpha)\,z^4 + (3 + t - 3s + K_3\alpha p + K_3\beta n)\,z^3 + (3s - 1 - 3t + K_3\alpha r + K_3\beta p + K_3\tau^2 n)\,z^2 + (3t - s + K_3\beta r + K_3\tau^2 p)\,z + (K_3\tau^2 r - t)\} = 0$$

where

$$K_3 = K_1K_2$$

$$\alpha = (1-\tau)^2$$

$$\beta = -(2\tau^2 - 2\tau - 1)$$

To satisfy the requirement for finite settling time, the following five conditions (which are merely the lower degree coefficients of the characteristic equation set equal to zero) must be true:

(1) $(s - 3 + K_3n\alpha) = 0$

(2) $(3 + t - 3s + K_3\alpha p + K_3\beta n) = 0$

(3) $(3s - 1 - 3t + K_3\alpha r + K_3\beta p + K_3\tau^2 n) = 0$

(4) $(3t - s + K_3\beta r + K_3\tau^2 p) = 0$

(5) $(K_3\tau^2 r - t) = 0$

Solving the above equations simultaneously gives

$$n = \frac{1}{8K_3}[2\tau^2 + 12\tau + 17]$$

$$p = -\frac{1}{8K_3}[4\tau^2 + 20\tau + 20]$$

$$r = \frac{1}{8K_3}[2\tau^2 + 8\tau + 7]$$

$$s = -\frac{1}{8}[2\tau^4 + 8\tau^3 - 5\tau^2 - 22\tau - 7]$$

$$t = \frac{1}{8}[2\tau^4 + 8\tau^3 + 7\tau^2]$$

The compensation equation by which the computer multiplies the error phase each sampled time is

$$\frac{H(z)}{L(z)} = \frac{z\left[2\tau^2 + 12\tau + 17\right)z^2 - (4\tau^2 + 20\tau + 20)\,z + (2\tau^2 + 8\tau + 7)]}{K_3(z-1)\left[8z^2 - (2\tau^4 + 8\tau^3 - 5\tau^2 - 22\tau - 7)\,z + \tau^2(2\tau^2 + 8\tau + 7)\right]} \tag{9}$$

The open-loop transfer response (Eq. 4) becomes

$$G_0(z) = \frac{\overline{K}(\alpha z^2 + \beta z + \tau^2)(nz^2 + pz + r)}{(z-1)^3(z^2 + sz + t)} \tag{10}$$

where $\overline{K} = K_1K_2/K_3$. The closed-loop transfer function response (Eq. 5) becomes

$$\frac{\hat{\theta}(z)}{\theta(z)} = \frac{\overline{K}\left[\alpha n z^4 + (\alpha p + \beta n)z^3 + (\alpha r + \beta p + \tau^2 n)z^2 + (\beta r + \tau^2 p)z - t\right]}{(z-1)^3(z^2 + sz + t) + \overline{K}\left[\alpha n z^4 + (\alpha p + \beta n)z^3 + (\alpha r + \beta p + \tau^2 n)z^2 + (\beta r + \tau^2 p)z - t\right]} \tag{11}$$

and the error closed-loop response is

$$\frac{E(z)}{\theta(z)} = \frac{(z-1)^3(z^2 + sz + t)}{\left\{\left[(z^5 + (s-3)z^4 + (3 - 3s + t)z^3 + (3s - 3t - 1)z^2 + (3t - s)z - t)\right] + \overline{K}(\alpha n z^4 + (\alpha p + \beta n)z^3 + (\alpha r + \beta p + \tau^2 n)z^2 + (\beta r + \tau^2 p)z + \tau^2 r)\right]\right\}} \tag{12}$$

Stability. The stability of a system is defined for values of open-loop gain constants. The gain of the integrator, K_1, is essentially a constant. The gain of a stable low-phase noise VCO, K_2, may vary as much as $\pm 5\%$ from any given nominal value. Therefore the normalized gain, $\overline{K}$, may vary $\pm 5\%$, so that the range of the normalized gain is $0.95 \leq \overline{K} \leq 1.05$. The stability of the closed-loop transfer function (Eq. 11) will be examined over the range of $\overline{K}$. The analysis will use the root locus technique.

The root locus is determined from the open-loop response $G_0(z)$, Eq. (10). The locations of the poles of the closed-loop transfer response are determined by the root locus plot for a value of $\overline{K}$. From the finite settling time constraint with $\overline{K} = 1.0$, the closed-loop transfer response is

$$\frac{\hat{\theta}(z)}{\theta(z)} = \frac{\left[\alpha n z^4 + (\alpha p + \beta n)z^3 + (\alpha r + \beta p + \tau^2 n)z^2 + (\beta r + \tau^2 p)z - t\right]}{z^5}$$

which has all its poles at the origin. As the normalized gain varies from 1.0, the poles move away from the origin. The condition for stable operation using the z-transform technique is that all the poles must remain within the unit circle.

A complete root locus plot is shown for four values of computer delay time τ in Figs. 36 to 39. Since the plots are symmetric about the real axis, only the upper half plane is shown. Figures 40 to 43 show detailed plots of the stable region for the same values of τ. A circle on each of the detailed plot figures indicates the maximum deviation of the closed-loop poles from the origin for a normalized gain variation of $\pm 5\%$.

Settling time. The settling time determines how rapidly the output will reach the steady-state condition, and how rapidly the error converges to zero. Since an inverse transform does not exist for the z-transform, the value of the error function in time can only be determined at the sample points. The equation for obtaining these points is

$$E(z) = \sum_{n=0}^{\infty} e(nT)\,z^{-n}$$

For the case where $\tau = 0$, $\overline{K} = 1.0$, Eq. (12) becomes

$$\frac{E(z)}{\theta(z)} = \frac{(z-1)^3(z + 0.875)}{z^4}$$

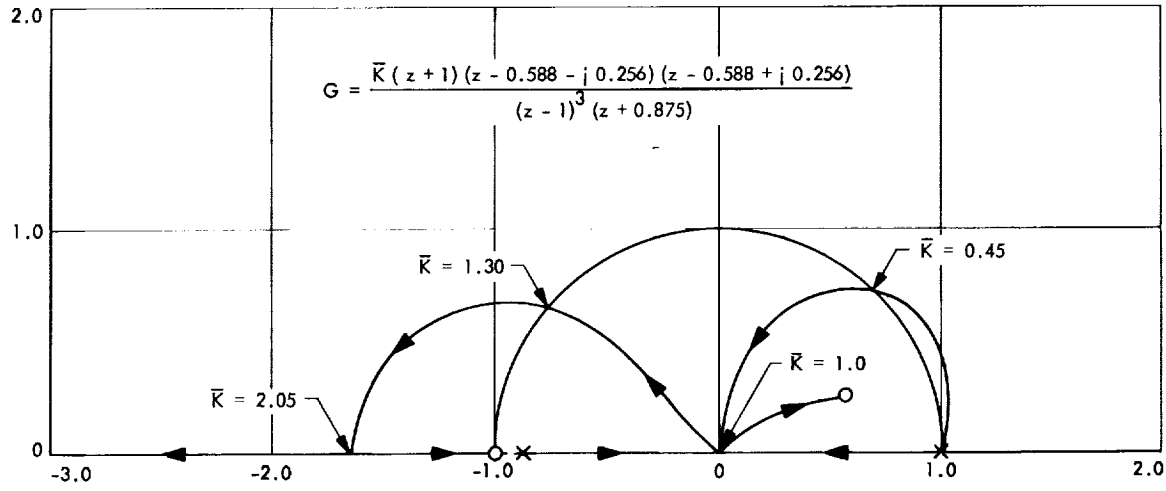

Fig. 36. Root locus plot, $\tau = 0$

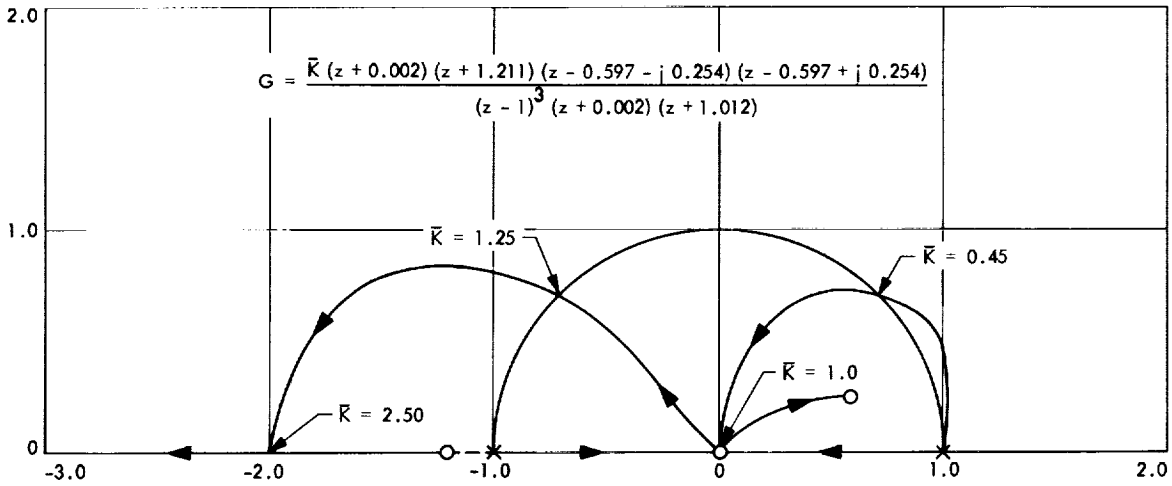

Fig. 37. Root locus plot, $\tau = 0.05$

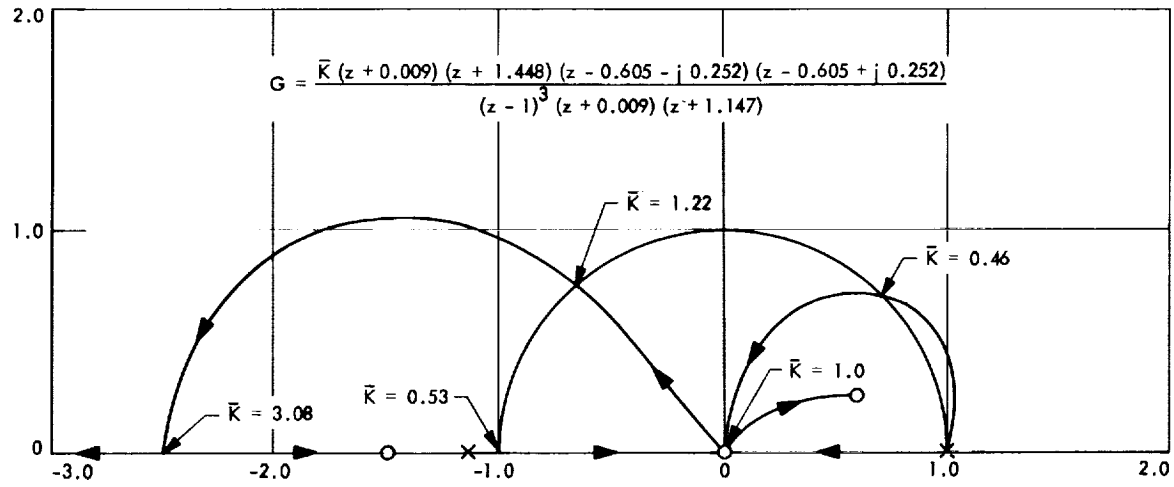

Fig. 38. Root locus plot, $\tau = 0.1$

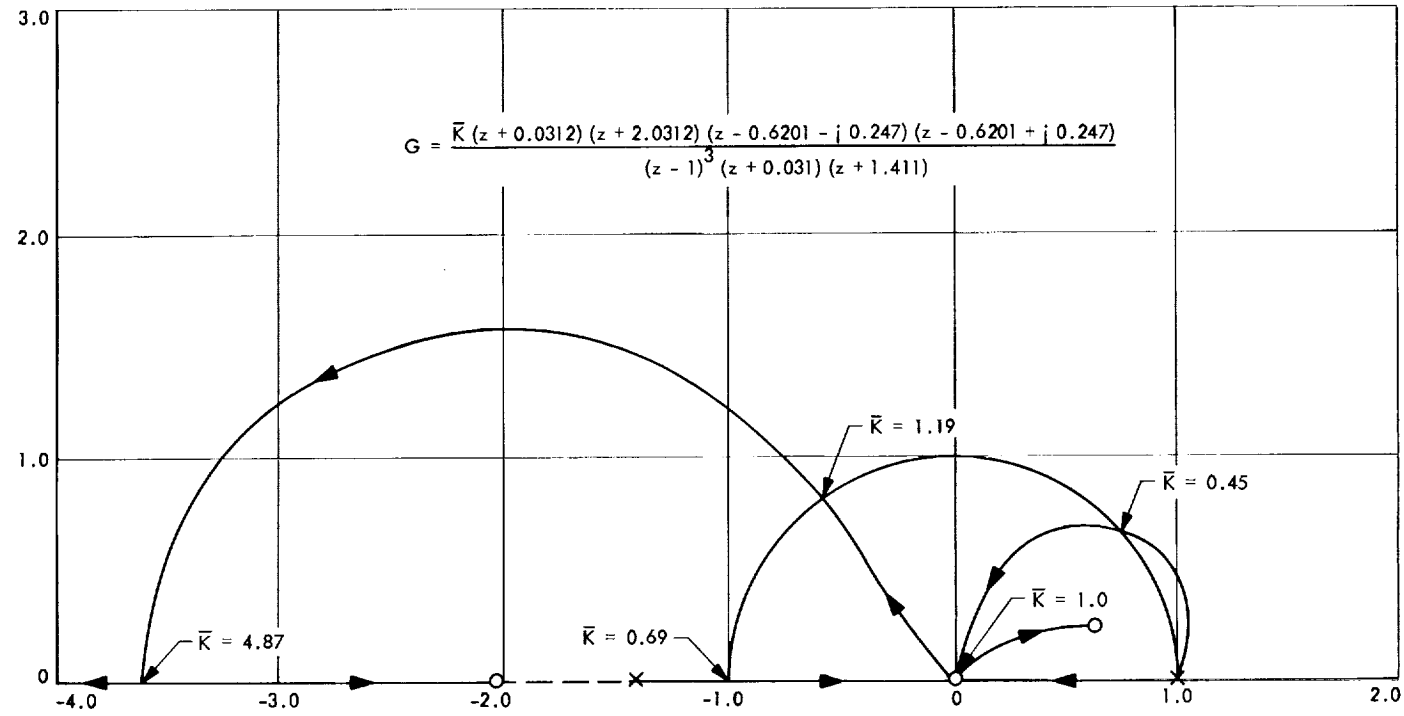

Fig. 39. Root locus plot, $\tau = 0.2$

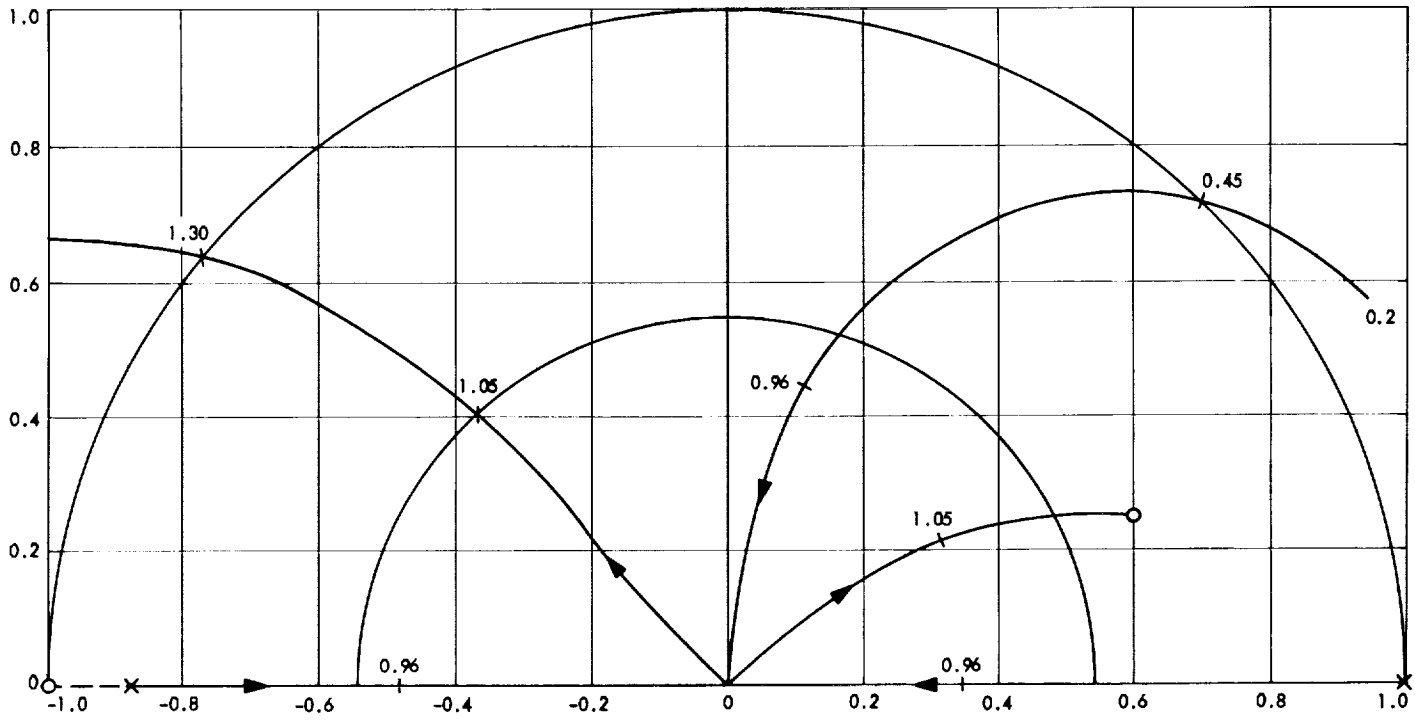

Fig. 40. Detailed root locus plot, $\tau = 0$

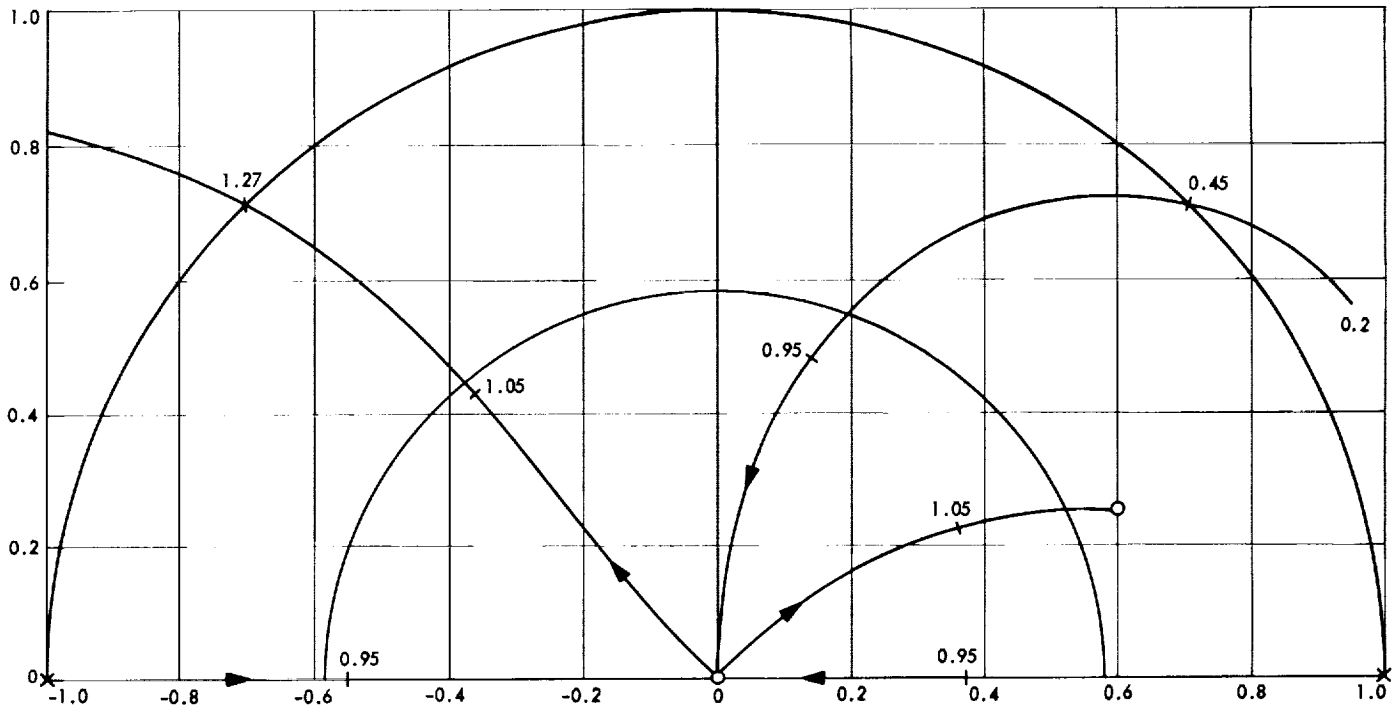

Fig. 41. Detailed root locus plot, $\tau = 0.05$

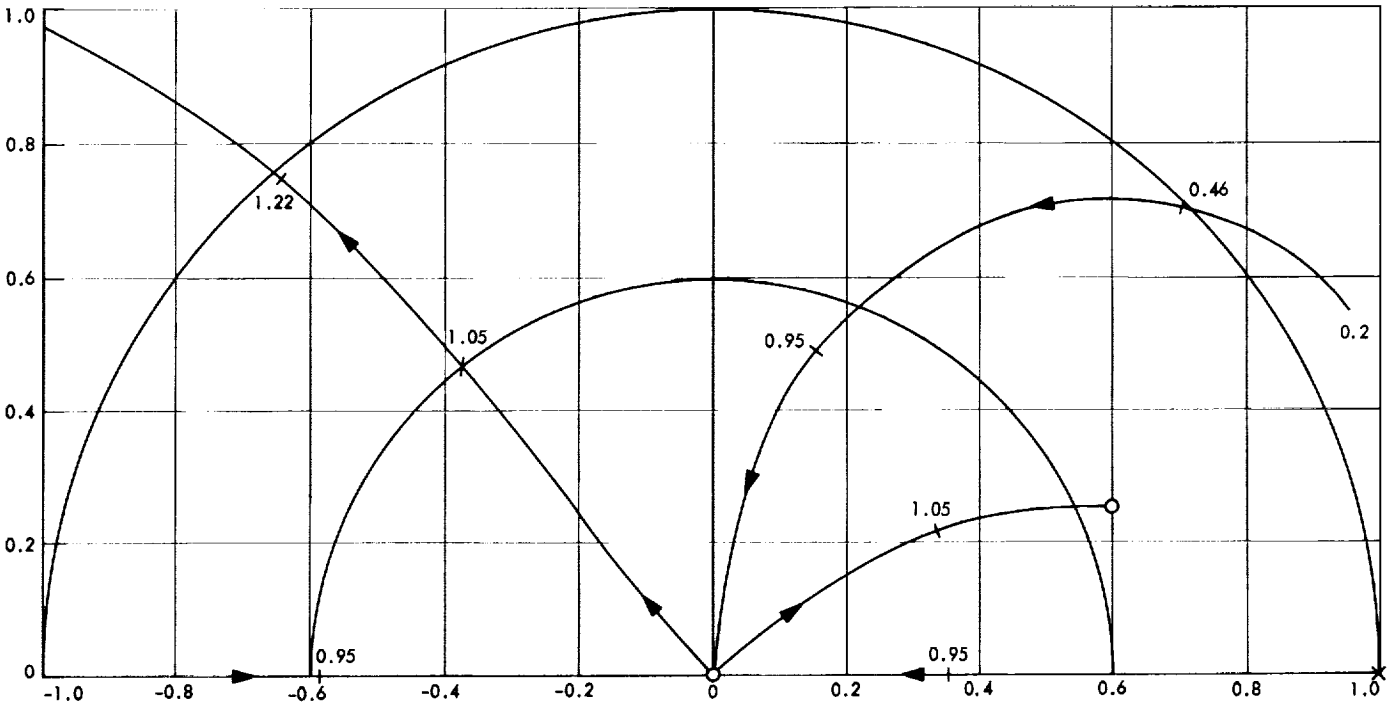

Fig. 42. Detailed root locus plot, $\tau = 0.1$

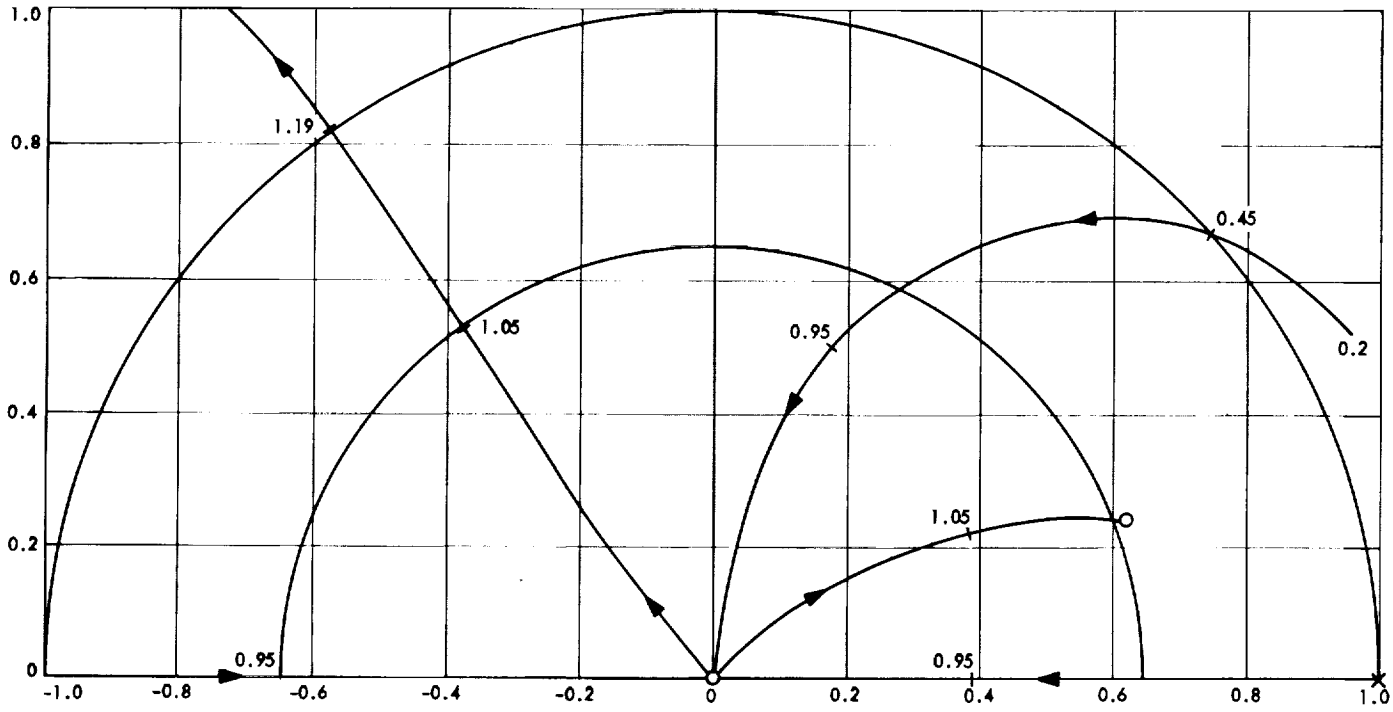

Fig. 43. Detailed root locus plot, $\tau = 0.2$

The phase error for three possible types of input phase is

(1) For a unit impulse input

$$E(z) = 1 - 2.125z^{-1} + 0.375z^{-2}\,1.625z^{-3} - 0.875z^{-4} + 0z^{-5} + \cdots$$

(2) For a unit step input

$$E(z) = 1 - 1.125z^{-1} - 0.75z^{-2} + 0.875z^{-3} + 0z^{-4} + \cdots$$

(3) For a unit ramp input

$$E(z) = 0 + z^{-1} - 0.125z^{-2} - 0.875z^{-3} + 0z^{-4} + \cdots$$

Therefore the error reaches zero steady state within five sample periods for any of the above inputs.

The conditions which result in the longest settling time occur when $\tau = 0.2$ and $\overline{K} = 0.95$. This is shown in Fig. 43. The error closed-loop response (Eq. 12) becomes

$$\frac{E(z)}{\theta(z)} = \frac{8z^5 - 12.4672z^4 - 10.2512z^3 + 25.5568z^2 - 10.4912z - 0.3472}{8z^5 - 0.62336z^4 - 0.51256z^3 + 1.27784z^2 - 0.52456z - 0.01736}$$

Again using a unit step input phase, the phase error equation is

$$E(z) = 1 - 0.48z^{-1} - 1.81z^{-2} + 1.02z^{-3} + 0.24z^{-4} + 0.44z^{-5} - 0.14z^{-6} + 0.13z^{-7} + 0.04z^{-8} + \cdots$$

Applying the final value theorem (Ref. 7) to the error closed-loop response equation with the above conditions shows that

$$E(z) \to 0 \quad \text{as } z \to 1$$

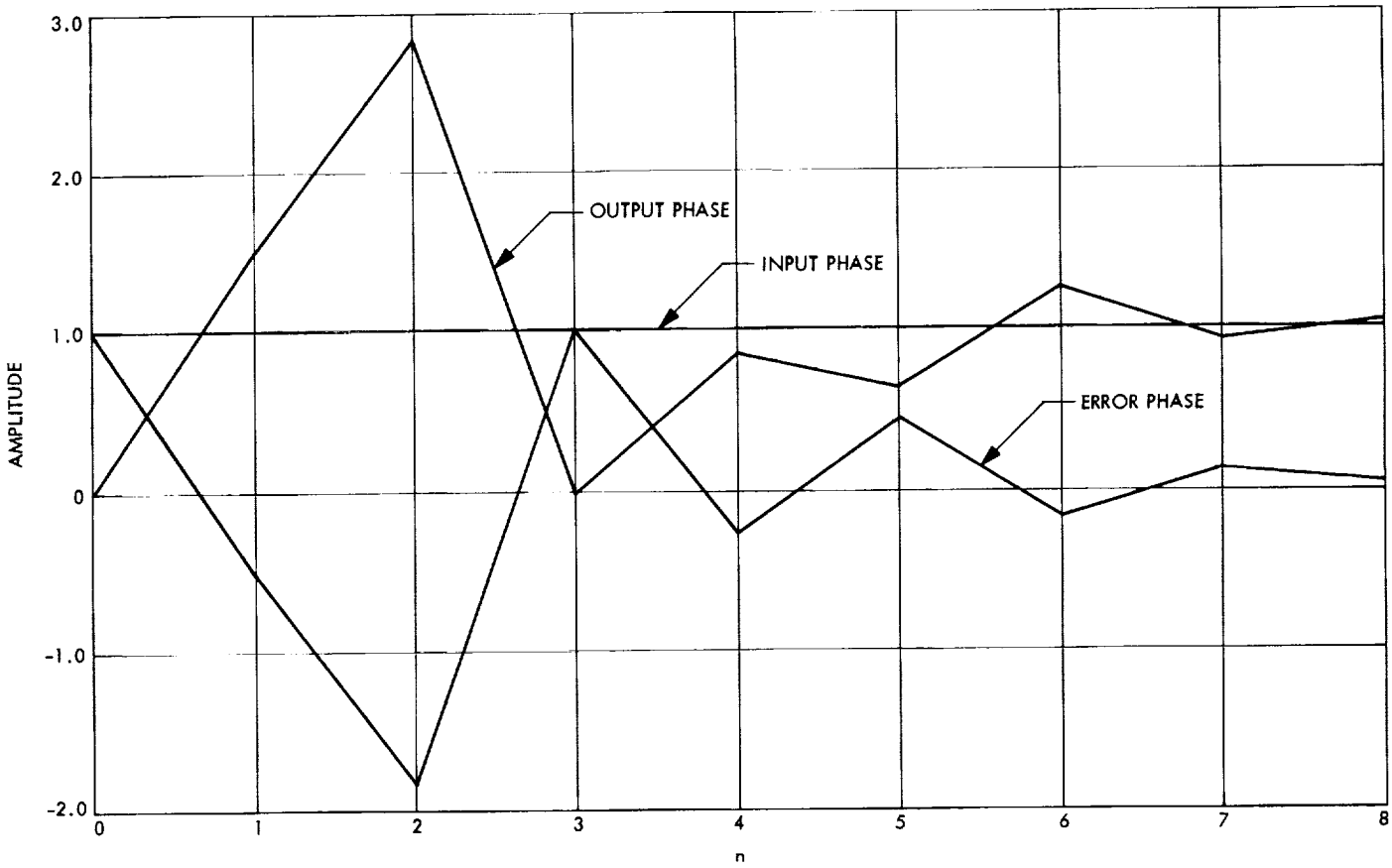

Fig. 44. Settling time for ECO when $\tau = 0.2, \bar{K} = 0.95$

A plot of the input step phase, the error phase and the output phase as a function of the sampled time for the longest settling time is shown in Fig. 44.

d. Conclusions. The analysis shows that the constraints placed on the system have been completely satisfied. Equation (9) and Figs. 40 to 43 show that the system is physically realizable and stable for a computer time delay up to two-tenths of a sample period. The settling time is finite and the steady-state error is zero for phase, frequency, or derivative of frequency inputs.

References

1. Viterbi, A. J., *Principles of Coherent Communication*, McGraw-Hill Book Company, Inc., New York, 1966.
2. Jury, E. I., *Sampled-Data Control Systems*, John Wiley & Sons, Inc., New York, 1958.
3. Tou, J. T., *Digital and Sampled-Data Control Systems*, McGraw-Hill Book Company, Inc., New York, 1959.
4. Murphy, G. J., *Basic Automatic Control Theory*, 2nd Ed., D. Van Nostrand Company, Inc., Princeton, New Jersey, 1966.
5. Horowitz, I. M., *Synthesis of Feedback Systems*, Academic Press, New York, 1963.
6. D' Azzo, J. J., and Houpis, C. H., *Feedback Control System Analysis and Synthesis*, McGraw-Hill Book Company, Inc., New York, 1960.
7. Ragazzini, J. R., and Franklin, G. F., *Sampled-Data Control Systems*, McGraw-Hill Book Company, Inc., New York, 1958.

C. Tracking and Data Acquisition Elements Research

1. Low-Noise Receivers, Microwave Maser Development, Second-Generation Maser, R. C. Clauss

a. Introduction. The performance of a traveling-wave maser is degraded by high-level interfering signals. This problem has been considered in relation to the diplexed operation of an S-band maser receiving system. The effects of power at the fundamental transmitter frequency (2115 MHz) and the transmitter harmonics (4230 through 16,920 MHz) have been observed with the second generation maser operating in the 2270- to 2300-MHz range. Degraded performance occurs in several ways: maser gain is reduced, noisy oscillations occur, and mixing has been observed at three particular frequencies. In general,

the maser should not be subjected to power levels greater than 0.1 mW at 2115 MHz or any of the transmitter harmonics.

b. Instrumentation. The effects of microwave power at 2115 MHz are determined by monitoring maser performance from 2270 to 2300 MHz. A block diagram of the test configuration is shown in Fig. 45. The 2115-MHz oscillator provides power to the maser input at levels up to 5 W. A waveguide bandpass filter is used to prevent oscillator or ambient noise from being amplified by the maser. The nonresistive termination of the maser at 2270 to 2300 MHz reduces the total system temperature to approximately 15°K. A swept receiver used with an X-Y recorder displays the maser passband, showing changes in gain and noise level.

Changes in maser performance caused by signals between 4 and 18 GHz have been measured, using test equipment as shown in Fig. 46.

c. Results. The maser comb structure has a low-frequency cutoff at 2200 MHz, and less than 10% of the available power at 2115 MHz is absorbed by the maser. Trace 1 in Fig. 47 shows the maser response with test signals of approximately −137 dBmW used to indicate the signal-to-noise ratio. A reduction of maser gain (~½ dB) is caused by 10 mW at 2115 MHz. Noisy oscillations occur and are observed on trace 2. The noise generation problem is unique to amplifiers using single-crystal yttrium iron garnet isolator material. Replacement of the first two isolator disks with polycrystalline material eliminated this phenomena. The gain reduction is not an isolator-

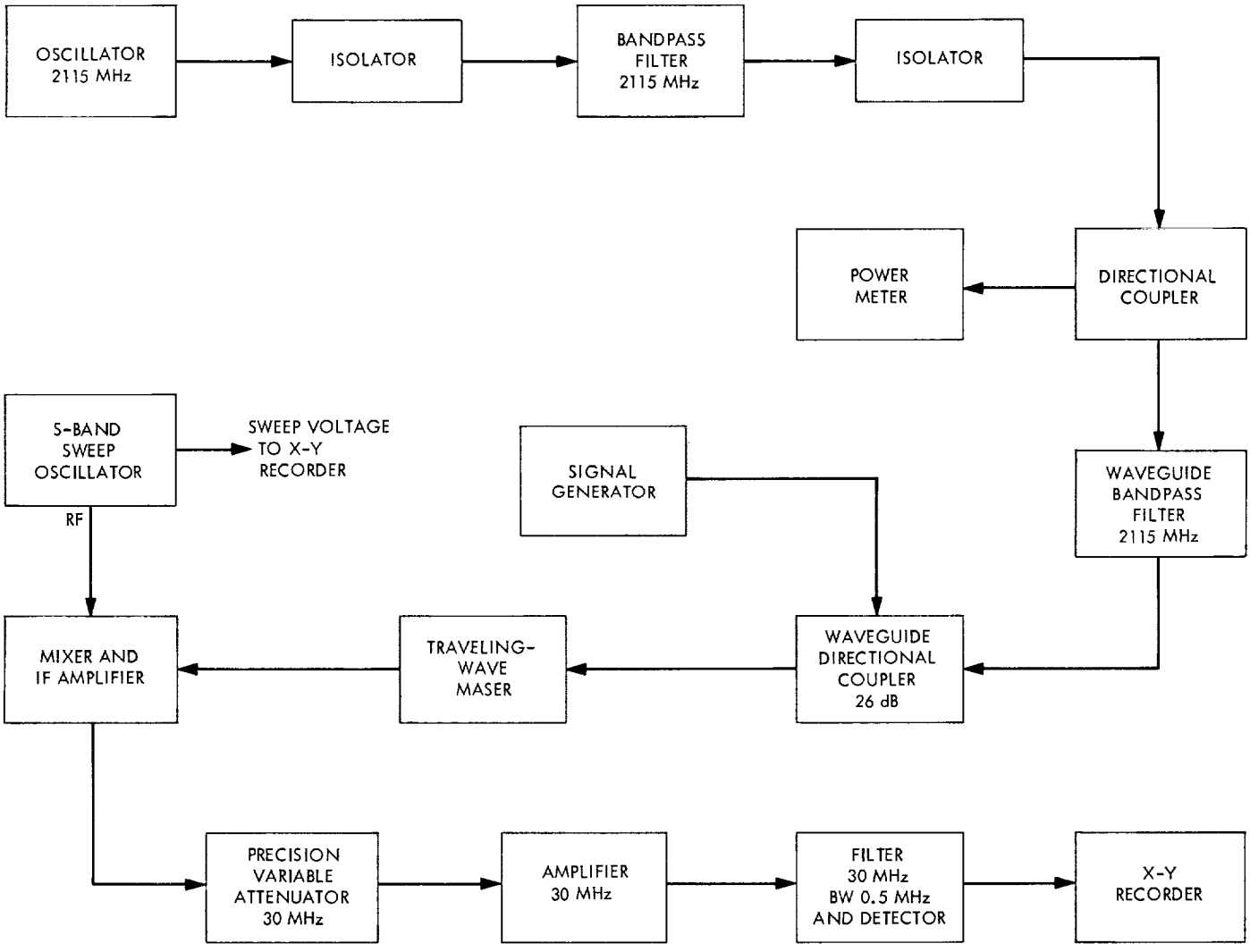

Fig. 45. Test configuration for effects of power at 2115 MHz

associated problem and did not change with the replacement of the single-crystal material. A power level of 60 mW at 2115 MHz caused a 0.7-dB gain reduction; 0.1 mW at 2115 MHz caused approximately a 0.05-dB gain reduction.

Signals at frequencies higher than the maser operating range travel through the maser in an unpredictable manner. Measurements using signals between 4 and 18 GHz, at power levels above 0.1 mW, indicate that gain reductions occur at frequencies where power is absorbed by the maser, in a somewhat random manner. The three traces shown in Fig. 48 are typical of data obtained while an interfering signal is swept through the indicated range. Figure 48 shows several gain reductions caused by a 20-mW signal sweeping from 7 to 8 GHz. As the interfering signal sweeps through 7.5 GHz, doubling and mixing (with the pump signal) occur in the maser. The isolator

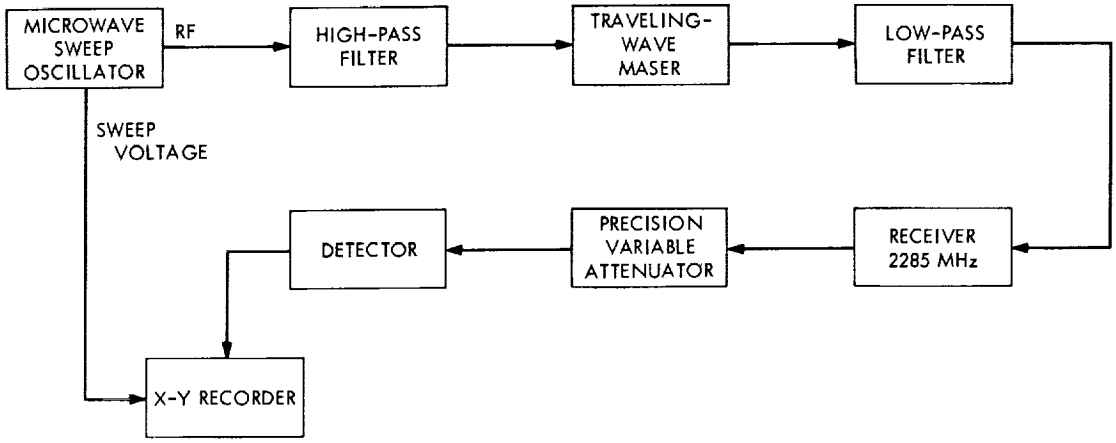

Fig. 46. Test configuration for effects of power between 4 and 18 GHz

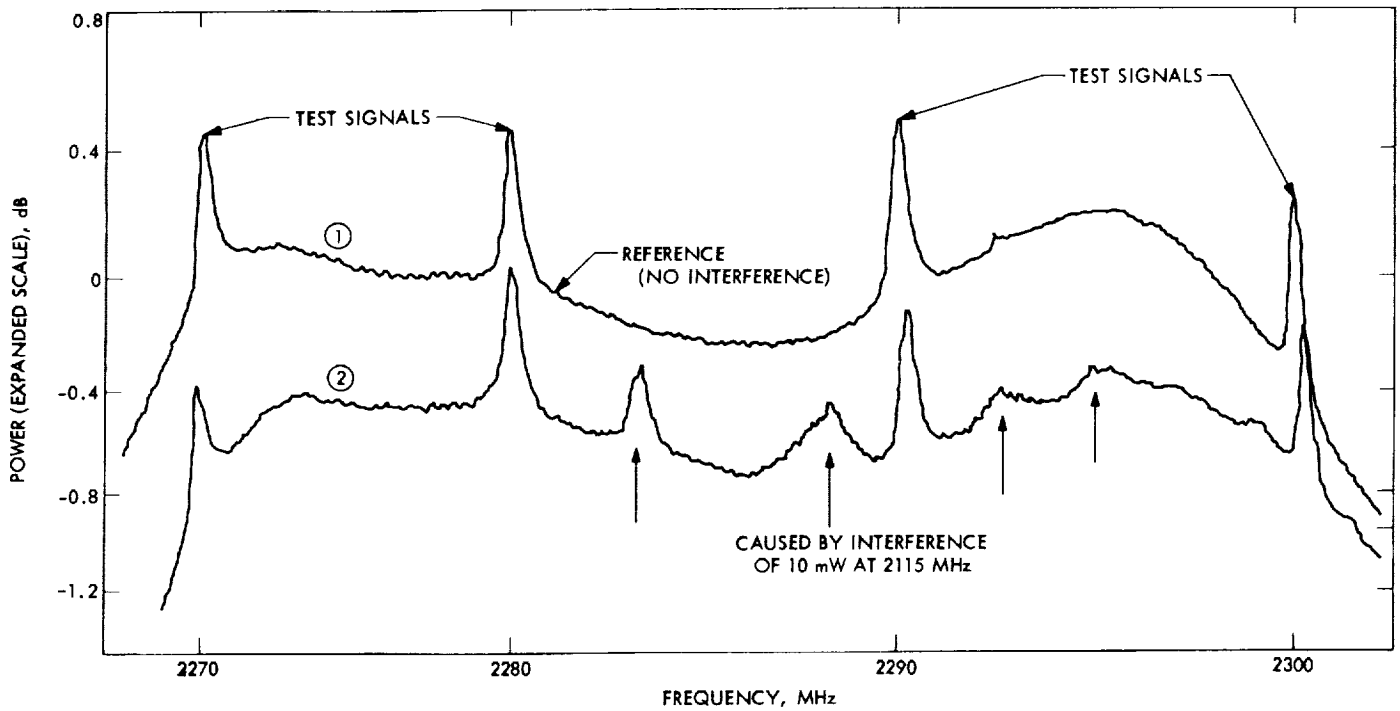

Fig. 47. X-Y recording showing effect of 10 mW at 2115 MHz

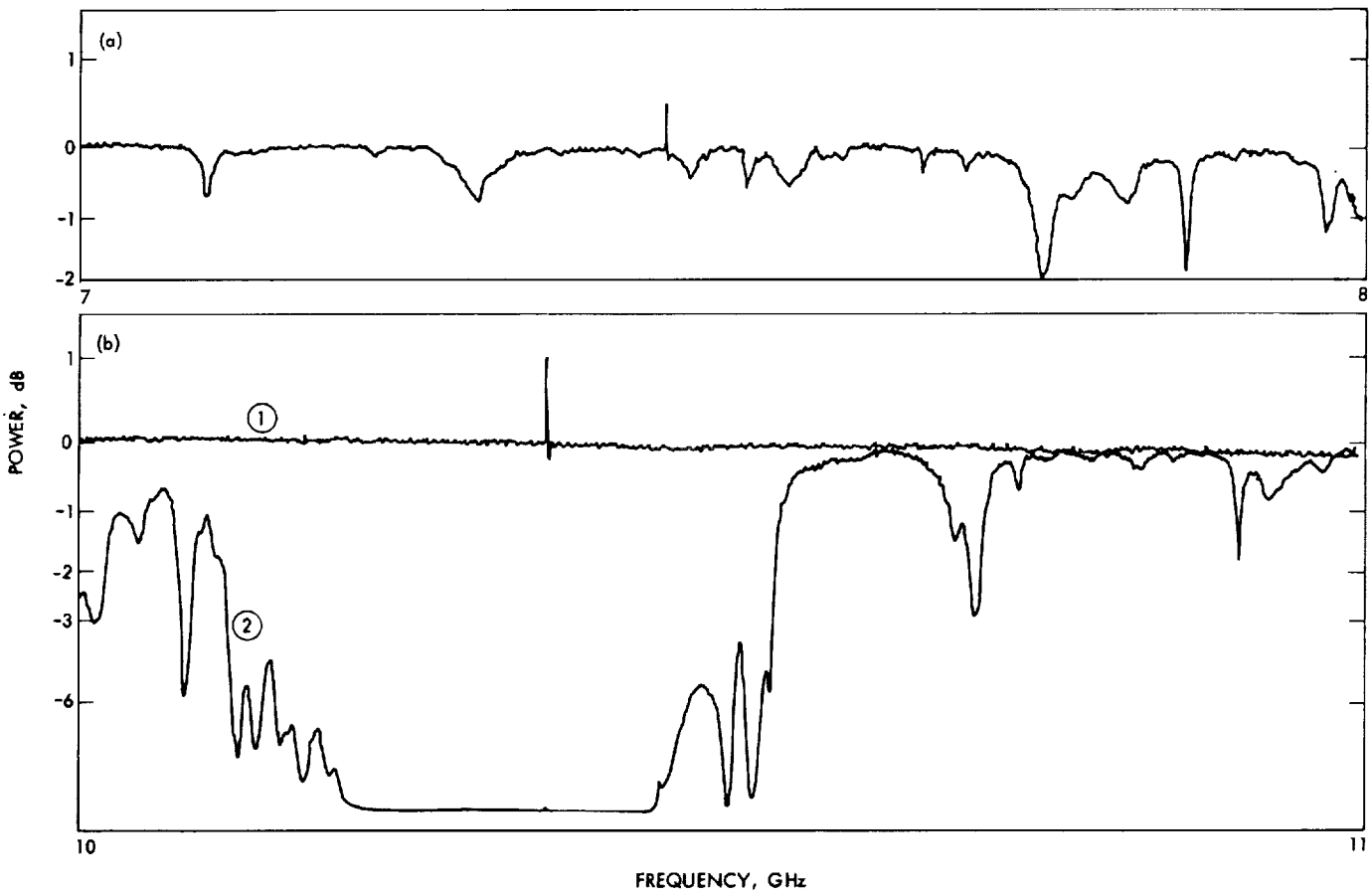

Fig. 48. Typical test data for interfering signals sweeping from (a) 7 to 8 GHz, and (b) 10 to 11 GHz

material probably accounts for these nonlinear phenomena. Traces 1 and 2 in Fig. 48(b) are the result of less than 0.1 and 20 mW power levels sweeping from 10 to 11 GHz. Gain reductions and mixing occur near 10.4 GHz. Signals near 10.4 GHz (the maser idle frequency) should be avoided at any power level.

The use of a bandpass or a low-pass filter in the maser input line has been considered and should reduce the sensitivity of the maser to interfering signals. This technique has been successfully used with an X-band traveling-wave maser to reduce pump power radiation.

2. Improved RF Calibration Techniques: Operating Noise Temperature Calibration of a Low-Noise Receiving System, *C. T. Stelzried*

a. Introduction. Low-noise receiving system operating noise temperature calibrations (Ref. 1) using the microwave ambient termination technique have been discussed in detail (SPS 37-42, Vol. III, p. 25). The calibrations are made by switching the maser input between the antenna and an ambient termination. The principal advantage of this technique is the long-term stability and reliability of the ambient termination. Another advantage is that it is not necessary to evaluate the waveguide losses when the operating noise temperature is defined at the maser input. This technique does depend on a previous calibration of the maser effective input noise temperatures.

The present analysis obtains a least squares criteria estimate of a series of power ratio differences when the maser input is alternately switched between the antenna and the ambient termination. This technique is superior to the averaged method previously employed. An error analysis with sample numerical estimates is presented which considers both dispersion and bias errors. The analysis has been programmed in Fortran IV and is currently being applied to the JPL receiving system research cones. Operational data are presented for the period of February 6 to June 11, 1968.

b. Analysis. The total operating noise temperature of a receiving system can be expressed[11]

$$T_{op} = T_A + T_e \tag{1}$$

where

T_A = antenna temperature, °K

T_e = receiver effective input temperature, °K

Figure 49 shows a simplified block diagram of the receiving system noise temperature instrumentation. The precision attenuator is adjusted for equal output power when the receiver input is alternately connected to the ambient load and the antenna. The power ratio for an individual measurement is

$$Y_{AP}(I) = \frac{T_P + T_e}{T_{op}(I)} \tag{2}$$

where

T_P = ambient termination physical temperature, °K

T_e = receiver effective input noise temperature, °K

$T_{op}(I)$ = individual operating noise temperature measurement (on antenna), °K

The equation is valid regardless of whether the temperatures are defined at the input to the first amplifier (as assumed in this article) or at the horn input.

[11]IRE Standards on Electron Tubes: Definitions of Terms, 1962 (62 IRE 7.S2) *Proceedings of the IEEE*, March 1962, p. 434.

$$T_{op}(I) = \frac{T_P + T_e}{Y_{AP}(I)} \tag{3}$$

The best estimate Y_{AP} in a least squares sense (Ref. 2) of the difference in a series of attenuator readings $Y_{AP}(I)$ is obtained from an existing computer program (JPL ID 5843000, CTS3B) used as a subroutine. The operating noise temperature is then given by

$$T_{op} = \frac{T_P + T_e}{Y_{AP}} \tag{4}$$

The ambient termination temperature is measured and the receiver effective input temperature (SPS 37-47, Vol. III, p. 237) is estimated or calibrated (Ref. 3). It is not necessary to know T_e accurately if $T_e << T_P$. An improved operational estimate of the receiver effective temperature is obtained from

$$T_e = T_M + T_F \tag{5}$$

and

$$T_F = \frac{T_M + T_P}{Y_{00} - 1} \tag{6}$$

where

T_M, T_F = first and second amplifier effective noise temperatures defined at the first amplifier input, °K

Y_{00} = power ratio at the receiving system output when the first amplifier (connected to the ambient termination) is alternately turned on and off

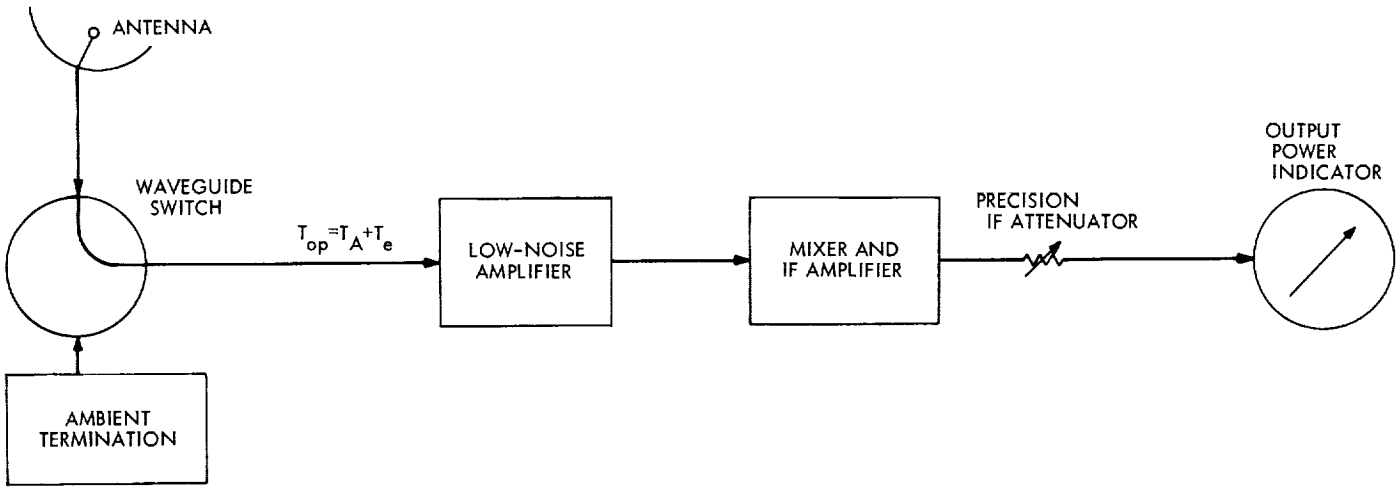

Fig. 49. Receiving system operating noise temperature calibration system block diagram

The assumption has been made that the noise temperature at the output of the nonoperational first amplifier is small compared to the noise temperature of the second amplifier.

An estimate of the statistical dispersion measurement probable error (Ref. 4) of T_{op} is given by

$$PE_{T_{op}} = \frac{PE_{Y_{AP}}}{10 \log_{10} e}(T_{op}) \tag{7}$$

where

$PE_{Y_{AP}}$ = statistical measurement probable error of Y_{AP} (dB) (obtained from output of computer program CTS3B), dB

An estimate of the total error (assuming the various sources of error are not correlated) found by differentiating Eq. (3) and accounting for statistical and mismatch errors is

$$PE_{T_{op/T}} = [PE^2_{T_{op/D}} + PE^2_{T_{op/T_P}} + PE^2_{T_{op/T_M}} + PE^2_{T_{op/Y_{AP}}} + PE^2_{T_{op/MM}}]^{1/2} \tag{8}$$

where

$PE_{T_{op/T_P}}$ = probable error of T_{op} due to an error in T_P

$$= \frac{T_{op}}{T_P + T_e} PE_{T_P}$$

$$\simeq \frac{30}{295 + 5} \simeq 0.02$$

$PE_{T_{op/T_M}}$ = probable error of T_{op} due to an error in T_M

$$= \frac{T_{op}}{T_P + T_e} PE_{T_M}$$

$$= \frac{30}{295 + 5}(0.5) \simeq 0.05$$

$PE_{T_{op/Y_{AP}}}$ = probable error of T_{op} due to an error in Y_{AP} assuming an attenuator peak nonlinearity a_2, dB/dB

$$\simeq \frac{1}{5} \frac{T_{op}}{10 \log_{10} e}(a_2) Y_{AP} \text{ dB}$$

$$\simeq \frac{1}{5} \frac{30}{4.3429}(0.02)(10) \simeq 0.28$$

$PE_{T_{op/MM}}$ = probable error of T_{op} (Ref. 5) due to antenna, ambient termination, and receiver VSWR mismatches (S_A, S_P, and S_e, respectively)

$$\simeq \frac{1}{5} \frac{T_{op}}{T_P + T_e} \left\{ \max: \left[1 - \frac{S_P}{S_A}\left(\frac{S_A S_e + 1}{S_P S_e + 1}\right)^2\right] T_P + \left[1 - \frac{1}{S_A}\left(\frac{S_A S_e + 1}{S_e + 1}\right)^2\right] T_e \right\}$$

$$\text{or } \left[1 - \frac{S_P}{S_A}\left(\frac{S_A + S_e}{S_P S_e + 1}\right)^2\right] T_P + \left[1 - \frac{1}{S_A}\left(\frac{S_A + S_e}{S_e + 1}\right)^2\right] T_e \Bigg\}$$

$$\text{or } \left[1 - \frac{S_P}{S_A}\left(\frac{S_A S_e + 1}{S_P + S_e}\right)^2\right] T_P + \left[1 - \frac{1}{S_A}\left(\frac{S_A S_e + 1}{S_e + 1}\right)^2\right] T_e \Bigg\}$$

$$\text{or } \left[1 - \frac{S_P}{S_A}\left(\frac{S_A + S_e}{S_P + S_e}\right)^2\right] T_P + \left[1 - \frac{1}{S_A}\left(\frac{S_A + S_e}{S_e + 1}\right)^2\right] T_e \Bigg\}$$

Letting $T_P = 295°\text{K}$, $T_e = 5°\text{K}$, $T_{op} = 30°\text{K}$, $PE_{T_P} = 0.2$, $PE_{T_M} = 0.05$, $a_2 = 0.02$ dB/dB, $S_A = 1.15$, $S_P = 1.02$, and $S_e = 1.15$ for a sample receiving system, then the error estimates are

$$PE_{T_{op/MM}} \simeq \frac{1}{5} \frac{30}{295 + 5} \left\{ \left[1 - \frac{1.02}{1.15}\left(\frac{1.15 \times 1.15 + 1}{1.02 \times 1.15 + 1}\right)^2\right] 295 + \left[1 - \frac{1}{1.15}\left(\frac{1.15 \times 1.15 + 1}{1.15 + 1}\right)^2\right] 5 \right\} \simeq 0.10$$

A small portion of the noise radiating from the receiver toward the termination is reflected back into the receiver. An exact analysis of this source is complicated by correlation effects (Ref. 5). This effect is small with the system analyzed above (less than 0.01°K) due to the low radiated power of the maser (on the order of 10°K) and the well-matched termination and need not be considered. The total error estimate (from Eq. 8 and assuming a system dispersion measurement error for Eq. 7 of 0.02°K) is 0.30°K. The assumption is made that the receiving system is linear from the input through to the precision attenuator (no amplifier saturation, etc.). A standard test routine has been developed to provide periodic verification of system linearity (JPL computer program ID 5844000, CTS22) using a standard RF signal generator. The largest source of error for the sample receiving system (representative of the present JPL research operational receiving systems) is due to the precision attenuator nonlinearity.

c. Operational data. Considerable operating noise temperature data have been collected for various receiving system configurations, operating frequencies and installations (on ground and on antenna). The present JPL "front end" research cones using the ambient load calibration technique are designated:

(1) S-band planetary radar (SPR) cone.

(2) S-band multifrequency (SMF) cone.

(3) S-band cassegrain ultra (SCU) cone.

(4) S-band cassegrain experimental (XCE) cone. Figure 50 shows this cone installed on the Mars DSS 210-ft antenna.

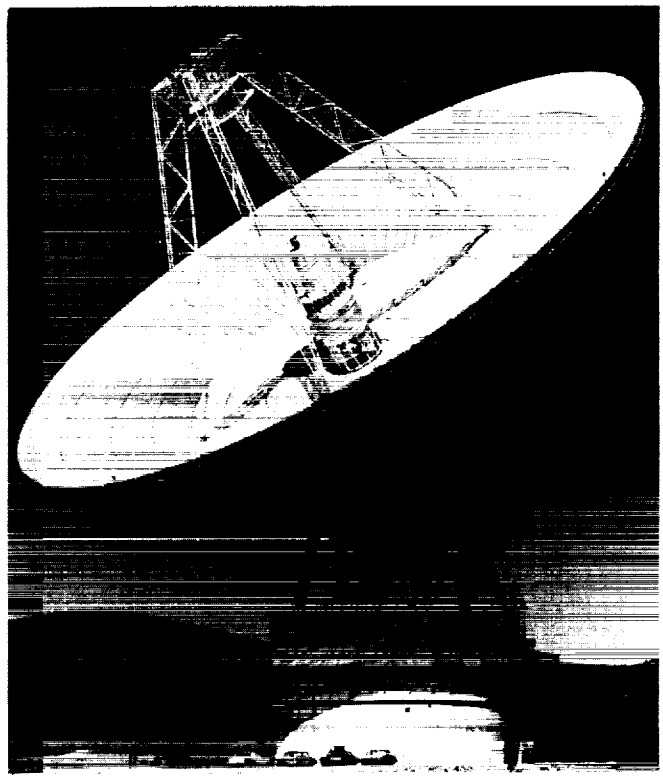

Fig. 50. SCE cone installed on Mars DSS 210-ft antenna

Table 5. Calibration parameters for Venus and Mars DSSs cassegrain cones

Cone (SN 01)	Mod	Frequency, MHz	Maser temperature T_M, °K	VSWR[a]			Comments
				S_A	S_P	S_e	
SPR	01	2295	5.3	1.237	1.352	1.172	See SPS 37-40, Vol. III, p. 98
		2388	5.0	1.015	1.006	1.094	
SPR	02	2295	5.3	1.250	1.280	1.174	Data obtained from R. Kolbly
		2388	5.0	1.084	1.020	1.463	
SMF	00	2297	7.2	1.026	1.033	1.252	See SPS 37-39, Vol. III, p. 85
		2388	7.0	—	—	—	
SCU	00	2295	4.1	1.013	1.005	1.222	See SPS 37-48, Vol. II, p. 52
		2388	4.1	1.030	1.253	1.252	
SCU	01	2295	5.4	1.044	1.001	1.266	See SPS 37-51, Vol. II
		2388	5.7	1.147	1.263	1.249[b]	
XCE	00	8448	13.7	1.010	1.006	1.020	See SPS 37-43, Vol. III, p. 59

[a] S_A, S_P, S_e = VSWR of antenna (right circular polarized), ambient termination, and maser input defined at maser input, respectively.
[b] Maser 1.

These cones are operated on the antennas of the Venus and Mars DSSs in a cassegrain configuration. The cones' calibration parameters are summarized in Table 5.

The above analysis has been programmed[12] in Fortran IV (JPL program ID 5841000, CTS20B). The input data is keyed to an operator data sheet (Table 6) to systemize the calibrations. Reflectometer readings of the antenna and ambient termination are included in the operational performance data. Although not as precise as a laboratory setup, this instrumentation (Ref. 6) allows the system input reflectometer measurements to be made quickly without disconnecting waveguide components.

[12]By L. Busch, Sect. 314.

Table 6. Operating noise temperature calibration data (typical)

5/1/68

NOISE TEMPERATURE CALIBRATION CTS/20B

(For use with JPL Computer Program ID # 5841000)

(1) Station: 13 (1)

(2) Cone: Type SCU (3) Serial No. 01 (6) Mod. 00 (8)

Configuration (10) Polarization (0, 1, 2 for RCP, LCP, Linear) 0 (11)

(3) Operator: LJW (12)

(4) Frequency: 2297.00 (15) Channel No. 00 (22)

(5) Time (GMT): Year 67 (24) Day No. 284 (26) Hour/Min 0830 (29)

(6) Mission: DAILY CHECK (33)

(7) Comments: (51)

(8) Outside weather: Humidity (%) 16 (69) Temperature (°C) 21.7 (71)

(9) Record 1 for yes: Clear weather 1 (75) Pre-Cal (76) Post-Cal (77)

Cone on ground 1 (78) Ant 30° EL (79) Zenith (within 5°) 1 (80)

(10) Maser off-on (db) on Ambient Load:	off	4.0 (1)	on	40.5 (6)
(11) Maser Gain (db) on Ambient Load	Ref/Gain	32.7 (11)	Maser/Gain	47.5 (16)
(12) Reflectometer (db) on Ambient Load:			Maser/VSWR	.9.7 (26)
on Antenna:	Maser/Gain	74.1 (31)	Maser/VSWR	43.0 (36)
(13) Ambient Load Temp. (°C)	Y-factor start	28.27 (41)	Y-factor end	28.24 (47)

Noise Temperature Y-factor Attenuator Readings (db):

(14) Antenna:	15.86 (1)	15.87 (8)	15.88 (15)	15.88 (22)
(15) Ambient Load:	29.82 (29)	29.83 (36)	29.82 (43)	

JPL 3388 (5-68)

Warning: Y-factor readings must be done with the IF filter in the broadband position. If RF spur located in pass band please note in comments and perform readings in narrow band position.

```
NOISE TEMPERATURE CALIBRATION   CTS20B
-------------------------------------------------------
STATION NO. 13
CONE    TYPE XCE  SERIAL NO. 01  MOD. 00
OPERATOR THC
FREQUENCY(MHZ) 8448.00      CHANNEL NO.
TIME(GMT)  YEAR   68  DAY NO.  54  HOUR 22  MIN.  0
MISSION  DAILY CHECK
COMMENTS
OUTSIDE WEATHER   HUM.(PCT) 25  TEMP.(C)  20.0
-------------------------------------------------------

          AA(I)   AP(I)   YAP(I)  TCP(I)
          ============================
          22.78   32.45    9.67   34.21
          22.61   32.34    9.73   33.74
          22.62   32.30    9.68   34.13
          22.56

-------------------------------------------------------

SYSTEM TEMPERATURES (DEG.K)
TOP          37.68
TE           14.66
TF            0.96

PROBABLE ERRORS IN SYSTEM TEMPERATURES (DEG.K)
PETOP/D     0.086
PETOP/TP    0.021
PETOP/TM    0.042
PETOP/YAP   0.102
PETOP/MP    0.041
PETOP/T     0.118
```

Fig. 51. Operating noise temperature computer program CTS20B measurement printout for the XCE cone pointed toward the zenith on Feb. 23, 1968

These data add to the confidence in the operating noise temperature data and have been invaluable as a trouble-shooting accessory.

Figure 51 shows a computer printout appropriate to the data sheet. These particular data were taken with the XCE cone at the Venus DSS operating at 8448 MHz pointed toward the zenith. Figure 52 shows the summary sheet for this system, operational on the ground, for the period February 6 to June 11, 1968. Operation of a cone on the ground prior to installation on the antenna verifies the performance and minimizes checkout time on the antenna.

A tabulation of the principal results of the operating noise temperature calibrations for the various research cone/antenna configurations using the ambient termination technique is presented in Table 7 for the period February 6 to June 11, 1968. The indicated errors are the standard deviation of the individual measurements and of the mean. These errors do not include instrumentation bias errors, such as those due to nonlinearity, etc. The system temperature averages were computed using only data with:

(1) Antenna at zenith.

(2) Clear weather.

SUMMARY OF RECEIVING SYSTEM DAILY NOISE TEMPERATURE CALIBRATIONS

CODE (0 FOR NO, 1 FOR YES)

STA.	CONE	CONFIG.	POLAR.	DP.	FREQ.(MHZ)										MISSION
	TIME (GMT)	HUM. (PCT)	TEMP. (C)	TEST PR PC	CLR. WTHR.	ZEN.	30DEG. EL	CONE ON GND.	REFL.(DB) AMB	ANT	GAIN (DB)	TF (K)	TOP (K)	PETOP/D (K)	PETOP/T (K)	COMMENTS
13	XCE/01/00	-0	RCP	RAP	8448.00											DAILY CHECKS
	38/ 3/40	40	10.0	0 0	1	1	0	1	51.6	44.0	42.1	1.08	34.12	0.04	0.31	CONE ON GROUND
13	XCE/01/00	-0	RCP	RLP	8448.00											DAILY CHECK
	38/ 6/ 5	40	7.2	0 0	1	1	0	1	42.5	34.5	35.5	1.33	32.57	0.02	0.30	
13	XCE/01/00	-0	RCP	ELL	8448.00											DAILY CHECK
	38/18/30	38	11.7	0 0	0	1	0	1	41.6	35.0	35.7	1.16	33.74	0.05	0.31	
13	XCE/01/00	-0	RCP	RLP	8448.00											DAILY CHECK
	39/ 2/20	40	10.	0 0	1	1	0	1	47.1	40.6	36.0	1.15	33.95	0.05	0.31	
13	XCE/01/00	-0	RCP	THP	8448.00											DAILY CHECK
	40/ 4/30	99	7.2	0 0	0	1	0	1	46.2	45.0	35.5	1.14	45.61	0.12	0.37	RAINING
13	XCE/01/00	-0	RCP	THP	8448.00											DAILY CHECK
	43/16/30	50	9.7	0 0	1	1	0	1	43.1	38.0	32.6	1.91	35.05	0.03	0.31	PREV.DAY PWR FAIL.
13	XCE/01/00	-0	RCP	ELL	8448.00											DAILY CHECK
	43/18/10	48	10.1	0 0	0	1	0	1	41.5	37.3	33.0	1.91	35.83	0.02	0.31	
13	XCE/01/00	-0	RCP	THP	8448.00											DAILY CHECK
	44/22/25	59	9.4	0 0	0	1	0	1	46.0	40.2	35.5	1.17	32.86	0.01	0.30	
13	XCE/01/00	-0	RCP	ELL	8448.00											DAILY CHECK
	47/17/40	65	10.0	0 0	0	1	0	1	43.0	35.1	36.0	1.08	32.67	0.01	0.30	WIPED CONE WINDOW
13	XCE/01/00	-0	RCP	THP	8448.00											DAILY CHECK
	50/15/50	30	19.4	0 0	1	1	0	1	44.4	38.8	36.0	1.02	32.81	0.03	0.30	
13	XCE/01/00	-0	RCP	RLP	8448.00											DAILY CHECK
	51/23/15	40	20.6	0 0	1	1	0	1	44.0	45.0	36.2	0.89	33.03	0.15	0.34	
13	XCE/01/00	-0	RCP	THP	8448.00											DAILY CHECK
	52/17/52	45	15.6	0 0	1	1	0	1	44.5	38.6	36.3	1.09	32.52	0.03	0.30	
13	XCE/01/00	-0	RCP	THP	8448.00											DAILY CHECK
	54/22/ 0	25	20.0	0 0	1	1	0	1	44.0	46.2	37.7	0.96	33.68	0.09	0.32	

Fig. 52. Computer program CTS20B summary printout for the XCE cone operational on the ground for Feb. 6 to June 11, 1968

Table 7. Maser gain, follow-up contribution and operating noise temperature parameters, Venus and Mars DSSs; February 6 to June 11, 1968

Cone	Location; installation	Configuration[a]	Frequency, MHz	Maser gain, dB	Follow-up contribution, dB	Operating noise temperature, °K
SCU	JPL Bldg. 238; on ground	—	2295	51.2 ± 0.42/0.13 11 data points	0.039 ± 0.005/0.002 7 data points	13.1 ± 0.27/0.10 7 data points
SPR	Venus DSS; on antenna	—	2388	39.0 ± 0.40/0.07 29 data points	0.717 ± 0.084/0.018 21 data points	21.1 ± 0.55/0.12 21 data points
XCE	Venus DSS; on ground	—	8448	36.0 ± 2.3/0.6 13 data points	0.122 ± 0.327/0.124 7 data points	33.5 ± 0.94/0.35 7 data points
SCU	Mars DSS; on antenna	0	2295	50.4 ± 3.8/0.9 19 data points	0.500 ± 0.680/0.196 12 data points	17.4 ± 1.09/0.31 12 data points
		5	2295	46.6 + 4.7/1.5 10 data points	0.476 ± 0.160/0.061 7 data points	28.7 ± 0.62/0.23 7 data points

[a]0 = Maser 1, R&D receiver. 5 = Maser 2, DSIF receiver 1.

(3) No RF spur in receiver pass band.

(4) $PE_{T/_{op}D}$ less than 0.10°K (from computer program CTS20B).

The maser gain is nominally optimized prior to each operating noise temperature calibration. Measurements are made approximately twice a month to check for amplifier saturation (verification of system linearity).

Considerable effort has been expended in effective noise temperature calibrations of the various masers during this and previous calibration periods. However, the measurement repeatability and accuracy under field conditions do not warrant changing the assigned maser effective input noise temperature from that obtained during initial cone calibrations.

Measurements have been taken of the increase of operating noise temperature at 2295 MHz at the Mars DSS during operation of the 2115-MHz transmitter at 10 and 20 kW. These data are summarized in Table 8 for both the SMF and the SCU cones. The indicated 1-σ tolerance of the mean is due to measurement dispersion only. These noise temperature measurements were made with the ambient termination in the SMF cone and with the gas tube noise source in the SCU cone. It should be noted that the increased temperatures at the higher power levels are not significant. The problem is significantly more pronounced with the SCU cone than the SMF cone. The maser installed in the SMF cone was transferred to the 3A module (Maser 2) when the SCU cone was installed on the antenna. This means that the two sets of data were made with the same maser, eliminating the maser as the principal difference. The cause for the temperature increase is unknown; it is speculated that it might be due to the beam noise from the transmitter at 2295 MHz, since it seems to be independent of transmitted power level.

Table 8. Summary of operating noise temperature increase data during transmitter operation

Cone	1968 Day no.	Increase in operating noise temperature, °K	
		10-kW Transmitter power	20-kW Transmitter power
SMF, Mod 00	53–61	0.09 ± 0.035 3 data points	0.11 ± 0.038 3 data points
SCU, Mod 01	14–161	0.56 ± 0.187 6 data points	0.60 ± 0.103 6 data points

References

1. Levy, G. S., et al., "The Ultra Cone: An Ultra Low-Noise Space Communication Ground Radio-Frequency System," MTT Special Issue on Noise (to be published).
2. Stelzried, C. T., Petty, S. M., "Microwave Insertion Loss Test Set," *IEEE Transactions on Microwave Theory and Techniques*, Vol. MTT-12, No. 4, July 1964, p. 475.
3. Stelzried, C. T., "Operational Performance of an H-band Coupled Cavity Transmission Maser," *Microwave Journal*, Vol. 10, No. 4, March 1967, p. 103.
4. Worthing, A. G., Geffner, J., *Treatment of Experimental Data*, John Wiley and Sons, New York, 1943.
5. Otoshi, T. Y., "The Effect of Mismatched Components on Microwave Noise Temperature Calibrations," MTT Special Issue on Noise (to be published).
6. Stelzried, C. T., *Reflectometer for Receiver Input System*, NASA Tech Brief, B67-10657, Dec. 1967, Clearinghouse for Federal Scientific and Technical Information, Springfield, Va.

3. Spacecraft CW Signal Power Calibration With Microwave Noise Standards,

C. T. Stelzried and O. B. Parham

a. Introduction. The continuous wave (CW) power level received from a spacecraft is an important parameter required for the evaluation of a deep space communication system. A precise measurement method which compares CW signal power with microwave noise power was used to calibrate the *Mariner IV* spacecraft received power level at Mars encounter (Ref. 1). These calibrations were performed with a minimum of station instrumentation modification. The difference between the diode detector sensitivity to noise and CW signal power due to imperfect square law characteristics has been eliminated by using a power meter detector (SPS 37-48, Vol. II, p. 54).

b. CW power calibration instrumentation. Precision CW calibration equipment for instrumenting the JPL Compatibility Test Area to support *Mariner* Mars 1969 testing has been made available for general DSN station checkout. This unit, RFT 294 (part 294 from radio frequency techniques group), is presently in operation at the Pioneer DSS. In addition a unit is scheduled for the Cape Kennedy Spacecraft Compatibility Station to be available in August 1968 to support *Mariner* Mars 1969. A simplified block diagram of the power meter detector is shown in Fig. 53. Extensive shielding has been provided to ensure bandwidth calibration accuracy. The power meter detector assembly interior is shown in Fig. 54. A dc voltage level sensor is used to give front panel indication of the narrow-band filter oven assembly operational readiness. Figure 55 shows a detailed schematic of the latest version of the power meter detector assembly. Figure 56 shows a plot of the bandpass in the narrow-band mode of operation. The measured average integrated noise bandwidth is 8.706 kHz for RFT unit 294.

Reference

1. Stelzried, C. T., and Reid, M. S., "Precision Power Measurements of Spacecraft CW Signal Level with Microwave Noise Standards," *IEEE Trans. Instrum. Meas.*, Vol. IM-15, No. 4, p. 318, Dec. 1966.

4. Mismatch Error Analysis of Radiometric Method for Line Loss Calibrations, *T. Y. Otoshi*

a. Introduction. A previous article (SPS 37-50, Vol. III, pp. 296–301) described a radiometric method which is useful for calibrating the loss of antenna-feed components that support the propagation of more than one waveguide mode and field of polarization. The purpose of this article is to present the calibration equation applicable to the general case for which system components are not necessarily matched. Once the general equation is derived, a computer can be utilized to calculate the unknown loss value or determine the limits of mismatch error when required phase angle and correlation coefficient data are not available.

b. Definition of symbols. Tables 9 and 10 list the symbols and definitions which will be used in the present analysis. The notation and standard definitions given in the IRE Standards on Electron Tubes (62 IRE 7.S2) are used as much as possible.

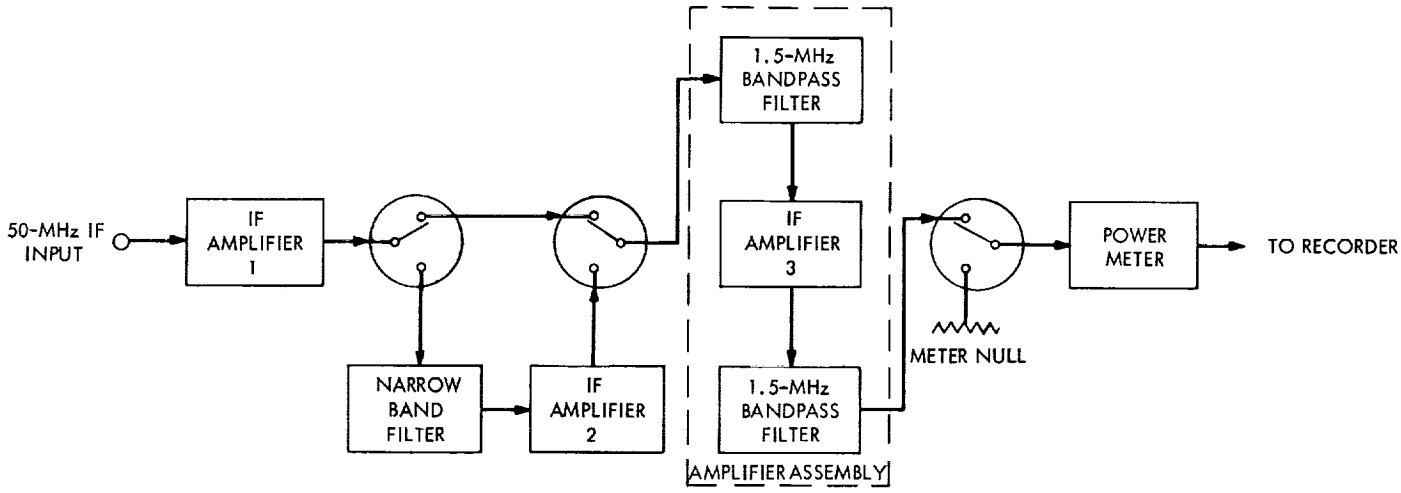

Fig. 53. Power meter detector simplified block diagram

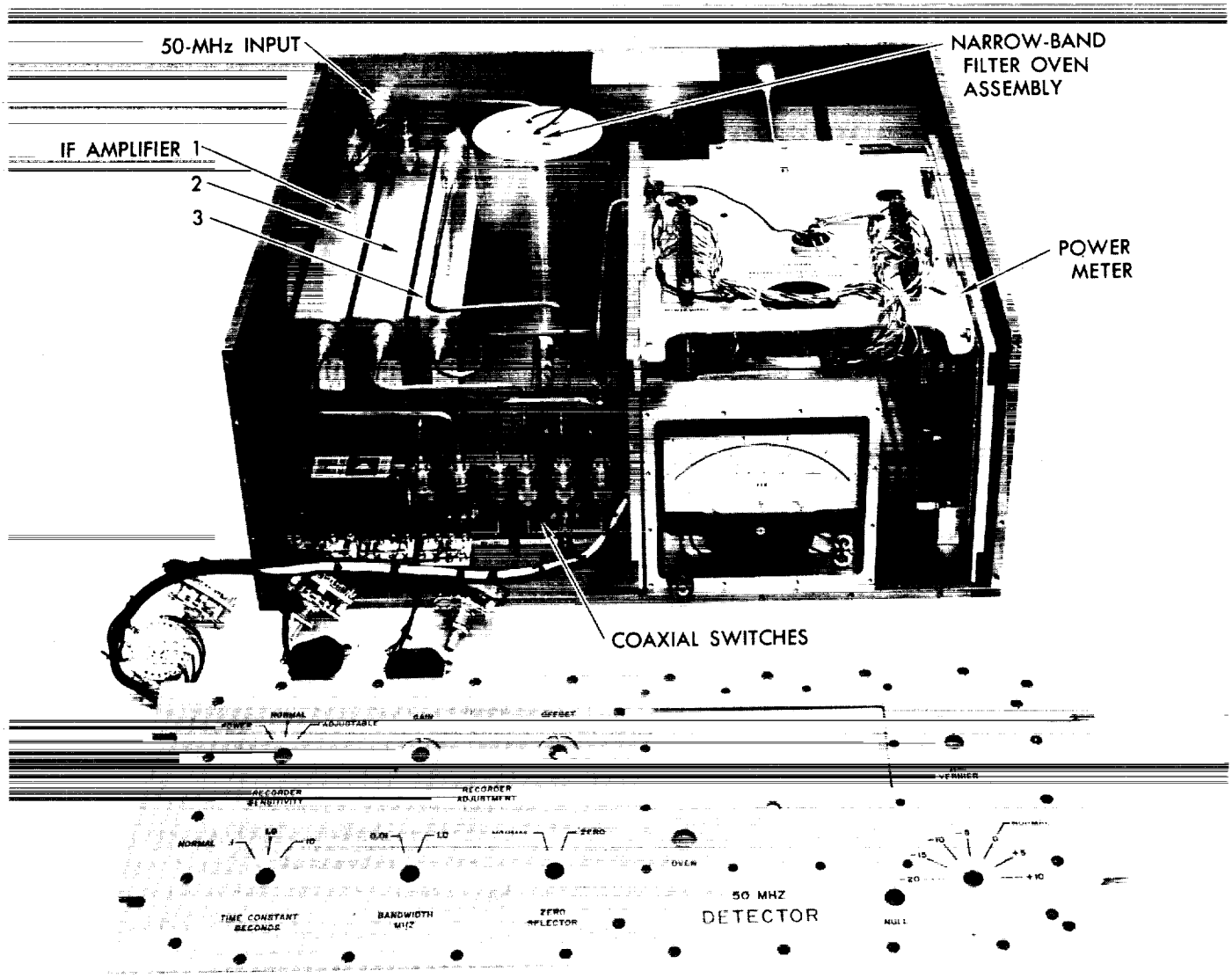

Fig. 54. IF power meter detector interior assembly

Table 9. Nomenclature for noise and physical temperatures[a]

Assumed matched case	General mismatched case	Definitions
T_A	T_a	Antenna noise temperature at horn aperture
T_{iA}	T_{ia}	Noise temperature of antenna input termination at port 1
T_{iH}	T_{ih}	Noise temperature of ambient load input termination at port 1
T_p	T_p	Physical or thermo-equilibrium temperature of a network representing a transmission line section
T_e	T_{ea}, T_{eh}	Effective input noise temperature (of the overall receiver) at port 1 when the receiver is connected to the antenna and hot input terminations, respectively
	T_{ea}	Direct wave component of the effective input noise temperature at port 1
	T_r	Noise temperature of the receiver which radiates toward the input termination. This noise temperature is defined at port 1
T_{opA}, T_{opH}	T_{opa}, T_{oph}	Operating noise temperature (of the system) at port 1 when the receiver is connected to the antenna and hot input terminations, respectively

[a]All noise temperatures given in this table are available noise temperatures. Noise temperatures and physical temperatures have units of degrees Kelvin.

Table 10. Nomenclature for voltage and power ratios

Assumed matched case	General mismatched case	Definitions
	$(b_{11})_k, (b_{12})_k$ $(b_{21})_k, (b_{22})_k$	Scattering coefficients for the kth network in the antenna line
	$(\Gamma_{1b})_k, (\Gamma_{2b})_k$	Voltage reflection coefficients as seen looking into the input and output ports, respectively, of the kth network in the antenna line
	Γ_a	Voltage reflection coefficient of the antenna noise source
	Γ_{ia}, Γ_{ih}	Voltage reflection coefficient of antenna and hot input terminations, respectively
	Γ_r	Voltage reflection coefficient of the receiver
	α_{ia}, α_{ih}	Mismatch loss factor at port 1 when the receiving system is in the antenna and hot input termination configurations, respectively
	τ_k	Available power gain (or loss) of the kth antenna network
L_k	L_k	Dissipative loss factor (≥ 1) of the kth antenna network when terminated in a matched load
	γ_{ia}, γ_{ih}	Coefficient expressing the degree of correlation between the direct and reflected wave receiver noise sources when receiver is connected to the antenna and hot input terminations, respectively (Ref. 2)

For mismatch error analysis, it is important to differentiate between those noise temperatures which would be calibrated if: (1) mismatch effects are neglected, and (2) mismatch effects are accounted for. Noise temperatures calibrated under conditions (1) and (2) above shall be referred to as apparent and actual noise temperatures, respectively. In this article the symbols used for apparent and actual noise temperatures differ only in the noise source description subscript. If this subscript is a capitalized letter, the noise temperature is apparent; if lower case, the noise temperature is actual (Table 9).

Primes identify those network parameters and noise temperatures of the substituted waveguide receiving system.

c. General case calibration equation. The radiometric method for feed component loss evaluation involves the calibration of operating noise temperature (of the antenna system) first with the components under evaluation installed and again after substitution by a waveguide section of known loss. As described in SPS 37-50, Vol. III, this method requires knowledge of the antenna noise temperatures at the feed-horn aperture when the system is in the normal and substituted waveguide feed configurations. These antenna temperatures are calculated by means of an antenna pattern integration technique (Ref. 1) with corrections made for meteorological variations and nonuniform ground brightness temperatures.

The method used for measurement of operating noise temperature (of a system) is described in detail in SPS 37-42, Vol. III, pp. 25–32. The procedure consists of switching the receiver input between the antenna and ambient load input terminations and measuring the ratio of the receiver output noise powers. The effective input noise temperature of the receiver is assumed to be known from previous calibrations by the Y-factor method which utilizes hot and cold thermal noise standards.

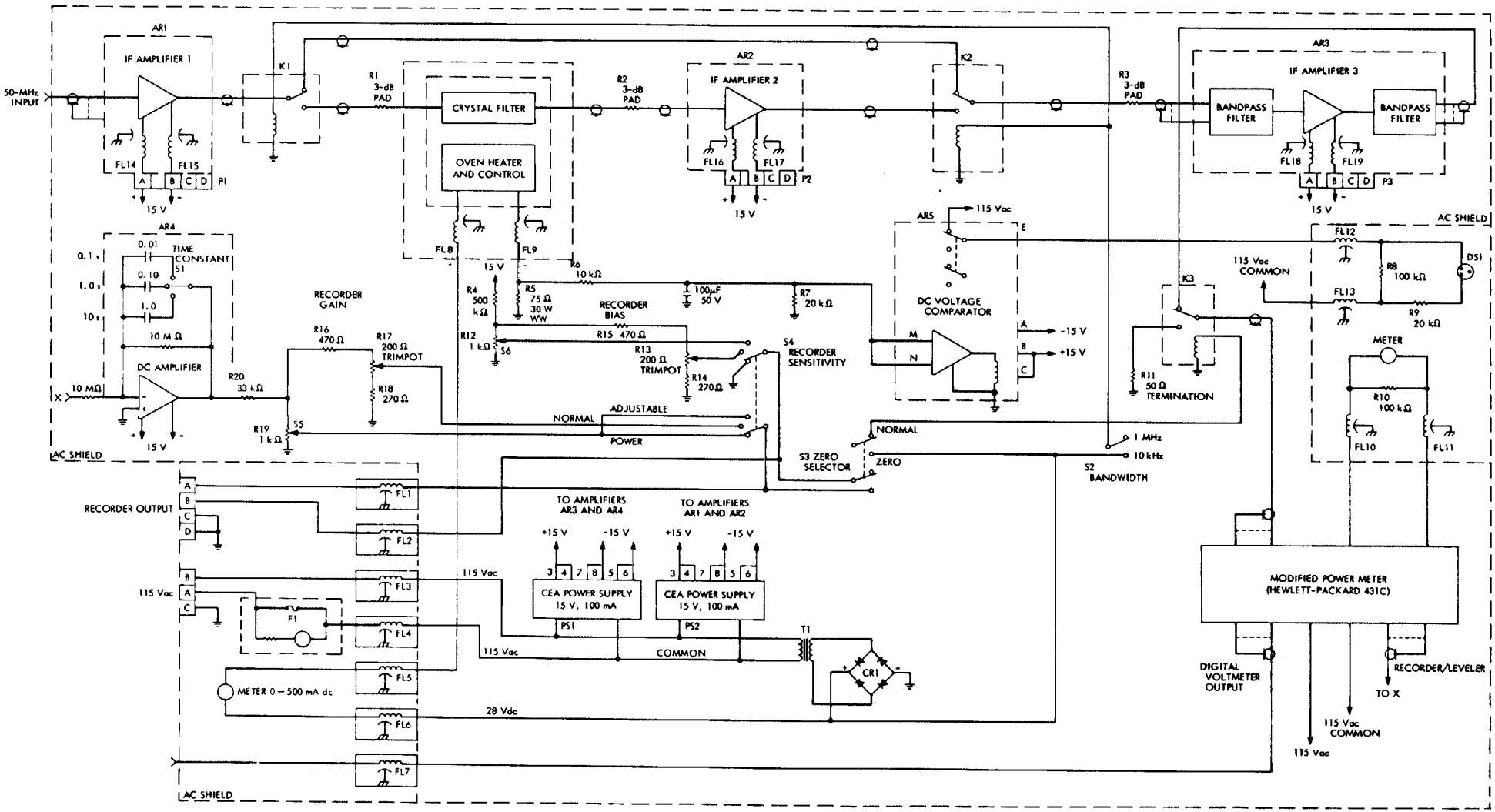

Fig. 55. Detailed schematic of power meter detector assembly

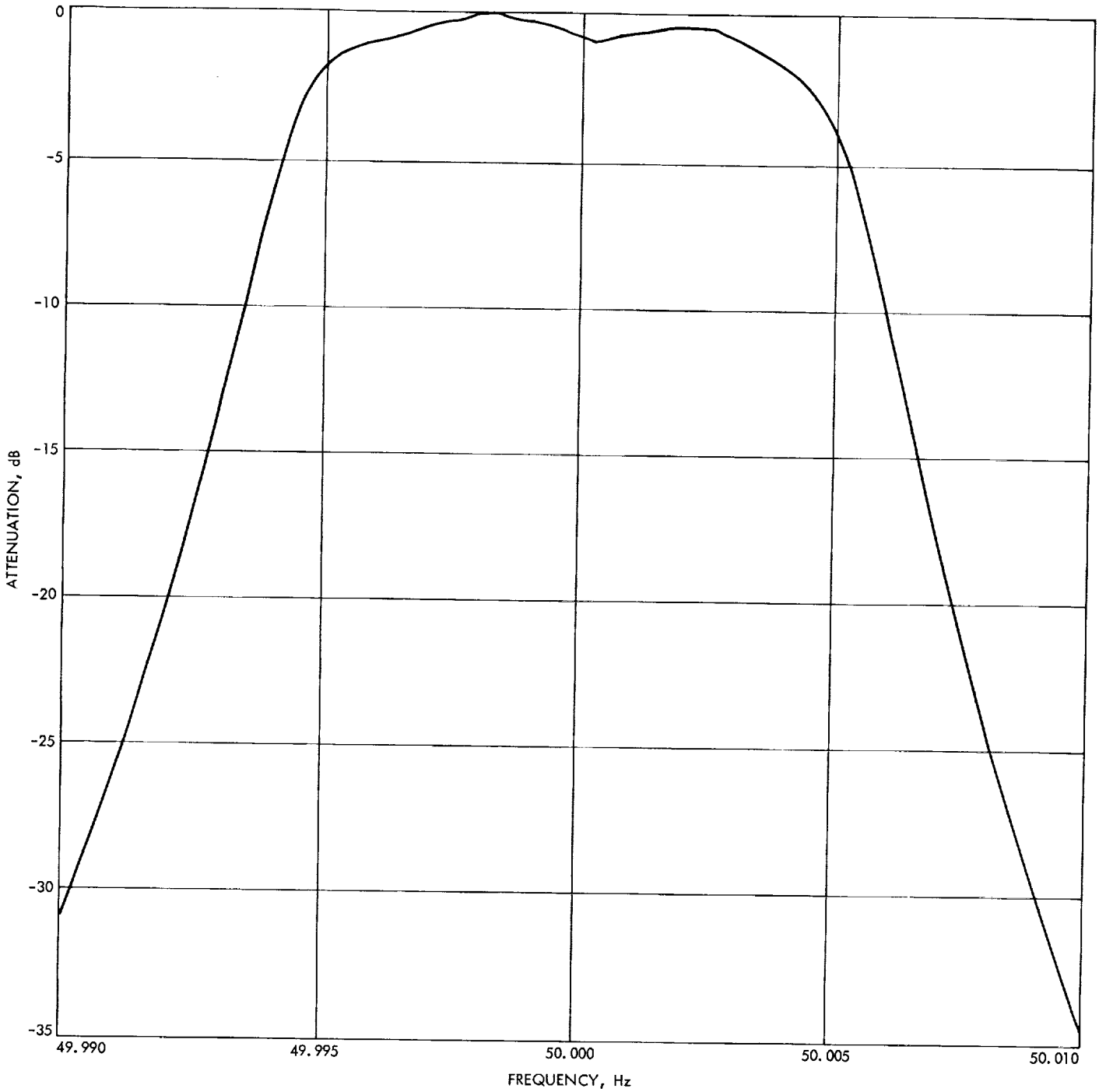

Fig. 56. Bandwidth curve of power meter detector (RFT 294)

Figure 57 shows a block diagram of the calibration system. When the receiver input is sequentially switched between the two antenna and hot (ambient) load input terminations, two independent Y-factors are measured. If the effects of mismatches are neglected, the following Y-factor relationships are assumed:

$$Y_{AH} = \frac{T_{opH}}{T_{opA}} \tag{1}$$

$$Y'_{AH} = \frac{T_{opH}}{T'_{opA}} \tag{2}$$

The difference in the two apparent operating noise temperatures is then calculated from

$$\Delta T_{opA} = T_{opA} - T'_{opA} = T_{opH}\left(\frac{1}{Y_{AH}} - \frac{1}{Y'_{AH}}\right) \tag{3}$$

If the effects of mismatches are accounted for, the measured Y-factors would be expressed as

$$Y_{AH} = \left(\frac{\alpha_{ih}}{\alpha_{ia}}\right)\frac{T_{oph}}{T_{opa}} \tag{4}$$

$$Y'_{AH} = \left(\frac{\alpha_{ih}}{\alpha'_{ia}}\right)\frac{T_{oph}}{T'_{opa}} \tag{5}$$

Substitutions of Eqs. (4) and (5) into Eq. (3) give

$$\Delta T_{opA} = \frac{T_{opH}}{\alpha_{ih}T_{oph}}\left(\alpha_{ia}T_{opa} - \alpha'_{ia}T'_{opa}\right) \tag{6}$$

which when algebraically manipulated[13] results in

$$\alpha_{ia}T_{opa} = \alpha'_{ia}T'_{opa} + \left(\frac{\alpha_{ih}T_{oph}}{T_{opH}}\right)\Delta T_{opA} \tag{7}$$

For the two antenna systems, the operating noise temperatures can be expressed in terms of the input termination and effective input noise temperatures as

$$T_{opa} = T_{ia} + T_{ea} \tag{8}$$

$$T'_{opa} = T'_{ia} + T'_{ea} \tag{9}$$

and for the receiving system whose input termination is an ambient load

$$T_{oph} = T_{ih} + T_{eh} = T_p + T_{eh} \tag{10}$$

$$T_{opH} = T_{iH} + T_e = T_p + T_e \tag{11}$$

Note that the effective input noise temperature is denoted differently for each system configuration. In the general case, the effective input noise temperature is dependent upon the voltage reflection coefficient of the input termination.

Substitution of Eqs. (8) to (11) into Eq. (7) and algebraic manipulation results in

$$\alpha_{ia}T_{ia} = \alpha'_{ia}T'_{ia} + \frac{\alpha_{ih}\left[T_p + T_{eh}\right]}{T_p + T_e}\Delta T_{opA} + \left[\alpha'_{ia}T'_{ea} - \alpha_{ia}T_{ea}\right] \tag{12}$$

The general case noise temperature of each antenna input termination at the output of three-cascaded lossy networks can be expressed in terms of available power gains as (Ref. 2)

$$T_{ia} = T_p - (T_p - T_a)\,\tau_1\tau_2\tau_3 \tag{13a}$$

$$T'_{ia} = T_p - (T_p - T'_a)\,\tau'_1\tau'_2\tau'_3 \tag{14a}$$

Let a new parameter β be introduced which is equal to the product of dissipative loss factor L and τ. Then

$$T_{ia} = T_p - (T_p - T_a)\frac{\beta_1\beta_2\beta_3}{L_1L_2L_3} \tag{13b}$$

$$T'_{ia} = T_p - (T_p - T'_a)\frac{\beta'_1\beta'_2\beta'_3}{L'_1L'_2L'_3} \tag{14b}$$

As may be seen from the block diagram in Fig. 57

$$L'_3 = L_3$$

for this radiometric calibration system, and because the antenna noise temperature at the horn aperture is the same for the general case as for the assumed matched case, we may let

$$T_a = T_A$$

$$T'_a = T'_A = T_A - \Delta T_A$$

[13]In this article, a net delivered noise temperature is represented as a product of the mismatch loss factor α and the available noise temperature T.

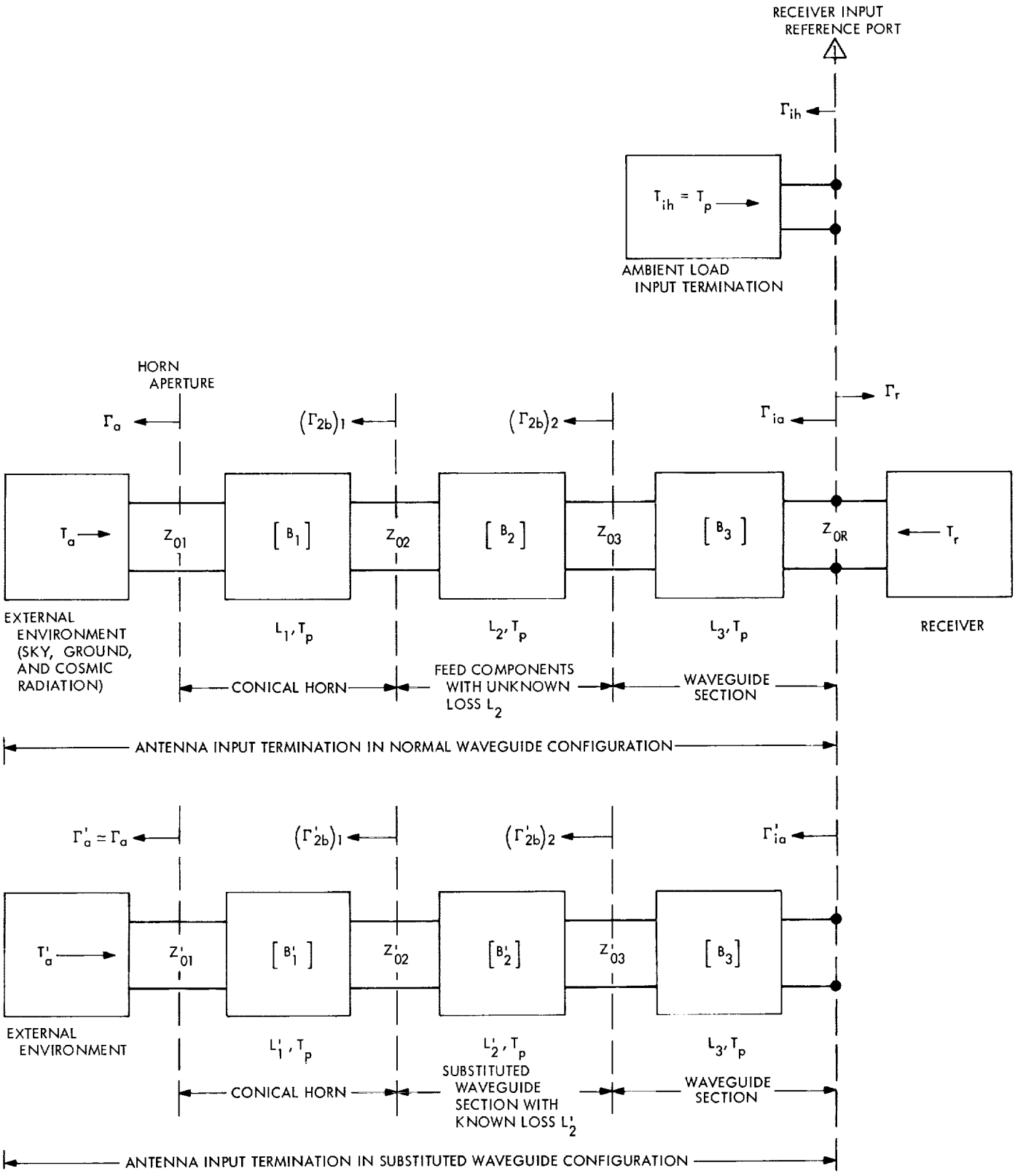

Fig. 57. Block diagram of radiometric loss calibration system

Substitution of these values into Eqs. (13b) and (14b) gives

$$T_{ia} = T_p - (T_p - T_A)\frac{\beta_1\beta_2\beta_3}{L_1L_2L_3} \tag{13c}$$

$$T'_{ia} = T_p - (T_p - T_A + \Delta T_A)\frac{\beta'_1\beta'_2\beta'_3}{L'_1L'_2L_3} \tag{14c}$$

and final substitutions of Eqs. (13c) and (14c) into Eq. (12) and solving for L_2^{-1} results in the expression

$$\frac{1}{L_2} = \left(\frac{\beta'_1\beta'_2\beta'_3\alpha'_{ia}}{\beta_1\beta_2\beta_3\alpha_{ia}}\right)\left(\frac{L_1}{L'_1L'_2}\right)\left(1 + \frac{\Delta T_A}{T_p - T_A}\right) - \left(\frac{1}{\beta_1\beta_2\beta_3\alpha_{ia}}\right)\left(\frac{L_1L_3}{T_p - T_A}\right)\left[\alpha_{ih}\left(\frac{T_p + T_{eh}}{T_p + T_e}\right)\Delta T_{opA} + (\alpha'_{ia}T'_{ea} - \alpha_{ia}T_{ea}) + T_p(\alpha'_{ia} - \alpha_{ia})\right] \tag{15}$$

The dissipative attenuation of the line section having the unknown loss is then calculated from

$$A_2 = 10\log_{10} L_2 \tag{16}$$

Expressions for the α's and β's are tabulated in Table 11, and expressions for effective input noise temperatures are given as

$$T_{eh} = \frac{(1 - |\Gamma_r|^2)}{\alpha_{ih}}\left\{T_{eo} + \left(\frac{\alpha_{ih}|\Gamma_{ih}|^2}{1 - |\Gamma_{ih}|^2}\right)T_r + 2\gamma_{ih}|\Gamma_{ih}| \times \left[\left(\frac{\alpha_{ih}}{1 - |\Gamma_{ih}|^2}\right)T_{eo}T_r\right]^{1/2}\right\} \tag{17}$$

$$T_{ea} = \frac{(1 - |\Gamma_r|^2)}{\alpha_{ia}}\left\{T_{eo} + \left(\frac{\alpha_{ia}|\Gamma_{ia}|^2}{1 - |\Gamma_{ia}|^2}\right)T_r + 2\gamma_{ia}|\Gamma_{ia}| \times \left[\left(\frac{\alpha_{ia}}{1 - |\Gamma_{ia}|^2}\right)T_{eo}T_r\right]^{1/2}\right\} \tag{18}$$

$$T'_{ea} = \frac{(1 - |\Gamma_r|^2)}{\alpha'_{ia}}\left\{T_{eo} + \left(\frac{\alpha'_{ia}|\Gamma'_{ia}|^2}{1 - |\Gamma'_{ia}|^2}\right)T_r + 2\gamma'_{ia}|\Gamma'_{ia}| \times \left[\left(\frac{\alpha'_{ia}}{1 - |\Gamma'_{ia}|^2}\right)T_{eo}T_r\right]^{1/2}\right\} \tag{19}$$

In the above, the effective input noise temperatures are written in terms of a direct wave component T_{eo} and reflected wave component. As was pointed out in Ref. 2, expressions of this type are useful when noise properties of the individual networks in the overall receiver are not known.

For the matched case

(1) All α's and β's become unity (Table 11)

(2) $T_e = T_{eo} = T_{eh} = T_{ea} = T'_{ea}$

and Eq. (15) becomes

$$\frac{1}{L_2} = \frac{L_1}{L'_1L'_2}\left[1 + \frac{\Delta T_A - (L'_1L'_2L_3)\Delta T_{opA}}{T_p - T_A}\right] \tag{20}$$

For small losses

$$L'_1L'_2L_3 \approx 1$$

so for the actual or assumed matched cases, the dissipative attenuation may be calculated from

Table 11. Equations for mismatch-related parameters

Parameter symbol	Equation
α_{ih}	$\frac{(1 - \lvert\Gamma_{ih}\rvert^2)(1 - \lvert\Gamma_r\rvert^2)}{\lvert 1 - \Gamma_{ih}\Gamma_r\rvert^2}$
α_{ia}	$\frac{(1 - \lvert\Gamma_{ia}\rvert^2)(1 - \lvert\Gamma_r\rvert^2)}{\lvert 1 - \Gamma_{ia}\Gamma_r\rvert^2}$
β_1	$\frac{(1 - \lvert\Gamma_a\rvert^2)(1 - \lvert b_{11}\rvert_1^2)}{\lvert 1 - (\Gamma_a)(b_{11})_1\rvert^2(1 - \lvert\Gamma_{2b}\rvert_1^2)}$
β_2	$\frac{(1 - \lvert\Gamma_{2b}\rvert_1^2)(1 - \lvert b_{11}\rvert_2^2)}{\lvert 1 - (\Gamma_{2b})_1(b_{11})_2\rvert^2(1 - \lvert\Gamma_{2b}\rvert_2^2)}$
β_3	$\frac{(1 - \lvert\Gamma_{2b}\rvert_2^2)(1 - \lvert b_{11}\rvert_3^2)}{\lvert 1 - (\Gamma_{2b})_2(b_{11})_3\rvert^2(1 - \lvert\Gamma_{ia}\rvert^2)}$
$\beta_1\beta_2\beta_3\alpha_{ia}$	$\frac{(1 - \lvert\Gamma_a\rvert^2)(1 - \lvert b_{11}\rvert_1^2)(1 - \lvert b_{11}\rvert_2^2)(1 - \lvert b_{11}\rvert_3^2)(1 - \lvert\Gamma_r\rvert^2)}{\lvert[1 - (\Gamma_a)(b_{11})_1][1 - (\Gamma_{2b})_1(b_{11})_2][1 - (\Gamma_{2b})_2(b_{11})_3][1 - \Gamma_{ia}\Gamma_r]\rvert^2}$

NOTE: Equations for α'_{ia}, β'_1, β'_2, and β'_3 can be obtained by priming the reflection coefficient symbols in the corresponding equations above. However, the Γ_a, $(b_{11})_3$, and Γ_r symbols need not be primed, since for this radiometric system, $\Gamma'_a \approx \Gamma_a$, $(b'_{11})_3 = (b_{11})_3$, and $\Gamma'_r = \Gamma_r$.

$$A_2 \approx 10 \log_{10}\left(\frac{L_1' L_2'}{L_1}\right) + \left(\frac{10 \log_{10} e}{T_p - T_A}\right)(\Delta T_{opA} - \Delta T_A) \tag{21}$$

The horn loss factors L_1 and L_1' do not necessarily have the same value, because different waveguide modes can be propagating in the horn when the system is in the normal and substituted feed configurations.

d. Mismatch error analysis. The actual value of A_2 can be calculated directly from Eq. (16) if phase angles and correlation coefficient values are known. Note that in Table 11, the mismatch-related parameters contain factors of the form $|1 - \Gamma_u \Gamma_v|^2$ which can be expressed as

Table 12. S-Band ultra cone input data for computer program

Ambient load input termination	
$T_{ih} = T_p = 305.9°K$	
$\|\Gamma_{ih}\| = 0.003$	
Antenna input termination in normal waveguide configuration[a]	
$T_a = T_A = 5.41°K$	
$\|\Gamma_a\| \approx 0.0$	
$\|b_{11}\|_1 = 0.002$	$\|\Gamma_{2b}\|_1 = 0.002$
$\|b_{11}\|_2 = 0.020$	$\|\Gamma_{2b}\|_2 = 0.016$
$\|b_{11}\|_3 = 0.009$	$\|\Gamma_{ia}\| = 0.006$
$A_1 = 10 \log_{10} L_1 = 0.0042$ dB	
$A_2 = 10 \log_{10} L_2 = 0.0200$ dB	
Antenna input termination in substituted waveguide configuration	
$\|\Gamma_a'\| = \|\Gamma_a\| \approx 0.0$	
$\|b_{11}'\|_1 = 0.002$	$\|\Gamma_{2b}'\|_1 = 0.002$
$\|b_{11}'\|_2 = 0.008$	$\|\Gamma_{2b}'\|_2 = 0.010$
$\|b_{11}'\|_3 = \|b_{11}\|_3$	$\|\Gamma_{ia}'\| = 0.018$
$A_1' = 10 \log_{10} L_1' = 0.0034$ dB	
$A_2' = 10 \log_{10} L_2' = 0.0058$ dB	
$A_3' = A_3$	
Common system parameters	
$T_p = 305.9°K$	
$T_e = 5°K$	$T_{eo} \approx T_e = 5°K$
$\Delta T_A = -0.37°K$	$T_r = 10°K$
$\Delta T_{opA} = -0.234°K$	$\|\Gamma_r\| = 0.100$

[a]Since parts of this system support propagation of circular polarization and two waveguide modes, effective reflection coefficient values were used for $|b_{11}|_1$, $|b_{11}|_2$, $|\Gamma_{2b}|_1$, and $|\Gamma_{2b}|_2$.

$$|1 - \Gamma_u \Gamma_v|^2 = 1 - 2|\Gamma_u||\Gamma_v| \cos(\Psi_u + \Psi_v) + |\Gamma_u|^2 |\Gamma_v|^2 \tag{22}$$

where Ψ_u and Ψ_v are, respectively, the phase angles of Γ_u and Γ_v. However, if only the magnitudes of Γ_u and Γ_v have been measured, then $|1 - \Gamma_u \Gamma_v|^2$ would be an uncertainty which has limits of $(1 \pm |\Gamma_u||\Gamma_v|)^2$. Another uncertainty in radiometric calibrations is usually the correlation coefficient γ which has limits of ± 1.

For the present error analysis, peak mismatch errors will be defined as the differences between the value of A_2 obtained from Eq. (21) for the assumed matched case and the maximum and minimum possible values obtained for the actual mismatched case. Because many uncertainties are involved in the radiometric calibration technique, it is difficult to derive general case expressions for the error limits. However, a numerical solution was readily obtained when Eq. (16) was programmed for the IBM 1620 computer. In this program, the phases of reflection coefficients (involved in the uncertainty factors) and magnitudes of correlation coefficients are stepped through their range of values in different possible combinations. Each new computed value of A_2 is checked against the previously computed value, and in this manner the maximum and minimum value of A_2 can be found.

Table 12 is a tabulation of computer program input data applicable to the S-band ultra cone. Using these input data, the computer determined the maximum and minimum possible values of A_2 to be 0.012 and -0.004 dB, respectively, for the most unfavorable correlated case. For the uncorrelated ($\gamma = 0$) case, the maximum and minimum possible values of A_2 were found to be 0.007 and 0.001 dB, respectively. These values of A_2 may be compared to the apparent A_2 value of 0.007 dB obtained when neglecting the effect of mismatches. Since the results of the uncorrelated case are believed to be the most likely, the largest mismatch error is

$$E_{A_2/\text{mismatch}} = (A_2)_{\text{apparent}} - (A_2)_{\min} = 0.007 - 0.001 = 0.006 \text{ dB}$$

References

1. *Computer Programs for Antenna Feed System Design and Analysis: Volume I. Programs and Sample Cases*, Technical Report 32-979. Edited by A. Ludwig. Jet Propulsion Laboratory, Pasadena, Calif., Apr. 15, 1967, pp. 143–158.
2. Otoshi, T. Y., "The Effect of Mismatched Components on Microwave Noise Temperature Calibrations, *IEEE Special Issue on Noise*, to be published September 1968.

5. Waveguide Flange Seal Loss Measurements,

C. T. Stelzried, D. L. Mullen, and J. C. Chavez

Waveguide transmission line losses are an important consideration in the design of the DSN low-noise receiving systems. The waveguide transmission line must also be pressure-tight, since these systems are normally operated at about 5-oz positive pressure, using nitrogen gas. These conditions are normally satisfied by the use of special heavy hand-lapped flanges. Figure 58 shows a WR 430 waveguide assembly during hand lapping.

Under some conditions it might be advantageous to use a seal which reduces the flange flatness tolerance required. A commercial WR 430 waveguide seal (5906-430-1)[14] is available that seems to meet these requirements (Fig. 59). The crosshatched effect on the inner surface provided by precision chemical etching is used to decrease ohmic contact resistance. The manufacturer's reported insertion loss determined from RF resistance measurements for this seal is 0.00004 dB, which is their limit of measurement reliability. Measurements have been made at JPL with a sample seal using the dc potentiometer insertion loss instrumentation (Ref. 1). The loss is measured to be less than 0.00005 dB (the present instrumentation resolution) at 2295 MHz which is in agreement with the above.

Although this loss for the seal is negligible for most applications, hand lapping of waveguide components is considered to be preferable for the research low-noise receiving systems. The seal cannot compensate for flange faces which deviate badly in flatness. Since the inside edge of the seal is raised, there is also a greater danger that improper assembly could result in nonuniform flange contact. This problem has been largly eliminated by the manufacturer with the introduction of the series-2 model. These units have an outer ridge on the flange face which reduces misalignment.

[14]Parker Seal Co., Culver City, Calif.

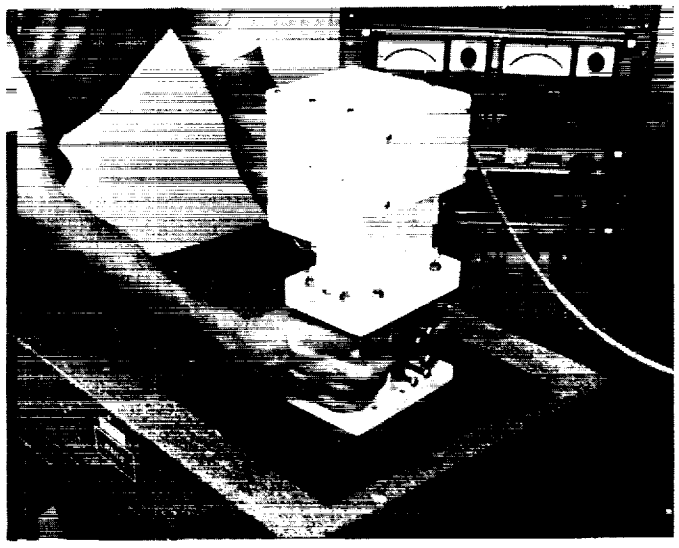

Fig. 58. WR 430 waveguide assembly hand-lapping process

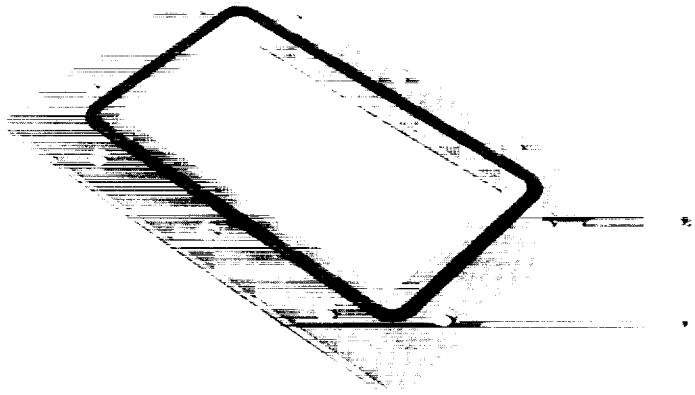

Fig. 59. Commercial WR 430 waveguide seal

Reference

1. Stelzried, C. T., Reid, M. S., and Petty, S. M., "A Precision DC Potentiometer Microwave Insertion Loss Test Set," *IEEE Trans. Instrum. Meas.*, Vol. IM-15, No. 3, September 1966, p. 98.

6. Efficient Antenna Systems: X-Band Gain Measurements, 210-ft-diam Antenna System,[15]

D. A. Bathker

a. Introduction. Late in 1966 a listen-only X-band cassegrain experimental (XCE) feedcone was constructed for the purpose of evaluating radio-frequency performance of the DSN ground antennas. The feedcone is compatible with DSN 85- and 210-ft diam reflectors and has been operated on the Venus DSS 85-ft diam antenna on two occasions during 1966 and 1967. RF performance of the 85-ft diam antenna system at X-band has been reported, using both radio astronomical (SPS 37-49, Vol. II, pp. 65–67) and independent ground-based techniques

[15]Made with assistance from Division 33 and Bendix Field Engineering teams at the Mars and Venus DSSs.

(SPS 37-50, Vol. II, pp. 49–52).[16] In February 1968 the XCE feedcone was operated on the Mars DSS 210-ft diam antenna, at 8448 MHz.

The RF optics efficiency prediction for the 210-ft diam antenna system is reported here. Also, reflector surface tolerance predictions, based on structural computations and field measurements reported in *Subsection D-1*, are included to yield an overall predicted system efficiency at the maser reference flange within the XCE feedcone. A portion of the February 1968 RF tests is shown to compare predicted with measured results.

b. Computed RF optics efficiency. The RF optics efficiency for the 210-ft diam antenna system at X-band is predicted by inputting the primary feed pattern (Fig. 60) and the subreflector configuration (Fig. 61) to the Rusch Scattering Program (Ref. 1). The scattered patterns shown in Figs. 62 and 63 illustrate slight distortion occurring near the edge of the paraboloid (illumination angle 50–60 deg) caused by the optimum S-band beam-shaping flange. As in the case of the earlier 85-ft diam

[16]A summary of all 85-ft reflector data will appear in Technical Report 32-1300, *Radiofrequency Performance of an 85-ft Diameter Ground Antenna: X-Band*, D. A. Bathker (in process).

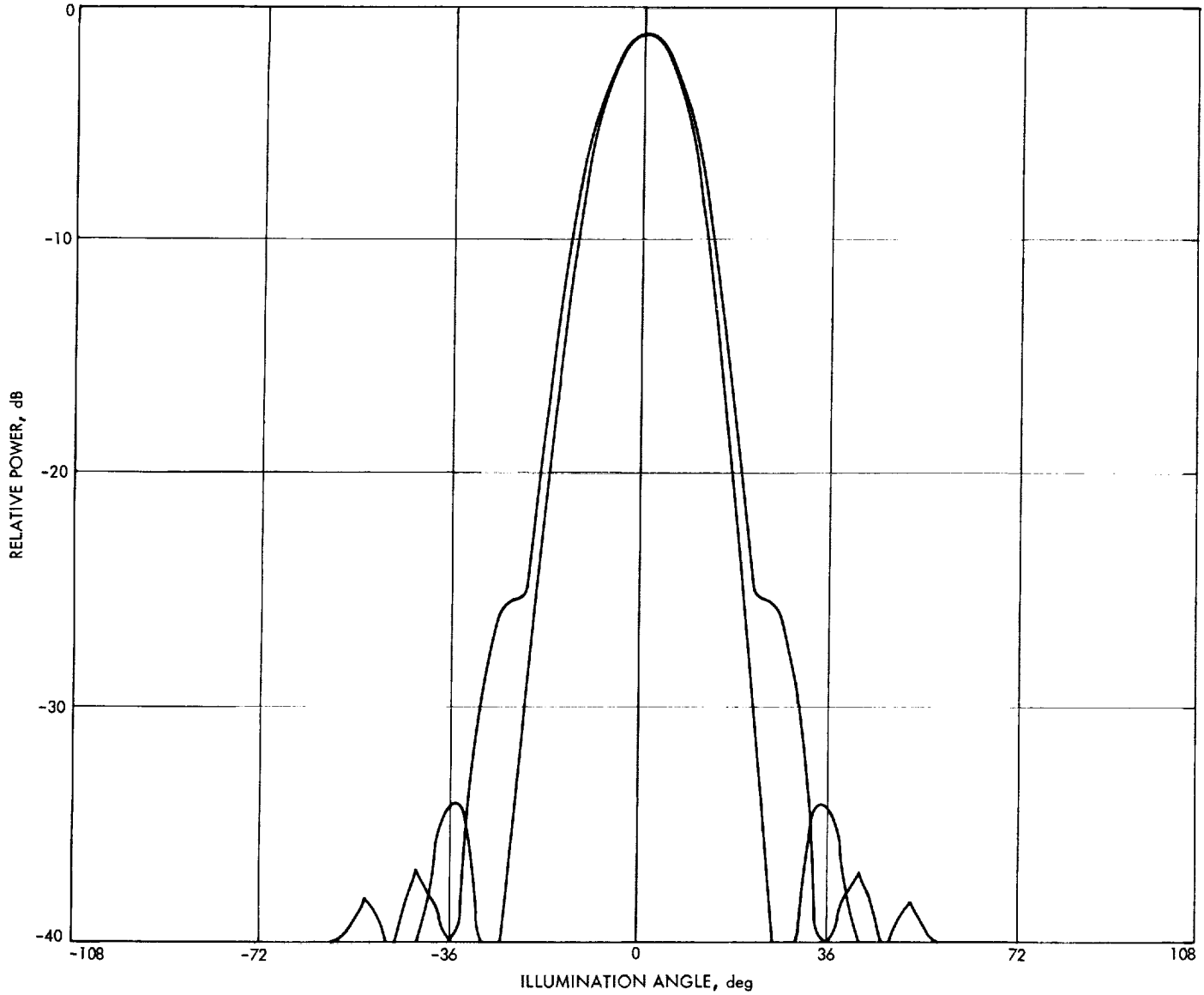

Fig. 60. Primary-feed radiation pattern, dual mode feed

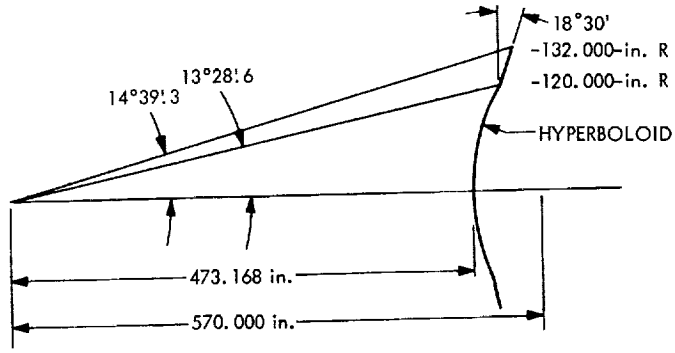

Fig. 61. Subreflector configuration

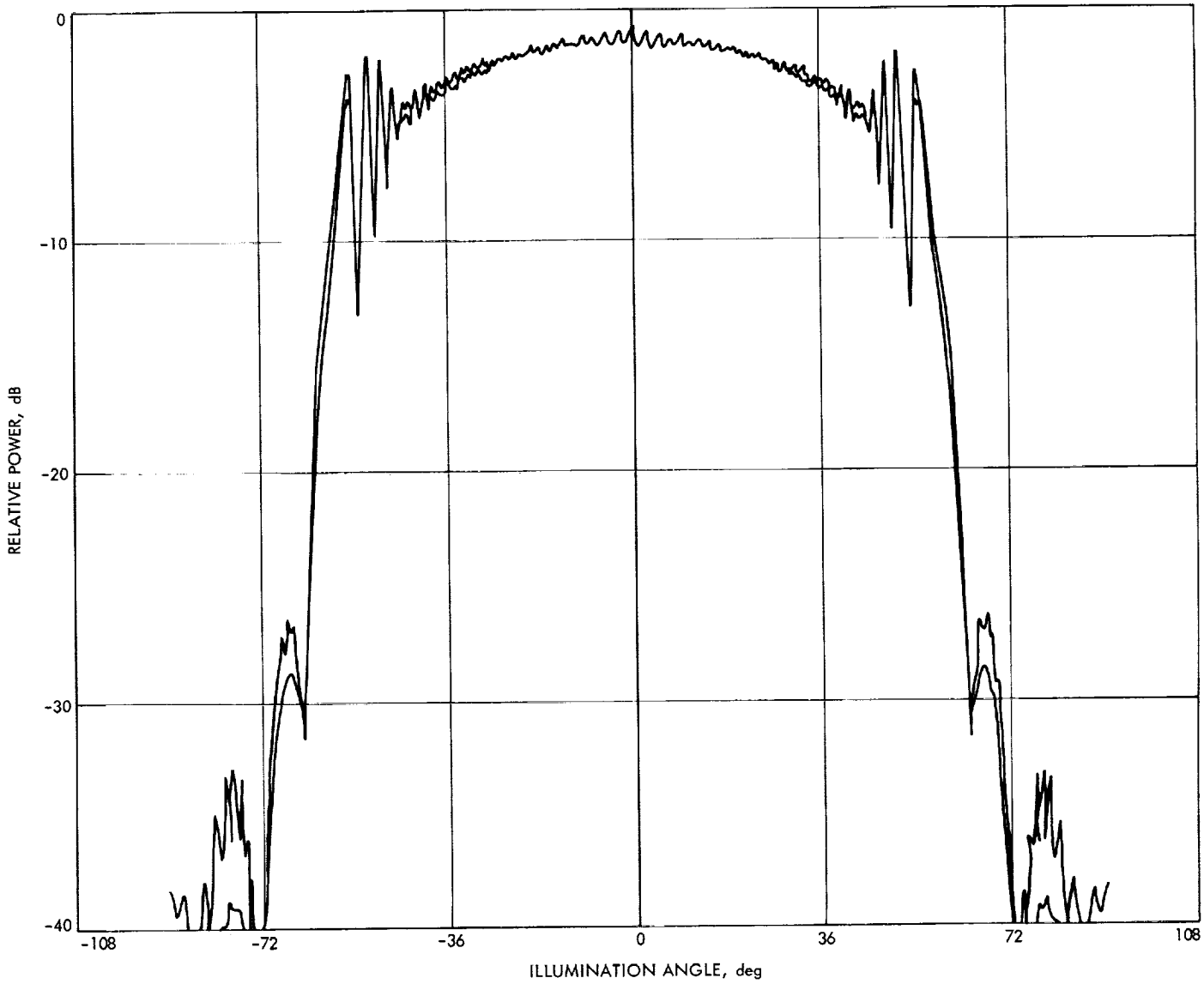

Fig. 62. Subreflector scattered radiation patterns, E- and H-plane amplitude

reflector X-band evaluation, the removal of the S-band flange was not warranted. The scattered patterns were then evaluated with the JPL Antenna Efficiency Program (SPS 37-26, Vol. IV, pp. 200–208). Results of that study, as they apply to the components under consideration, are summarized in Table 13.

Table 13. Feed efficiency, XCE feedcone

Parameter	Value, %
Forward spillover	7.22
Rear spillover	0.20
Illumination efficiency	86.81
Cross-polarization efficiency	99.94
Phase efficiency	96.62
Subreflector blocking efficiency	96.45
Overall feed efficiency	74.86 ±0.20

An optical analysis of the 210-ft diam antenna quadripod shows that the structure blocks 6.255% of the available aperture. Assuming that the percentage of intercepted energy equals the percentage of area, which constitutes accepting "pie-slice" approximations of the blocked areas in the aperture, it has been shown

$$\eta' = \eta (1 - B)^2$$

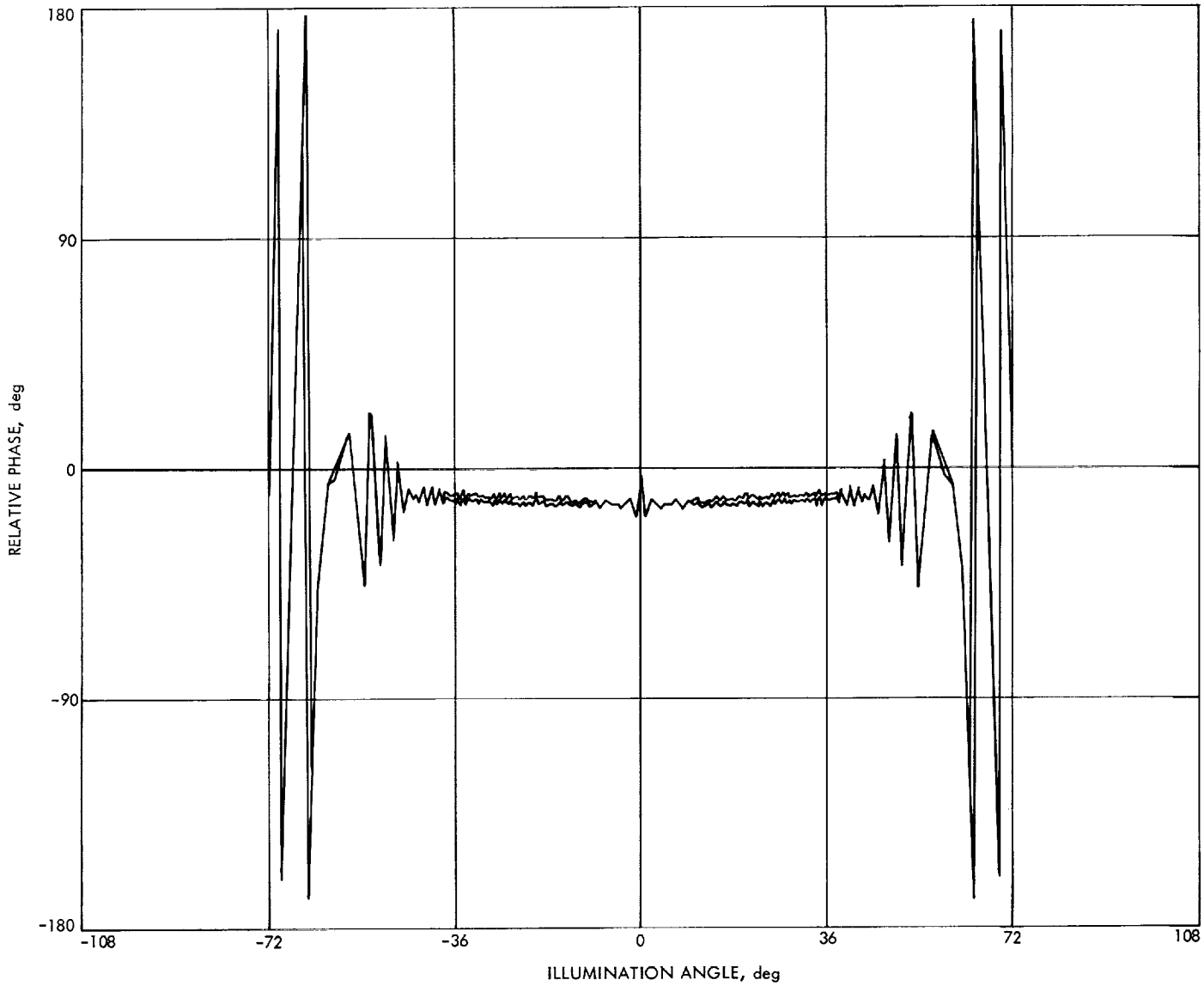

Fig. 63. Subreflector scattered radiation patterns, E- and H-plane phase

where η'/η is the blocking efficiency, and B is the fractional area blocked (SPS 37-41, Vol. III, pp. 89–90). Actually $B = \sigma A$, where σ is defined as an average RF opacity and A is the optically blocked area. Because of the large wavelength size of the quadripod cross section at X-band, the opacity is estimated to be $0.8 < \sigma < 1.2$. Table 14 gives the components considered and the overall quadripod blockage efficiency, assuming the estimated opacities represent 1-σ limits.

The dissipative attenuation between the antenna reference flange and the maser reference flange was previously measured as (0.150 ± 0.0018 dB), 3 σ. Estimates of turnstile junction and horn losses are 0.025 and 0.018 dB, respectively. Table 15 gives the components considered and the overall waveguide efficiency.

The final value for the RF optics efficiency of the 210-ft diam antenna system, when fed with the XCE feedcone, may be obtained from Tables 13, 14, and 15 as

$$\eta_0 = 0.6292 \pm 0.024$$

where the tolerance quoted is an estimated 1-σ value, exclusive of surface tolerance.

c. Computed surface tolerance efficiency. In *Subsection D-1* the 210-ft diam reflector computed surface distortion is considered as a function of elevation angle, augmented with measured distortions for the primary panels, subreflector panels, and setting tolerances (Item I, Table 19 of above-mentioned article). Figure 64 shows the relation between gain loss and surface tolerance for a frequency of 8448 MHz according to the methods of Ruze (Ref. 2).

Table 14. Quadripod efficiency

Parameter	Value, %
Blocked area A	6.255
Opacity σ	80–120
Quadripod blockage efficiency η'/η	87.88 ± 2.4

Table 15. Waveguide efficiency, XCE feedcone

Component	Attenuation, dB
Antenna to maser flanges	0.150 ± 0.002
Turnstile junction	0.025 ± 0.025
Feedhorn	0.018 ± 0.018
Overall waveguide efficiency	95.65 ±0.22%

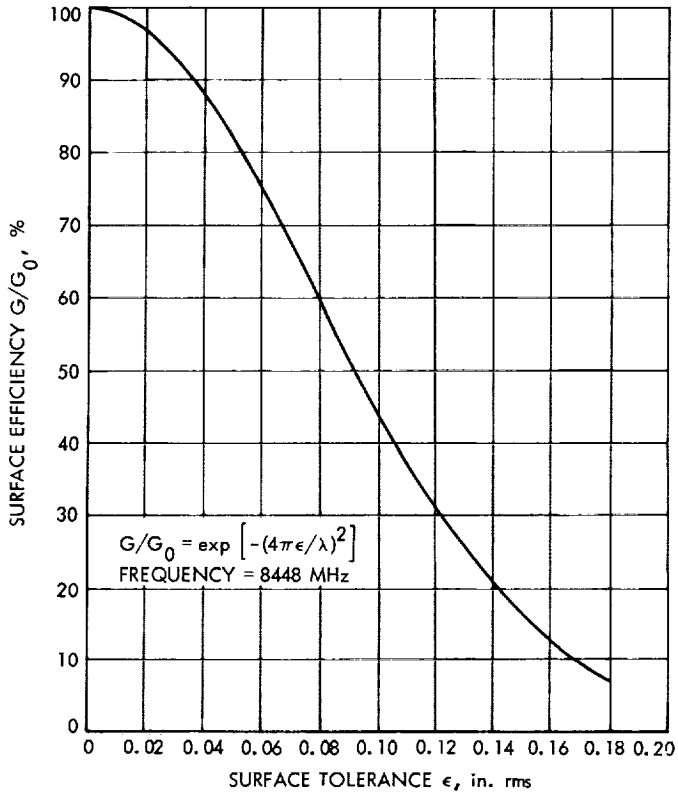

Fig. 64. Surface efficiency as a function of surface tolerance

d. Computed overall system efficiency and gain. Table 16 shows the computed surface tolerance, surface tolerance efficiency, and computed overall system efficiency and gain of the 210-ft antenna system when fed with the XCE feedcone. Table 16 surface tolerances quoted are representative of reasonable environmental conditions. Environmental effects are beyond the scope of this reporting. Approximately 0.2-dB dissipation loss within the XCE feedcone is included.

Table 16. Computed system efficiency and gain

Elevation angle, deg	Surface tolerance, in. rms	Surface tolerance efficiency, %	Overall system efficiency, %	System gain, dB
0	0.066	70.6	44.4	71.5
15	0.058	76.4	48.0	71.9
30	0.051	81.4	51.2	72.2
45	0.048	83.2	52.3	72.3
60	0.055	78.6	49.5	72.0
75	0.074	64.4	40.5	71.1
90	0.102	43.5	27.4	69.4

e. Measured overall system efficiency. As stated in *Subsection D-1*, the computed total surface tolerance figures (Item I, Table 19 of referenced article) are representative of a paraboloid of changing focal length as a function of elevation angle. Item D of the same table gives the computed focal length change required to maintain optimum gain as observed on the control room indicator, and the computed focal length change is plotted in Fig. 65.

Figure 65 also shows RF data which were obtained by maximizing receive system noise temperature on source, using the hyperboloid axial drives. Focusing was the first step taken in the February 1968 X-band evaluation. When found repeatable for the source ascending and descending in elevation angle, the data in Fig. 65 were used to manually correct the antenna focus for all following data. The source M84 (a spherical galaxy in Virgo) was selected as a high elevation angle calibrator.

Figure 66 shows the efficiency measurements made using four selected sources. The assumed source flux densities, distributions, and beam correction factors may be inferred from the 100% efficiency temperature quotations given. As improved values of radio astronomical flux become available, certain corrections may be possible. For example, the Virgo (3C274) data appear consistently low when compared with the Venus data. It is beyond the scope of this reporting to study the flux tolerances.

All data are plotted as measured, i.e., the effect of the atmosphere is included in the overall system efficiency concept. A first-order estimate of atmospheric attenuation at 10 deg elevation angle is 2% in terms of efficiency. The measured data are seen to fit the computations remarkably well. Measured data were obtained on a 24-h/day basis, i.e., no attention was given to possible thermal effects during the bright days. Similarly, no attention was given to possible wind distortions; however, the maximum wind velocity was always below 20 mph.

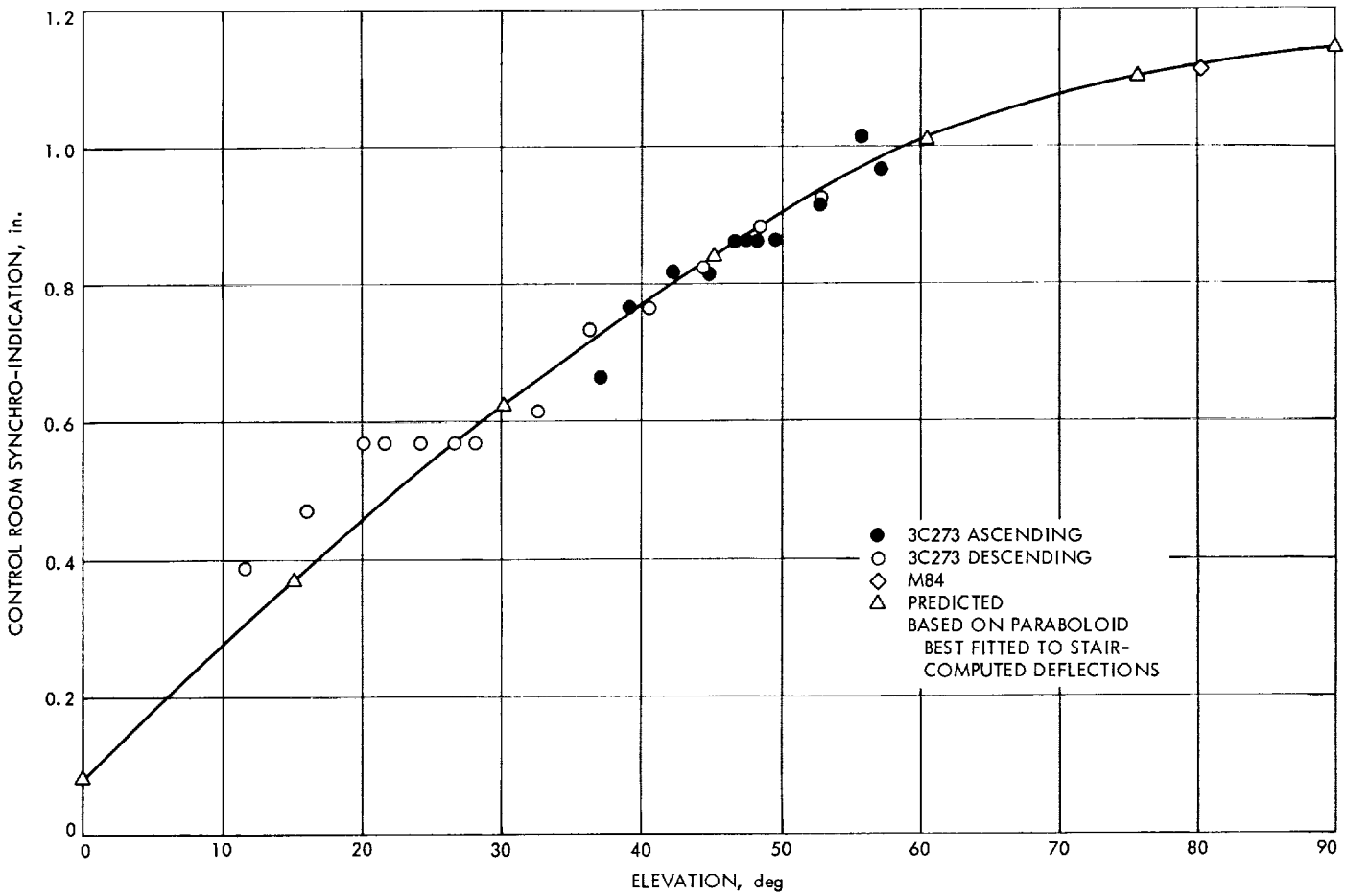

Fig. 65. Focus as a function of elevation angle

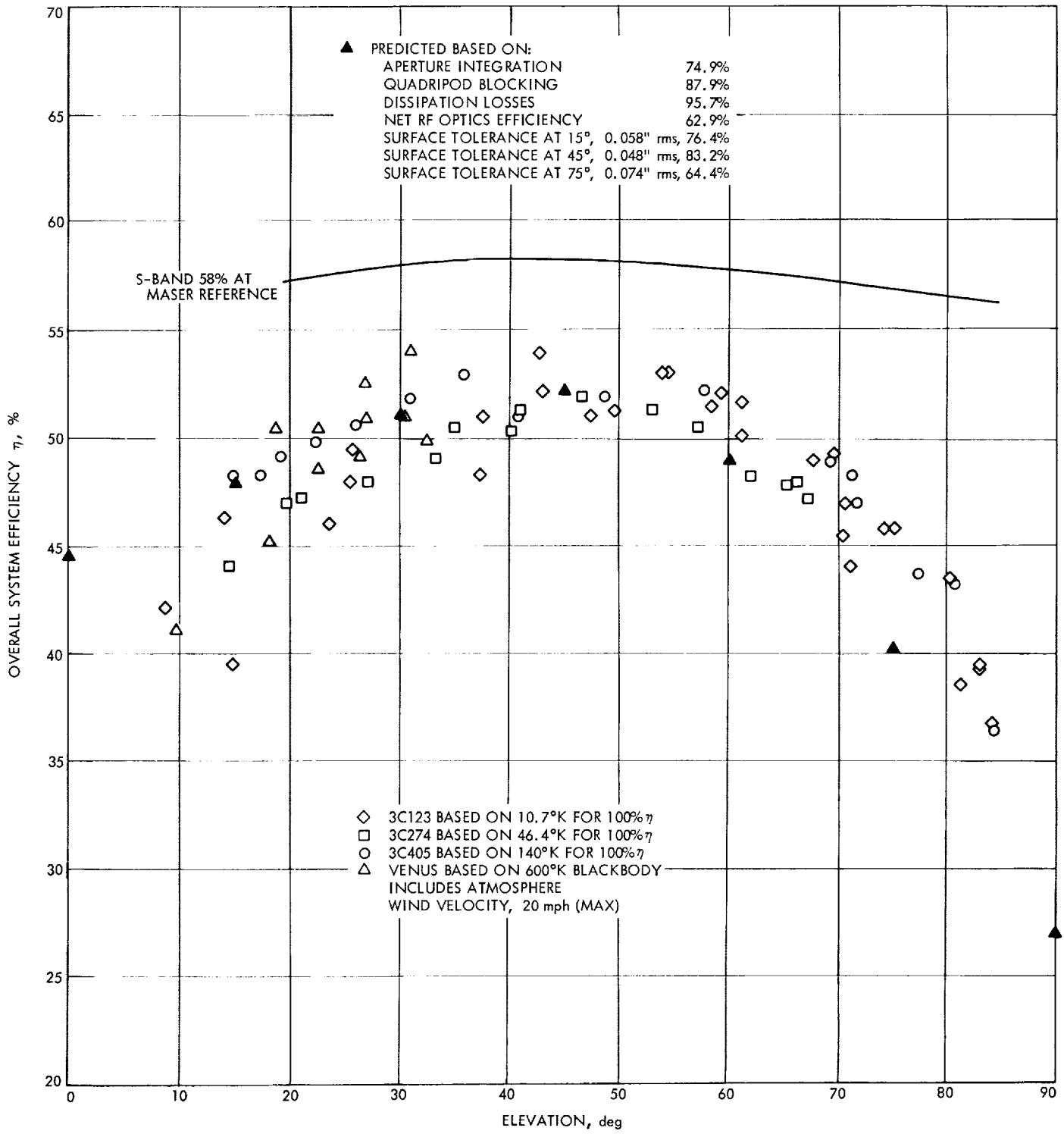

Fig. 66. Measured overall system efficiency at maser reference flange

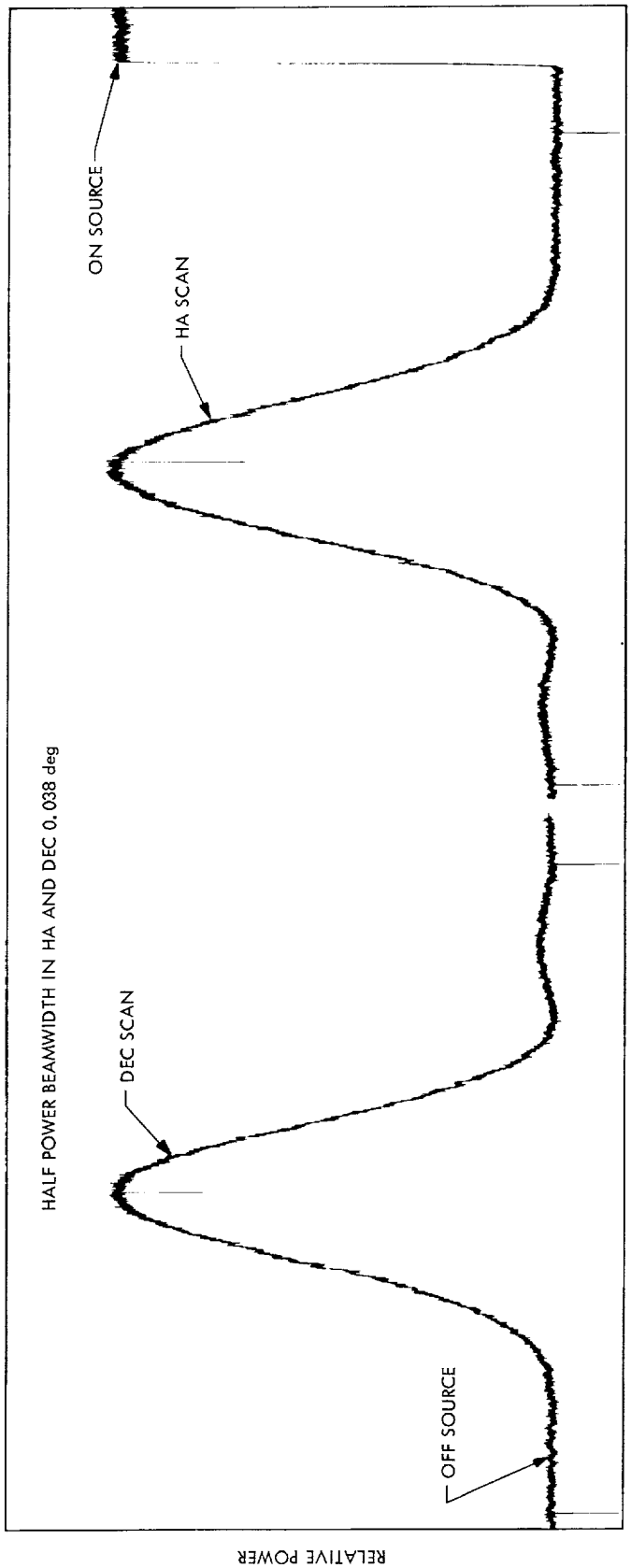

Fig. 67. Scan of 3C273 at 35 deg elevation

Because of the manual focusing as a function of elevation angle, Fig. 66 represents the best performance presently available. The possibility that the measured surface distortion (Table 18 in *Subsection D-1*) rather than the computed (Table 19 in the same article) more nearly fits the RF data above 60 deg elevation is apparent in Fig. 66. This would indicate the surface tolerance may approximate 0.090 in. rms near zenith.

f. Conclusions. The February 1968 X-band RF tests on the 210-ft diam antenna system have confirmed the previous RF optics and structural deflection computations. There is some evidence that the structural computations near zenith may be conservative.

The system performance is seen to be very good, with a peak system gain of 72.3 dB and a peak system efficiency of 52%. Scans of the quasar 3C273 at 35 deg elevation angle confirm the expected narrow (0.038 deg) beamwidth. Figure 67 shows declination and hour angle scans, respectively, for this source which produced an increase in system temperature of 25°K. Performance of the pointing system was found to be excellent for the narrow beamwidth for elevation angles above 20 deg. Possible refinement of corrections for atmospheric refraction below 20 deg elevation may be necessary.

References

1. Rusch, W. V. T., *Scattering of a Spherical Wave by an Arbitrary Truncated Surface of Revolution*, Technical Report 32-434. Jet Propulsion Laboratory, Pasadena, Calif., May 1963.
2. Ruze, J., *Physical Limitations on Antennas*, Technical Report 248. Research Laboratory of Electronics, Massachusetts Institute of Technology, Cambridge, Mass., Oct. 1952. (See also John Ruze, "Antenna Tolerance Theory—A Review," *Proc. IEEE*, Vol. 54, No. 4, April 1966, pp. 633–640.)

D. Supporting Research and Technology

1. Primary Reflector Analysis (210-ft-diam Antenna),

M. S. Katow

a. Introduction. This article describes the methods used to analytically compute the distortions of the 210-ft-diam antenna's reflector structure under gravity loadings. The deflections were output from the STAIR structural computing program (Refs. 1 and 2), and the distortions were evaluated by the rms of the residuals after best fitting by a paraboloid using the RMS program (SPS 37-40, Vol. IV, p. 176 and Ref. 3).

Comparisons were made to field-measured results in terms of the rms of the distortions and by the computer-organized contour plots of the residuals.

Finally, the total distortion of the RF pathlengths due to the primary reflector surface errors was added to the subreflector surface errors and to the equivalent rms error due to its lateral offsets for every 15 deg in elevation angle. All surface panels were set and aligned with the primary reflector positioned at an elevation angle of 45 deg.

In *Chapter III-C-6*, D. Bathker presents the results of X-band field tests on the 210-ft-diam antenna. Those results are compared with the final total distortions herein.

Since the best-fitting paraboloid included the focal length as a parameter in the fitting process, the refocussing was accomplished in the field test by translating the subreflector in the axial direction at each elevation angle. In normal S-band operations, refocussing is not done since the somewhat larger effective rms at the extremes of the elevation angles results in minor loss in efficiency.

b. Formulation of the structure. The input-data size limitations of the STAIR program limited the structural input to only one quadrant because of the following factors:

(1) The gravity loading data could only be directly generated within the size limitations and computed with minor changes of the coding.[17]

(2) At least three loading conditions could be computed per run.

(3) The data card count was already large (about 6000).

(4) Each computer run required 1½ h initially (now reduced to 50 min).

(5) The low-use experience of applied computer analysis to antenna design did not justify the additional cost and difficulties of a ½-section analysis.

Since the elevation wheel truss portion of the reflector structure assembly was only truly symmetric about one plane, the need arose to consider the ½ section of data. The nonsymmetry about the other plane resulted from the open section required between the two elevation gears for rotational clearance to the optical tower, located on the azimuth axis. Thus, the structural functions of these removed cross bracings needed to be assessed as to their effect on the deflections due to gravity loadings.

[17]This limitation was increased to 1200 total joints in Ref. 2.

Considering that the main trusses which are most effective in reducing deflections were in-plane and considering the negligible effects of the cross-bracings which are required mainly as restraints against the torsional forces or movements between the elevation wheels, it was decided that the assumed symmetry of one quadrant data would adequately represent the complete structure.

With one (first) quadrant of data, the computations for gravity load deflections required two separate computer runs, one with symmetric restraints on the joints in the boundary planes and the other with antisymmetric restraints on the joints. By use of restraints on the joints in the boundary planes satisfying the equations of condition noted in Ref. 4 and shown in Figs. 68 and 69 for the symmetric and antisymmetric loadings, respectively, the deflections for the gravity "off–on" or 1.0-g loads were computed.

Since the gravity vector in practice changes only in its direction to the symmetric axis of the reflector structure, the deflections from the setting position (45-deg elevation angle) of the surface panels were easily computed by resolving the gravity vector into two components, the one component parallel and the other normal to the symmetric axis of the reflector structure. As shown in Fig. 70, the deflections at zenith look are the sum of the changes in the above described components. The symmetric load component increased from 0.7 to 1.0 g, and the antisymmetric load component decreased to 0 from 0.7 g.

The deflections from the symmetric and the antisymmetric loading cases were actually added in the paraboloid best-fitting computer program (Ref. 3). The rms of the residual distortions, as well as the parameters of the best-fitting paraboloid, were output. The program also produced, using the SC 4020 plotter connected to the IBM 7094 computer, a contour level map of the residual distortions in terms of ½-RF pathlength errors after best fitting.

c. Results. The results for the STAIR-computed cases for the horizon look (0 deg) and zenith look (90 deg), with the surface panels set to "perfect" paraboloid at 45-deg elevation angle, are shown on the left-hand sides of Figs. 71 and 72. These contour level patterns were duplicated as produced by the plotter except for the enlarged numbers that show the values of the contour levels and the increased-width zero (0.0) level lines. The rms values in Figs. 71 and 72 refer only to the panel support points in the reflector structure.

The technique used for the field readings is illustrated in Fig. 73. Using as the geometric base the arc length from a strap gage that was used to drill the panels for the target placement holes and the computed instrument angle θ, the surface panels were adjusted to a paraboloid shape, and the target readings were also used to measure the deflection under the gravity loadings. The readings were continuously measured and checked with respect to a four-target datum reference plane at all elevation angles. After best fitting, the results are shown on the right-hand sides of Figs. 71 and 72.

The distortion vectors in the field data contour charts were all assumed to be normal to the line of sight as read by the theodolite, and conversions to vectors parallel to the symmetric axis of the paraboloid were made by dividing the readings by the cosine of the instrument angles. Although it is possible to compute the direction of the deflection vectors from the STAIR program as a first-order correction to obtain a more conservative result, the data was best-fitted after it was assumed that the measured deflection vectors were parallel to the normals to the paraboloid. The new values were rms = 0.063 in. for the zenith-look case and rms = 0.034 in. for the horizon-look case.

To establish the rms distortion values compatible for RF performance calculations, it was necessary to compute the surface distortion at a 45-deg-elevation panel-setting position and add it to the distortions caused by the gravity loading at the zenith- and horizon-look positions as a change from the 45-deg position. For the 45-deg elevation setting position, the rms distortion of the surface-panel setting error was added as a random error to (1) the surface-panel manufacturing error, and (2) the subreflector manufacturing error. Since all alignment of the surface panels was done for the 45-deg position, no error was assigned for any misalignment. Table 17 gives the measured surface distortion at a 45-deg elevation angle.

Table 17. Measured surface distortion of 210-ft-diam antenna at 45-deg elevation angle

Error source	Error, in. rms
Surface-panel setting	0.019
Primary surface-panel manufacturing	0.035
Subreflector manufacturing	0.027
Total ½-RF-pathlength error	0.048

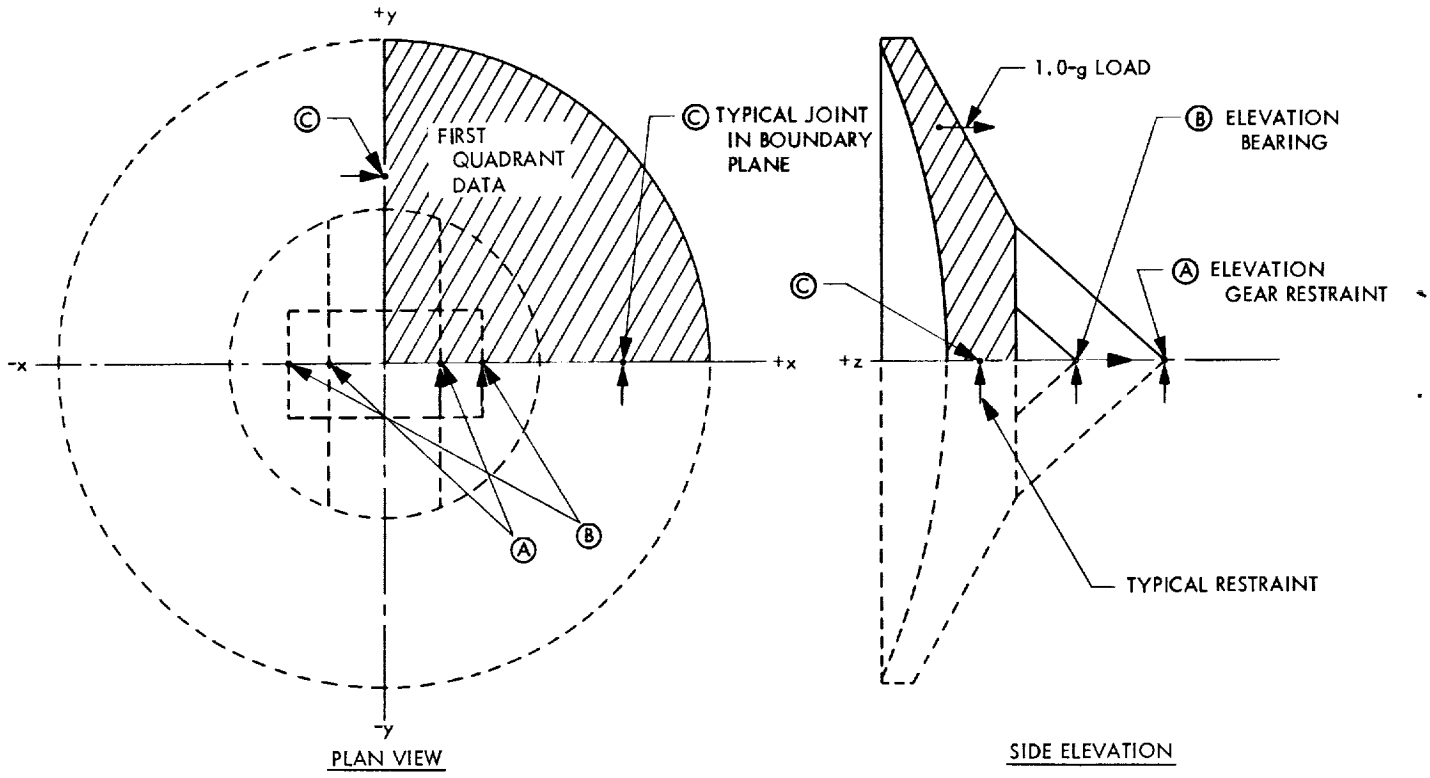

Fig. 68. Symmetric loading—boundary restraints for first quadrant data

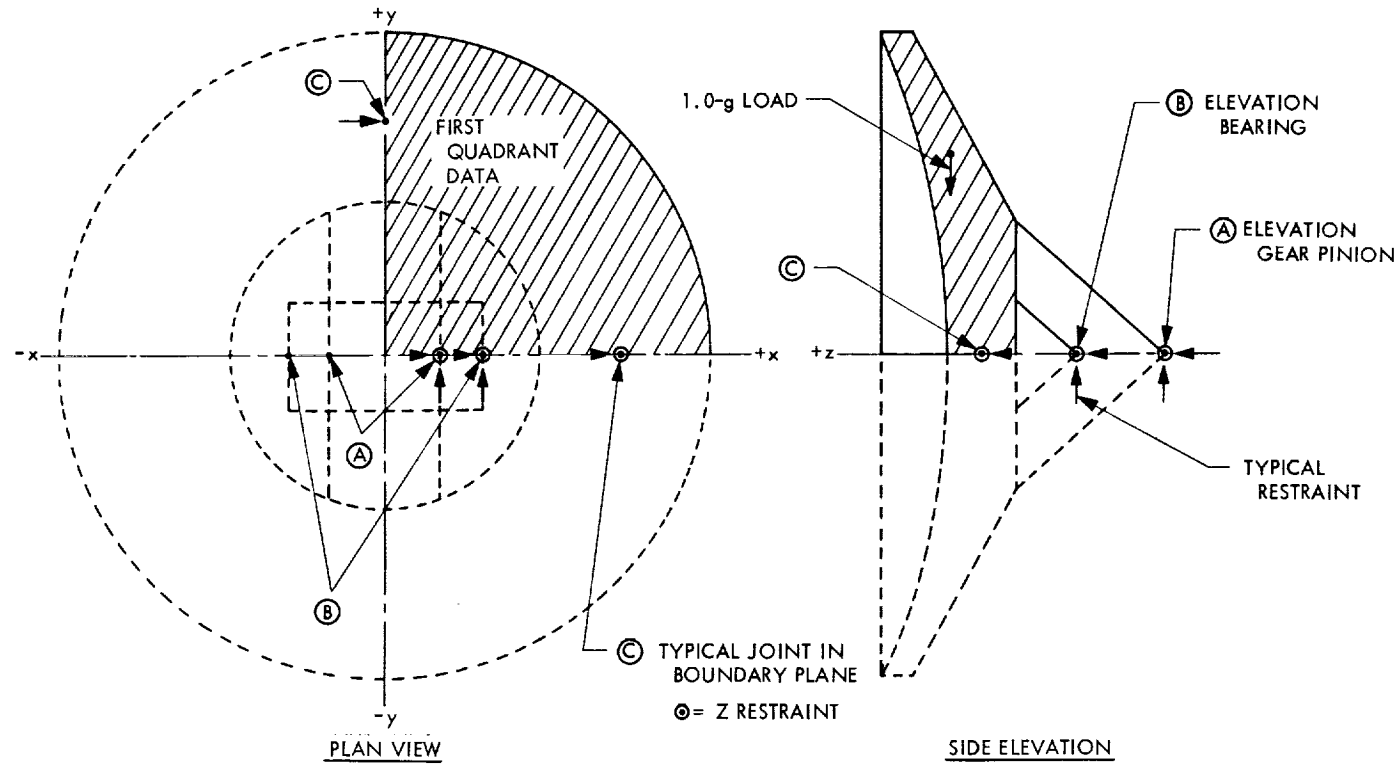

Fig. 69. Antisymmetric loading—boundary restraints for first quadrant data

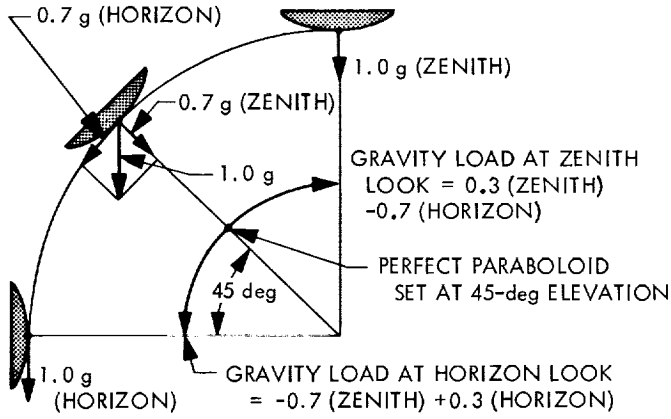

Fig. 70. Gravity loading diagram for deflection computation

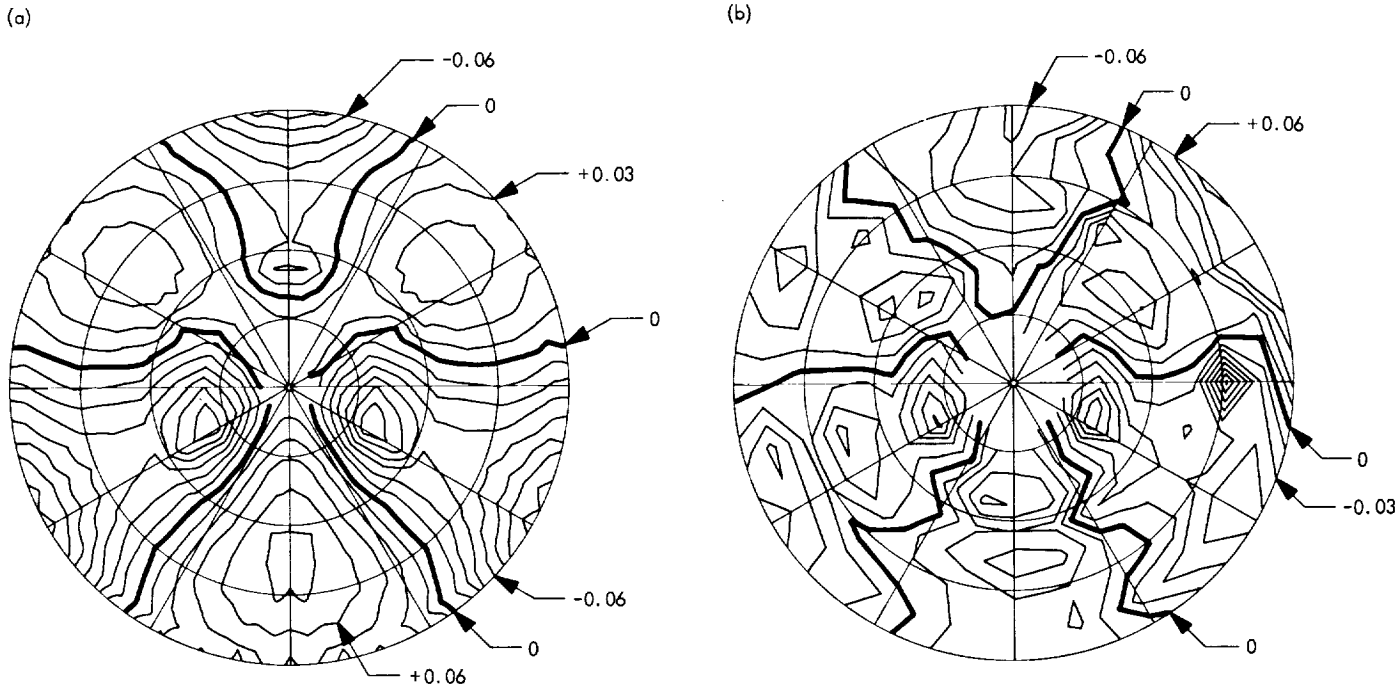

Fig. 71. Horizon-look contour maps of 1/2-RF-pathlength errors: (a) computed, (b) field reading after best fit

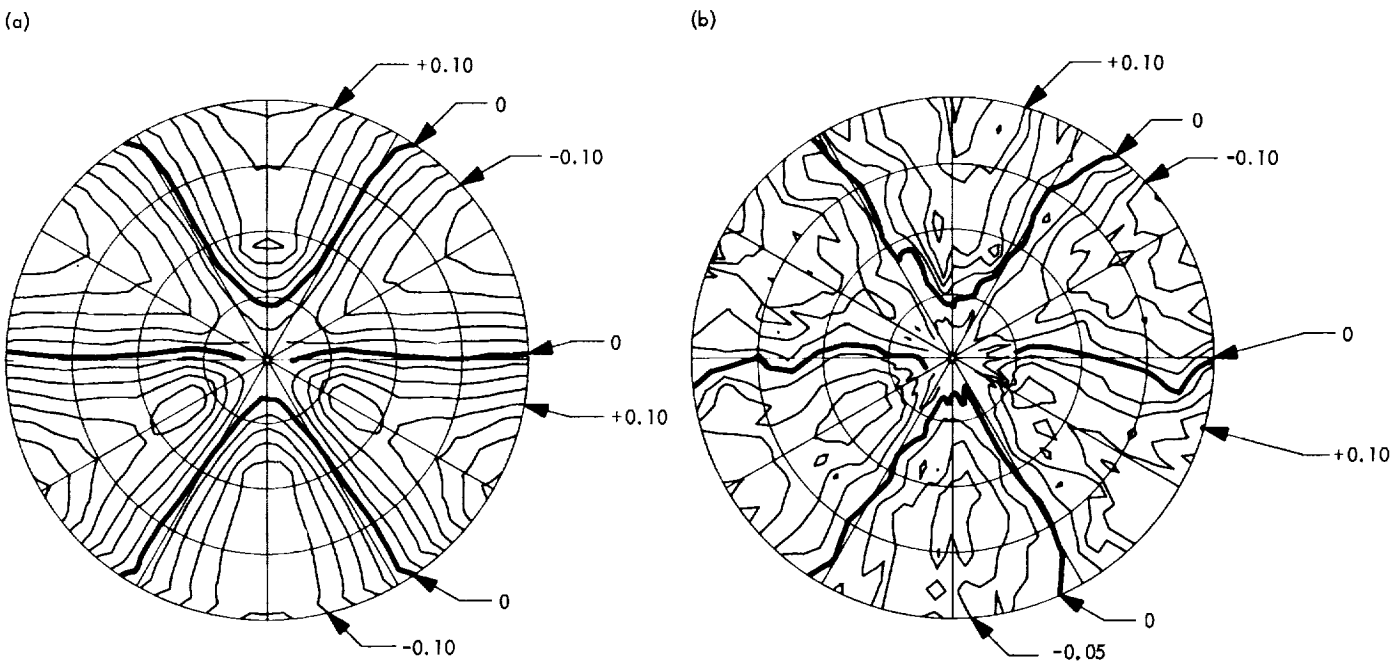

Fig. 72. Zenith-look contour maps of 1/2-RF-pathlength errors: (a) computed, (b) field reading after best fit

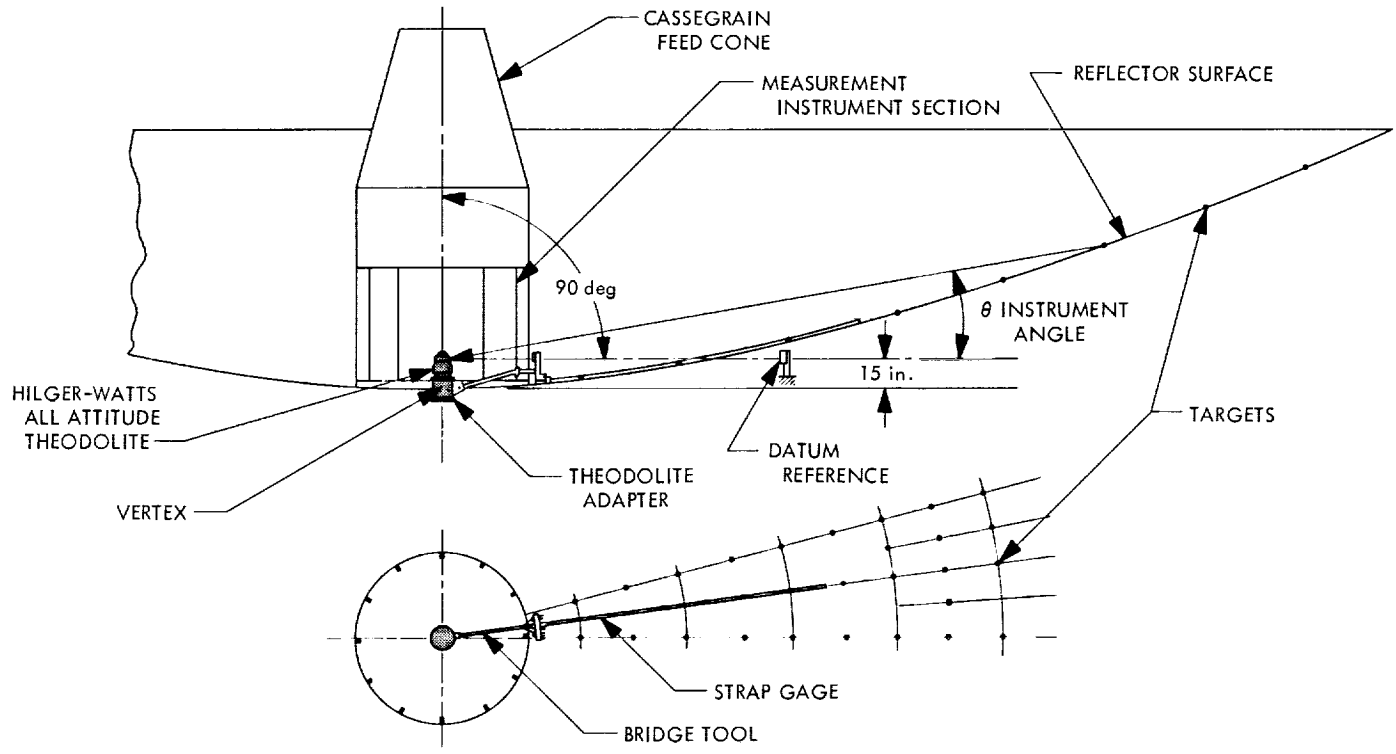

Fig. 73. Surface measuring technique

For the horizon-look and the zenith-look positions of the primary reflector, distortions in addition to those of the 45-deg position are: (1) the reflector structure gravity deflections of the surface panels' supporting points, and (2) the equivalent rms distortion from the lateral and axial offsets of the subreflector. These equivalent rms errors are read from Fig. 74, whose values were computed by the Radiation programs (Ref. 5). Table 18 gives the field-measured results and Table 19 gives the computed results.

Table 18. Measured surface distortion of 210-ft-diam antenna at 0- and 90-deg elevation angle

Source	Error, in. rms	
	0 deg	90 deg
45-deg elevation ½-RF-pathlength error	0.048	
Reflector structure gravity deflections from 45-deg elevation	0.034	0.063
Subreflector lateral offset	0.020	0.050
Total ½-RF-pathlength error	0.062	0.094

References

1. *STAIR (Structural Analysis Interpretive Routine),* Lincoln Manual No. 48. Lincoln Laboratory, Massachusetts Institute of Technology, Lexington, Mass., July 1962.
2. Katow, M. S., Bartos, K. P., Matsumoto, R., *JPL Modified STAIR System-Operating Procedures,* Technical Memorandum 33-304. Jet Propulsion Laboratory, Pasadena, Calif., June 1, 1968.
3. Katow, M. S., and Schmele, L., *Utkn-Schmele Paraboloid RMS Best-Fit Program,* in Technical Report 32-979, Vols. I and II, p. 75. Edited by A. Ludwig. Jet Propulsion Laboratory, Pasadena, Calif., April 15, 1967.
4. Newell, J. S., "The Use of Symmetric and Anti-Symmetric Loadings," *J. Aeronaut. Sci.*, p. 235, 1939.
5. Bathker, D., *Radiation Pattern Programs,* in Technical Report 32-979, Vols. I and II, p. 107. Edited by A. Ludwig. Jet Propulsion Laboratory, Pasadena, Calif., April 15, 1967.

Table 19. Computed surface distortion of 210-ft-diam antenna from change in direction of gravity vector from 45-deg elevation

Source	Elevation angle, deg						
	0	15	30	45	60	75	90
Best-fit paraboloid data							
Vertex *y*-coordinate, in.	1.588	1.403	0.806	0.0	−1.121	−2.426	−3.829
Vertex *z*-coordinate, in.	0.070	0.044	0.021	0.0	−0.016	−0.026	−0.029
Rotation *x*-axis, rad	0.001015	0.000894	0.000548	0.0	−0.000712	−0.001539	−0.002427
Focal length change, in.	−0.693	−0.439	−0.203	0.0	0.156	0.253	0.285
Quadripod apex *z*-deflection, in.	−0.025	−0.015	−0.009	0.0	0.004	0.007	0.010
Subreflector *z*-deflection, in.	−0.048	−0.028	−0.017	0.0	0.004	0.007	0.010
Subreflector axial indicated position, in.	−0.77	−0.48	−0.22	0.0	0.16	0.27	0.31
Subreflector lateral *y*-direction deflection, in.	−1.1	0.5	0.1	0.0	0.9	1.8	2.8
Subreflector lateral offset equivalent error, in. rms	0.019	0.008	0.001	0.0	0.015	0.031	0.050
axial offset equivalent error, in. rms	0.058	0.036	0.017	0.0	0.012	0.020	0.023
Best-fit paraboloid reflector structure distortion from 45-deg, in. rms	0.040	0.032	0.018	0.0	0.023	0.048	0.075
45-deg ½-RF-pathlength, in. rms				0.048			
			(Field measured distortion used for 45-deg position)				
Total ½-RF-pathlength—focussed axially distortion, in. rms	0.065	0.058	0.051	0.048	0.055	0.075	0.102
Total ½-RF-pathlength—focussed only at 45 deg distortion, in. rms	0.085	0.068	0.054	0.048	0.057	0.077	0.105

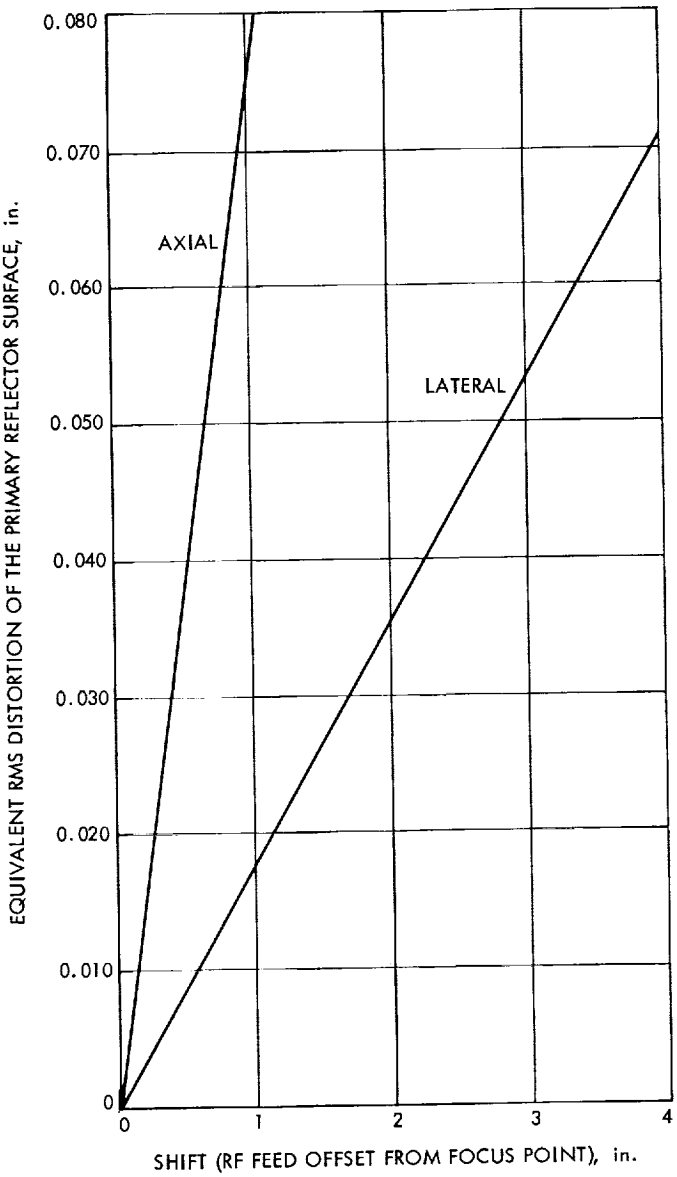

Fig. 74. Rms (equivalent) vs feed point axial and lateral shifts for 210-ft-diam antenna

2. Antenna Structure Joint Integrity Study (Phase II),

V. Lobb and F. Stoller

a. Introduction. Experience with antenna structures constructed of galvanized members has shown that their connections have a tendency to slip under long duration loading. In these structures where deflection is a failure criteria, this slip at connections is a serious problem. Slip in galvanized joints has resulted in distortion of the reflector parabola and in tolerance degradation in other components of the antenna. A prime problem has been the loss of gear running clearance between the pinion and bull gear for both declination and hour angle motion. These antennas are subjected to varying conditions for a large moveable structure, such as drive and wind vibration, rapidly varying dynamic loading, load reversal, and sustained loads.

So that a means of eliminating this problem could be devised, a joint integrity study was started. Phase I is a five-part bolt testing program currently in progress, the first two parts of which have been reported in SPS 37-47, Vol. II, pp. 135–138 and SPS 37-50, Vol. II, pp. 177–179, respectively. Phase II is a bolted-joint study which consists of a thorough testing of bolted structural assemblies exposed to long-term static shear stress, long-term static shear stress with a superimposed transverse vibration, and short-term static shear stress with repetitive load reversals. This research program studied the effect of such variables as joint and fastener coatings, bolt design and strength level, shear and tension stress, and balanced design tension-shear ratio. Tests and parts of the data resolution were performed at a subcontractor's facility. The economics of fabricating and maintaining structural members exposed to weathering in isolated locations require the use of corrosion-resistant protective coatings. While coatings on faying surfaces are known to have definite effects on joint performance under short-term loading, no specific information has been available as to how they contribute to joint behavior over a prolonged period of time.

The study of time-dependent-slip in bolted assemblies represents a new area of consideration in the field of mechanically fastened connections. The results are of general interest because of the importance of dimensional integrity in various types of connections. Reduced test results of the Phase II activity are presented in this article. A future JPL Technical Memorandum will present the specifications, test data, apparatus description, etc.

b. Test results. Tests were made of 110 bolted joints. The joints, consisting of A36 steel plates and angles, were fastened with high-strength bearing bolts and hex head bolts in ASTM A325 and A490 strength grades.[18] Both the high-strength bearing bolts and hex head bolts were used to assemble friction-type and bearing-type joints.

The steady-state slip behavior of structural connections tested in series A and B followed the general patterns schematically illustrated in Fig. 75. Curve A represents the behavior of bolts with very poor slip resistance. The

[18]ASTM = American Society for Testing Materials.

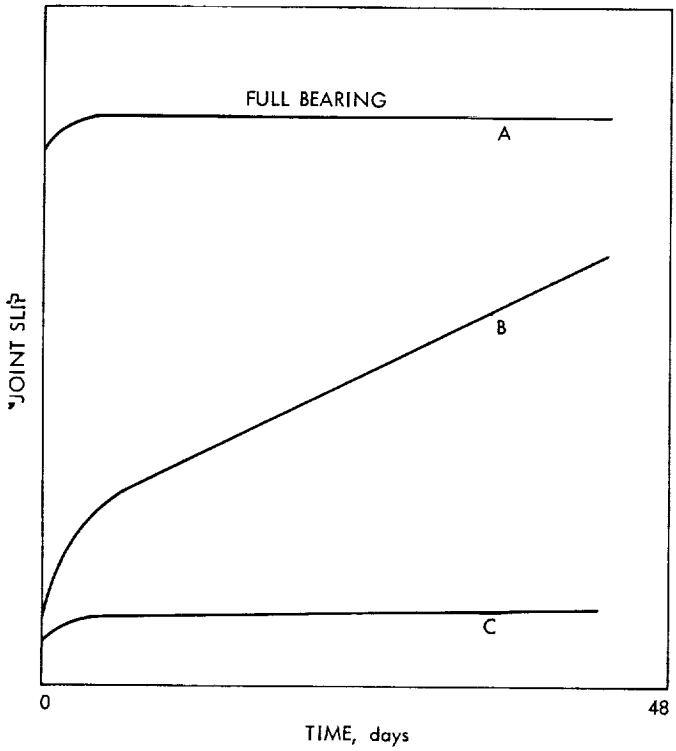

Fig. 75. Typical joint slip curves (series A and B)

relative joint movement was rapid, being restrained only when complete bearing was achieved. Curve B is representative of the behavior of most highly loaded friction connections. Joint extension was noticeable immediately after loading, but after a relatively short period of time steady behavior occurred. Curve C is typical of bolted connections with good slip resistance. After initial extension, a very low slip rate or a zero slip rate was observed.

Typical examples of the three curves and their physical properties are as follows (faying surface coating generally affected the joints' slip resistance): curve-A-type joint slip occurred on a red-oxide-painted surface; curve-B-type joint slip occurred on galvanized and red-oxide-painted surfaces; curve-C-type joint slip occurred on mill-scale and inorganic zinc-painted surfaces.

The joint deformation that occurred in the series C load reversal tests for mill-scale faying surface is illustrated in Fig. 76. Several of these tests demonstrated the same behavior under sustained load as was experienced in series A and B, and this is evidenced by the positive or negative slope of the curve during the 2-h period. These specimens were not assembled in bearing so that, when the load was reversed, the joint deformation returned to zero and then became negative. After unloading, in either tension or compression, considerable recovery of the joint deformation occurred.

The results of series C stress reversal tests on inorganic zinc-silicate faying surfaces were radically different than the data generated in the series A and series B tests. Although the general relations between joint slip and bolt-type or joint slip and shear stress appear to be approximately the same, the maximum deflections are quite inconsistent with the data on the effect of faying surface condition. Under a condition of stress reversal, the

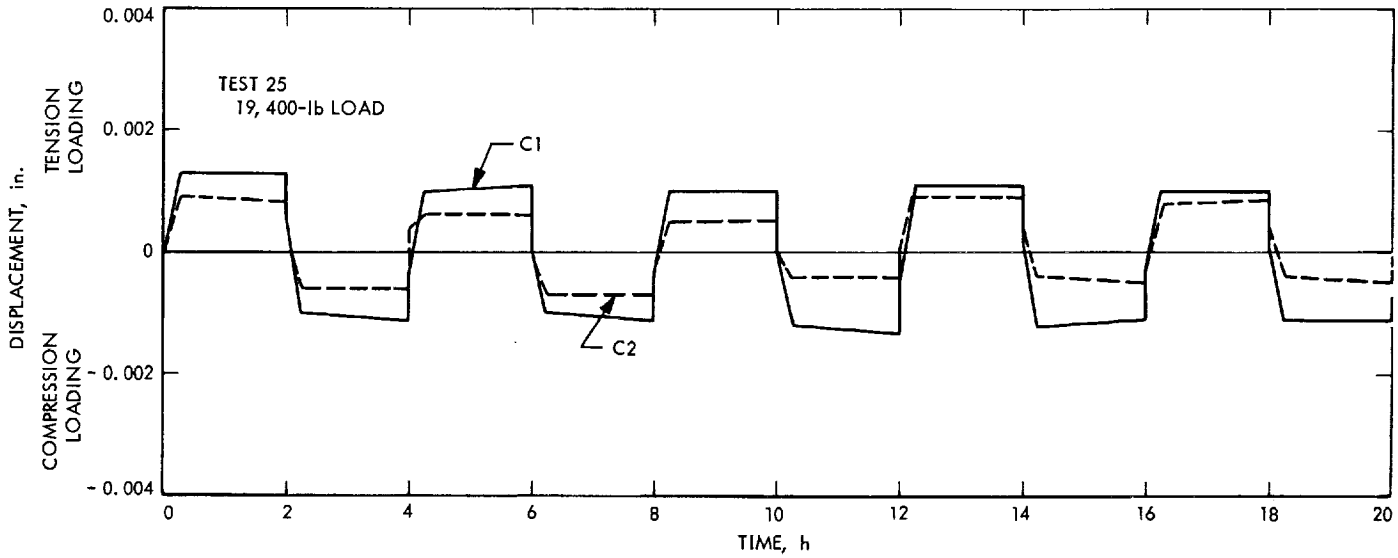

Fig. 76. Deflection time graph for mill-scale faying surface

inorganic-zinc coating breaks down and frets away, causing a reduction of bolt preload, which allows increased joint slip. This breakdown is shown on the deflection time graph (Fig. 77). The peak deflection occurs after several cycles and is four times that of a mill-scale faying surface.

Figure 78, the graph for galvanized faying surfaces, shows a definite variation in the deflection behavior of the galvanized joints after cyclic loading. After several cycles of load reversal, these joints showed a tendency to "lock up" or cold weld so as to reduce the amount of deflection occurring. However, these deflections still were greater by a factor of two than joints with mill-scale faying surfaces. Furthermore, under sustained load, the slope of the deflection curves was unaffected by this factor.

Joint slip data of series A, B, and C show no significant effect of bolt finish on slip performance. Several otherwise identical joint pairs, except for having galvanized, mechanical zinc-coated, and inorganic zinc-painted fasteners, show no repeatable difference in joint slip. None of the three protective finishes provides a substantial advantage over the others.

The effect on joint slip caused by adding a transverse vibration to the joints (series B) was little at stresses below 10,000 lb/in.[2] Above that level, the total joint slip in high-strength hex head bolts was increased considerably by the addition of vibration, but for the high-strength bearing bolt (HSBB) there was no effect on the total joint slip. However, the addition of vibration had little or no effect for either type of bolt on the slip rate (in./h).

When bearing bolts are used, faying surface coatings, such as paint and galvanize, create no change in fatigue life over a mill-scale faying surface. In service conditions requiring friction-type joints, two high-strength bearing

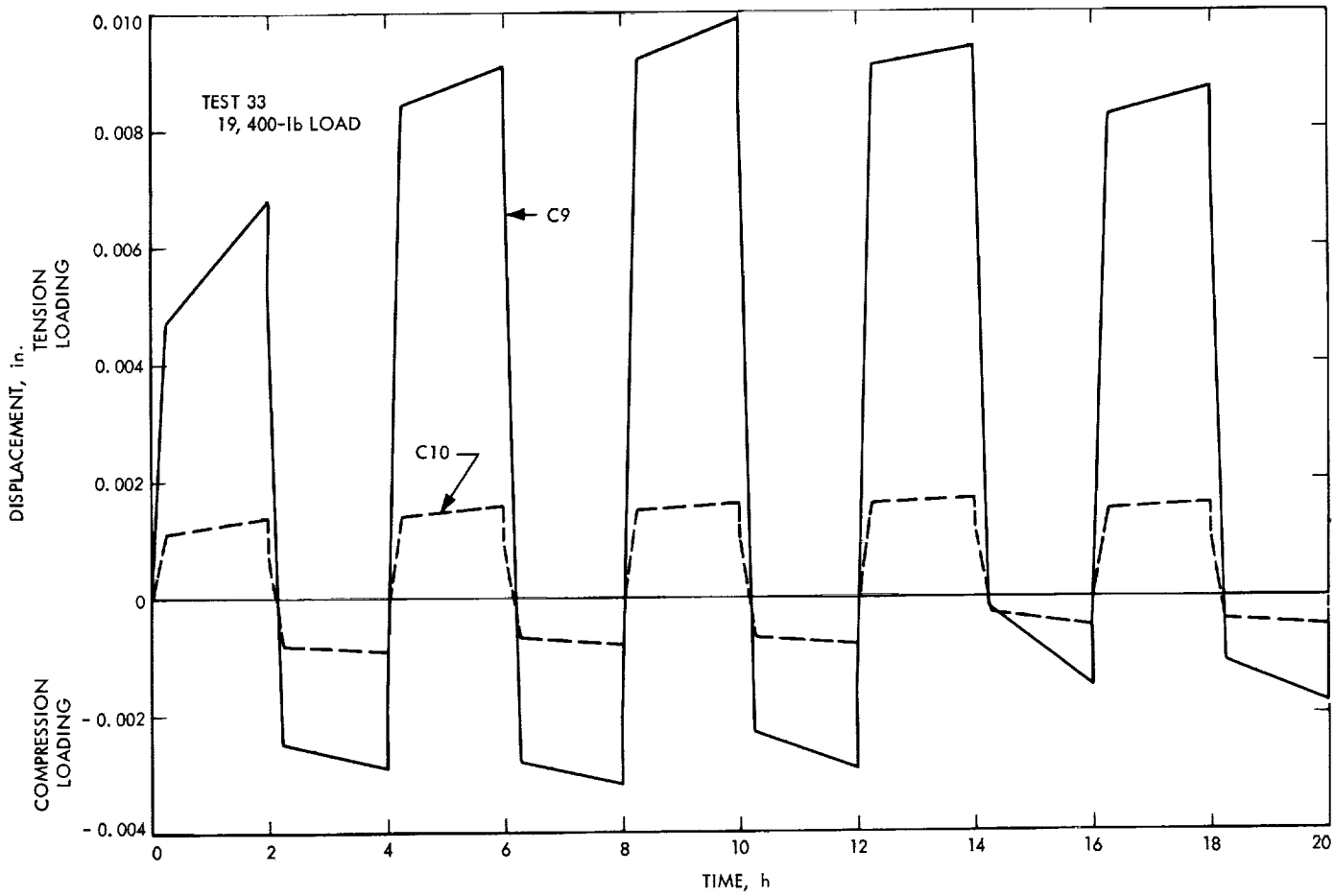

Fig. 77. Deflection time graph for inorganic zinc-silicate faying surface

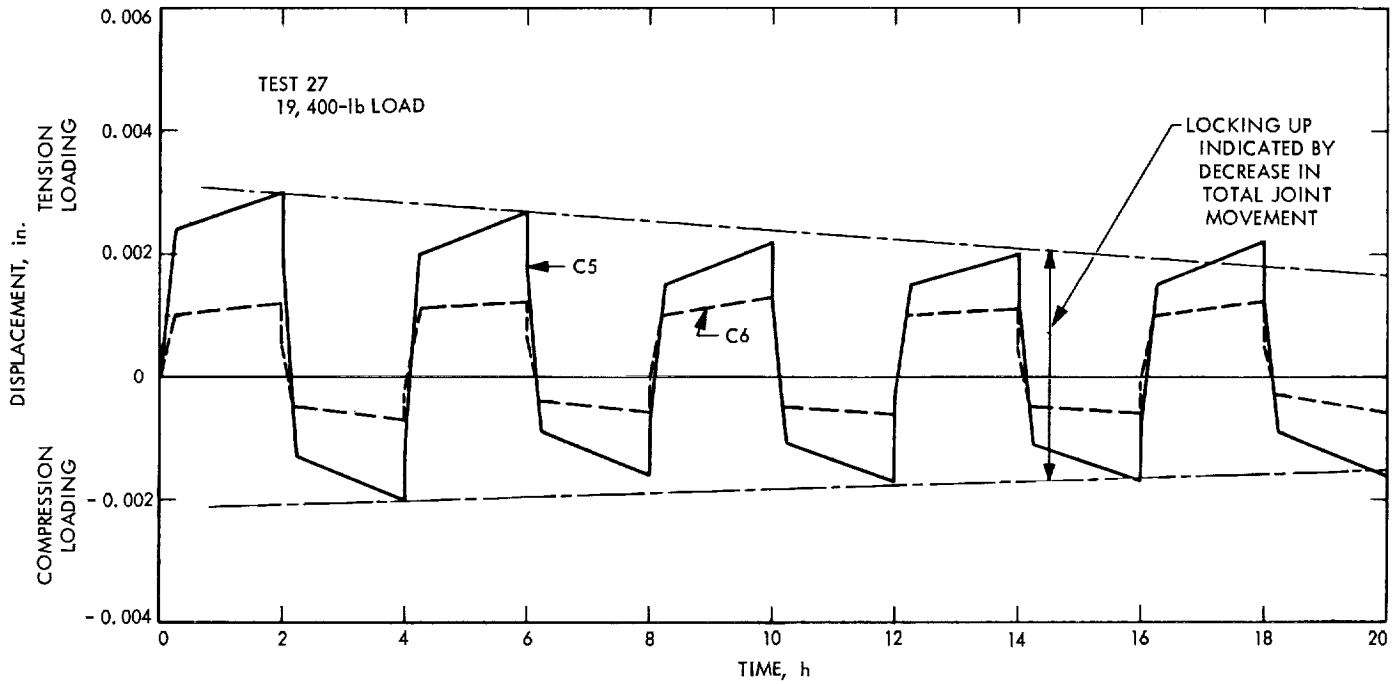

Fig. 78. Deflection time graph for hot-dip galvanize faying surface

bolts can be substituted for three hex head bolts without causing any change in the time-dependent slip behavior of the joint.

Figure 79 is a graph of nominal bolt shear stress versus the logarithm of the joint slip under load (Δ) for the galvanized joints in series A and B. On this semilog plot, the value of Δ increases in approximately a direct proportion to the shear stress although the rate of increase is considerably lower for the high-strength bearing bolt than it is for the hex head bolts. At shear stresses below 11,000 lb/in.^{2}, the average Δ is quite similar for either type of bolt (approximately 0.001 in.). Above 11,000 lb/in.^{2} there is greater divergence, but at any given stress level the high-strength bearing bolt has considerably less total slip than does the hex head bolt.

In the high-strength bearing bolted joints, there is relatively little difference in the magnitude of Δ at the various stress levels. There are two factors that allow slip with these types of bolts: (1) a reduction in the amount of interference due to variations in hole size, and (2) elongation of the bolt hole under load. Thus, the general trend for the high-strength bearing bolted joints follows closely the general trend of hole elongation (shown in approximation).

The most significant influence on joint slip behavior was the bolt shear stress level (Fig. 79). On the other hand, attempts (Fig. 80) to relate the time-dependent slip factors with member tension stress were not as successful. There is a qualitative relation between joint slip and tension stress, but there is considerable scatter and overlap in the data. The reason for this is that, with changing tension-shear ratios, several shear stresses can occur in any given tension stress range. Since slip behavior is more closely related to shear stress, comparisons based on tension stress are inconsistent.

The highest high-strength bearing bolt slip rate (in./h) value recorded was only 4.86×10^{-6}. Thus, at the higher stress allowed for bearing-type joints (22,000 lb/in.^{2} with A325 bolts and 32,000 lb/in.^{2} with A490 bolts), and regardless of faying surface condition, the high-strength bearing bolt provides a slip rate lower than or equal to that considered acceptable for friction-type joints under current practice.

At stresses below 15,000 lb/in.^{2}, the faying surface condition had no effect on total slip in the high-strength bearing bolted joints. In high-strength bearing bolted joints (static stress or unidirectional loading stressed above 15,000 lb/in.^{2}), galvanized surfaces caused somewhat more slip than did other types of faying surfaces.

The most significant effect of faying surface condition on joint slip occurred in the joints fastened with hex

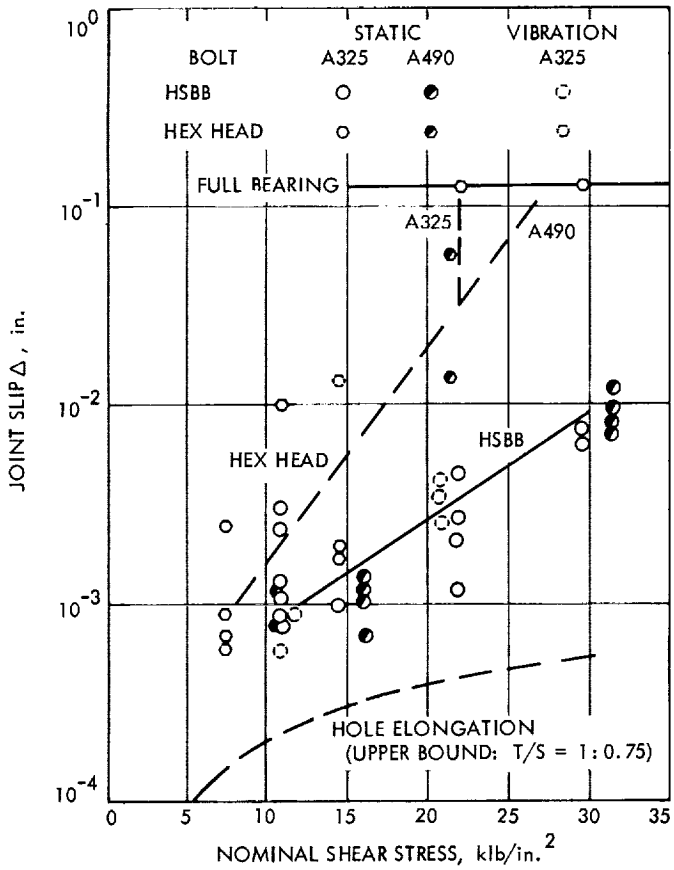

Fig. 79. Joint slip vs shear stress (series A and B galvanized)

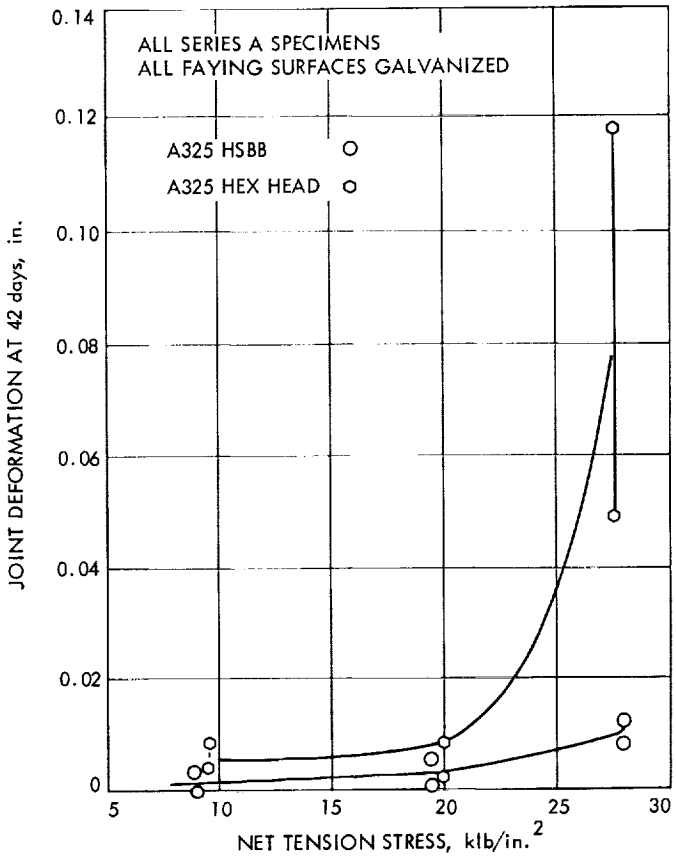

Fig. 80. Tension stress vs joint deformation

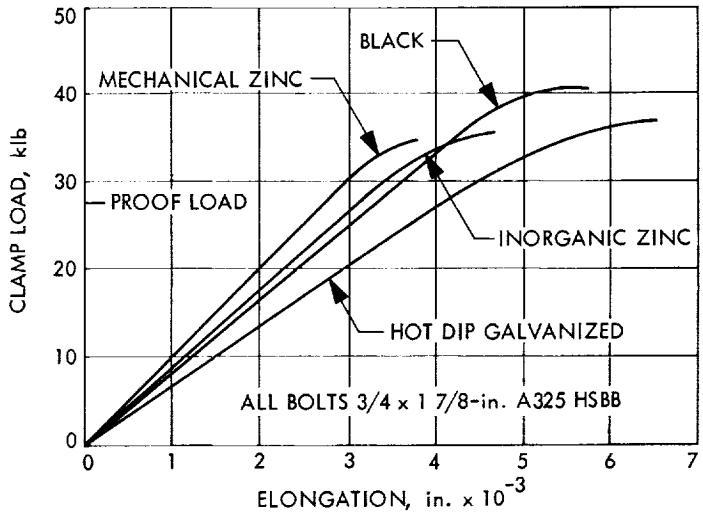

Fig. 81. Typical calibration curves

head bolts. In order of increasing slip resistance (for hex head joints under static stress or unidirectional loading), these were: galvanized faying surfaces, red-oxide primer-painted and plain mill-scale faying surfaces, and inorganic zinc-painted faying surfaces. On reviewing the uncorrected joint deformations, it became apparent that the red-oxide primer joints experienced high deformation on application of the test load. In this respect, the order of increasing slip resistance would be: red-oxide-primer-painted faying surfaces, galvanized faying surfaces, plain mill-scale faying surfaces, and inorganic zinc-painted faying surfaces.

Staggering the direction of bolt insertion did not affect the performance of the high-strength bearing bolt joints. In the case of interference-type bolts, slip due to plating occurs only relative to the general trend of hole elongation if such occurs and if an interference or bearing joint is actually achieved.

Bolts (ASTM A325 and A490 class) coated with inorganic zinc silicate or mechanical zinc plating required additional lubrication on their respective nuts (also the inorganic zinc bolt thread had to be chased) to reduce assembly torques to prevent bolt failures prior to reaching the required minimum tension values. Figure 81

shows the reduced elongation of these two finishes, which was caused by the added bolt torque.

The use of inorganic zinc as a corrosion-protective coating proved unsuitable since it produced very high and erratic bolt torques which caused bolt failures. In addition, the bolt threads had to be chased on a coated bolt due to the thread becoming filled with paint, making it impossible to install the nut.

The effect of bolt assembly direction is not normally a significant factor unless the bolt grips are large enough that a disparity can exist between member thicknesses. If the outer ply is thin, the body taper required may cause a reduced interference fit in the thin outer ply. To obtain full bearing it is necessary to use a thicker washer (or washers) and longer bolts. In addition, to minimize this effect a staggered bolt insertion is specified even though in these tests no significant difference in slip could be determined due to direction of bolt assembly.

3. Measurement of Wind Torque (210-ft-diam Antenna), *H. McGinness*

a. Introduction. For several reasons, it is desirable to know the magnitudes of the azimuth and elevation axis torques acting on the 210-ft-diam antenna at the Mars DSS. Especially, it is desirable to ascertain the following: axis torques as a function of wind velocity, an axis torque time spectrum, and azimuth axis torque variations versus short-time intervals for the purpose of improving the servo control drive system. From Fig. 82, it may be seen that the summation of the drag link moments about the azimuth axis is approximately equal to the applied wind torque (the applied wind torque is slightly greater, because the vertical axis bearing contributes some resistance). Therefore, if the loads in the drag links could be measured and recorded, all of the desirable objectives could be obtained without interfering with the normal operation of the antenna.

b. Attempt at measuring drag link loads. It was believed that the drag link loads could be measured by semiconductor strain gages attached to the drag links. From wind tunnel model studies, it was predicted that the azimuth axis torque in in.-lb would be approximated by:

$$T_A = 2.47\,(10^4)\,v^2 \qquad (1)$$

where v is the wind velocity in mph.

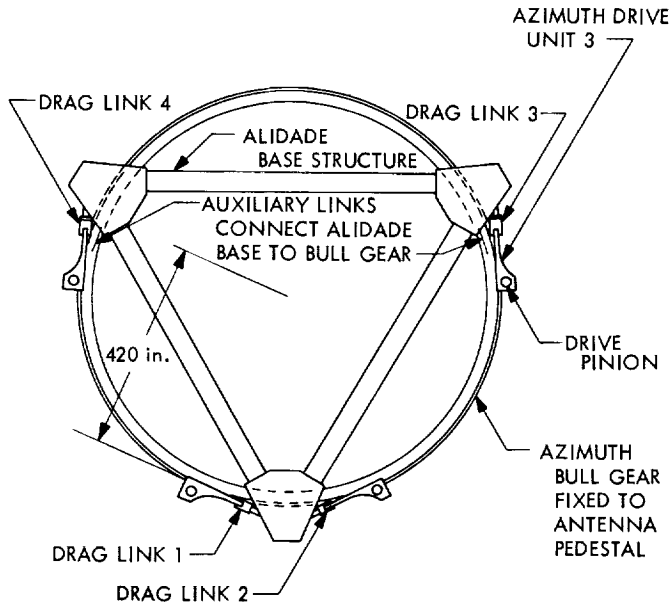

Fig. 82. Configuration of azimuth drive and alidade base

In order to determine the proper strain gage location, a quarter scale model of the drag link was made, instrumented with many strain gages, and statically loaded both in tension and compression. It was determined that a gage located as shown in Fig. 83 produced the same absolute output value when loaded in either tension or compression and that the stress at this point in lb/in.^{2} is given by the following expression:

$$\sigma = \frac{P}{1.2\,A} \qquad (2)$$

where P is the applied axial load and A is the cross sectional area.

From Fig. 82, it may be seen that there are four azimuth axis drag links spaced 420 in. from the center. Thus, the expected stress in the drag link, using Eqs. (1) and (2) and setting A at 112 in.^{2}, may be expressed as

$$\sigma = \frac{T_A}{4\,(420)\,1.2\,(112)} = \frac{2.47\,10^4\,v^2}{4\,(420)\,1.2\,(112)} = 0.11\,v^2 \qquad (3)$$

It is desirable to detect wind velocities as low as 10 mph, and Eq. (3) shows that a stress of 11 lb/in.^{2} must be resolved. It was deemed that only semiconductor-type strain gages with their high-gage factors, together with high-quality amplifiers, could resolve such small stresses.

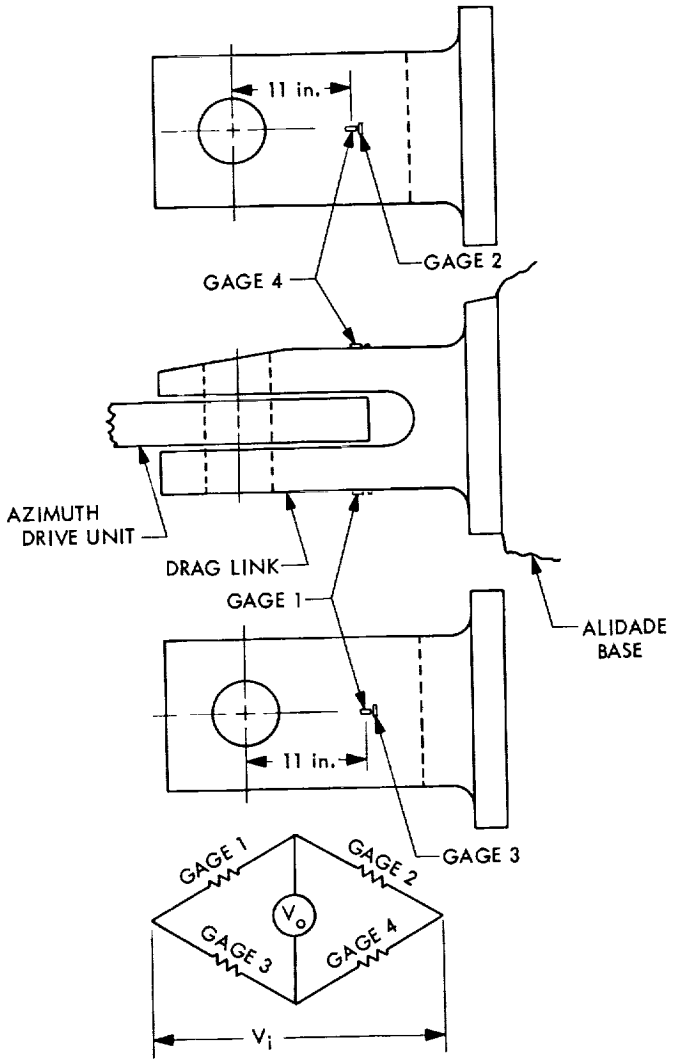

Fig. 83. Drag link showing strain gage locations and circuitry

It was decided to instrument one drag link with four semiconductor gages having gage factors of 56 and connected into a bridge circuit (Fig. 83). The ratio between bridge output to input voltage for this configuration is

$$\frac{V_o}{V_i} = f\left(\frac{1+\nu}{2}\right)\frac{\sigma}{E} \tag{4}$$

where f is the gage factor, ν is Poissons ratio, and E is the modulus of elasticity. Taking 56, 0.30, and 29 (10^6) as respective values of f, ν, and E, and substituting Eq. (3) into (4), there is obtained,

$$\frac{V_o}{V_i} = 0.138\,(10^{-6})\,v^2 \tag{5}$$

Even though these stresses and voltage ratios are very small, it was believed that the instrumentation could be made good enough so that significant voltage outputs would not be masked by temperature drifts to which semiconductor gages are particularly sensitive.

In September 1966, the strain gages were attached to one drag link. Prior to cementing on the gages, all load was removed from the link by disconnecting the hydraulic drive motor at this link and then setting the drive pinion at the middle of its backlash range. The temperature of the link, through the use of heating strips and thermocouples, was held at a constant temperature during the curing of the strain gage cement.

In order to temperature-compensate the bridge, the temperature of the 1,400-lb drag link had to be held constant at various values as different amounts of compensation were attempted. The temperature was raised by energizing the heating strips and lowered by the application of dry ice. Known loads were applied to the link by use of a hydraulic jack and pressure gage (Fig. 84). After three days of such attempts, it was concluded that satisfactory compensation could not be obtained under these field conditions. The random drifts observed were large in comparison to the calibration

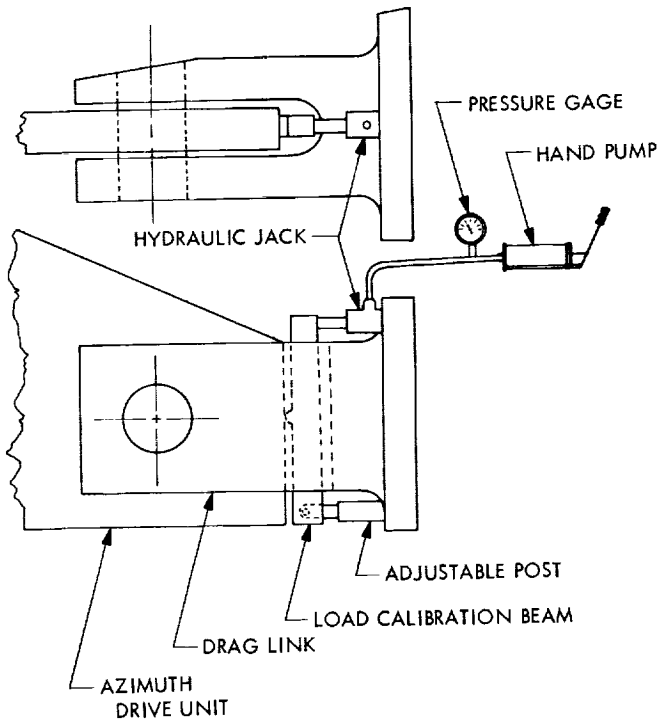

Fig. 84. Method of calibrating strain gages

loads. It is now believed that only by instrumenting the drag link in a temperature-controlled room can satisfactory bridge compensation be achieved.

It is logical to ask if an auxiliary link can be attached to the drag link so that the deflection over the entire length of the drag link is concentrated into a short portion of the auxiliary link. An analysis will show that in order to resolve a stress of 11 lb/in.^{2} it is necessary to match the thermal expansion coefficient of the auxiliary parts to that of the drag link to within one part in 6,000, a virtually impossible task. Therefore, these attempts at obtaining the objectives ended in failure.

c. Auxiliary drag link method. A much less elegant method may prove to be workable in obtaining some of the objectives. It involves the use of two auxiliary links connecting the alidade base structure to the bullgear mounting flange (Fig. 82). Normally, the wind forces are transmitted through the drag links into the drive gear pinions which in turn bear against the teeth of the bullgear. If the auxiliary links are installed, and all drive pinions set at the midpoints of their backlash ranges, then the wind torque forces would pass through the auxiliary links only. If the two auxiliary links are sufficiently preloaded one against the other, then under the application of a wind torque the sense of the force (tension or compression) in each link will not change. Thus, it is possible to guarantee that each auxiliary link will always be in tension.

By making a neck on a short section of each auxiliary link, the stress can be made sufficiently high so that conventional strain gages, having gage factors of 2 or 3 but being relatively free from temperature drifts, can be used as force sensors. The problem is to keep the overall deflection of the auxiliary links within the backlash range of the pinion bullgear mesh. Preliminary calculations indicate that this barely can be done. The use of such auxiliary links is restricted to antenna nonoperational periods, because the links have to be installed at particular azimuth angles. Therefore, the wind torque data collection rate would be relatively slow. It is thought that the links could be installed and/or removed within an hour or less. Use of this scheme would be limited to antenna maintenance periods not requiring azimuth rotation.

4. Analysis of Venus DSS Modifications for Surface Hysteresis, *V. Lobb, J. Carlucci, and F. Stoller*

a. Introduction. A severe calibration problem occurred during X-band RF measurements on the 85-ft-diam az-el antenna at the Venus DSS. Repeatable data could not be achieved under identical measurement conditions. The problem was isolated to the structural area—to surface hysteresis. This hysteresis was due to loose bolting in the dish backup and panel mount structure, and to slippage and bending in the panel mounting hardware.

The hysteresis problem was solved by using a new bolting procedure and high-strength bolts on the dish, new panel mounting hardware, and a new JPL-developed surface measuring system. In addition, surface accuracy was improved, at various elevation angles, by significant amounts.

This article gives results of an RMS Best-Fit computer study conducted on the upgraded antenna. The surface setting procedure used at the Venus DSS is discussed. Results of field measurements taken of the newly set reflector parabola are evaluated.

b. RMS Best-Fit computer program study. An engineering study was conducted on the upgraded antenna (after surface modifications and after modifying the antenna to accommodate a 400-kW transmitter), using the RMS Best-Fit computer program to determine probable deviations from a true parabola after best fitting by focal length change. Several runs were processed using different setting angles (30, 35, and 40 deg from horizon). The rms deviation contour plot at zenith look for a setting at 40 deg is shown in Fig. 85.

The data processed was output from the STAIR[19] program run on the final reflector modifications, with all added loads. These data were run through the RMS Best-Fit program, by first putting the sine and cosine of the various selected setting angles in the control cards of the SLOP[20] program. This program then took the correct vectorial deflection change for dish rotation from the setting angle to horizon or zenith and added or subtracted it from the zenith or horizon gravity "on–off" case to correct for a perfect set parabola at the selected setting angle. The RMS Best-Fit program then processed these data to give the horizon or zenith rms deviations with a perfect set parabola at a given angle.

Table 20 shows the change in rms deviation versus elevation angle. It is apparent that the horizon and zenith rms deviations are almost exactly equal at 40 deg; thus, this was the selected setting angle.

[19]STAIR = Structural Analysis Interpretive Routine.
[20]SLOP = STAIR Load Program.

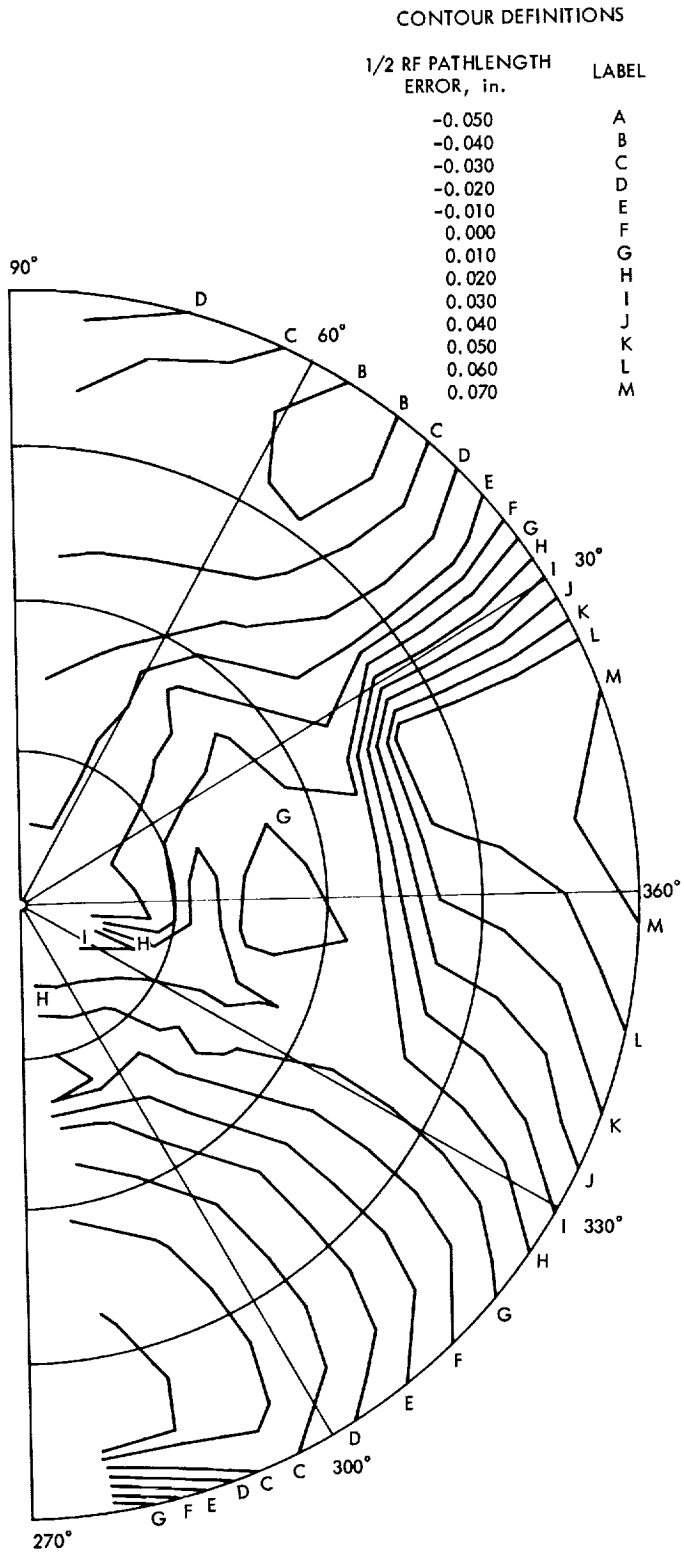

Fig. 85. Contour plot of 85-ft-diam az–el antenna zenith look (panels set at 40-deg elevation; focal length fit = 0.0277 in. rms)

Table 20. Horizon or zenith rms deviation for various elevation setting angles

Final dish position	Elevation setting angle, deg	Deviation, in. rms	
Zenith (gravity off–on)	Basic computer data	0.0399	
Horizon (gravity off–on)	Basic computer data	0.0354	
Zenith	30	0.0295	
Horizon	30	0.0267	
Zenith	35	0.0285	
Horizon	35	0.0271	
Zenith	40[a]	0.0277	Correct setting position
Horizon	40	0.0276	

[a]See Fig. 85.

c. Surface setting procedure. Surface setting at the Venus DSS was different than previous station surface setting in three ways. First, the tees of the attachment hardware were doweled to the top chord of the reflector trusses, and the angles which support the panels were doweled to these tees (this was to eliminate hysteresis effects in panel mounting hardware). The doweling was done after the rough set of the surface was completed and before the surface panels were placed. Second, the actual shimming of the panels was done at a 40-deg elevation position, not measured at this position and shimmed at zenith as was done at the other stations. Third, the dish was shimmed quite accurately to a parabolic contour of ±0.005 in.

Special panel attachment hardware setting tools were developed to allow the hardware to be set to a parabola within an ⅛ in. prior to placing of the panels. There was some difficulty with about 10% of the clips, but overall the attachment hardware setting worked well. The dowel pins prevent any movement of the attachment hardware after setting and under changing loads.

The datum plane used for setting the dish was somewhat different than those at other stations because three datum targets were used instead of four. Since the reflector parabola is supported by an integral square girder structure which is supported at four points (two supports being the elevation bearings and two being ball jack screws) with the square girder structure cantilevered over the ball jack screws as it supports the reflector structure (the ball screws were checked for linearity and found to be linear within 0.008 in.), the use of four targets neither equally spaced nor at 180 deg to each other would make it impossible to establish a repeatable datum plane. However, due to the antenna's construction, these points were the true "hard points" of the structure and should be used. One of the ball jack screws and the two elevation bearings were selected as a datum plane. This gave a three-point datum plane which would permit the theodolite to be repeatably set (or bucked in) to make dish measurements.

The linearity of the ball screws was well within the working tolerance to which the reflector was being set; so, using one point of the two was permissible. A little experimentation was required to properly orient the foot screws of the theodolite so that the instrument could be rapidly set to the unequally spaced datum targets.

The surface was set by using horseshoe shims 0.125-, 0.060-, 0.030-, and 0.010-in. thick. The surface was shimmed to a tolerance of ±0.005 in. variance from the theodolite crosshair zero. This was not too difficult for targets within 25 ft of the instrument, but as the distance exceeded this, the resolutions became more difficult and a variance would occur from night to night in panel targets that had been zero-set on a previous night. Less than 5% of the points exceeded 0.020 in., with only one point exceeding 0.030 in. (when the surface was read several days after setting and in a 15- to 18-mph wind).

d. Field measurements and hysteresis evaluation. Field measurements were taken of the newly set reflector parabola during early May 1968. These data were processed on the RMS Best-Fit computer program to determine deviations from a true parabola after best fitting focal length changes. Each point on the dish surface was weighed in proportion to the actual surface area it represented. The contour maps were plotted using the SC-4020 plotter (SPS 37-40, Vol. IV, p. 176).

Six field readings were taken in sets of three on two different nights. The first three readings determined the 40-deg rms deviation, the zenith rms deviation, and then the hysteresis by remeasuring the 40-deg rms deviation that same night. Because of the need to have the antenna back in service, only one set of data could be taken. Also, wind conditions were not optimum since the winds varied from 15 mph early in the evening to 25 mph early in the morning at the conclusion of the measurements.

CONTOUR DEFINITIONS

1/2 RF PATHLENGTH ERROR, in.	LABEL
-0.090	A
-0.080	B
-0.070	C
-0.060	D
-0.050	E
-0.040	F
-0.030	G
-0.020	H
-0.010	I
0.000	J
0.010	K
0.020	L
0.030	M
0.040	N
0.050	O
0.060	P
0.070	Q
0.080	R
0.090	S

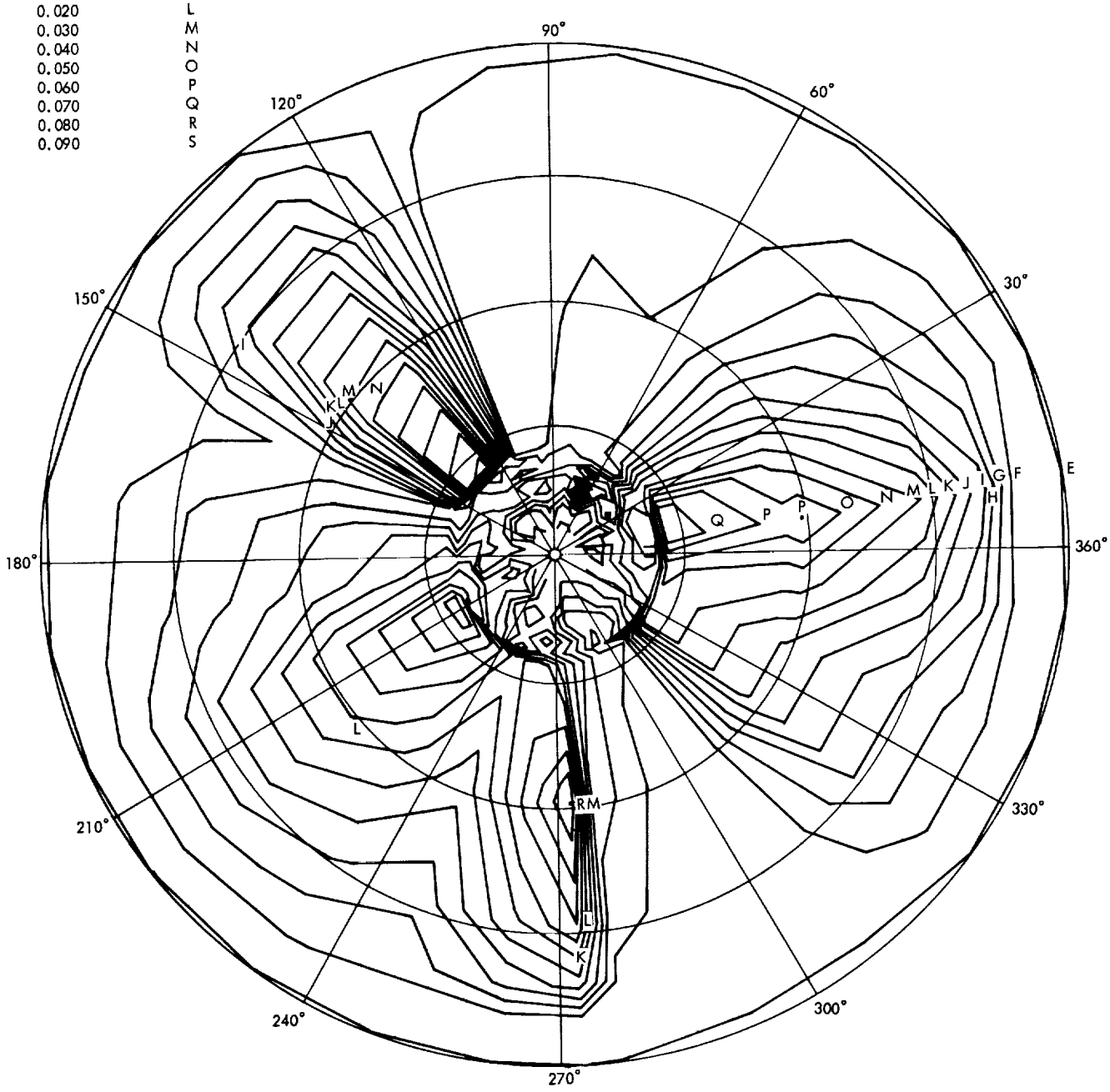

Fig. 86. Contour plot of 85-ft-diam az–el antenna field reading 2 (zenith position; focal length fit = 0.0253 in. rms)

CONTOUR DEFINITIONS

1/2 RF PATHLENGTH ERROR, in.	LABEL
-0.150	A
-0.140	B
-0.130	C
-0.120	D
-0.110	E
-0.100	F
-0.090	G
-0.080	H
-0.070	I
-0.060	J
-0.050	K
-0.040	L
-0.030	M
-0.020	N
-0.010	O
-0.000	P
0.010	Q
0.020	R
0.030	S

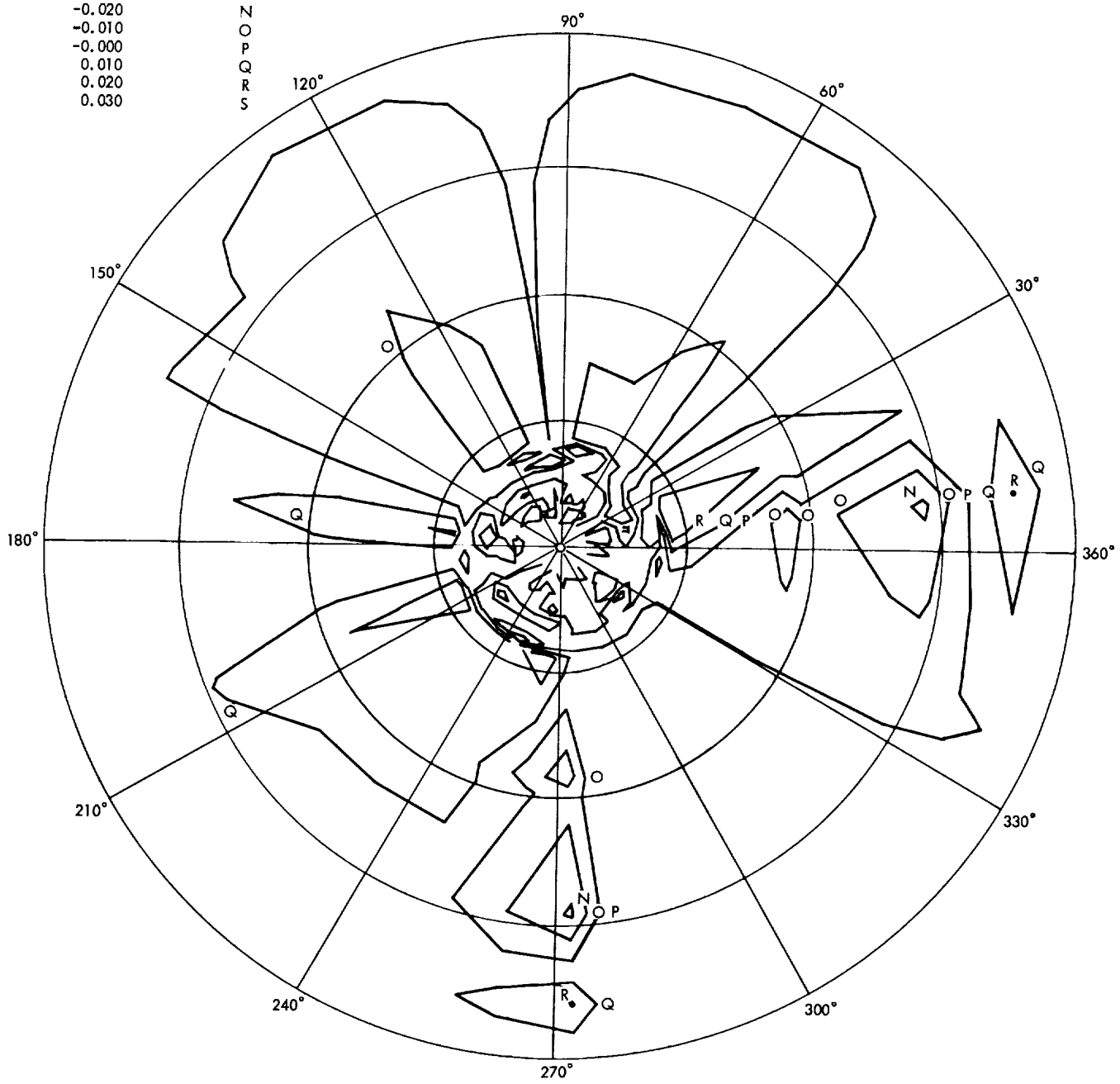

Fig. 87. Contour plot of 85-ft-diam az–el antenna field reading 4 (40-deg position; focal length fit = 0.0133 in. rms)

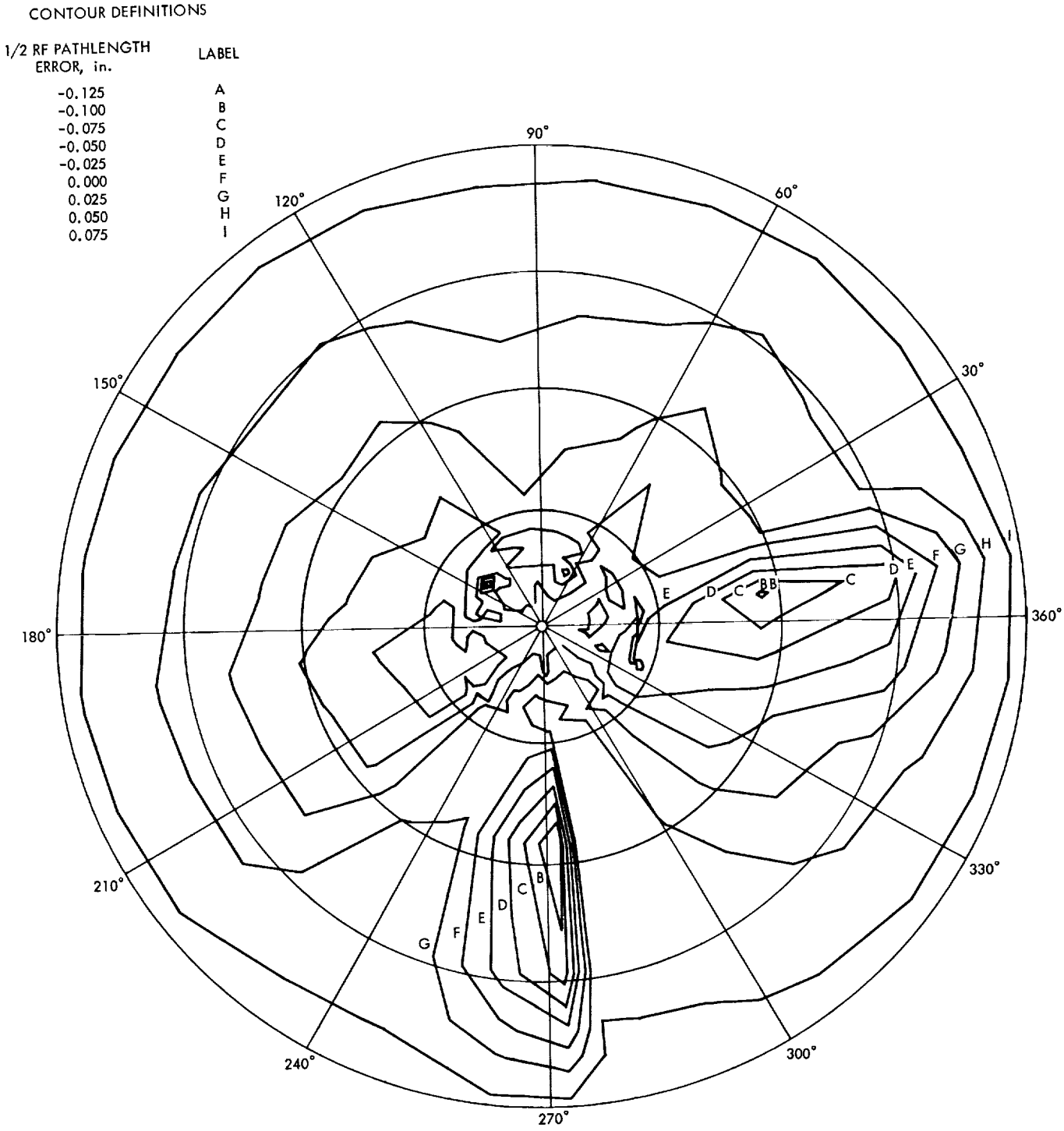

Fig. 88. Contour plot of 85-ft-diam az–el antenna field reading 5 (horizon position; focal length fit = 0.0263 in. rms)

The second set of three readings was taken a few nights later under similar conditions, except that the horizon position was used as the intermediate condition instead of the zenith. Table 21 summarizes the six readings. Figures 86–88 are contour plots for field readings 2, 4, and 5.

The hysteresis, as an rms value, can be evaluated by comparing Table 21 readings 1 to 3 and 3 to 4 (hysteresis after a two-day period) and 4 to 6. The average rms hysteresis value is 0.0018 in. This rms hysteresis value of 0.0018 in., compared to a previously measured rms hysteresis (SPS 37-47, Vol. II, pp. 115–121) of 0.005 in., shows a reduction in the rms hysteresis value by a factor of 2.8.

A more meaningful hysteresis comparison (since it relates directly to significant focal point movements, dish shape, and pointing) is actual dish deflection, with each point compared against each point. The compared average deflection is 0.007 in. (reading 1 compared to reading 3) versus 0.090 in. measured in February 1967 (SPS 37-47, Vol. II, pp. 115–121). This is a hysteresis reduction factor of almost 13.

The improvement in the rms deviation of the antenna, comparing the 40-deg position now used to the 45-deg position measured in the past, is 0.011 versus 0.35 in., an improvement factor of 3. The zenith rms deviation of 0.0253 in. can be compared to the past measured zenith rms deviation of 0.044 in., which is approximately an improvement factor of 2. The horizon rms deviation was not measured previously.

Table 21. Field measurements of reflector parabola focal length fit

Field reading	Antenna position, deg	Focal length fit, in. rms	Wind velocity, mph
1	40	0.0096	18
2	Zenith	0.0253	22
3	40	0.0114	25
4	40	0.0133	25
5	Horizon	0.0263	20
6	40	0.0116	22

Comparing the rms deviation obtained from the computer run based on a perfect parabola setting at 40-deg against the actual field measurements obtained with an rms-deviation setting of 0.011 in. at 40 deg gives the following:

Position	Computer value, in. rms	Actual value, in. rms	Difference, %
Horizon	0.0277	0.0263	5
Zenith	0.0276	0.0253	8

The overall dish rms deviation (including surface panel deviation) is now 0.018 in. (min) to 0.029 in. (max). This will certainly improve the antenna's performance at S- and X-band and will allow some possible K-band use.

IV. Development and Implementation

A. Space Flight Operations Facility

1. Communications Processor/7044 Redesign System Test Series, *R. G. Polansky*

a. Introduction. This is the third in a series of SPS articles describing tests being conducted to document the behavior of the communications processor (CP)/IBM 7044R system under various conditions. (See SPS 37-50, Vol. II, pp. 150–151; SPS 37-51, Vol. II, pp. 96–98.) The third and fourth tests have been completed. The objectives of these tests, the results obtained, and the CP statistics are documented in this article.

Test 4 will be the last test run for at least 2 mo. During this period, the 7044/CP system will be modified so that shortcomings observed during the test series can be minimized or eliminated. A test on the final system configuration will then be run to verify its performance.

b. Description of third test. The third test was run using a mode 2 SFOF hardware system (7044-disk-7094 combination) and the joint *Mariner* Venus 67/*Surveyor F* programming system. High-speed *Surveyor* data at rates of 137, 550, and 1100 bits/s, in addition to *Mariner* data at 33 bits/s, were input to the 7044 from the telemetry processing system (TPS). The objectives of this test were to determine:

(1) The effects of multimission processing in the 7044 on telemetry data displayed by the 7044/CP system.

(2) The effects of updating the CP's drum on 7044 and CP delays.

(3) The apportionment of total CP delay among the various CP activities.

(4) System behavior during recovery actions taken in the 7044 and CP systems.

The results obtained are compared with results obtained from the first two tests. Differences, if any, are attributable to the additional load of running two missions in the 7044/CP system as opposed to the one mission used in each of the first two tests.

c. Results of third test. No differences in system delays were noted by processing dual-mission data in the 7044 as compared with the single-mission processing previously done. Table 1 shows the system delays determined during this test. The CP-in-to-CP-out and 7044-input-to-CP-out delays shown include 2-s time bias, due to different clock sources being used. The exact value is unknown. In the next test, the clocks will be exactly synchronized at test start time.

The two CP drum updates attempted, each took about 2 s. No effects on system performance were noted during drum update. It is felt that this was not an adequate indication of what happens during a drum update, due

Table 1. System delays determined for test 3

Data type	7044-input-to-7044-out delay, s			CP-in-to-CP-out delay,[a] s			7044-input-to-CP-out delay, s		
	Av	High	Low	Av	High	Low	Av	High	Low
137 bits/s (*Surveyor*)	16.1	22	11	9.1	13	3	25.3	31	19
550 bits/s (*Surveyor*)	6.0	10	4	9.5	13	6	15.4	23	11
1100 bits/s (*Surveyor*)	4.6	9	3	8.2	12	5	12.6	17	9
33 bits/s (*Mariner*)	—	—	—	9.1	12	5	—	—	—

[a]Average = 9.1 s for CP-in-to-CP-out delay.

to the relatively low volume of traffic in the system. There were no means to exercise this function with heavy traffic.

The average delay between the time the data were available to the CP and the time they were written onto the CP drum was 6.47 s, which includes the 2s+ of time bias discussed above. If we assume this time bias to be 2.3 s (a reasonable number based on observations made during the test), the delay is 4.17 s. This figure includes the buffering delays in the 7044, the 7044/CP interface delays, and a 4-s timer[1] on the CP input.

The average delay between CP drum write and CP output is 2.52 s, once the backlog created by NASCOM and data header printing is eliminated. This is caused by the action of a 5-s software timer in the output interface of the CP.[2]

A backlog of data is generated on the CP drum, since data are processed for output by the 7044 concurrent with NASCOM header and data generation. The backlog is equivalent in time to the time it takes the CP to output the NASCOM and data headers to a 100-word/min output device. For *Mariner* headers, a maximum delay of 14 s has been observed. For *Surveyor* headers, a maximum delay of 21 s has been observed. This backlog diminishes with time, assuming that the steady-state duty cycle of the output to a given data printer is less than 100%. (It normally runs between 50 and 90%, depending on the data format being output.)

In the results of the second test (SPS 37-51, Vol. II, pp. 96–98), 7044/CP interface delays were discussed. The mechanics of this interface are now completely understood and are shown in Figs. 1a and 1b for messages sequentially generated to routing indicators JWAS, JWBS, ···, JWGS. Tables 2 and 3 give calculated and measured delays applicable to Figs. 1a and 1b, respectively.

During the third test, the *Surveyor* data rate was increased to the point that *Mariner* data were no longer output to the CP. This input saturation rate was 6500 bits/s, which corresponds to about 600 words/s at the 7044 input.

The first of four recovery actions attempted on the 7044/CP system was the 7044 internal restart. No unexpected results were observed. The sequence of events followed is listed below:

7044 operator	Internal restart 7044
Data chief	Select subchannels 3, 4, 5, and 6 as required
Data chief	Enter "process" messages
TPS operator	Enter data ID words
Data chief	Enter administrative printer mask
Data chief	Enter "assign" and "enable" commands as required
MSA[a] input/output operator	Re-enter all format requests
CP operator	No action required

[a]MSA = mission support area.

[1]All data traffic sent from the 7044 to the CP is loaded into pack areas. Each time data stops, a 4-s timer is set. If this timer expires before more data is received, the data in the pack area are written onto the drum.

[2]Once a path is established to a 100-word/min output device, all available data on drum for that device are sequentially transmitted to the device. If all available data have been transmitted and no more have been received, a 5-s timer is set. When the timer has expired, a check is made to see if more data have been received. If so, the data are transmitted to the device. If not, the timer is again reset to 5 s and the procedure is repeated. The average value of this delay should be 2.5 s, if the system is working as designed. (The observed time was 2.52 s.)

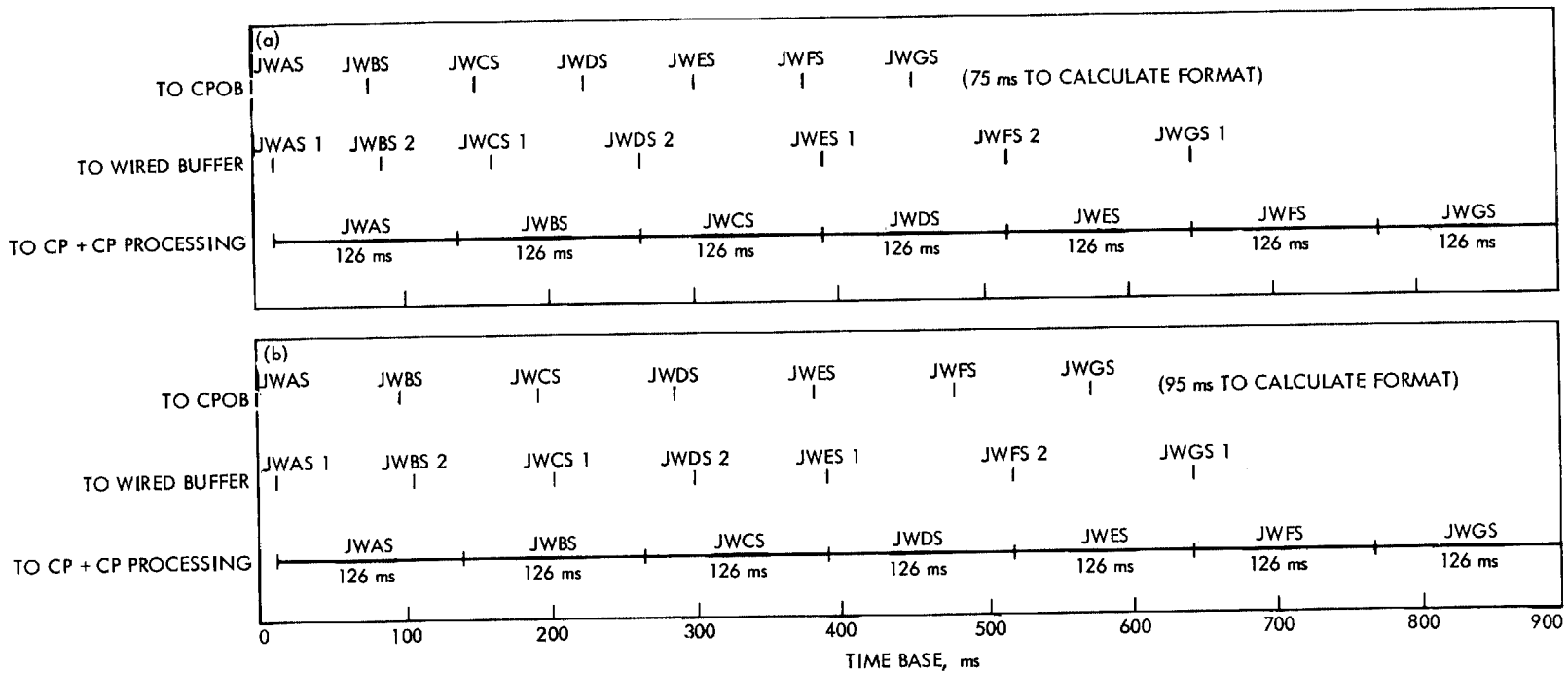

Fig. 1. Model of CP/7044 interface delays: (a) applicable at *Surveyor* data rates up to 1100 bits/s, (b) applicable only at *Surveyor* 4400-bits/s data rate

Table 2. Calculated and measured delays applicable to Fig. 1a

Routing indicator	Delay (CPOB → WB),[a] ms	
	Calculated	Measured
JWAS	10	10
JWBS	10	10
JWCS	10	10
JWDS	37	45
JWES	88	90
JWFS	139	140
JWGS	190	190

[a]CPOB = communications processor output buffer.
WB = wired buffer.

Table 3. Calculated and measured delays applicable to Fig. 1b

Routing indicator	Delay (CPOB → WB),[a] ms	
	Calculated	Measured
JWAS	10	10
JWBS	10	10
JWCS	10	10
JWDS	10	15
JWES	10	29
JWFS	39	56
JWGS	70	77

[a]CPOB = communications processor output buffer.
WB = wired buffer.

The receipt of the 7044 restart block by the CP automatically closed out all messages to 100-word/min data printers, causing a large number of simultaneous drum input/output requests in the CP. This number was equal to twice the number of TTY machines being driven by the 7044/CP system. The 7044 internal restart itself took 17 s, which is a representative time for such a recovery.

The second recovery action attempted was the 7044 cold restart. Again, the results were as expected. The sequence of events was the same as for the internal restart, except that the 7044 was newly loaded. This recovery took 52 s. All other observations were as noted for the internal restart.

The third recovery attempted was the 3-2 CP recovery. The sequence of events for this recovery is very critical, if 7044 data are not stopped first. Data were not stopped, and the sequence shown below was followed:

CP operator	Initiate 3-2 recovery from console
CP operator	Set 7044 in and on
CP operator	Enable RIT
Data chief	No action required

The recovery was successful and took 29 s. If the above sequence is violated, there is a high probability that the CP will fault. A safer way of doing the 3-2 recovery is to stop all data going into the CP first; however, this takes much more time, and formats and data must later be re-entered into the system.

A highly undesirable feature of the 3-2 recovery is the playback of up to the last 5 min of data received by the CP. For normal NASCOM traffic this is fine; however, the backlog of data from the 7044 can delay real-time data display 5 min per restart on a permanent basis, if the duty cycle of the data output is near 100%.

The fourth and last CP recovery attempt was the 3-1 recovery. Of three 3-1 recoveries attempted, only one was successful. After each of the unsuccessful ones, it was necessary to newly load the entire system from tape. It is conjectured that the system as written onto drum at initialization time for recovery purposes is not write/read verified. It has been observed that 3-1 recovery attempts have always had a low probability of success. This area should be investigated further.

d. CP statistics from third test. The maximum of 46 drum input/output requests was made, which corresponded to closing out active messages to all 23 teletype display teleprinters then being used with end-of-message characters after a recovery. As with the second test, a minimum of three timer list entries was needed for the CP in its idle condition. The maximum of 51 entries was used, which corresponded to timer list entries for the input (AA timer) and output (drum re-read timer) of each of the 24 teletype printers being exercised plus the three normal system timers. The maximum of 53 pack areas was used.

A maximum of 18 validation queue entries was made. This figure occurred when the 7044 discovered it had attained false sync with the *Mariner* data stream. The queue remained at a value of 16 for over 1 min until the 7044 regained true sync with the *Mariner* data. The reason for this is not understood.

The average "busy rate" of the CP was 8.4% during idle time and 30% during high-activity periods. The maximum busy rate of 88.8% occurred during predict

transmission to the CP at a time when all 25 possible teletype machines were being driven.

e. Description of fourth test. The fourth test was run using a mode 2 and a mode 3 SFOF system. Each system was configured for *Mariner* Venus 67 and *Surveyor F*. During the early part of the test, each system processed data from one mission. Later, the mode 3 7044 was turned back and both data streams were input to the mode 2 string. The objectives of this test were to determine:

(1) The effects of multimission data handling in the JPL CP for two cases:
   (a) One mission operating in each of two 7044s, and both 7044s outputting data through the CP.
   (b) Two missions operating in one 7044, and the 7044 outputting data through the CP.

(2) The effects of modifying internal CP timers on data processed and displayed by the 7044/CP system.

(3) The effects of removing the 100-ms timer installed in the 7044/CP interface.

(4) The effects of exercising the 3-1 and 3-2 recovery sequences in the CP, while both tracking and telemetry data are being routed.

f. Results of fourth test. As determined in test 3, no differences in system operation or delay times were noted in comparing the test 4 results with the single-mission results previously obtained. This was true for both cases tested (see objectives 1a and 1b, above). System delays for the two cases tested, along with calculated values for the same parameters, are shown in the first two columns of Table 4.

In the second phase of this test, both the AA timer and the drum re-read timer in the CP were reduced in value. This reduction had no apparent bad effects on CP operation. The busy rate remained about constant, but the CP throughput delay decreased as expected. The

Table 4. Average 7044/CP delays observed as a function of system configuration

Delay type	Delay, s								
	Surveyor mode 3 *Mariner* mode 2	*Surveyor* and *Mariner* in one mode 2							
	(4, 5)[a]	(4, 5)[a]	(3, 5)[a]	(2, 5)[a]	(1, 5)[a]	(1, 4)[a]	(1, 3)[a]	(1, 2)[a]	(1, 1)[a]
CP in → drum write (*Surveyor*)	4.4 4.4[b]	4.1 4.4[b]	3.9 3.4[b]	2.2 2.4[b]	1.5 1.4[b]	1.8 1.4[b]	1.3 1.4[b]	1.6 1.4[b]	1.1 1.4[b]
Drum write → CP out (*Surveyor*)	2.4 2.5[b]	2.6 2.5[b]	2.5 2.5[b]	2.7 2.5[b]	2.5 2.5[b]	2.3 2.0[b]	1.6 1.5[b]	1.2 1.0[b]	0.5 0.5[b]
Time tag → CP out (*Surveyor*)	23.7 23.5[b]	23.5 23.5[b]	24.0 22.5[b]	22.8 21.5[b]	20.8 20.5[b]	21.7 20.0[b]	20.8 19.5[b]	20.1 19.0[b]	19.0 18.5[b]
CP in → drum write (*Mariner*)	4.3 4.4[b]	4.1 4.4[b]	3.8 3.4[b]	2.2 2.4[b]	1.5 1.4[b]	1.8 1.4[b]	1.3 1.4[b]	1.2 1.4[b]	1.1 1.4[b]
Drum write → CP out (*Mariner*)	2.6 2.5[b]	2.8 2.5[b]	2.4 2.5[b]	2.4 2.5[b]	2.6 2.5[b]	1.8 2.0[b]	1.3 1.5[b]	0.7 1.0[b]	0.5 0.5[b]
CP in → CP out (*Surveyor*)	6.8 6.9[b]	6.7 6.9[b]	6.4 5.9[b]	4.9 4.9[b]	4.0 3.9[b]	4.1 3.4[b]	2.9 2.9[b]	2.8 2.4[b]	1.6 1.9[b]
CP in → CP out (*Mariner*)	6.9 6.9[b]	6.9 6.9[b]	6.2 5.9[b]	4.6 4.9[b]	4.1 3.9[b]	3.6 3.4[b]	2.6 2.9[b]	1.9 2.4[b]	1.6 1.9[b]

[a](X, Y) where X = value of AA timer in CP and Y = value of drum re-read timer in CP; all times are in seconds.
[b]Calculated values.

last seven columns in Table 4 show these delays, along with the calculated values for the same parameters.

In an abbreviated test with the 100 ms delay removed from the 7044/CP interface, the system performed as expected, and message segment frequency, during maximum interface activity periods, was increased by a factor of four. The test showed that the original reason for the delay's insertion no longer exists.

In SPS 37-51, Vol. II, pp. 96–98, it was stated that the 7.9-s 7044 delay of telemetry data was a worst-case condition during predict transmission. This statement was not true. In test 4, a larger block of predicts was transmitted to the CP. The 7044 delay at its output interface increased to a maximum of 14.5 s. This figure would be even higher if the *Mariner* data rate had been 8⅓ instead of 33⅓ bits/s.

Several 3-2 and 3-1 recoveries on the CP were attempted on the CP. Telemetry and tracking data were not stopped during these attempts. The following observations were made:

(1) The STOP ALL message from the 7044 was not necessary during the recoveries.

(2) During all 3-2 recovery attempts, the CP and 7044 ran into accounting problems with the tracking data. It appeared that the CP was recycling message numbers for these data and causing the data to go to intercept. The program is not supposed to operate in this manner.

(3) As before, only one of three 3-1 recoveries was even partially successful. A reload was required in two cases. In the partially successful recovery, the written procedure was followed; however, the operator had to perform a number of extra manual operations to get the system completely back to operational status.

It was observed that a given 7044 can output data to up to 50 data sinks through the CP; however, the CP is incapable of routing these data to more than 25 machines due to the length of a queuing list in the machine.

g. CP statistics from fourth test. The maximum of 25 simultaneous drum input/output requests was made. Had all the conditions been exactly *wrong*, this number could have been as high as 56. The maximum of 62 timer list entries was used. This number could have been as high as 65 for the configuration used. The maximum of 56 pack areas was used, and the maximum of 13 validation queue entries was made.

During high-activity periods, the busy rate averaged 30%. The maximum rate of 90% occurred during predict transmission.

B. Deep Space Instrumentation Facility

1. Venus DSS Activities, *E. B. Jackson, M. A. Gregg, and A. L. Price*

a. Experimentation. The 30-ft-diam antenna continued to be used for transmission of time synchronization signals at 8.45 GHz and for radiometric observations of the planet Venus at 23 GHz. Successful planetary radar operations were resumed with good total spectrum returns being received from the planets Venus and Mercury in both monostatic and bistatic modes of operation. Figure 2 illustrates the typical monostatic return, and Fig. 3 illustrates the typical bistatic return. The improvement in signal-to-noise ratio generated by the additional 8-dB gain of the 210-ft-diam antenna for receiving is clearly seen.

Taking advantage of an opportunity which only occurs every 19 yr, the 85-ft-diam antenna and the 450-kW transmitter were used to transmit radar signals to the asteroid Icarus. Closest approach of 6,353,270 km was predicted to occur at approximately 2058Z on June 14, 1968. At that time, assuming an asteroid diameter of 1 km and a radar reflectivity at 2388 MHz of 100%, the received signal strength, using the 210-ft-diam antenna at the Mars DSS, would have been approximately −181 dBm. Complete results from this mission are not available at this time. Preliminary data indicate that the actual received signal strength was −187 dBm.

b. Subsystem performance. The Venus DSS S-band 2388-MHz receiver provides one phase-locked channel and two open-loop channels. In addition, the special 455-kHz loop in the receiver can provide some phase-locked information when operating in the open-loop mode. The receiver still retains the capability of accepting 455-kHz signals, via the microwave link, from either of the two R&D receivers at the Mars DSS when operating in the bistatic mode.

The 8448-MHz X-band receiver continues to serve as an X-band transmitter output and modulation monitor in the time synchronization experiment. The operation of the transmitter phase modulator was checked during this reporting period. The carrier power suppression was

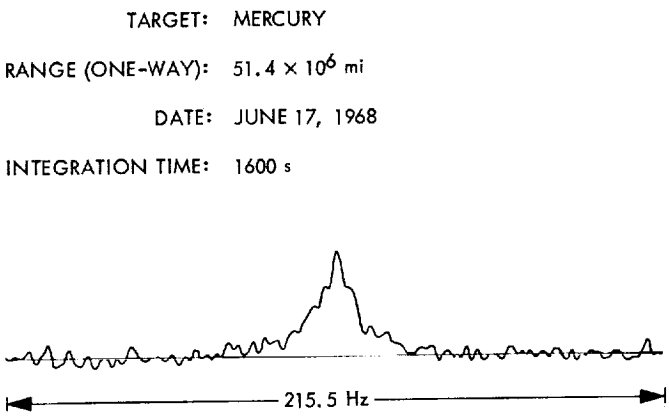

Fig. 2. Power density spectrum for monostatic planetary radar operation

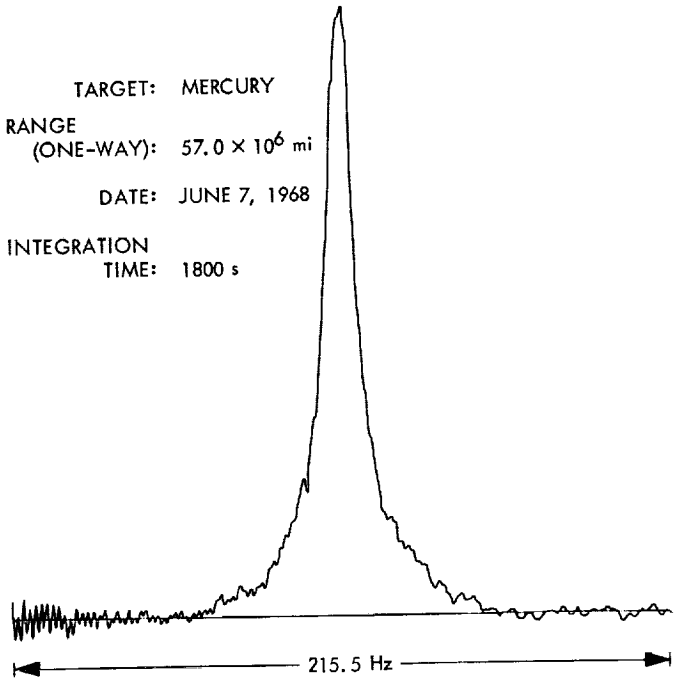

Fig. 3. Power density spectrum for bistatic planetary radar operation

measured to be greater than 40 dB, which represents only a small change from that measured several months ago.

Because of continuing problems in the programmed local oscillator, the tape reader has been replaced with another reader until repairs can be accomplished.

At the present time, the Venus DSS 2295-MHz receiver is disabled pending the arrival of the 2295- to 30-MHz converter, which is still mounted in the feed cone at the mars DSS.

c. System improvements

Receiving systems. A cone test area is being set up on the southeast side of Building G-60. This will allow operation and testing of the maser as well as all other cone-mounted receiving equipment. Complete control and instrumentation capabilities for the maser will be available in a laboratory directly adjacent to this area.

S-band transmitting systems. The cooling water plumbing to the antenna and high-power test area was modified utilizing 6-in.-diam fiberglass pipe with 4-in. rotary joints at the elevation axis. New manifolds were fabricated from the 6-in. pipes for the test area and underneath the electronics room. A complete new platform was fabricated and mounted on the antenna to support the antenna pump and filters for the lines which will supply 400 gal/min of cooling water.

All associated equipment of the transmitter needed for full operation (i.e., waveguide switch, waveguide-to-cone, water-load monitor components, water load, nitrogen pressure regulator, and exciter antenna box and power supplies) was installed in the electronics room. New cable trays were installed under the electronics room, and cables in the wrap-up were re-routed.

A water-to-water heat exchanger and pump with associated flow indicators was installed on the antenna for cooling the cone waveguide and feed system.

2. Monitor System (Phase I) Monitor Criteria Data,

R. M. Thomas

The monitoring of performance, configuration, and status for the DSS and its subsystems requires monitor criteria data (MCD). In order that MCD be generated, accessed, and used in the most efficient way, MCD are developed in sets of approximately 269 parameters per set. Each set corresponds to a particular DSS and its subsystem configuration, subsystem status, and the operational phase of the mission. This consists of DSIF switch configurations, subsystem status, DSN and DSIF tolerances, and alarm conditions. Presently, the monitor system (phase I) software design could (if necessary) make use of a maximum of 500 MCD sets. For example, *Surveyor* used the equivalent of 15 MCD sets. *Mariner* Mars 1969 will be the first mission to make use of MCD sets.

These data are generated in the SFOF and put on a magnetic tape, which is shipped to the DSS. Upon arrival at the DSS, a tape-to-tape program will take the MCD parameters from the magnetic tape and put them on a dual cartridge magnetic tape recorder (Mag Pak). The desired set is then selected and called into working memory by the DSS computer operator. Accessing any parameter(s) of a given set is accomplished by utilizing the format discussed later in this article. Each DSS will only have *one* nonstandard MCD set. A nonstandard set is defined as the set that was called into auxiliary core, modified, and is currently being used in working core (memory). A capability exists for changing 32 critical MCD parameters in real time.

Either the SFOF or DSS operator can change these 32 parameters as follows, but in either case the DSS operator must put the modified set in working core if it is going to be used. The DSS operator will be able to: (1) take an MCD set from the magnetic pack and put it in working core, (2) take the MCD set in auxiliary core and put it in working core, and (3) change any one or all of the 32 critical MCD parameters in working core. The SFOF will be able to do the following in real time: (1) call an MCD set from the Mag Pak and place it in auxiliary core and modify the MCD set, (2) modify the existing MCD set in auxiliary core, and (3) define a new MCD set, transmit it to the DSS, and place it in auxiliary core. The DSS and SFOF capabilities explained above can be represented diagramatically (Figs. 4 and 5).

When generating the MCD to be put on magnetic tape (from the disk file) by a 7094 computer program, only one MCD parameter is placed on each card. Hence, the sets of desired MCD parameters are punched on cards, read by a card reader, and placed on magnetic tape by the 7094 program. These tapes will have a two-fold purpose: (1) the tapes will serve as a master record MMCD (master monitor criteria data) file, and (2) a direct copy will be shipped to the DSS for use as previously discussed.

SFOF real-time MCD updating can be accomplished from either disk (mode 2) or magnetic tape (mode 4). In mode 2, the 7044 requests the MCD from the 7094, which in return gets the MCD from the disk file and gives it back to the 7044 and then to the TTY for transmission to the station. Using mode 4, the 7094 puts the MCD on tape, and the tape is physically transported to the 7044 and peripheral equipment for accessing and transmitting to the station by TTY via the 7044. Generally, mode 4 will be used. The user (in mode 2 or 4) will ask that a message be prepared and transmitted via the 7044

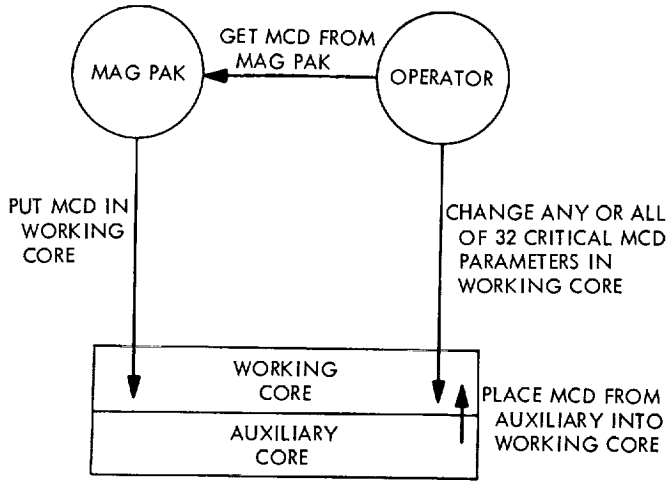

Fig. 4. DSS MCD capabilities

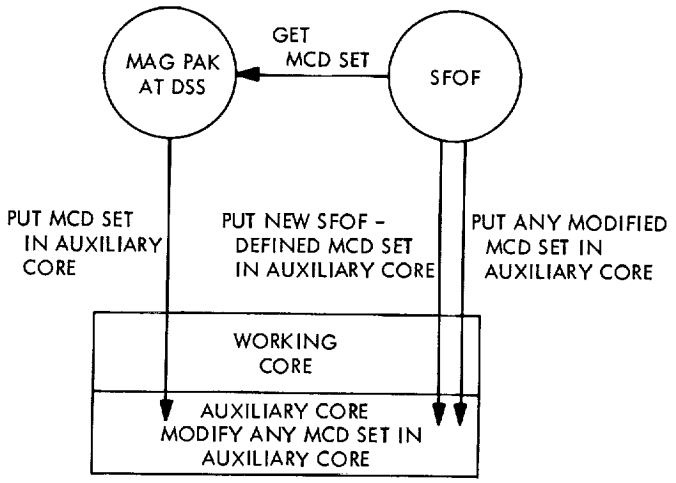

Fig. 5. SFOF MCD capabilities

by TTY to the digital instrumentation subsystem (DIS). The MCD address structure aids in accessing and modifying of any parameter(s) of any set. This address structure consists of set, subset, parameter address, computer word, bit position, parameter value, condition, and format. To change any MCD parameter, the SFOF operator would input the set, subset, parameter address, and parameter value.

A typical set of MCD would consist of:

(1) Configuration (DSIF switch positions) and subsystem status parameters for microwave, transmitter, receivers 1 and 2, doppler (1-, 2-, and 3-way), angle (hour angle and declination), ranging, subcarrier demodulator assembly (SDA 1, 2, 3, and 4), telemetry and command processor (TCP 1 and 2), and the automatic data switching systems α and β.

(2) Tolerances and nominal (expected) values are also contained in each set for the transmitter receiver, automatic gain control/static phase error, doppler (1-, 2-, and 3-way), angle (hour angle and declination), ranging, TCP, SDA, DIS, RF, and telemetry predicts.

3. DSIF/Ground Communications Interface Assembly,

E. Garcia

a. Introduction. Previous articles (SPS 37-50, Vol. II, pp. 168–172, and SPS 37-51, Vol. II, pp. 100–104) have presented the DSIF/ground communications interface assembly (DGI) functional requirements, theory of operation, implementation plans, and a detailed description of the DGI buffer cabinet assembly. This article presents a description of the DGI buffer assembly new module development.

Four new module types are being developed, in order to meet functional and interface requirements of the DGI and external interfacing subsystems. The new modules are being constructed with enough flexibility and to the same mechanical and electrical specifications of the Hi-Rel module line such that they may be used in future projects.

b. Level converter. The level converter (LC-33) module has been developed to meet the interface requirement to drive other assemblies with bipolar signals. The LC-33 module contains six identical interface circuits. Each unit is designed to condition a unipolar logic input level and produce a bipolar logic output level. The units are designed by Dynamics Instrumentation Co., and use high reliability components that have been burned-in for 168 h.

The level converter electrical characteristics per circuit are as follows:

Power input	+12 Vdc ±10% at 15 mA −12 Vdc ±10% at 15 mA
Signal input	0 to +25 Vdc maximum at 0.5 mA or less; threshold of +4.0 ±0.5 V
Signal output	+6 ±0.5 to −6. ±0.5 Vdc; short-circuit proof
Output impedance	100 Ω or less
Rise and fall time	1 μs or less
Input/output logic	+4.5 V or greater input produces +6-V output; +3.5 V or less produces −6-V output

c. Signal generator. The signal generator (SG-270) module has been developed to meet the *Mariner* Mars 1969 270-Hz telemetry bit rate, for use as a DGI-simulated output data clock. The SG-270 module contains one sealed can-type module manufactured by CTS Knight Corp. The basic crystal oscillator is cut for a frequency of 2.7 MHz. By use of integrated circuits, four output frequencies are brought out. All components are burned-in for 168 h at +125°C and are chosen from the JPL Hi-Rel Preferred Parts List.

The signal generator electrical characteristics are as follows:

Power input	+12 Vdc ±10% at 2.5 mA −12 Vdc ±10% at 2.5 mA
Signal output	270,000 Hz at 0 to +5 ±0.5 Vdc squarewave 27,000 Hz at 0 to +5 ±0.5 Vdc squarewave 2700 Hz at 0 to +5 ±0.5 Vdc squarewave 270 Hz at 0 to +12 Vdc ±10% squarewave
Frequency stability	±50 parts per million; after initial stabilization period, frequency is 3 parts in 10^8 per day for one yr
Output wave shape	50 ±2% duty cycle with a bit width distortion of ±1% or less

d. Shift register and word detector. The shift register (SR-33) and word detector (WD-33) modules have been developed to meet the DGI requirement for a hardware 24-bit word sync detection capability. The DGI sync word detection function is mechanized using three SR-33s, eight bit shift register modules, and one word detector module. The function performed is that of comparing a serial bit stream every bit time (sample rate of 1 MHz) to a predetermined bit pattern configuration of 24 bits. A correlation output signal is provided out of the WD-33 module, whenever the input serial bit stream correlates to within 0, 1, 2, or 3 preprogrammed allowable random errors of the 24-bit pattern configuration.

These two basic-type modules are being manufactured by Space General Corp., and make use of discrete and integrated circuit components. All components employed are chosen from the JPL Preferred Parts List and undergo a 168-h burn at +125°C in screening tests.

Shift register. The shift register module contains an 8-bit shift register, eight clocked *nand* gates, and eight wired *or nand* gates. The module is designed to perform five basic functions by means of jumper wires: (1) serial input/parallel output, (2) parallel input/serial output, (3) serial input/clocked parallel output, (4) clocked parallel input/serial output, and (5) preset 8-bit word generator. Its electrical characteristics are:

Input power	+12 Vdc ±10% at 15 mA
Parallel input	0 to +12 ±3 Vdc input (type I) 0 to +5 ±1 Vdc input (type II)
Serial input	0 to +5 ±1 Vdc
Serial output	0 to +5 ±1 Vdc
Ored nand output	0 to +5 ±1 Vdc
Clock input	0 to +5 ±1 Vdc; squarewave up to 3 MHz
Parallel output	Clocked 0 to +5 ±1 Vdc Direct 0 to +5 ±1 Vdc

Word detector. This module was designed as a special-purpose module containing all logic elements required to complement any number of SR-33 modules interconnected as a word pattern correlator. Thus, it contains the necessary input data clock-sample clock synchronization circuit, SR-33 shift clock amplifiers, start-stop 2-bit shift register, 3-bit decimal counter, and 3-bit decimal comparator. Its uses as part of the standard Hi-Rel line are limited; however, this limitation was accepted in order to make the SR-33 module more versatile. The word detector electrical characteristics are:

Power input	+12 Vdc ±10% at 30 mA
Data clock input (f_d)	0 to +12 ±3 Vdc squarewave; 50 ±2% duty cycle
Sample clock input (f_s)	0 to +12 ±3 Vdc squarewave; 50 ±2% duty cycle
Word detection $\Delta f = (f_s - f_d)$	Δf minimum must equal in Hz the number of bits in word input plus 2 cycles for start-stop
2-bit shift register input	0 to +5 ±0.5 Vdc
3-bit decimal comparator input	0 to +5 ±0.5 Vdc for each line; only one line at +5 Vdc at a time for correct comparison
Clock amplifier output	0 to +5 ±0.5 Vdc at 30 mA

4. DSIF Station Control and Data Equipment,

E. Bann, A. T. Burke, J. K. Woo, and P. C. Harrison

a. Antenna pointing subsystem phase I. The antenna pointing subsystem (APS) has been implemented in the DSIF stations to provide the capability of pointing the station antennas under computer control. Descriptions of the interim APS and the APS phase I (APS-I) have been given in previous issues of SPS, Vol. II.

Acceptance testing of APS interface (API) racks is essentially complete, and API units have been accepted for all station commitments at the Echo, Woomera, Tidbinbilla, Johannesburg, Robledo, and Cebreros DSSs.

Installation of APS-I is being accomplished in three steps: (1) first the SDS 910 computer is separated from its digital instrumentation subsystem (DIS) phase I configuration and retrofitted to a standard SDS 910 computer, (2) the API rack is then connected to the SDS 910 computer and an APS-I diagnostic is performed to ensure correct operation at the unit level, and (3) finally, the station system cables are installed and testing is completed with APS-I in its operational configuration utilizing its operational program. Steps 1 and 2 have been completed at the Echo and Johannesburg DSSs and will be completed at the Woomera and Cebreros DSSs by the end of July 1968. The installation at the Tidbinbilla and Robledo DSSs does not include Step 1, since the DISs are not being updated at this time.

b. Telemetry and command processor phase II. The Telemetry and Command Processor Phase II (TCP-II) provides the DSIF with a mission-independent telemetry and command processing capability for real-time operation. The TCP-II is in the process of expansion (TCP-II-C) to increase the telemetry processing capability to support the DSIF multiple-mission telemetry system.

The installation of the TCP-II-C equipment is proceeding on schedule at the DSSs. Installation and checkout has been completed at the Echo, Cape Kennedy, and Johannesburg DSSs and is currently in process at the Cebreros DSS. The TCP-II-C equipment has been shipped to the Woomera DSS.

The necessary equipment to implement the changeover from a 60-wpm teletype operation to a 100-wpm operation has been supplied to all DSSs.

c. Frequency and timing subsystem phase II. The frequency and timing subsystem phase II (FTS-II) was

subjected to a design review and was accepted as presented. Evaluation of the FTS-II prototype is continuing at the contractor's facility with the resultant logic pulse jitter maximum of 10 ns with respect to the selected frequency source.

Assembly of the production equipment is underway and the preliminary testing of some of the subassemblies has been accomplished.

5. Echo DSS Reconfiguration, *F. M. Schiffman*

a. Introduction. The Echo DSS is the first DSIF station to start the engineering modification and upgrade (reconfiguration) in support of future spacecraft missions such as *Mariner* Mars 1969. The Echo DSS reconfiguration was started in early February 1968 and is expected to be completed by mid-July 1968. A series of station integration tests are scheduled to validate system, subsystem, and equipment reconfiguration.

b. Objectives. The objectives of the Echo DSS reconfiguration are:

(1) To provide required support capability for the *Mariner* Mars 1969 mission (primary objective).

(2) To implement a number of subsystem modifications, other than those required for the *Mariner* Mars 1969 mission.

(3) To perform the equipment maintenance heretofore precluded by station mission support assignments.

(4) To facilitate and complete subsystem transfer agreements from engineering to operations.

(5) To configure each of the effected stations consistent with the Goldstone-duplicate-standard concept.

c. Modification phases. The Echo DSS reconfiguration included five distinct modification phases, which were:

(1) Antenna teardown: removal of antenna mounted equipment, cables, and water lines.

(2) Control room teardown: removal and inspection of cables and equipment.

(3) Antenna rebuilding: re-installation of cables and trays, equipment, hydraulic and water lines, and addition of new declination room and equipment.

(4) Control room rebuilding: re-installation of new and old cables, modification and relocation of equipment, and addition of cable trays.

(5) Station integration testing: verification that the station is configured and functions as specified.

d. Subsystem modifications. Eight subsystems required modification during the Echo DSS reconfiguration as follows:

Subsystem	Modification
Antenna mechanical	Upgrade hydraulic drive
	Upgrade hour angle and declination drive skids
	Thicken structure of support members
	Rebolt
	Limit polar wheel travel (±89 to ±105 deg)
	Add new cable wrapups
	Resurface and align dish
	Adjust limit switch and optical tracking aid
	Add declination room
Telemetry command processor	Remove existing 8k core memory and install 16k core
	Add analog equipment rack and cables
Digital instrumentation	Remove SDS 910 computer
	Modify rate selection and period register
	Increase core from 8 to 16k
	Add magnetic pack
	Add communications buffer
Receiver III-C	Install subcarrier demodulator
	Install analog-to-digital converters
	Install digital phase shifters
Demultiplexer	Install new demultiplexer
Simulator I	Install new simulator I

e. Control room layout. Figure 6 illustrates the reconfigured Echo DSS control room layout.

FOLDOUT FRAME 1

FOLDOUT FRAME 2

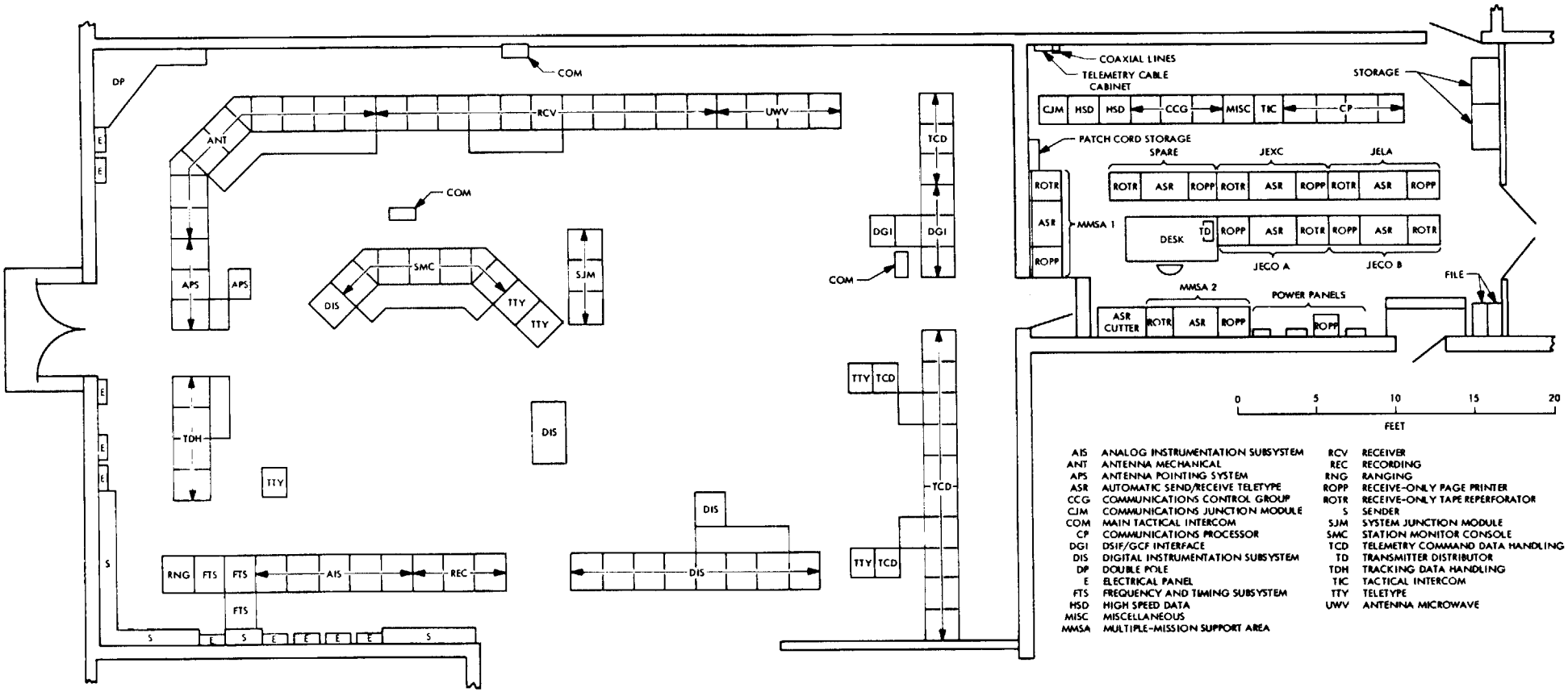

AIS	ANALOG INSTRUMENTATION SUBSYSTEM	RCV	RECEIVER
ANT	ANTENNA MECHANICAL	REC	RECORDING
APS	ANTENNA POINTING SYSTEM	RNG	RANGING
ASR	AUTOMATIC SEND/RECEIVE TELETYPE	ROPP	RECEIVE-ONLY PAGE PRINTER
CCG	COMMUNICATIONS CONTROL GROUP	ROTR	RECEIVE-ONLY TAPE REPERFORATOR
CJM	COMMUNICATIONS JUNCTION MODULE	S	SENDER
COM	MAIN TACTICAL INTERCOM	SJM	SYSTEM JUNCTION MODULE
CP	COMMUNICATIONS PROCESSOR	SMC	STATION MONITOR CONSOLE
DGI	DSIF/GCF INTERFACE	TCD	TELEMETRY COMMAND DATA HANDLING
DIS	DIGITAL INSTRUMENTATION SUBSYSTEM	TD	TRANSMITTER DISTRIBUTOR
DP	DOUBLE POLE	TDH	TRACKING DATA HANDLING
E	ELECTRICAL PANEL	TIC	TACTICAL INTERCOM
FTS	FREQUENCY AND TIMING SUBSYSTEM	TTY	TELETYPE
HSD	HIGH SPEED DATA	UWV	ANTENNA MICROWAVE
MISC	MISCELLANEOUS		
MMSA	MULTIPLE-MISSION SUPPORT AREA		

Fig. 6. Echo DSS control room layout

C. DSN Systems and Projects

1. MMTS: Installation and Testing, W. C. Frey

a. Introduction. Installation of the multiple-mission telemetry system (MMTS) includes verifying proper operation of: (1) the subcarrier demodulator assemblies (SDAs), two of which are required per station; (2) the MMTS test rack; and (3) the telemetry command processor (TCP) in the phase II-C configuration, including the digital phase shifters. In addition, all MMTS functional interfaces are checked between the SDAs and the TCP, the SDAs and the digital instrumentation subsystem (DIS), and between the TCP and the DIS. Functional interfaces are verified using MMTS project-supplied software operating in the DIS and TCP computers.

Testing of the MMTS equipment is accomplished in three phases: (1) checkout of the computer and digital equipment with MMTS demonstration software; (2) testing of the SDA, combined with the computer and digital equipment, with test signals input through the SDA up-converter; and (3) checkout of the SDA combined with the computer and digital equipment, with signals from the receiver applied to the 10-MHz telemetry input of the SDA.

b. Computer and digital equipment tests. In order to evaluate the computer and digital equipment performance, the MMTS demonstration software has been modified to operate in the TCP phase II-C equipment configuration. The software performs the bit synchronization and detection functions. The program outputs bit error rate and an estimate of signal-to-noise ratio. The demonstration software has been implemented as an MMTS test program in the DSN. A test signal input of an integrated PN data stream, with noise added, was provided to the analog-to-digital converter input of the TCP. The input signal-to-noise ratio was calibrated, using the signal-to-noise ratio estimator (SNORE) program in the TCP. The SNORE program has also been modified to be compatible with the TCP phase II-C. The SNORE program runs with hard-wired bit sync and detection and provides an excellent reference for the input signal-to-noise ratio of test signals supplied to the TCP.

The MMTS demonstration program performance was then compared to the SNORE program. The output of the demonstration program of bit error rate and signal-to-noise ratio indicated performance agreement with the SNORE reference within 0.1 dB at all stations; thus, the bit sync and detection functions performance were verified as operating properly in the TCP phase II-C configuration. The tests were run at ST_B/N_0 of 5.2 dB at 270 bits/s.

c. SDA/TCP phase II-C up-converter tests. Tests were conducted using the baseband input (up-converter) of the SDA to verify performance of the SDA and its operation in conjunction with the demonstration software in the TCP phase II-C. The up-converter input consisted of a PN data stream modulating a subcarrier, with noise added. The performance of the system was measured by the signal-to-noise ratio estimate of the MMTS demonstration software located in the TCP. The following data were obtained for the JPL compatibility test area and are typical for all stations:

Test	Bit rate, bits/s	Subcarrier frequency, kHz	Up-converter input ST_B/N_0, dB	Measured ST_B/N_0 by demonstration software, dB
1	270	34	5.2	4.62
2	270	34	−1.0	−1.48
3	66.66	34	5.2	4.61
4	33.33	24	5.2	4.48
5	8.33	24	5.2	4.32

The degradations encountered in this test mode are primarily due to the uncertainty of the calibration of the signal-to-noise mixer and to dynamic range limitations of the up-converter. The test data taken at the stations are within the + and − 1-dB tolerance allowed in setting up the signal-to-noise ratio.

d. System tests. System testing involved use of the receiver 10-MHz telemetry output as a signal source for the MMTS equipment. The telemetry modulation input of the test transmitter was used as input for a subcarrier modulated with data test signal input. Signal-to-noise ratio in the carrier tracking loop was measured for a calibration of input ST_B/N_0.

The MMTS demonstration program was used to measure system performance. Results of these tests indicate that MMTS performance is within specifications after the known degradations of the receiver and the MMTS equipment have been introduced into the resultant data. Additional reporting on the system tests will be presented in a future SPS article.

e. DSS implementation. Installation and checkout of the new MMTS have been completed on schedule at the compatibility test area, as well as at the Echo, Cape Kennedy, Johannesburg, Cebreros, and Woomera DSSs. Installation and checkout of the new MMTS at the Mars DSS is scheduled to begin in early September. The Tidbinbilla and Robledo DSSs will be provided with MMTS in February 1969.

2. MMTS: SDA/Receiver–Exciter Interface, *J. H. Wilcher*

a. Introduction. The installation of the subcarrier demodulator assemblies (SDAs) as part of the receiver–exciter subsystem requires that portions of the receiver–exciter be modified to interface with the SDAs.

b. Receiver–exciter modifications. Each SDA requires the following signals from the receiver–exciter subsystem:

Function	Level
10-MHz reference	10 dBm
10-MHz IF (receiver 1)	−66 dBm
10-MHz IF (receiver 2)	−66 dBm
5-MHz reference	10 dBm
Switching	28 Vdc
Lamp	24 Vdc

Since the number of SDAs which will be interfaced with the receiver–exciter varies from one to four, the SDA/receiver–exciter modification kits were designed to handle four SDAs at all sites.

Four unused 10-MHz reference signals were available at cabinet 8 of the receiver–exciter for use with the

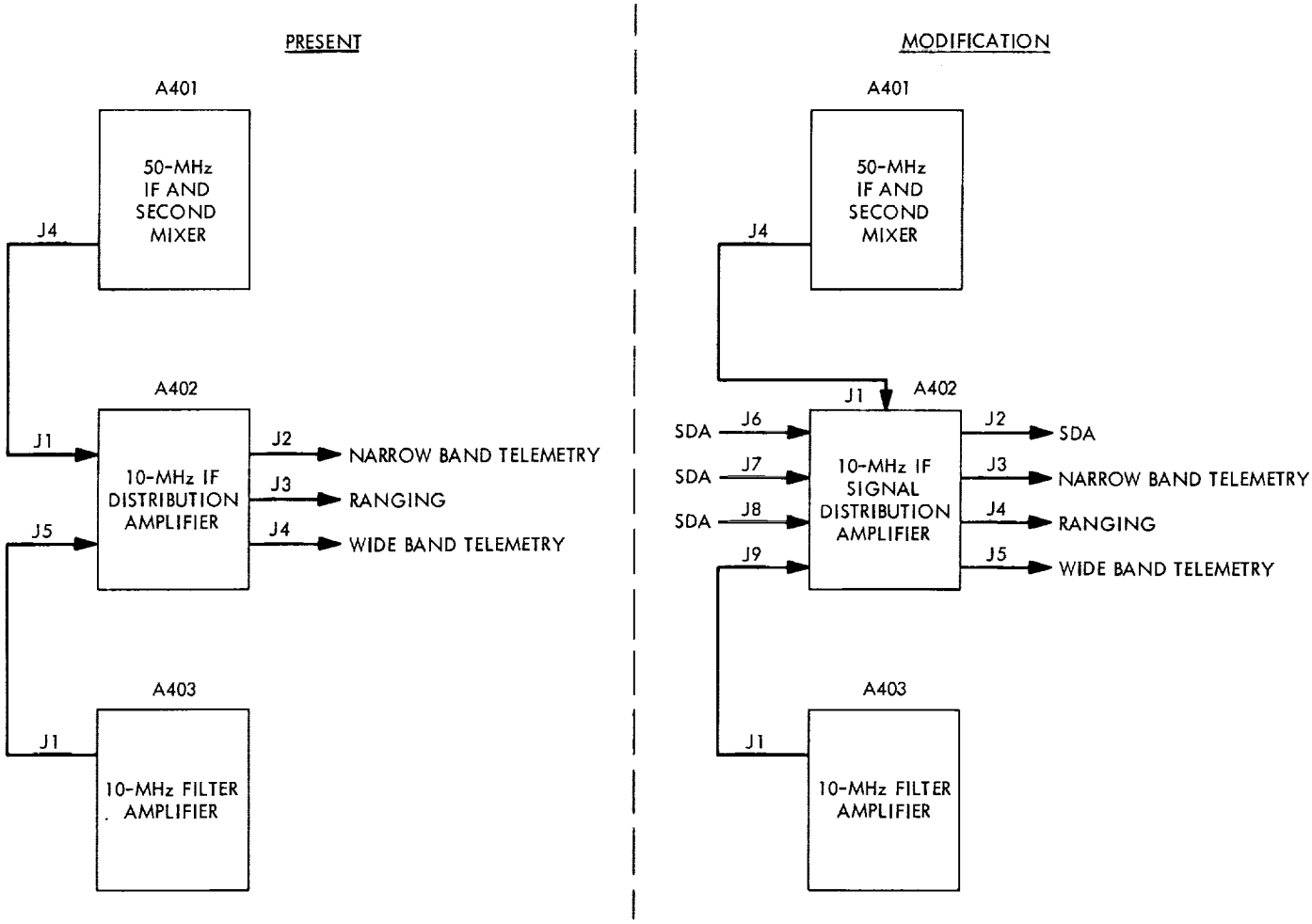

Fig. 7. SDA/receiver–exciter functional interface (cabinets 5 and 8)

SDAs. These signals were made available at the cabinet 8 interface plate.

No additional 10-MHz IF signal outputs were available from either receiver, so a new 10-MHz IF signal distribution amplifier was constructed (SPS 37-51, Vol. II, pp. 116 and 117) to provide the additional required outputs. This module was constructed so that it could physically replace the present 10-MHz IF signal distribution amplifier (Fig. 7). These units will be installed in both receivers 1 and 2 (cabinets 5 and 8).

The 5-MHz reference signal was to be utilized only by the receiver–exciter synthesizer, and no distribution of this signal was previously made. In order to furnish signals to the SDAs, a 5-MHz distribution amplifier, similar in construction to the 10-MHz IF signal distribution amplifier, was constructed and will be installed in a previously unused module location of the receiver–exciter (cabinet 4). The 5-MHz signal from the frequency and timing subsystem (FTS) will be distributed to the receiver–exciter synthesizer and to the SDAs from this module (Fig. 8).

The +28-Vdc switching supply voltage and the +24-Vdc lamp supply voltage were made available on multipin connectors at an interface plate located at the rear of receiver–exciter cabinet 7.

3. MMTS: Bit-Sync Loop Lock Detector, *J. W. Layland, N. A. Burow, and A. Vaisnys*

a. Introduction. A preliminary study of the signal-to-noise ratio (SNR) estimator as a lock indicator for a bit-sync loop was presented in SPS 37-48, Vol. III, pp. 209–212, which showed feasibility and presented some approximate formulas, valid for strong SNR, on which to base a preliminary design. Since that time, a considerable amount of experimental data on the SNR estimator has been accumulated. This article presents those data, together with a more accurate analytical approximation to the SNR estimator in an out-of-lock condition, and describes the zone-threshold lock indicator adopted for the final version of the MMTS demonstration software system.

b. The SNR estimator. Let I_i denote the integral of the received demodulated signal over the ith bit period. The sign of I_i is used as the ith received data bit. The SNR estimate $\hat{R}$ is constructed from the N most recent I_i as

$$\hat{R}_m = \frac{\frac{1}{2}\left(\frac{1}{N}\sum_{i=1}^{N} |I_{m+1-i}|\right)^2}{\frac{1}{N-1}\sum_{i=1}^{N}\left(|I_{m+1-i}| - \frac{1}{N}\sum_{j=1}^{N}|I_{m+1-j}|\right)^2} \quad (1)$$

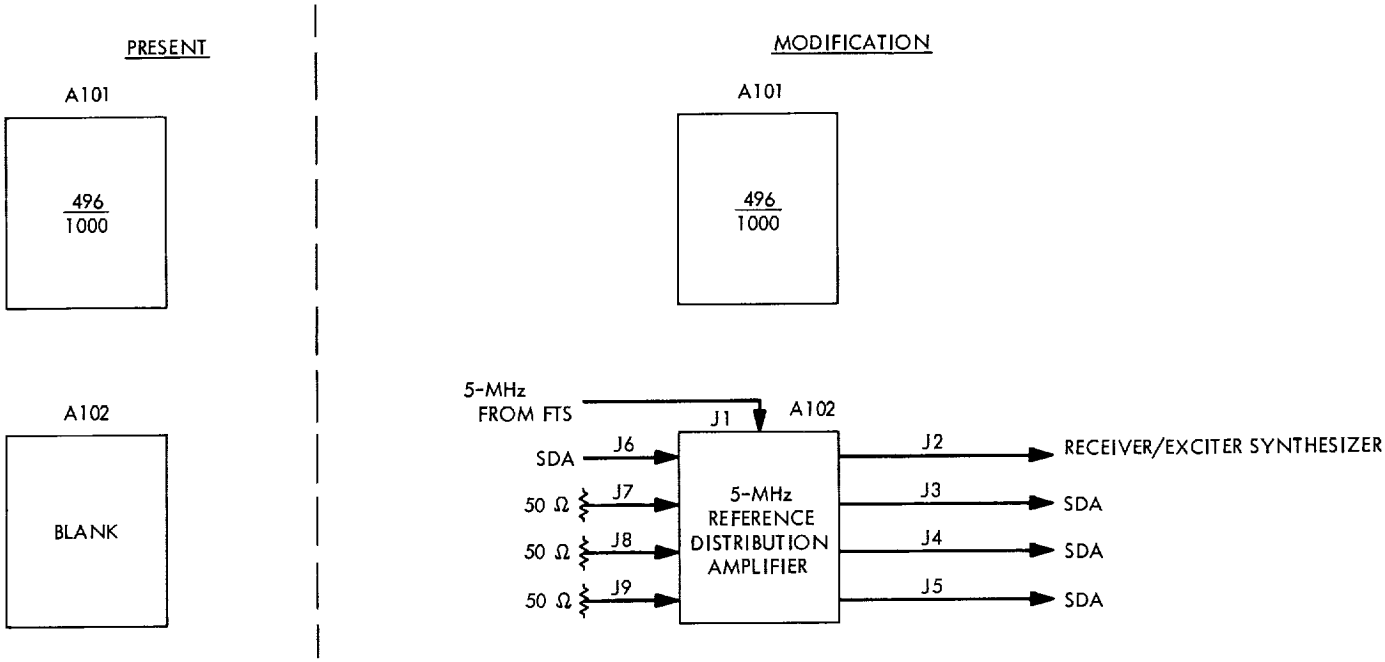

Fig. 8. SDA/receiver–exciter functional interface (cabinet 4)

where $|x|$ denotes the absolute value of x. The averaging over N bit periods could equivalently be a digital low-pass filter with "time constant" equal to N bit periods with no significant change in the results. Let R be the true SNR and assume the local bit-timing reference is perfectly synchronized with the received signal. Then, as N grows large, the estimator $\hat{R}$ converges in probability to the function $R^*(R)$, plotted in Fig. 9.

$$R^*(R) = \frac{\{R^{1/2}[1 - 2\,\mathrm{erfc}\,(2R)^{1/2}] + \pi^{-1/2}\,e^{-R}\}^2}{1 + 2\left(R - \{R^{1/2}[1 - 2\,\mathrm{erfc}\,(2R)^{1/2}] + \pi^{-1/2}\,e^{-R}\}^2\right)} \tag{2}$$

A similar result can be obtained if a bit timing offset exists. Let that offset be θ, in fractions of a bit duration, and assume that data sign transitions occur with probability p at each of the possible transition points. If no transition falls within the time interval of the bit integral I_i, its mean and variance are identical to what they would have been with no timing offset. If a transition occurs there, however, the signal amplitude is reduced by the factor $(1 - 2|\theta|)$, while the noise variance is unaffected. Let

$$\left.\begin{aligned} A(R,\theta) &= p\{R^{1/2}(1 - 2|\theta|)\,\{1 - 2\,\mathrm{erfc}\,[(2R)^{1/2}(1 - 2|\theta|)]\} + \pi^{-1/2}\exp[-R(1 - 2|\theta|)^2]\} \\ &\quad + (1 - p)\,\{R^{1/2}\,[1 - 2\,\mathrm{erfc}\,(2R)^{1/2}] + \pi^{-1/2}\,e^{-R}\} \\ B(R,\theta) &= R[p(1 - 2|\theta|)^2 + (1 - p)] \end{aligned}\right\} \tag{3}$$

Then, if a static offset of θ is maintained, it can be easily shown that the SNR estimate $\hat{R}$ will converge in probability to

$$R^*(R,\theta) = \frac{A^2(R,\theta)}{1 + 2[B(R,\theta) - A^2(R,\theta)]} \tag{4}$$

Further, let

$$\left.\begin{aligned} A_s(R) &= \int_{-1/2}^{1/2} d\theta\, A(R,\theta) \\ B_s(R) &= \int_{-1/2}^{1/2} d\theta\, B(R,\theta) \end{aligned}\right\} \tag{5}$$

Then, if the bit timing loop is slowly slipping cycles throughout the measurement period, and enough cycles are slipped throughout this period that the distribution of static timing offset is essentially uniform, the SNR estimate $\hat{R}$ will converge in probability to

$$R_s^*(R) = \frac{A_s^2(R)}{1 + 2[B_s(R) - A_s^2(R)]} \tag{6}$$

For large R, Eqs. (4) and (6) reduce to Eqs. (13) and (14) of SPS 37-48, Vol. III, pp. 211–212, respectively. $R^*(R,\theta)$ is plotted in Fig. 10 as a function of θ for various values of R. Certain special points are marked on each of the lines denoting an input SNR: "+" denotes the value of $R_s^*(R)$ associated with this input SNR, calculated by numerical integration; "0" denotes the median experimental value for $\hat{R}_s(R)$.

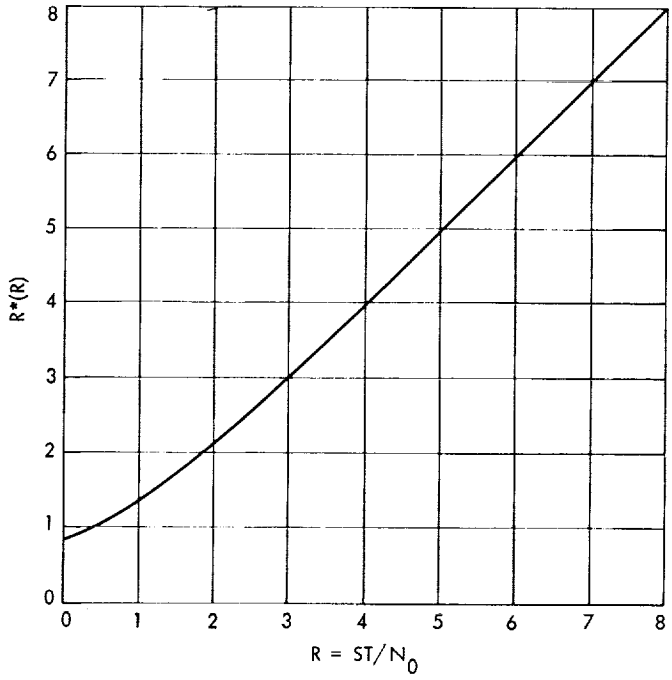

Fig. 9. Asymptotic value of the estimator $\hat{R}$ vs R

c. Experimental distribution of R. Values of $\hat{R}(R)$ and $\hat{R}_s(R)$ were obtained experimentally for input SNRs of 0, 2.5, 5.2, 7.5, and 10.0 dB. The samples making up each $\hat{R}$ were filtered in a bandwidth equivalent to 0.3% of the bit rate for input values of $S_T/N_0 \geq 7.5$ dB and 0.1% of the bit rate for input values of $S_T/N_0 > 7.5$ dB. Distributions for each test contain a minimum of 10,000 independent samples. For convenience, a bit rate of 250 bits/s

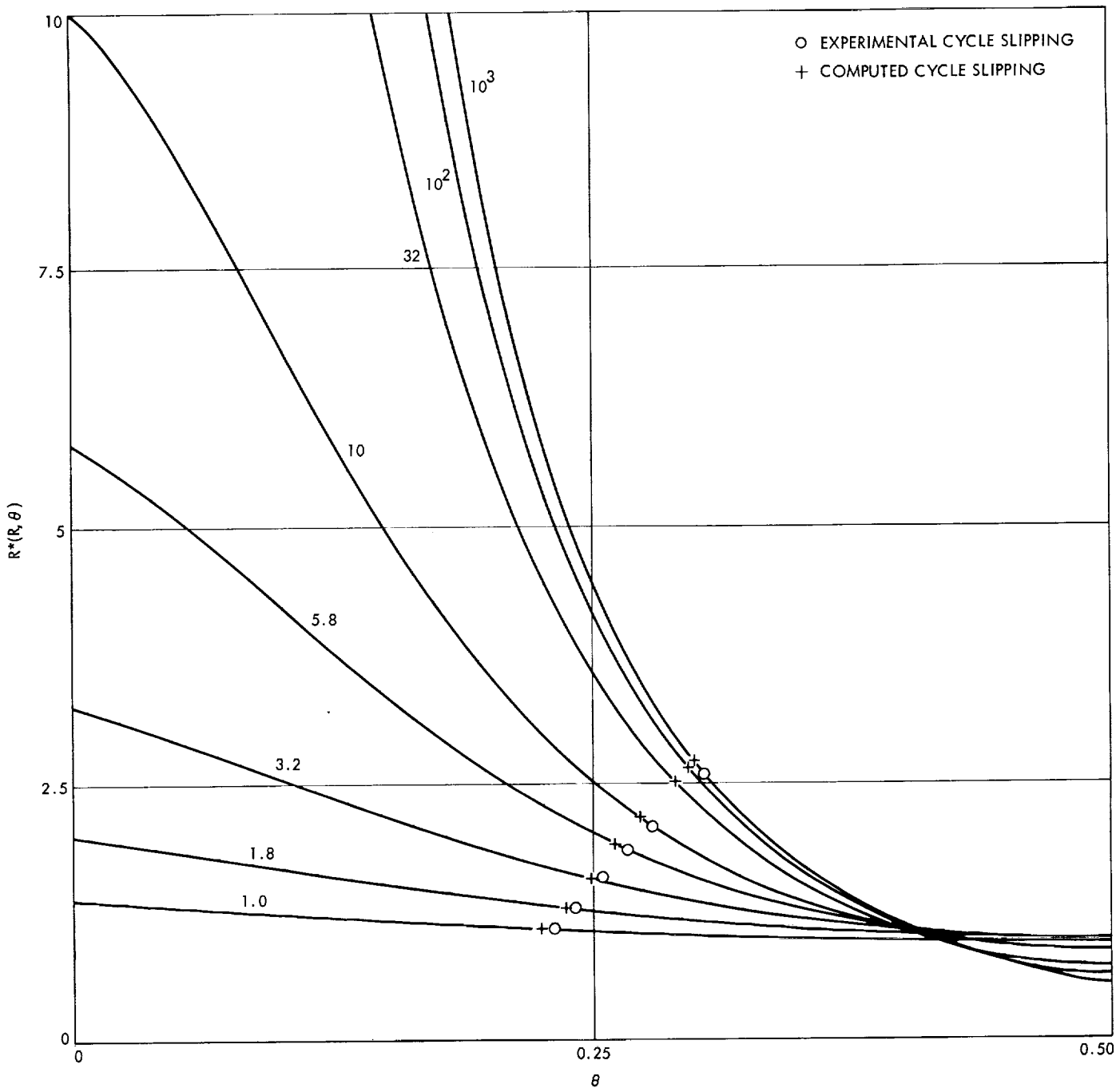

Fig. 10. $R^*(R,\theta)$ vs θ for $R = 1$ to 10^3

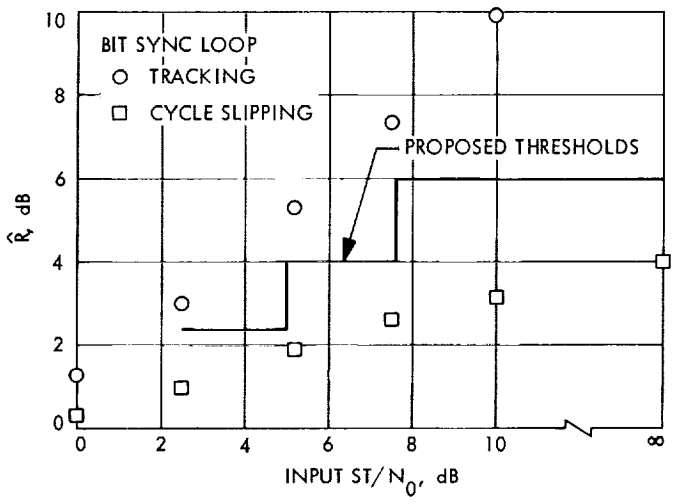

Fig. 11. Mean values of the experimental $\hat{R}$ distributions for loop in lock and cycle slipping

was arbitrarily selected. For the cycle slipping case, the offset was 3.6% of the bit rate. The means of $\hat{R}(R)$ and $\hat{R}_s(R)$ are plotted in Fig. 11, and the distributions are plotted in Fig. 12.

d. Zoned lock indicator thresholds. Selection of threshold for the bit-sync loop lock detector of the final MMTS demonstration system has proceeded under the following ground-rules:

(1) As few distinct thresholds as possible should be used.

(2) The probability of false alarm when in lock at the lowest SNR in the zone should be roughly equivalent to the probability of false in-lock indication at the highest SNR in the zone when slipping cycles, and both should be small. This should result in a good failure indicator but a relatively poor data quality indicator. The zones and their thresholds are as follows:

$R \geq 7.6$ dB, out of lock if $\hat{R} < 6$ dB

$7.6 > R \geq 5.0$ dB, out of lock if $\hat{R} < 4.0$ dB

$5.0 > R \geq 2.5$ dB, out of lock if $\hat{R} < 2.4$ dB

Projection of these thresholds in Figs. 10, 11, and 12 shows that they adequately differentiate the in-lock and out-of-lock conditions of the bit timing loop. For SNR below 2.5 dB, the variation of $\hat{R}$ with θ becomes so slight as to make assignment of a zone threshold impossible and to make use of $\hat{R}$ as a bit-sync loop lock detector of questionable validity, even with a threshold computed from the true input SNR.

4. MMTS: 10-MHz Quadrature Generator and Phase Switch, *R. B. Crow*

A 10-MHz quadrature generator and phase switch has been developed for the subcarrier demodulator assembly (SPS 37-46, Vol. III, pp. 221–230) to be used in the multiple-mission telemetry system.

The block diagram of the quadrature generator and phase switch (Fig. 13) illustrates that it is a small subsystem packaged in a single module. The purpose of the unit is to act as a signal phase switch to demodulate (1) the subcarrier in the data channel (0-deg channel) so that the output of the unit is 10-MHz × data, (2) the subcarrier in the quadrature channel (270-deg channel) so that the output of the unit is 10-MHz × data, and (3) the product of subcarrier × data in the error channel (90-deg channel) so that the output is a 10-MHz signal.

The module has the following characteristics:

(1) The quadrature phase relationship (at the subcarrier frequency) between the three outputs is maintained to within ±0.5 deg up to a subcarrier frequency of 250 kHz and to within approximately ±2 deg at a subcarrier frequency of 1 MHz.

(2) The carrier suppression versus subcarrier and data frequency is a minimum of −40 dB for the following conditions:
   (a) Subcarrier frequency from dc to 1 MHz.
   (b) Data frequency from dc to 250 kHz.
   (c) Temperature variations over the range of 0 to +50°C.
   (d) Power supply variations of ±5%.

(3) The insertion loss of each signal phase switch is a nominal −1.5 ±0.5 dB, and the output linearity is at +3 dBm.

(4) The monitor outputs deliver ±0.7 Vdc into a 50-Ω load and have a rise time of 20 ns.

This unit is unique in DSIF modules in that it uses both linear and digital integrated circuits along with discrete components mounted on a printed circuit board (Fig. 14).

The ±1.75-V power supply (used for all the digital integrated circuits) uses an integrated-circuit operational amplifier and discrete transistor as a shunt regulator. This

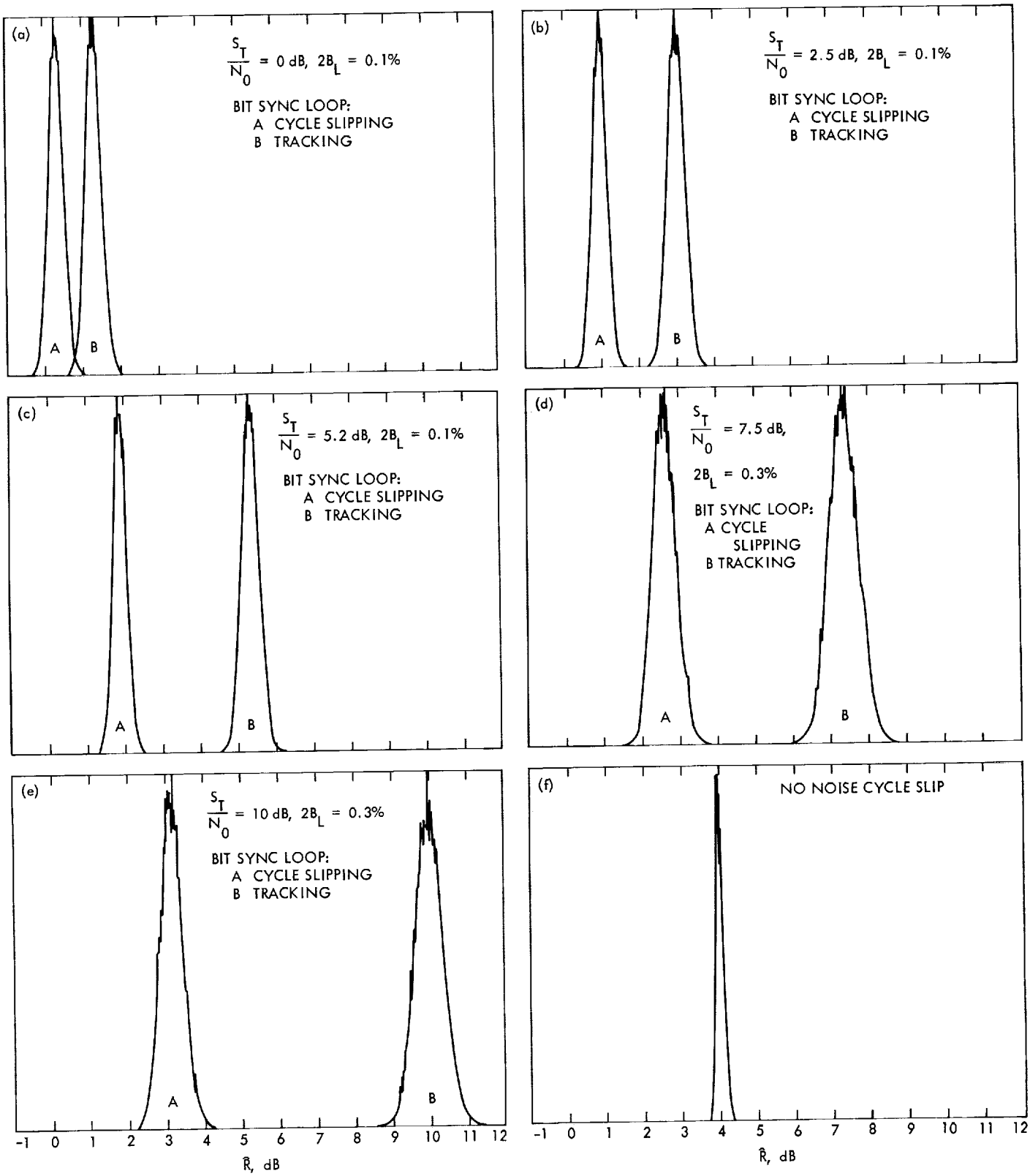

Fig. 12. Experimental density functions of $\hat{R}$

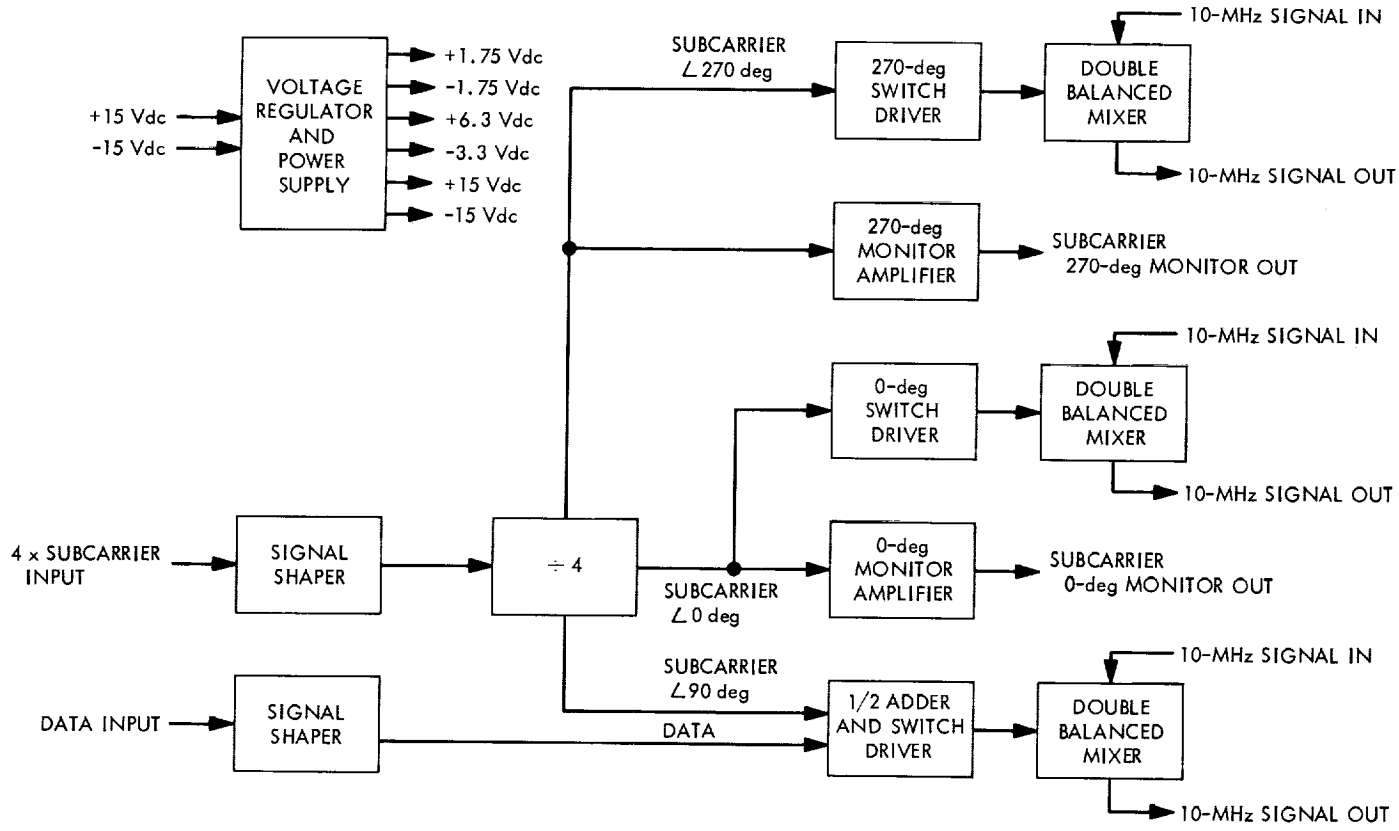

Fig. 13. Block diagram of quadrature generator and phase switch

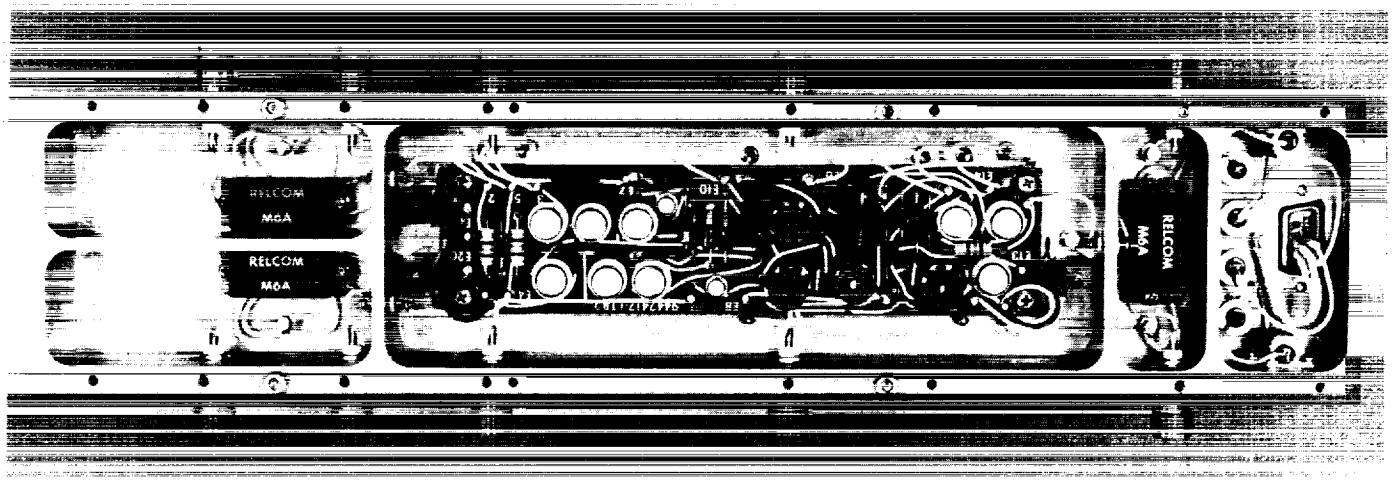

Fig. 14. Quadrature generator

arrangement was chosen to minimize the RF interference impressed on the ±15 Vdc power supply lines. The required voltage for the other integrated circuits was established using shunt zener regulation.

The ×4 subcarrier frequency input signal (a sine wave) is first shaped by a Schmitt trigger and then used to drive two flip-flops. The divide-by-four circuit is used to obtain 90- and 270-deg phase shifts. The data input is shaped

in a voltage comparator circuit to preserve the time symmetry of the data waveform.

The data and the subcarrier are digitally multiplied together in the error channel to remove all modulation from the 10-MHz input signal. This is accomplished by using a half-adder. A pair of *nand* gates is used to properly condition the data signal so that it presents the proper input to the half-adder.

An integrated circuit buffer amplifier is used to drive the double balanced mixer (i.e., the signal phase switch). There is a level adjustment in the buffer amplifier so that the dc level of the input to the double balanced mixer can be adjusted. This is necessary since carrier suppression is the product of both the time-asymmetry and the dc-level balance.

The data and quadrature channels (0 and 270 deg) are identical to the error channel (90 deg) with one exception; there is no multiplication of subcarrier × data. However, half-adders have been installed in each signal path in order to make the time delay for all channels equal. This is necessary in order to meet the quadrature phase specification.

The only adjustment required for this unit is to set one potentiometer for each channel to achieve an area balance (time-asymmetry × dc-level) of the video switching signal to the double balanced mixers in order to optimize the carrier suppression.

5. MMTS: Performance of Subcarrier Demodulator,

M. H. Brockman

a. Introduction. This article provides theoretical performance characteristics for the telemetry subcarrier demodulator which are applicable to a wide range of data rates for both uncoded and coded binary phase-shift-keyed (PSK) telemetry. Application to the *Mariner* Mars 1969 mission is presented to illustrate use of the performance characteristics.

b. Telemetry subcarrier tracking loop. A functional description of the telemetry subcarrier demodulator shown in Fig. 15 was presented in an earlier article (SPS 37-49, Vol. II, pp. 100–113). The upper (data) channel of Fig. 15 was treated in SPS 37-46, Vol. III, pp. 189–202, and in SPS 37-48, Vol. II, pp. 124–129. In the present

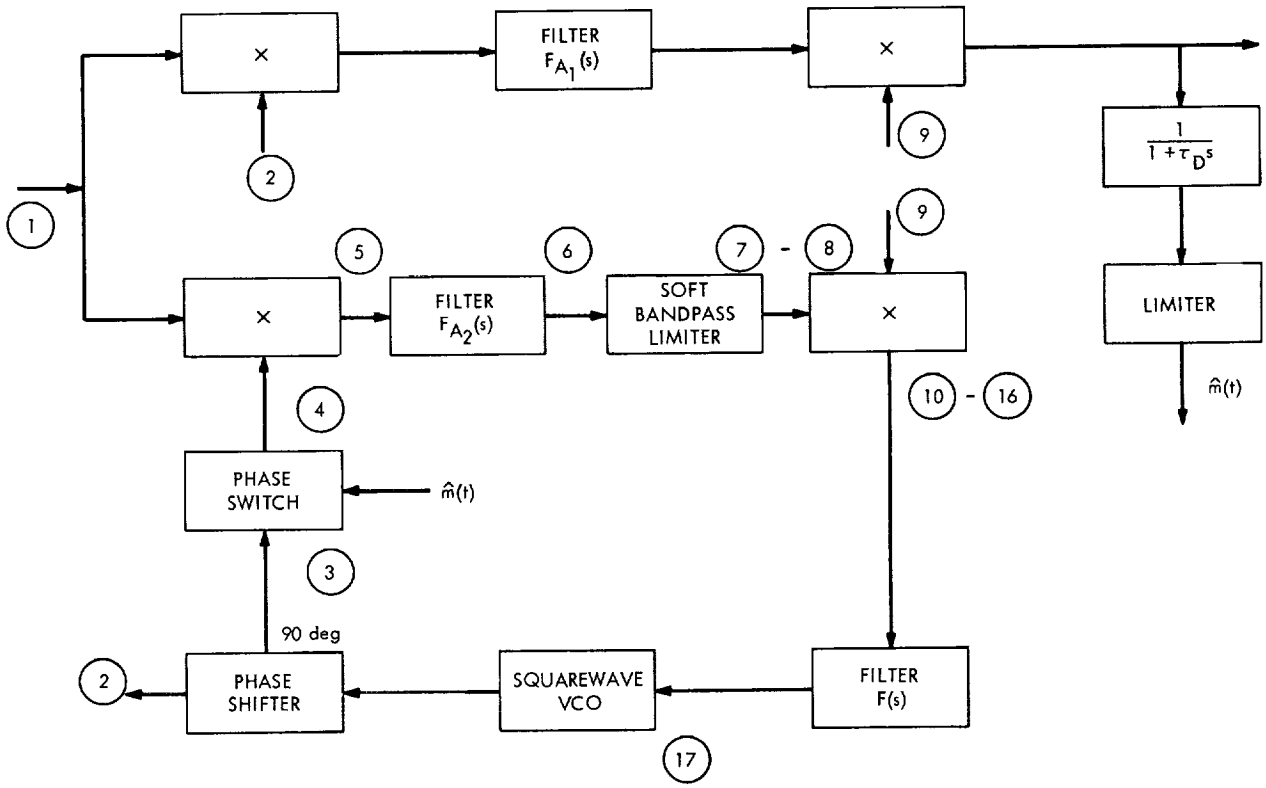

Fig. 15. Telemetry subcarrier demodulator functional block diagram

article, the soft (finite gain) bandpass limiter is incorporated into the subcarrier tracking loop to provide the performance characteristics developed herein for a second-order loop. The assumptions made in SPS 37-46, Vol. III, apply herein.

The input signal is an RF signal (at IF frequency f_2 Hz or ω_2 rad/s) phase-modulated with a squarewave telemetry subcarrier ω_{sc}, which is, in turn, biphase-modulated with the data $m(t)$. Because the modulation waveform is binary, the signal can be written as

$$\underbrace{2^{1/2}A\cos m_{ps}\cos\omega_2 t}_{\text{carrier}} + \underbrace{2^{1/2}A\sin m_{ps}\times m(t)\times \text{SQR}(\omega_{sc}t+\theta)\times\sin\omega_2 t}_{\text{sidebands}} + n_2(t) \tag{1}$$

where m_{ps} is the peak phase modulation index in radians (due to telemetry) and $m(t)$ is ± 1, depending on the data. The term θ is the input telemetry subcarrier phase, which is considered as non-time varying in this simplified analysis. The term $n_2(t)$ represents input receiver noise (gaussian and white) for the receiver bandwidth at this point in the system which has a double-sided noise spectral density of

$$\frac{N_0}{2}\cdot\frac{N_0}{2} = \frac{k\times T\times 1}{2}\ \text{W/Hz}$$

where k is Boltzmann's constant, 1.38×10^{-23} J/°K, and T is the equivalent noise temperature of the receiving system. Total input signal power is A^2 (an impedance of unity is assumed to simplify the expression for power), where $A \ll 1$.

The signals obtained from the squarewave subcarrier voltage-controlled oscillator (VCO) at ② and ③ (in Fig. 15) are

$$\text{SQR}[\omega_{sc}t+\hat{\theta}(t)] \tag{2}$$

and

$$\text{SQR}[\omega_{sc}t+\hat{\theta}(t)] \tag{3}$$

The data symbol stream estimate $\hat{m}(t)$ biphase-modulates the squarewave sine subcarrier VCO at ③ + and $-\pi/2$ rad, which provides

$$\hat{m}(t)\ \text{SQR}\ [\omega_{sc}t+\hat{\theta}(t)] \tag{4}$$

The input signal, Expression (1), is multiplied in the lower multiplier in Fig. 15 by the squarewave sine subcarrier signal biphase-modulated with $\hat{m}(t)$, Expression (4) to provide

$$\hat{m}(t)\,(2)^{1/2}A\cos m_{ps}\ \text{SQR}\ [\omega_{sc}t+\hat{\theta}(t)]\cos\omega_2 t + \alpha'\,(2)^{1/2}A\sin m_{ps}\ \text{SQR}\ [\omega_{sc}t+\theta]\ \text{SQR}\ [\omega_{sc}t+\hat{\theta}(t)]\sin\omega_2 t + n_5(t) \tag{5}$$

where $\alpha' = \overline{m(t)\hat{m}(t)}$ (SPS 37-46, Vol. III) and where the noise term $n_5(t)$ is $n_2(t)$ in Expression (1), multiplied by $\hat{m}(t)\ \text{SQR}\ [\omega_{sc}t+\hat{\theta}(t)]$.

Assumption: It is assumed that the relative broadening in the noise spectrum due to this multiplication is small enough to be ignored. Therefore, the noise term of $n_5(t)$ at ⑤ in Fig. 15 has a double-sided noise spectral density of $N_0/2$. This is a conservative assumption. Note, also, that in the upper channel, the input noise is multiplied by SQR $[\omega_{sc}t+\hat{\theta}(t)]$, *which determines $\hat{m}(t)$. In the lower channel, the input noise is multiplied by* SQR $[\omega_{sc}t+\hat{\theta}(t)]$, *which provides noise which is statistically independent of $\hat{m}(t)$, which is, in turn, multiplied by $\hat{m}(t)$.*

After passing through the lower filter F_{A_2}, Expression (5) becomes

$$F_{A_2}\{\hat{m}(t)\,(2)^{1/2}\,A\cos m_{ps}\ \text{SIN}\ [\omega_{sc}\,t+\hat{\theta}(t)]\cos\omega_2 t+\alpha'\,(2)^{1/2}\,A\sin m_{ps}\ \text{COS}\,(\omega_{sc}\,t+\theta)\ \text{SIN}\ [\omega_{sc}\,t+\hat{\theta}(t)]\sin\omega_2 t\}+n_6(t) \tag{6}$$

The noise term $n_6(t)$ represents the receiver noise at the lower filter F_{A_2} output with a double-sided noise spectral density of $n_0/2$. The ratio of noise powers represented by $n_6(t)$ and $n_2(t)$ is equal to the ratio of noise bandwidths at ⑥ and ① in Fig. 15. The noise term $n_6(t)$ is centered about f_2. For the condition that the noise bandwidth of F_{A_2} is much less than $2f_{sc}$, the first term of Expression (6) is effectively zero.

The signal plus noise [last two terms of Expression (6)] is applied to the soft bandpass limiter whose output saturates at V_L (rms amplitude). Designate the ratio ν as

$$\nu=\frac{V_L}{G_{SL}\,A\sin m_{ps}} \tag{7}$$

where $\nu<1$ and G_{SL} is the soft limiter gain in its linear region. The output of the soft bandpass limiter in the frequency interval centered about f_2 becomes

$$\alpha_{SL}\,\alpha'\,(2)^{1/2}\,A\sin m_{ps}\times\text{COS}\,(\omega_{sc}\,t+\theta)\ \text{SIN}\ [\omega_{sc}\,t+\hat{\theta}(t)]\sin\omega_2 t+n_{s_L}(t) \tag{8}$$

where α_{SL} is the soft bandpass limiter signal–voltage suppression factor. It should be noted that α_{SL} is a function of both ν and α', since α' affects the signal-to-noise ratio into the bandpass limiter.

The reference signal at ⑨ in Fig. 15 is

$$(2)^{1/2}\sin\omega_2 t \tag{9}$$

Assumption. It is assumed that the received carrier power is such that the phase noise error in the RF carrier tracking loop is small enough so that it can be ignored.

The output of the lower coherent linear amplitude detector is the multiplication of Expression (8) by Expression (9), which provides (ignoring double frequency terms and orthogonal terms which are filtered out):

$$\alpha_{SL}\,\alpha'\,A\sin m_{ps}\ \text{COS}\,(\omega_{sc}\,t+\theta)\ \text{SIN}\ [\omega_{sc}\,t+\hat{\theta}(t)]+n_{10_L}(t) \tag{10}$$

where

$$\alpha_{SL}=\text{function}\left(\frac{\nu\,\alpha'\,A\sin m_{ps}}{\frac{N_0}{2}\times 2NBW_{F_{A_2}}}\right)$$

Assumption. Since it is assumed that the $\theta-\hat{\theta}(t)$ is much less than $\pi/2$ rad, the portion of the product of the squarewave cosine and sine terms centered about dc is proportional to

$$\left[\theta-\hat{\theta}(t)\Big/\frac{\pi}{2}\right]$$

where the phase difference is expressed in radians.

The other portion of the squarewave cosine and sine product is a double-frequency squarewave which is filtered out by filter $F(s)$.

As discussed previously, the error signal out of the lower coherent amplitude detector due to the signal alone is linearly related to the difference in phase between the received squarewave telemetry subcarrier and the squarewave subcarrier VCO. Its value is zero when θ and $\hat{\theta}(t)$ are

equal, positive in sign when $\theta > \hat{\theta}(t)$, and negative in sign when $\theta < \hat{\theta}(t)$.

Consider next the noise term $n_{1_{0_L}}(t)$ in Expression (10). The noise power represented by the noise term is

$$P_N = \Gamma_{SL} \times \frac{N_0}{2} \times NBW_{F_{A_2}} \tag{11}$$

which can be written

$$\sigma^2_{NV_2} = \Gamma_{SL} \times \frac{N_0}{2} \times NBW_{F_{A_2}} \tag{12}$$

Consequently, the rms noise voltage is

$$\sigma_{NV_2} = \left(\Gamma_{SL} \times \frac{N_0}{2} \times NBW_{F_{A_2}}\right)^{1/2} \text{ rms amplitude} \tag{13}$$

where Γ_{SL} (soft limiter performance factor) is the ratio of the soft bandpass limiter input signal-to-noise spectral density to that at the bandpass limiter output (Refs. 1, 2, and SPS 37-36, Vol. IV, pp. 242–244).

Since, in this application, the soft limiter operates in its linear region at high signal levels (see *Paragraph f*), it does not enhance the output signal-to-noise ratio as is the case for a hard (infinite gain) limiter. Consequently, Γ_{SL} approaches unity as the signal level increases. The soft bandpass limiter performance factor can be approximated by the equation

$$\Gamma_{SL} = \frac{1 + 0.345 \times \left(\frac{P_S}{P_N}\right)_{F_{A_2}} + 50 \times \left(\frac{P_S}{P_N}\right)^5_{F_{A_2}}}{0.862 + 0.690 \times \left(\frac{P_S}{P_N}\right)_{F_{A_2}} + 50 \times \left(\frac{P_S}{P_N}\right)^5_{F_{A_2}}} \tag{14}$$

where the signal-to-noise ratio parameter

$$\left(\frac{P_S}{P_N}\right)_{F_{A_2}} = \frac{(\alpha' A \sin m_{ps})^2}{\frac{N_0}{2} \times 2NBW_{F_{A_2}}} \text{ at } \theta - \hat{\theta}(t) = \frac{\pi}{2} \text{ rad} \tag{15}$$

The limiter performance factor Γ_{SL} is shown in Fig. 16. The soft limiter performance factor Γ_{SL} does vary somewhat with ν [Expression (7)] as it (Γ_{SL}) approaches unity; but this effect, which is relatively small, has been ignored here.

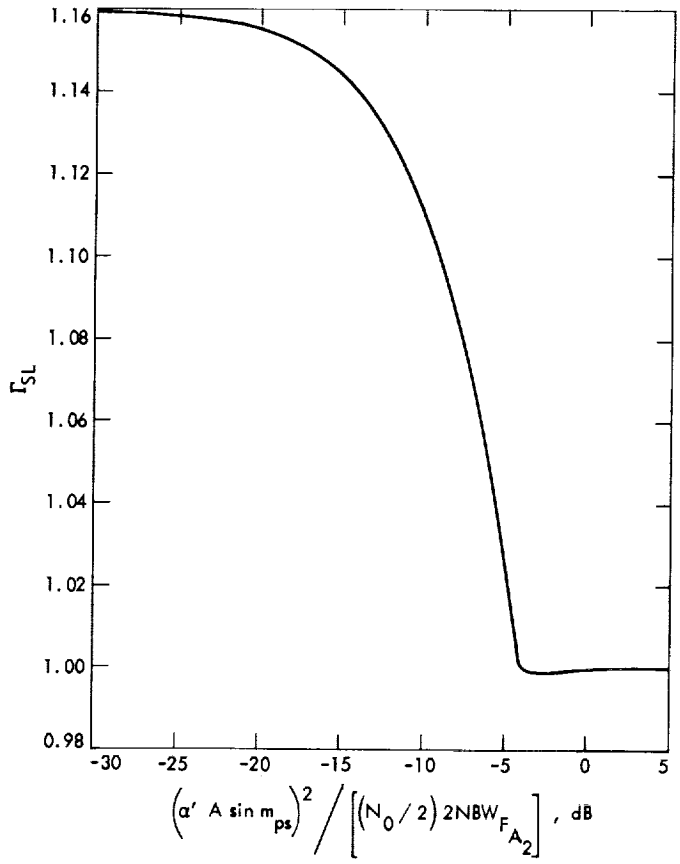

Fig. 16. Ratio of input signal-to-noise spectral density to output signal-to-noise spectral density vs soft bandpass limiter input signal-to-noise ratio parameter

Consider for a moment the signal portion of Expression (10). Note that if $\theta - \hat{\theta}(t)$ is equal to $\pi/2$ rad, the output signal power from the lower coherent amplitude detector is $(\alpha' A \sin m_{ps})^2$, relative to the input noise spectral density into the soft bandpass limiter. Consequently, conversion of the rms noise voltage to equivalent phase noise can be accomplished by normalizing the noise voltage to the signal voltage. The resultant expression at the output of the lower coherent amplitude detector is

$$\left.\begin{aligned} &\frac{\pi}{2} \times \frac{\sigma_{NV_2}}{\alpha' A \sin m_{ps}} \text{ rad rms} \\ &\text{or} \\ &\Gamma^{1/2}_{SL} \times \frac{\pi}{2} \times \frac{\left(\frac{N_0}{2}\right)^{1/2}}{\alpha' A \sin m_{ps}} \times \left(NBW_{F_{A_2}}\right)^{1/2} \text{ rad rms} \end{aligned}\right\} \tag{16}$$

After passing through the filter $F(s)$, the signal plus noise represented by Expression (10) controls the output phase of the subcarrier VCO

$$F(\omega)\left[\alpha_{SL}\,\alpha' A \sin m_{ps}\left\{\cos(\omega_{sc}t+\theta)\,\sin[\omega_{sc}t+\hat{\theta}(t)]\right\}+n_{1O_L}(t)\right] \tag{17}$$

Since $\theta = \int \omega dt$, the VCO functions as an integrator.

c. Linear model of the subcarrier tracking loop. The lower loop in Fig. 15 can now be treated as a linear model of the phase-locked loop (Ref. 3) with the constraint that at minimum signal level the probability of the phase noise error exceeding 90 deg $<<$ 1. Figure 17 shows the resulting linear model of the subcarrier phase-tracking loop.

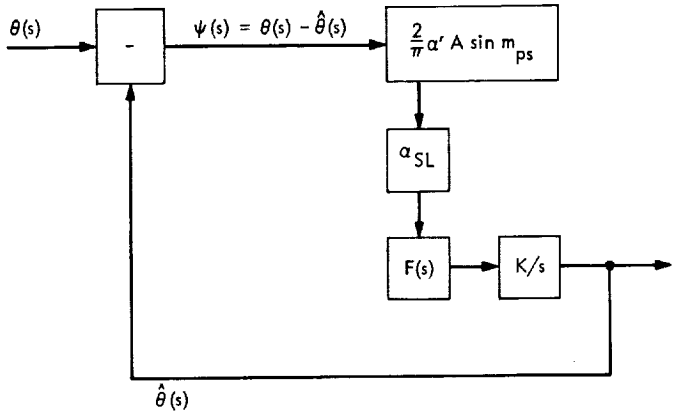

Fig. 17. Linear model of subcarrier phase-tracking loop

The subcarrier squarewave VCO becomes K/s in this mathematical model, where K is the effective gain constant of the VCO in rad/s/V. Note that the open loop gain at dc is

$$\alpha_{SL}\,\frac{2}{\pi}\,K\,\alpha' A \sin m_{ps}$$

in units of 1/s (SPS 37-46, Vol. III). The transfer function of the subcarrier loop is

$$H(s)=\frac{\hat{\theta}(s)}{\theta(s)}=\frac{\alpha_{SL}\,\frac{2}{\pi}\,K\,\alpha' A \sin m_{ps}\times F(s)}{s+\alpha_{SL}\,\frac{2}{\pi}\,K\,\alpha' A \sin m_{ps}\times F(s)} \tag{18}$$

The two-sided noise bandwidth of the subcarrier phase-tracking loop is

$$BW_{SCL}=\frac{1}{2\pi j}\int_{-j\infty}^{+j\infty}|H(s)|^2\,ds \text{ Hz} \tag{19}$$

and the variance of the phase noise at the output of the loop is (SPS 37-46, Vol. III)

$$\sigma_{\theta n}^2=\Gamma_{SL}\times\frac{\frac{N_0}{2}}{\left(\frac{2}{\pi}\right)\alpha' A \sin m_{ps}\Big)^2}\times BW_{SCL}\text{ rad}^2 \tag{20}$$

Note that $A \sin m_{ps} = S^{1/2}$.

d. Second-order subcarrier tracking loop. For a second-order loop with a passive integrator, the filter $F(s)$ is of the form

$$F(s) = \frac{1 + \tau_2 s}{1 + \tau_1 s} \tag{21}$$

where

$$\tau_2 = R_2 C \text{ and } \tau_1 = (R_1 + R_2)C$$

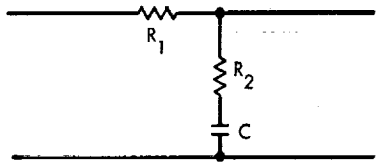

Therefore, from Expression (18), the transfer function of a second-order loop becomes

$$H(s) = \frac{\alpha_{SL}\frac{2}{\pi} K\alpha' A \sin m_{ps} \times \left(\frac{1 + \tau_2 s}{1 + \tau_1 s}\right)}{s + \alpha_{SL}\frac{2}{\pi} K\alpha' A \sin m_{ps} \times \left(\frac{1 + \tau_2 s}{1 + \tau_1 s}\right)}$$

which can be rewritten as

$$H(s) = \frac{1 + \tau_2 s}{1 + \left(\tau_2 + \frac{1}{\alpha_{SL}}\frac{2}{\pi} K\alpha' A \sin m_{ps}\right)s + \left(\frac{\tau_1}{\alpha_{SL}}\frac{2}{\pi} K\alpha' A \sin m_{ps}\right)s^2} \tag{22}$$

Define a quantity r' as

$$r' = \alpha_{SL}\frac{2}{\pi} K\alpha' A \sin m_{ps} \times \frac{\tau_2^2}{\tau_1} \tag{23}$$

and the transfer function becomes

$$H(s) = \frac{1 + \tau_2 s}{1 + \tau_2\left(1 + \frac{\tau_2}{r'\tau_1}\right)s + \frac{\tau_2^2}{r'}s^2} \tag{24}$$

From Ref. 2, the two-sided noise bandwidth of the second-order subcarrier tracking loop (Expression 19) is

$$BW_{SCL} = \frac{r' + 1}{2\tau_2\left(1 + \frac{\tau_2}{r'\tau_1}\right)} \tag{25}$$

At the design point, the two-sided noise bandwidth is

$$BW_{SCL_0} = \frac{r'_0 + 1}{2\tau_2\left(1 + \frac{\tau_2}{r'_0\tau_1}\right)} \tag{26}$$

From Expression (20), the variance of the phase noise at the output of the second-order loop is

$$\sigma^2_{\sigma n} = \Gamma_{SL} \times \left(\frac{1}{\alpha'_0}\right)^2 \times \left(\frac{\pi}{2}\right)^2 \times \frac{N_0}{ST_{SY}} \times \frac{T_{SY}}{2} \times \frac{r'_0 + 1}{2\tau_2\left(1 + \frac{\tau_2}{r'_0\,\tau_1}\right)} \text{ rad}^2 \tag{27}$$

at the design point.

Consequently, for a given τ_D/T_{SY}, ST_{SY}/N_0, symbol rate $(1/T_{SY})$, and probability that the data symbol stream does switch on successive symbols, the rms phase error $\sigma_{\theta n}$ at design point can be calculated from Expression (27), where α'_0 is obtained from Fig. 18 (included here from SPS 37-46, Vol. III for reference) and α_{SL} from Fig. 19.

Consider next the manner in which $\sigma^2_{\theta n}$ varies with ST_{SY}/N_0 for a given symbol rate for the second-order loop. Expressions (25) and (26) can be rewritten as

$$BW_{SCL} = \frac{\tau_1 r' + \tau_1}{2\tau_2\tau_1\left(1 + \frac{\tau_2}{r'\tau_1}\right)} \tag{28}$$

and

$$BW_{SCL_0} = \frac{\tau_1 r'_0 + \tau_1}{2\tau_2\tau_1\left(1 + \frac{\tau_2}{r'_0\tau_1}\right)} \tag{29}$$

respectively.

Since at the design point

$$\alpha_{SL_0} = \text{function}\left(\frac{\nu\,\alpha'_0\,A \sin m_{ps}}{\frac{N_0}{2} \times 2NBW_{F_{A_2}}}\right)$$

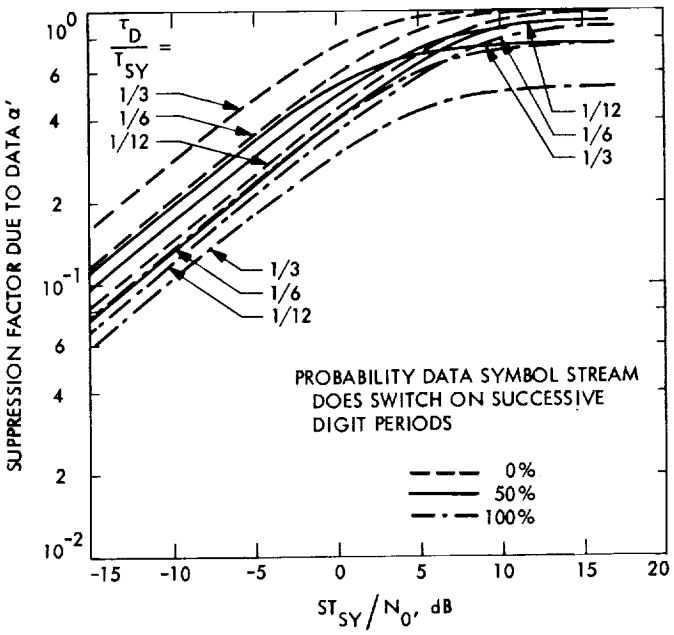

Fig. 18. Multiple-mission telemetry subcarrier demodulator suppression factor due to data vs ratio of signal energy per symbol to noise spectral density

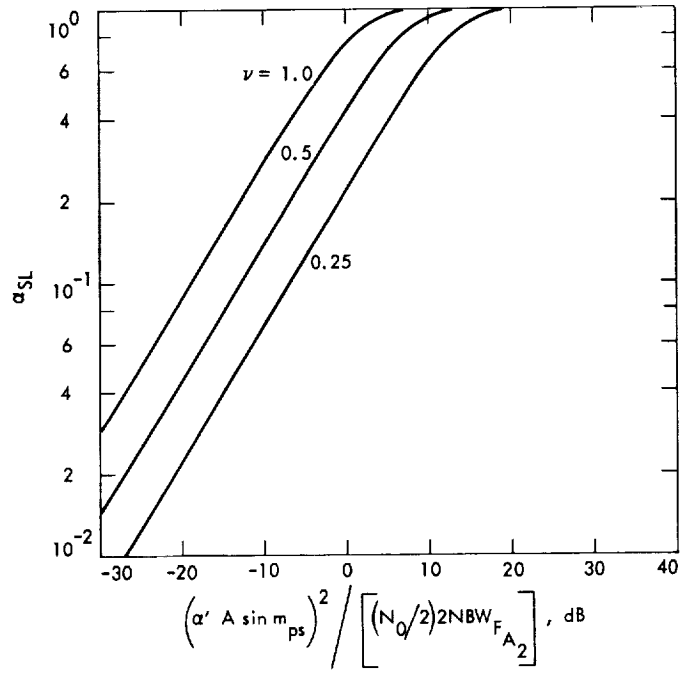

Fig. 19. Signal–voltage suppression factor vs soft bandpass limiter input signal-to-noise ratio parameter

and at some other signal level

$$\alpha_{SL} = \text{function}\left(\frac{\nu\,\alpha' A \sin m_{ps}}{\frac{N_0}{2} \times 2NBW_{F_{A_2}}}\right)$$

inspection of Expression (23) shows that

$$r' = \frac{\alpha_{SL}}{\alpha_{SL_0}} \times r'_0 \tag{30}$$

Using Expression (25), Expression (28) becomes

$$BW_{SCL} = \frac{\frac{\alpha_{SL}}{\alpha_{SL_0}} \times r'_0\,\tau_1 + \tau_1}{2\tau_2\tau_1\left(1 + \frac{\tau_2}{\frac{\alpha_{SL}}{\alpha_{SL_0}}\,r'_0\,\tau_1}\right)} \tag{31}$$

For the condition that $\tau_2 \ll r'_0\,\tau_1$,

$$BW_{SCL} = \frac{\frac{\alpha_{SL}}{\alpha_{SL_0}} \times r'_0}{2\tau_2} + \frac{1}{2\tau_2} \tag{32}$$

which becomes

$$BW_{SCL} = \frac{\alpha_{SL}}{\alpha_{SL_0}}\,r'_0\left(\frac{BW_{SCL_0}}{r'_0 + 1}\right) + \frac{BW_{SCL_0}}{r'_0 + 1}$$

or

$$BW_{SCL} = \frac{BW_{SCL_0}}{r'_0 + 1}\left(1 + r'_0\,\frac{\alpha_{SL}}{\alpha_{SL_0}}\right) \tag{33}$$

Consequently, for the second-order loop, a change in ST_{SY}/N_0 from the design point provides an α' from Fig. 18, α_{SL} from Fig. 19, and $\sigma^2_{\theta n}$ is recalculated from the expression

$$\sigma^2_{\theta n} = \Gamma_{SL} \times \left(\frac{1}{\alpha'}\right)^2 \left(\frac{\pi}{2}\right)^2 \times \frac{N_0}{ST_{SY}} \times \frac{T_{SY}}{2} \times BW_{SCL_0} \times \frac{\left(1 + r'_0\,\frac{\alpha_{SL}}{\alpha_{SL_0}}\right)}{(r'_0 + 1)} \tag{34}$$

e. Effect of subcarrier tracking-loop phase error on demodulated ST_{SY}/N_0. Reduction in demodulated ST_{SY}/N_0 relative to the input ST_{SY}/N_0 to the telemetry subcarrier demodulator (i.e., demodulation efficiency) results from rms phase noise error in the subcarrier tracking loop and/or from the phase error due to doppler frequency shift on the received subcarrier frequency and its attendant doppler rate. The effect of these phase errors on demodulated ST_{SY}/N_0 was developed in SPS 37-48, Vol. II, pp. 124–129. For cases of phase error $\Delta\theta$ due to subcarrier doppler and rms phase error $\sigma_{\theta n}$ due to gaussian receiver noise, reduction in demodulated ST_{SY}/N_0 relative to input ST_{SY}/N_0 is

$$\frac{\text{demodulated } \frac{ST_{SY}}{N_0}}{\text{input } \frac{ST_{SY}}{N_0}} = \left[1 - \left(\frac{2}{\pi}\right)^{3/2} \sigma_{\theta n} - \left(\frac{2}{\pi}\right) \Delta\theta\,\text{erf}\left(\frac{\Delta\theta}{(2)^{1/2}\,\sigma_{\theta n}}\right)\right]^2 \tag{35}$$

It should be pointed out that using the expected value of ST_{SY}/N_0, as developed in the above analysis, to determine bit or word error probability from Ref. 4 will provide a good approximation to the correct error probability since the variance on $S^{1/2}$ in demodulated ST_{SY}/N_0 will be small at minimum operating condition for a given mission.

f. Soft bandpass limiter—a special application.

Approximation of characteristics. Consider the error function

$$\left.\begin{aligned} y &= \text{erf}\,(x) \\ &= \frac{2}{\pi^{1/2}} \int_0^x e^{-z^2}\,dz \end{aligned}\right\} \tag{36}$$

which has the characteristic that as $x \to 0$, $dy/dx = 2/\pi^{1/2}$. Consequently, linear extrapolation of y with x provides $y = 2/\pi^{1/2}$ at $x = 1.0$. Consider this value of y as the soft bandpass limiter output for $x > 1$. Consistent with asymptotic values, the function

$$y = \begin{cases} \frac{2}{\pi^{1/2}} \cdot x & \text{for } x \leq 1.0 \\ \frac{2}{\pi^{1/2}} & \text{for } x > 1.0 \end{cases} \qquad (37)$$

is another approximation for the soft bandpass limiter characteristic (Fig. 20). This approximation will be used in the following development. Note that for $x > 1.0$, the slope $dy/dx = 0$.

Operation in telemetry subcarrier phase-locked loop. Automatic gain control in the DSIF receiver provides a constant input signal level to the telemetry subcarrier demodulator. Consequently, the receiver noise into the subcarrier demodulator varies with received signal; for example, as the signal-to-noise spectral density ratio S/N_0 decreases, the receiver noise level increases. The error signal in the subcarrier tracking loop is generated at the input to the lower channel of Fig. 15 prior to the predetection filter F_{A_2} and the soft bandpass limiter. During normal in-lock operation, this error signal is very small compared to $\pi/2$ rad. Hence, for the condition of essentially zero receiver noise into the soft bandpass limiter, operation is in the linear region. As a result, during normal operation, any nonlinear effects for this special application result from the presence of gaussian receiver noise at the input to the soft bandpass limiter.

The resulting problem then becomes one of determining the statistical average (expectation) of the slope of the soft bandpass limiter for a signal-plus-noise input with a normal probability density function.

$$p(x) = \frac{1}{(2\pi)^{1/2}\sigma} \exp\left(-\frac{x^2}{2\sigma^2}\right) \qquad (38)$$

as shown in Fig. 21.

Designate the expected slope as α_{SL} so that

$$\alpha_{SL} = \frac{2}{\pi^{1/2}} \cdot \text{probability}\,(-1 \leq \text{signal} + \text{noise} \leq +1) + 0 \cdot \text{probability}\,(-1 > \text{signal} + \text{noise} > +1)$$

or

$$\alpha_{SL} = \frac{2}{\pi^{1/2}} \frac{2}{(2\pi)^{1/2}\sigma} \int_0^x \exp\left(-\frac{x^2}{2\sigma^2}\right) dx \qquad (39)$$

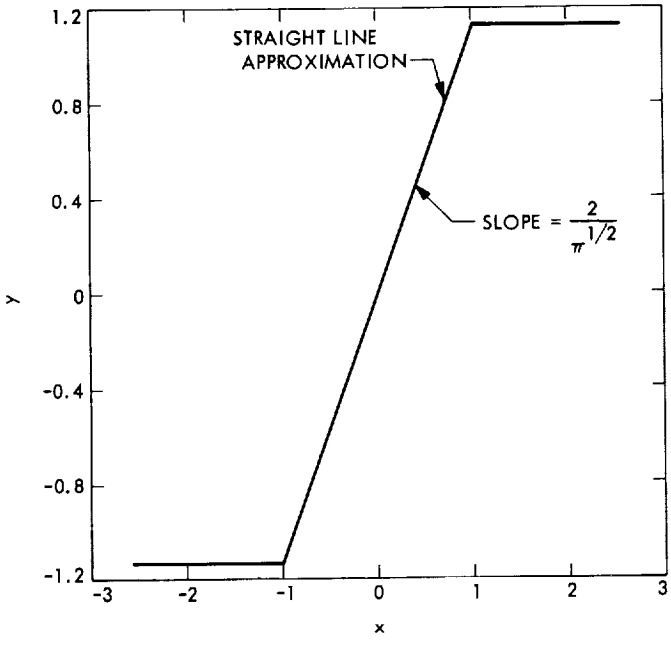

Fig. 20. Soft bandpass limiter characteristic

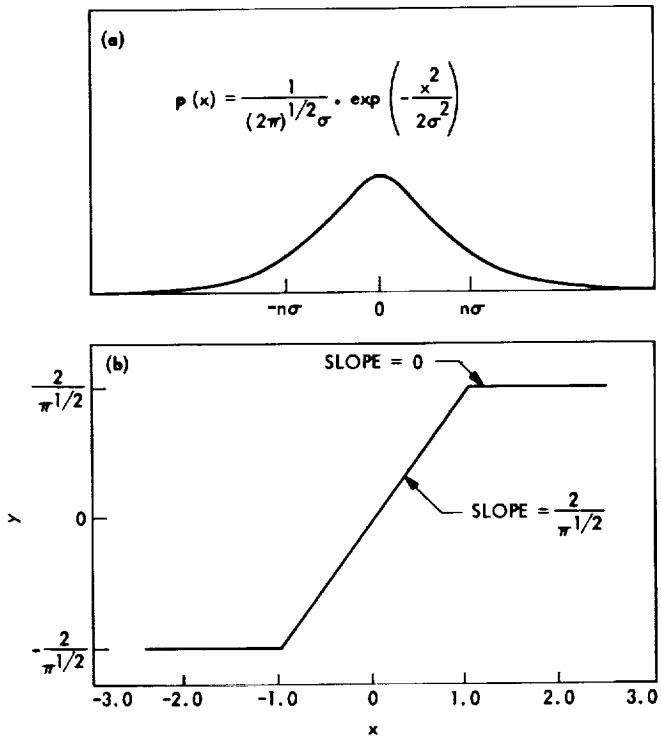

Fig. 21. (a) Input probability density function and (b) soft limiter characteristic

This expression can be written in the form

$$\left.\begin{aligned} \alpha_{SL} &= \frac{2}{\pi^{1/2}} \int_0^{\left(\frac{2}{\pi}\right)^{1/2} \frac{x}{\sigma}} e^{-z^2}\, dz \\ &= \operatorname{erf}\left[\left(\frac{2}{\pi}\right)^{1/2} \cdot \frac{x}{\sigma}\right] \end{aligned}\right\} \qquad (40)$$

In order to establish a signal-to-noise ratio parameter into the soft bandpass limiter, consider Fig. 22. The signal input to the limiter is

$$\alpha' S^{1/2} \frac{\theta - \hat{\theta}}{\frac{\pi}{2}}$$

which is a linear function of the phase error in the subcarrier tracking loop from 0 to $\pi/2$ rad. The limiting level is set so that the output of the soft bandpass limiter is linear with slope $2/\pi^{1/2}$ over the input signal level range

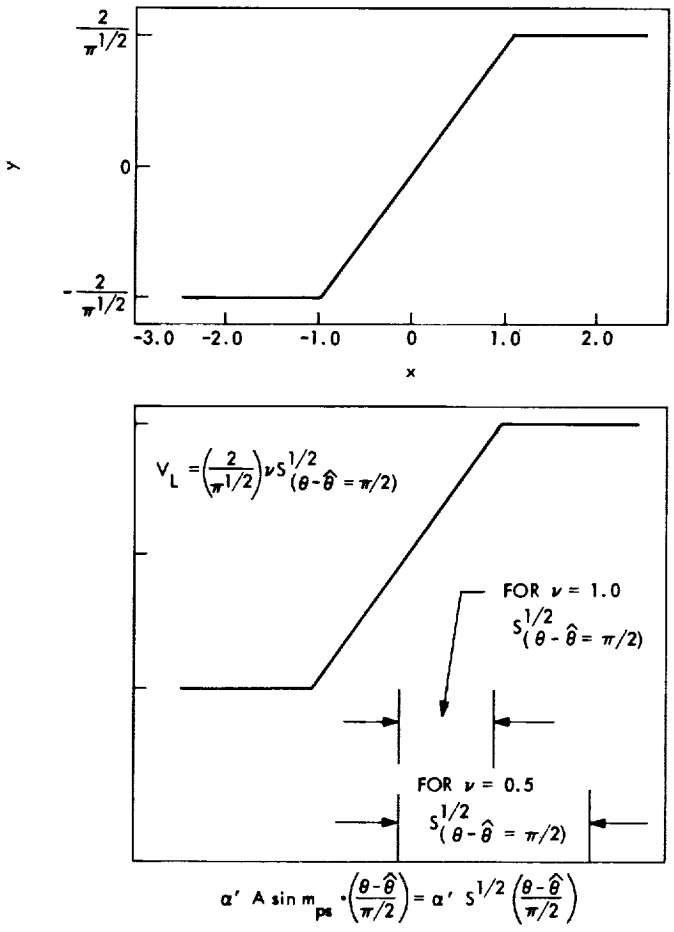

Fig. 22. Soft limiter signal parameters

of $\nu S^{1/2}_{(\theta-\hat{\theta}=\pi/2)}$. The rms phase noise input to the soft bandpass limiter is

$$\sigma_{NV} = \left(\frac{N_0}{2} \times 2\,NBW_{F_{A_2}}\right)^{1/2}$$

Consequently, Expression (40) can now be written as

$$\alpha_{SL} = \operatorname{erf}\left[\left(\frac{2}{\pi}\right)^{1/2} \cdot \frac{\nu\,\alpha' S^{1/2}_{(\theta-\hat{\theta}=\pi/2)}}{\left(\frac{N_0}{2} \times 2\,NBW_{F_{A_2}}\right)^{1/2}}\right] \qquad (41)$$

which provides Fig. 19. It is interesting to note that comparison of Fig. 19 for $\nu = 1.0$ with the hard limiter signal suppression characteristics (Refs. 1 and 2) at low signal-to-noise conditions provides results which are in close agreement, as would be expected.

g. Subcarrier tracking loop design and telemetry demodulator performance. In the following discussion, the concept of mission dp and moc are outlined. Also, the design parameters for the telemetry subcarrier demodulator are presented in light of equipment dp, with subsequent development of some basic performance characteristics that are applicable to a large range of binary PSK telemetry applications.

Design considerations. In the overall telecommunications system design for any given mission utilizing PSK telemetry, a bit (or word) error rate is specified at minimum operating condition (moc), which determines the signal energy per bit to noise spectral density ratio ST_B/N_0 (moc) for any given coding. At mission moc, some loss (generally a small fraction of a dB) is allocated to the telemetry subcarrier demodulator in the total telecommunications link attenuation between spacecraft and DSIF tracking station. In examining the performance of the telemetry subcarrier demodulator, ST_B/N_0 (moc) must be transformed into ST_{SY}/N_0 (moc) (ratio of signal energy per symbol to noise spectral density at moc). In particular,

$$\frac{ST_{SY}}{N_0} = \frac{1}{l} \times \frac{ST_B}{N_0} \qquad (42)$$

where l = symbols/bit. For example, for uncoded data $l = 1$, while for biorthogonal block-coded data $l = 2^{n-1}/n$, where n represents bits/word. In order to examine the subcarrier demodulator performance at signal levels below moc, the concept of mission design point (dp) is introduced so that performance can be specified and verified below moc. At mission dp, a 10% bit error rate

is specified, which then determines the corresponding ST_B/N_0 (dp) and, consequently, ST_{SY}/N_0 (dp) for any given coding.

The subcarrier-demodulator phase tracking loop is designed as a second-order loop with three closed-loop noise bandwidths—narrow, medium, and wide—which have nominal two-sided values of 0.03, 0.375, and 1.5 Hz, respectively, at the equipment dp with $r_0' = 2$ (0.707 damping). A bandwidth of 0.15 Hz, which is used to insure acquisition during operation in the narrow (0.03-Hz) bandwidth, is also provided. The predetection filter F_{A_2} in the subcarrier tracking loop has a nominal noise bandwidth of 500 Hz, while the predemodulation filter F_{A_1} in the upper (data) channel of Fig. 15 has a selectable noise bandwidth of 500 Hz, 5 kHz, 50 kHz, 500 kHz, or 3 MHz. The nominal design point parameters for the subcarrier tracking loop are summarized in Table 5. The design point open loop gain, shown here as G_0', relates to the preceding analysis as follows:

$$G_0' = \alpha_{SL_0} \frac{2}{\pi} K \alpha_0' A \sin m_{ps} \qquad (43)$$

Performance characteristics. Figure 15 and the ensuing analysis reveals that the performance of the telemetry subcarrier tracking loop is uniquely related to the signal-to-noise spectral density ratio parameter $(\alpha')^2 \times S/N_0$ in the predetection filter F_{A_2} for any signal level, telemetry data rate, or coding scheme within the capabilities of the DSIF S-band system. Consequently, a set of basic performance characteristics can be determined analytically for the telemetry subcarrier demodulator by application of the general analysis of *Paragraph d*, which will, in turn, provide detailed performance for a very large number of applications for binary PSK telemetry.

Application of the design parameters in Table 5 to the analysis [Expression (33)] provides Fig. 23, which shows the two-sided, closed-loop noise bandwidth BW_{SCL} (narrow, medium, or wide) as a function of $(\alpha')^2 \times S/N_0$ from equipment dp to strong signal levels. Since, as a conservative figure, the subcarrier tracking loop will automatically acquire within its two-sided, closed-loop noise bandwidth, the characteristic shown in Fig. 23 can be used to provide information on the frequency uncertainty of the received subcarrier which the telemetry subcarrier demodulator will accommodate at any particular signal level condition.

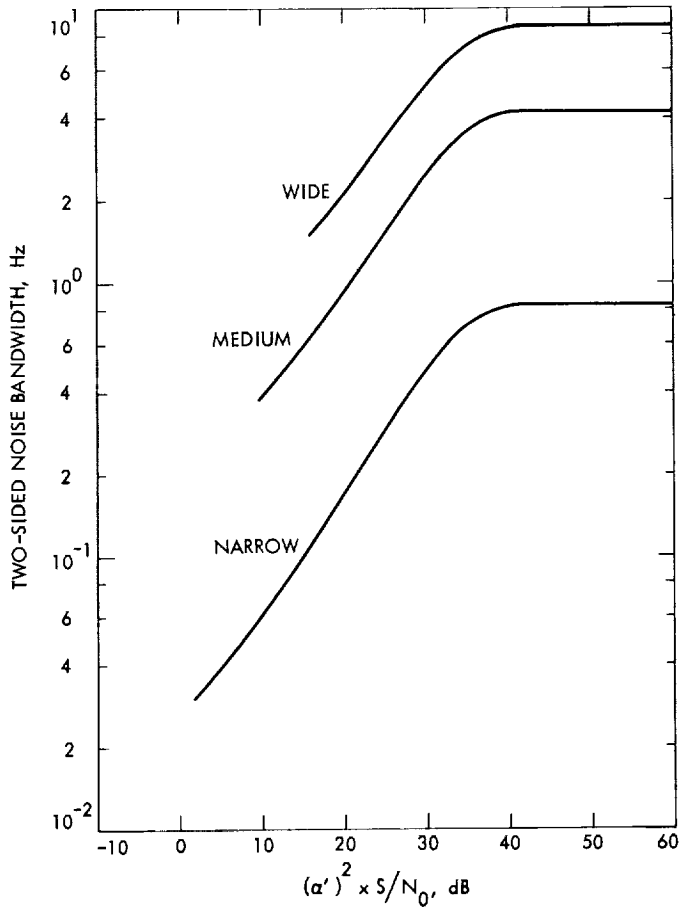

Fig. 23. Telemetry subcarrier demodulator two-sided closed-loop noise bandwidth vs predetection signal-to-noise spectral density ratio parameter

Table 5. Subcarrier loop design point parameters

Design point noise bandwidth, Hz	$(\alpha_0')^2 \times \frac{S}{N_0}$, dB	Soft bandpass limiter			G_0, 1/s	r_0', ratio	τ_1, s	τ_2, s
		α_{SL_0} ratio	ν ratio	Γ_{SL} ratio				
0.03	1.7	0.0244	0.50	1.16	10	2.0	12500	50
0.375	9.7	0.061	0.50	1.15	250	2.0	2000	4
1.50	15.7	0.123	0.50	1.12	500	2.0	250	1

Consider next application of the design parameters in Table 5 to Expression (34). This provides the subcarrier tracking loop rms phase noise error $\sigma_{\theta n}$ (shown in Fig. 24) as a function of $(\alpha')^2 \times S/N_0$ for the three noise bandwidth designs represented in Fig. 23. The $\sigma_{\theta n}$ characteristic shown in Fig. 24 is applicable to any probability of data symbol stream switching and for any ratio of τ_D/T_{SY} selected (Fig. 18).

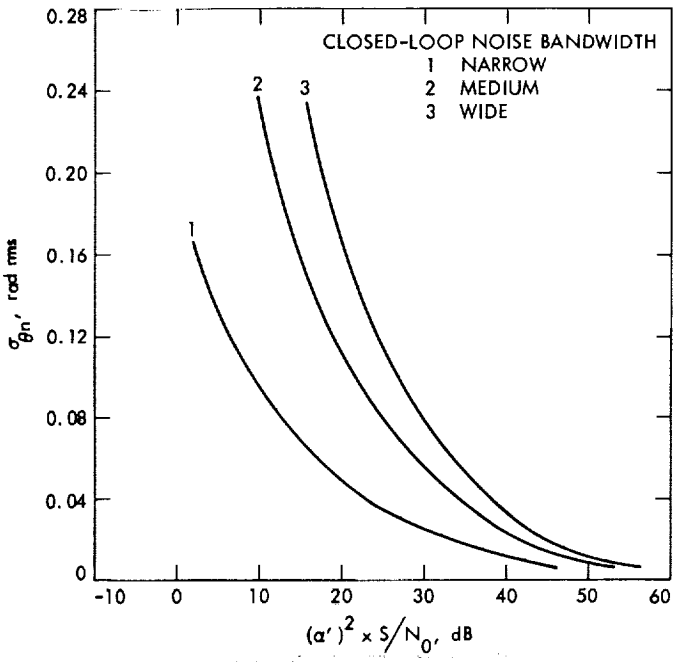

Fig. 24. Telemetry subcarrier demodulator rms phase noise error vs predetection signal-to-noise spectral density ratio parameter

Using the information on rms phase error $\sigma_{\theta n}$ presented in Fig. 24, the ratio of demodulated ST_{SY}/N_0 to input ST_{SY}/N_0 (demodulation efficiency) is determined from Expression (35) for various values of phase error due to doppler frequency shift and/or rate. Figures 25a, b, and c show the resulting characteristic as a function of $(\alpha')^2 \times S/N_0$ for the three bandwidth designs which have the same general application as Fig. 24.

The effect of subcarrier frequency offset and/or doppler shift on subcarrier loop performance is determined from the following relationship for phase error $\Delta\theta$:

$$\Delta\theta = \frac{\Delta F}{G} \tag{44}$$

Application of the design parameters provides the nominal characteristics shown in Figs. 26a and b, which have the same general application as the performance characteristics presented in Figs. 24 and 25.

As a convenience in using the performance characteristics shown in Figs. 23 through 26, the data suppression α' curves of Fig. 18 are shown in Fig. 27 as $\log_{10}(\alpha')^2$ versus ST_{SY}/N_0 for τ_D/T_{SY} equal to ⅓ and ⅙.

h. Application to Mariner Mars 1969. The *Mariner* Mars 1969 missions will include both uncoded and block-coded PSK telemetry with biorthogonal coding. Application of the telemetry subcarrier demodulator performance characteristics in *Paragraph g* of this article provides the theoretical demodulator performance capability for these missions.

For *Mariner* Mars 1969, the uncoded telemetry data rates are 8⅓, 33⅓, 66⅔, and 270 bits/s with a bit error rate of $5/10^3$ at minimum operating condition, which corresponds to an ST_{SY}/N_0 (moc) of +5.2 dB (Ref. 4). A 10% bit error rate at mission dp corresponds to an ST_B/N_0 (dp) of −1.0 dB. Consider the data rate of 8⅓ bits/s at $ST_B/N_0 = -1$ dB for the case where $\tau_D/T_{SY} = ⅓$ and an assumed 50% probability that the data bit stream switches on successive bit periods (note: $T_B = T_{SY}$).

$$\frac{ST_B}{N_0} = -1.0\,\text{dB}$$

For 8⅓ bits/s,

$$\frac{1}{T_B} = +9.2\,\text{dB/bit}$$

$$\therefore \frac{S}{N_0} = +8.2\,\text{dB}$$

From Fig. 27,

$$(\alpha')^2_{\text{dB}} = -6.2\,\text{dB}$$

$$\therefore (\alpha')^2 \times \frac{S}{N_0} = +2.0\,\text{dB}$$

For operation on narrow subcarrier loop bandwidth:

From Fig. 23,

$$BW_{SCL} = 0.031\,\text{Hz}$$

From Fig. 24,

$$\sigma_{\theta n} = 0.65\,\text{rad rms}$$

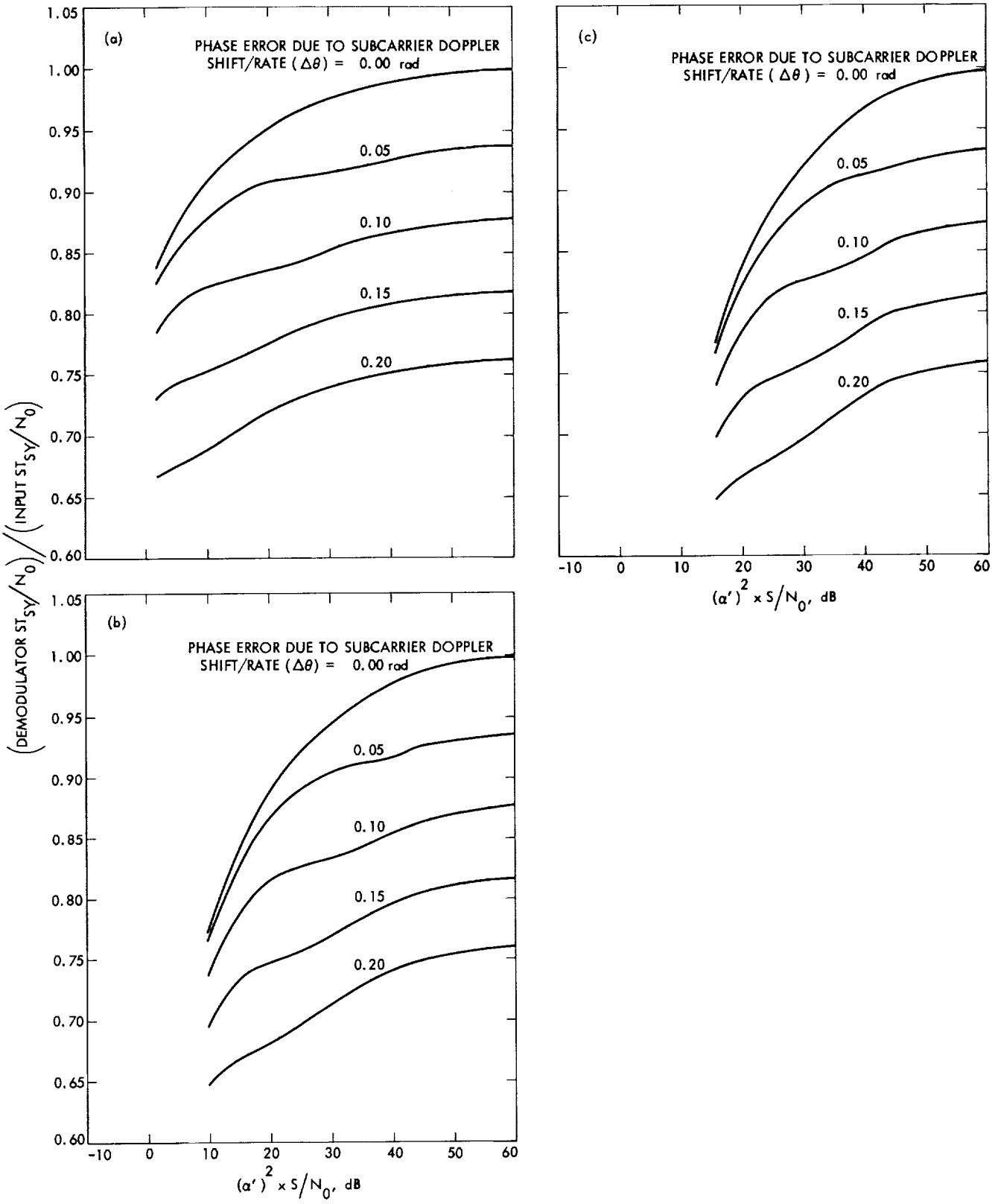

Fig. 25. Demodulated ST_{SY}/N_0 vs telemetry demodulator predetection signal-to-noise spectral density ratio parameter, subcarrier loop noise bandwidth: (a) narrow, (b) medium, (c) wide

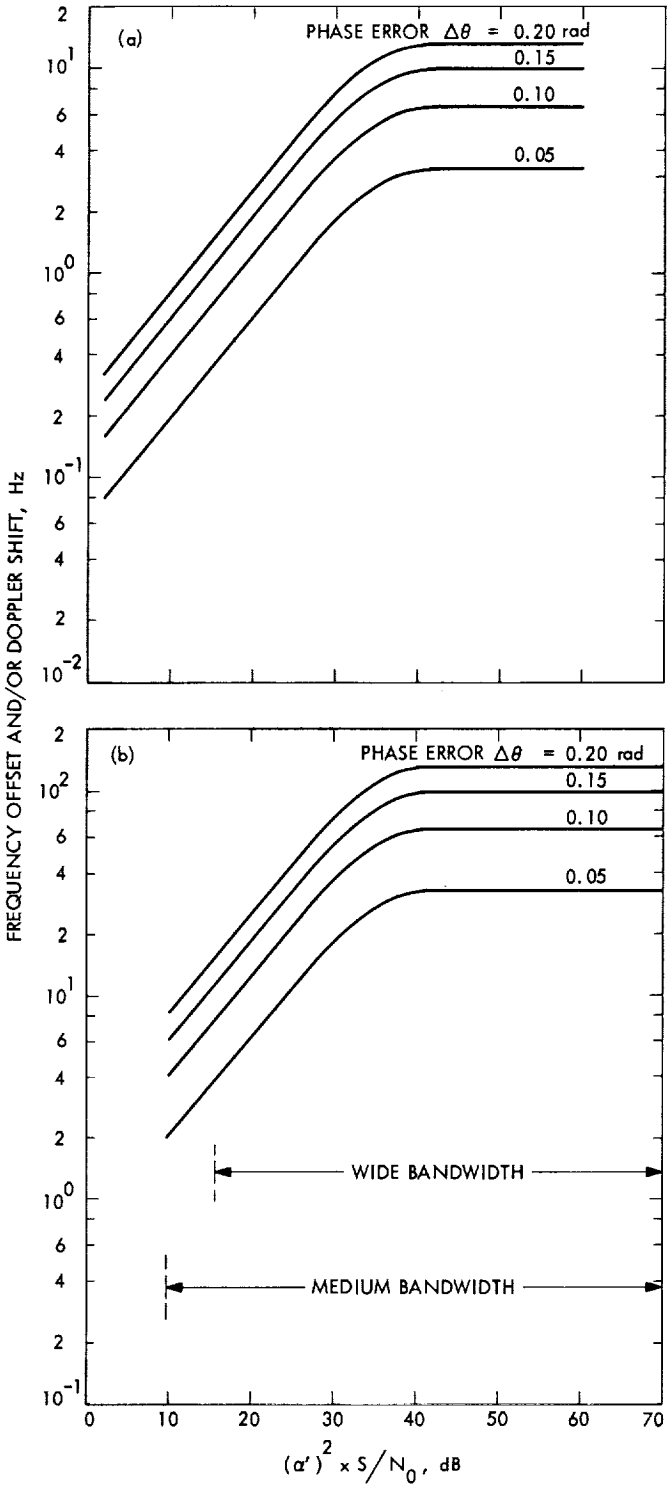

Fig. 26. Subcarrier frequency offset vs signal-to-noise spectral density ratio parameter, subcarrier loop noise bandwidth: (a) narrow, (b) medium or wide

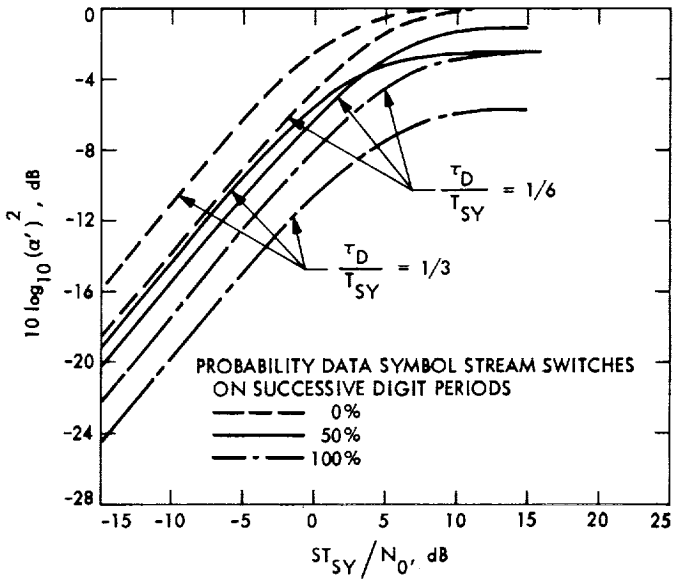

Fig. 27. Telemetry subcarrier demodulator data suppression factor vs ratio of signal energy per symbol to noise spectral density

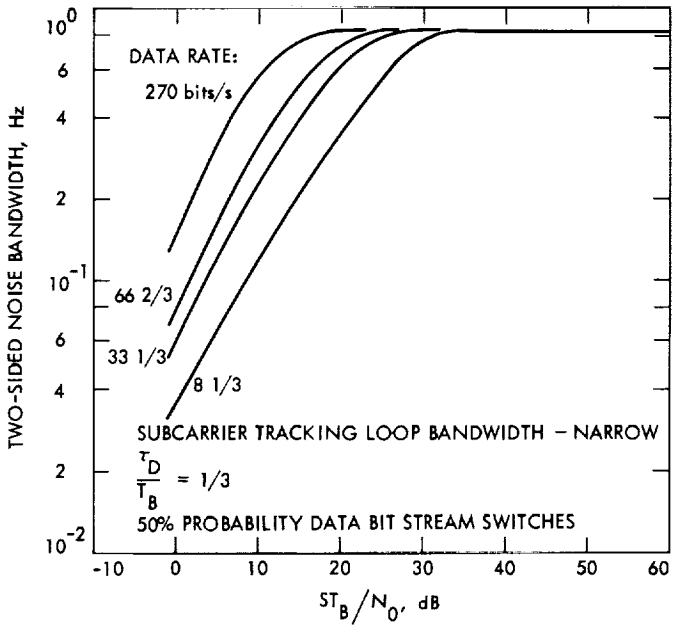

Fig. 28. *Mariner* Mars 1969 uncoded telemetry, telemetry demodulator two-sided closed-loop noise bandwidth vs ratio of signal energy per bit to noise spectral density

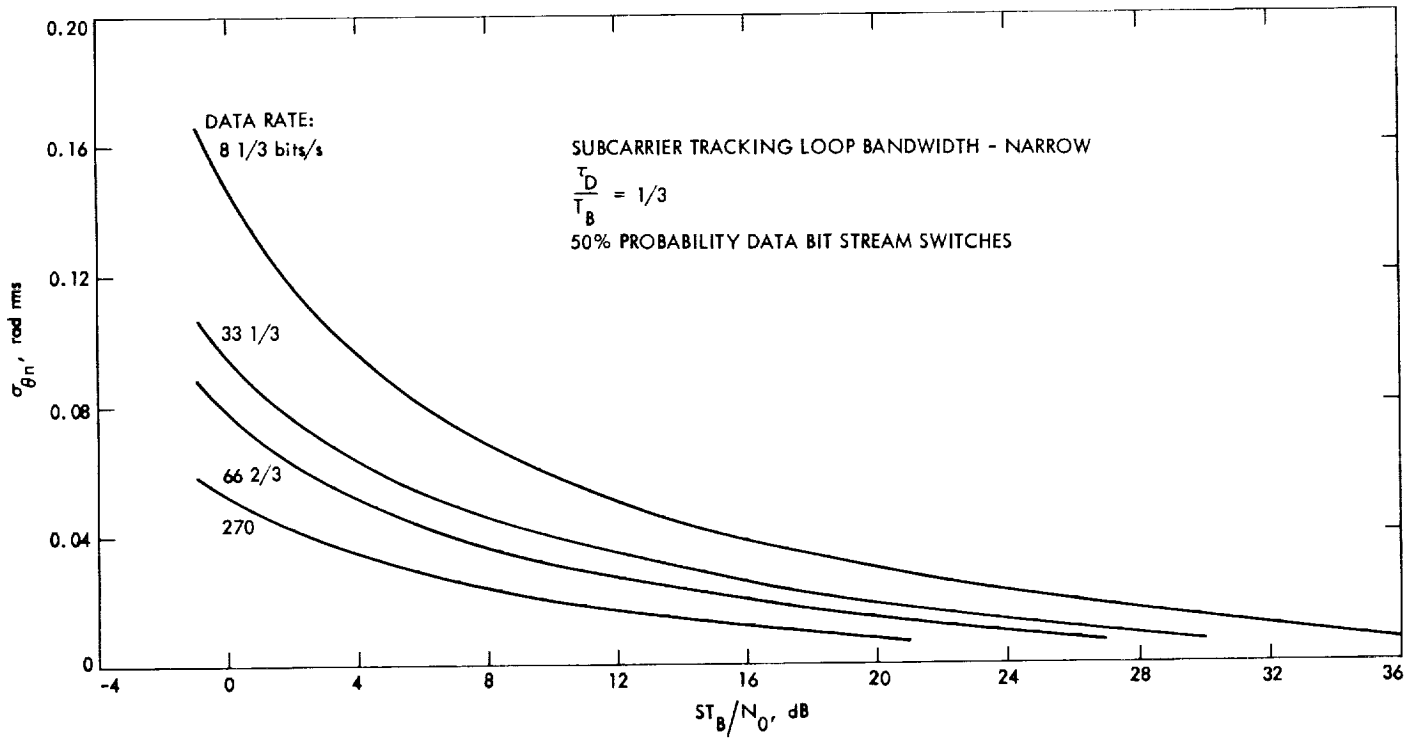

Fig. 29. *Mariner* Mars 1969 uncoded telemetry, telemetry demodulator rms phase noise error vs ratio of signal energy per bit to noise spectral density

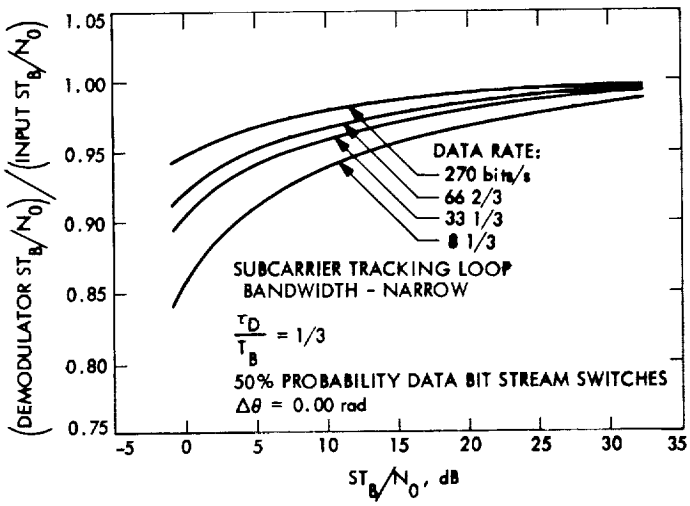

Fig. 30. *Mariner* Mars 1969 uncoded telemetry, demodulation efficiency vs ratio of signal energy per bit to noise spectral density

From Fig. 25 for $\Delta\theta = 0$ rad,

$$\frac{\text{demodulated } \frac{ST_B}{N_0}}{\text{input } \frac{ST_B}{N_0}} = 0.840$$

Proceeding in this manner, the performance characteristics shown in Figs. 28, 29, and 30 are obtained for uncoded data rates of 8⅓, 33⅓, 66⅔, and 270 bits/s.

References

1. Davenport, W. B., "Signal-to-Noise Ratios in Bandpass Limiters," *J. Appl. Phys.*, Vol. 24, No. 6, pp. 720–727, June 1953.
2. Tausworthe, R. C., *Theory and Practical Design of Phase-Locked Receivers, Vol. I,* Technical Report 32-819. Jet Propulsion Laboratory, Pasadena, Calif., Feb. 15, 1966.
3. Jaffe, R. M., and Rechtin, E., "Design and Performance of Phase-Lock Circuits Capable of Near-Optimum Performance Over a Wide Range of Input Signals and Noise Levels," *IRE Trans. Info. Theory,* Vol. IT-1, pp. 66–76, Mar. 1955.
4. Golomb, S. W., Baumert, L. D., Easterling, M. F., Stiffler, J. J., and Viterbi, A. J., *Digital Communications.* Prentice-Hall, Inc., Englewood Cliffs, N.J., 1964.

6. High-Rate Telemetry Project: Subcarrier Demodulator Performance, *M. H. Brockman*

This article provides information on the performance of the telemetry subcarrier demodulator which incorporates a soft bandpass limiter in the subcarrier tracking loop. Reference material pertaining to the following discussion is contained in *Subsection 5* of this SPS (MMTS: Performance of Subcarrier Demodulator).

For *Mariner* Mars 1969, the block-coded telemetry data will have a data rate of 16.2 kbits/s with 6 bits/word. At minimum operating condition (moc), a 1% word-error rate is specified which corresponds to an ST_B/N_0 (moc) of very nearly +3.0 dB (Ref. 1). Since $l = 2^5/6$ symbols/bit, and $ST_{SY}/N_0 = 1/l \times ST_B/N_0$, the corresponding ST_{SY}/N_0 (moc) is −4.3 dB with a symbol rate of 86.4 ksymbols/s. At mission dp, a 10% bit-error rate corresponds to an ST_B/N_0 (dp) of very nearly −1.0 dB, which provides an ST_{SY}/N_0 (dp) of −8.3 dB. Consider the case at ST_{SY}/N_0 (dp), where $\tau_D/T_{SY} = 1/3$ and there is an assumed 50% probability that the data symbol stream switches.

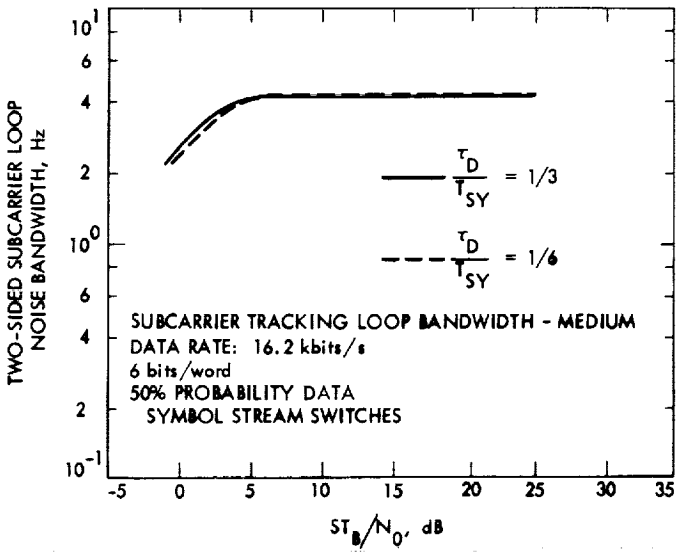

Fig. 31. *Mariner* Mars 1969 high-rate block-coded telemetry, telemetry demodulator two-sided closed-loop noise bandwidth vs ratio of signal energy per bit to noise spectral density

$$\frac{ST_{SY}}{N_0} = -8.3 \text{ dB}$$

For 86.4 ksymbols/s,

$$\frac{1}{T_{SY}} = +49.4 \text{ dB/symbol}$$

$$\therefore \frac{S}{N_0} = +41.1 \text{ dB}$$

From Fig. 27, (*Subsection 5*)

$$(\alpha')^2_{\text{dB}} = -12.6 \text{ dB}$$

$$\therefore (\alpha')^2 \times \frac{S}{N_0} = +28.5 \text{ dB}$$

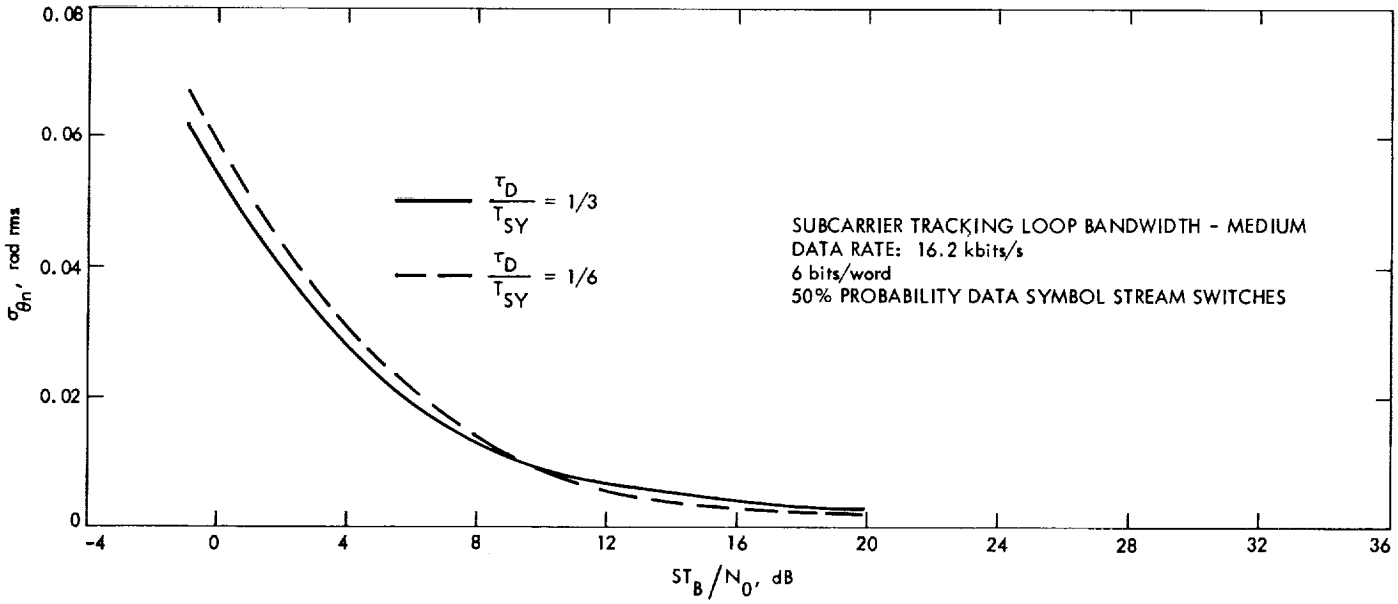

Fig. 32. *Mariner* Mars 1969 high-rate block-coded telemetry, telemetry demodulator rms phase noise error vs ratio of signal energy per bit to noise spectral density

For operation on medium subcarrier loop bandwidth:

From Fig. 23,

$$BW_{SCL} = 2.18 \text{ Hz}$$

From Fig. 24,

$$\sigma_{\theta n} = 0.062 \text{ rad rms}$$

From Fig. 25c, for $\Delta\theta = 0$ rad,

$$\frac{\text{demodulated } \frac{ST_{SY}}{N_0}}{\text{input } \frac{ST_{SY}}{N_0}} = 0.938$$

Continuing in this manner, the performance characteristics shown in Figs. 31, 32, and 33 are obtained for τ_D/T_{SY} equal to ⅓ and ⅙. The transformation of ST_{SY}/N_0 to the corresponding ST_B/N_0 has been made in Figs. 31, 32, and 33 as a convenience in interpreting the resulting performance.

It should be pointed out that the characteristics discussed above for the block-coded phase-shift key at 16.2 kbits/s and 6 bits/word are based on the assumption that the data symbol rate and subcarrier frequency are incoherent (statistically independent). They are, however, coherent in this case with three subcarrier cycles per symbol period. As a consequence, selection of τ_D/T_{SY}

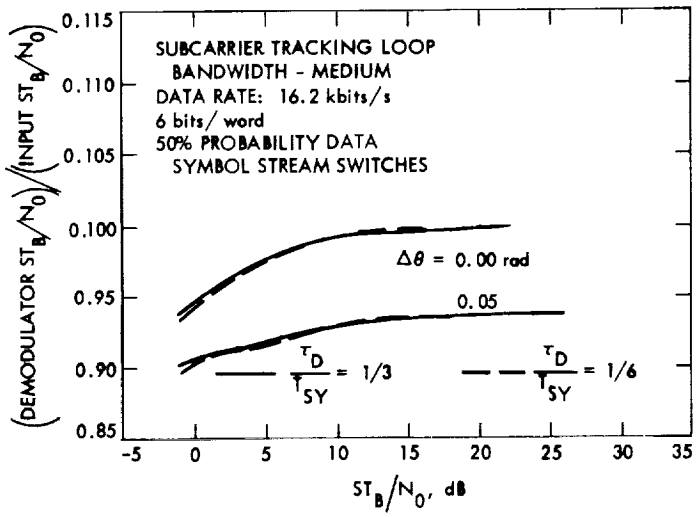

Fig. 33. *Mariner* Mars 1969 high-rate block-coded telemetry, demodulation efficiency vs ratio of signal energy per bit to noise spectral density

will, in all probability, be based on minimizing the phase error $\Delta\theta$ which results from this coherence, should it be significant (see SPS 37-51, Vol. II, pp. 136–140). Figure 33 illustrates the effect of the phase error $\Delta\theta$ on the demodulation efficiency of the telemetry subcarrier demodulator.

Reference

1. Golomb, S. W., et al., *Digital Communications.* Prentice-Hall, Inc., Englewood Cliffs, N.J., 1964.

V. Operations and Systems Data Analysis

A. Ground Communications Facility Operations

1. Flight Project Support, F. E. Bond, Jr.

a. Pioneer Project. The normal complement of voice and teletype circuits interconnecting the SFOF and the DSIF stations assigned to track the *Pioneer VIII* spacecraft was provided as scheduled. Received data were provided for tracking and data analysis to SFOF users, as well as to contractor personnel at TRW in Redondo Beach, California, and to the Ames Research Center at Palo Alto, California, over discrete voice and teletype circuits allocated for this purpose. All real-time DSN communications support was provided in accordance with existing plans.

Plans are currently being developed relative to the ground communications required for the *Pioneer IX* mission. Initial indications reveal that this mission will require communications of a somewhat more complex nature than previous *Pioneer* missions, but that the total communications support required is within the capabilities of the DSN/GCF.

b. Mariner V extended mission operations. The DSIF was scheduled to reacquire the *Mariner V* spacecraft on July 22, 1968, and to continue tracking until January 22, 1969. In view of this requirement, total communications plans were developed and documented for the committed support. As of this date, the spacecraft has not been reacquired, but full communications support is available when needed for telemetry, tracking, and command activities.

The operational simplex teletype circuit from the SFOF to Stanford University required by the *Mariner V* Extended Mission Operations (MEMO) Project is installed and operational. The operational simplex teletype circuits to the University of Iowa and the University of Colorado, both from the SFOF, and a similar circuit to the Massachusetts Institute of Technology, from Goddard Space Flight Center, have been installed in accordance with MEMO requirements.

c. Mariner Mars 1969 Project. Because of the complex communications requirements established by the *Mariner* Mars 1969 Project and the necessity for initial audio, teletype, and video configurations in the assigned SFOF areas, efforts are now underway to define the total requirements and design the configurations. Subsequent to such actions, all operational communications plans will be documented to ensure that the required DSN/GCF support will be efficiently provided during the simulation, launch, and cruise phases of the *Mariner* Mars 1969 spacecraft.

d. Biosatellite Project. Based on preliminary information, communications plans are being developed to receive high-speed data from the Space Tracking and Data Acquisition Network (STADAN) over DSN/GCF circuits at the SFOF for further processing in SFOF computer facilities. The original proposals for this support specify that two 30-day missions are contemplated and that data flow will occur for approximately 10 h each day during the scheduled missions for March and September 1969.

B. DSN Systems Data Analysis

1. Computation of the Normal Matrix for Discrete Multidimensional Approximations, A. C. Johnson

a. Introduction. Occasionally, it is desirable to obtain a multidimensional linear least-squares polynomial approximation to a function whose value is known only for a discrete or finite set of points. This problem arises, for example, when obtaining estimates of antenna pointing errors.

In this connection, the following questions have been asked: "How does one form the normal equations or the normal matrix when there are two or more variables?" and, "Precisely how does the number of data points used enter into the approximation problem?"

When considering two or more variables, the formulation of the normal matrix, while not difficult, is quite tedious and is generally known to the mathematician only. The number of data points used is directly related to the approximation problem, and the answers can be deduced from the general theory of approximations on normed linear spaces. It will be noted that the results presented can easily be extended to the case of any number of variables and is not limited to polynomial approximations. This method is a more general and straightforward approach to the formulation and computation of the normal matrix corresponding to discrete multidimensional approximations.

b. Abstract formulation of the discrete linear approximation problem. Let V denote the linear space of all bounded functions $f(x, y)$ defined on a given region D in two-space.

$$D = (x, y), \qquad a \leq x \leq b, c \leq y \leq d$$

Let (x_i, y_j)—$i = 0, 1, \cdots N$; $j = 0, 1, \cdots M$—be any set of points D' in D.

$$D' = (x_i, y_j), \qquad (x_i, y_j) \in D; i = 0, 1, \cdots N; j = 0, 1, \cdots M$$

Now introduce an "equivalence" relation on V, $f_1 \sim f_2$, if, and only if,

$$f_1(x_i, y_j) = f_2(x_i, y_j), \qquad (x_i, y_j) \in D'$$

Let $\overline{V}$ denote the family of all equivalence classes of functions in V. If a is a constant and $\overline{f} \in \overline{V}$, then by $\overline{af}$ is meant the equivalence class of af, denoted by $\overline{af}$. With this definition of scalar product, it is easy to prove that $\overline{V}$ is a linear space. Moreover, the dimension of $\overline{V}$ is finite and may be deduced in the following way.

The function $f \in V$ is equivalent to the function g_f where

$$g_f(x, y) = \begin{cases} f(x, y), & (x, y) \in D' \\ 0, & \text{otherwise} \end{cases}$$

Let

$$\overline{\epsilon}_{ij}(x, y) = \begin{cases} 1, & (x, y) = (x_i, y_j), i = 0, 1, \cdots N \\ & \quad j = 0, 1, \cdots, M \\ 0, & \text{otherwise} \end{cases}$$

Then the $(N + 1)(M + 1)$ vectors, $\overline{\epsilon}_{ij}(x, y)$, are linearly independent and every $\overline{g}_f$ is a linear combination of the $\overline{\epsilon}_{ij}$.

$$\overline{g}_f(x, y) = \sum_{i=0}^{M} \sum_{j=0}^{N} f(x_i, y_j)\, \overline{\epsilon}_{ij}(x, y)$$

Thus, the dimension of $\overline{V}$ is $(N + 1)(M + 1)$ [so that V is algebraically equivalent to the vector space of $(N + 1)(M + 1)$-tuples].

Next, define an "inner" product of two vectors $\overline{f}_1$ and $\overline{f}_2$ in $\overline{V}$ by means of the function

$$\left\langle \overline{f}_1, \overline{f}_2 \right\rangle = \sum_{i=0}^{N} \sum_{j=0}^{M} f_1(x_i, y_j)\, f_2(x_i, y_j) \tag{1}$$

The following relations are easily verified directly from the definitions

$$\left\langle a\overline{f}_1, b\overline{f}_2 \right\rangle = ab \left\langle \overline{f}_2, \overline{f}_1 \right\rangle, \qquad a \text{ and } b \text{ are constants} \tag{2}$$

$$\left\langle \overline{f}_1 + \overline{f}_2, \overline{f}_3 \right\rangle = \left\langle \overline{f}_1, \overline{f}_3 \right\rangle + \left\langle \overline{f}_2, \overline{f}_3 \right\rangle \tag{3}$$

$$\left\langle \overline{f}_1, \overline{f}_1 \right\rangle = 0, \qquad \text{if, and only if, } \overline{f}_1 = \overline{0} \tag{4}$$

i.e., f_1 is equivalent to the function which is identically zero on D. The Relations (2), (3), and (4) show that the inner product defined here is a positive definite, symmetric bilinear function and hence can be used to define a "suitable" norm on $\overline{V}$. (By a "suitable" norm or "distance" function, one usually means a real-valued function on $\overline{V} \times \overline{V}$ which satisfies our intuitive notions of distances between points in space. For example, the distance between distinct points should be positive.) By definition, the "norm" of $\overline{f} \in \overline{V}$, or the "distance" of $\overline{f}$ from $\overline{0} \in \overline{V}$, is defined as

$$||\overline{f}|| = \langle \overline{f}, \overline{f} \rangle^{1/2} = \left[\sum_{i=0}^{M} \sum_{j=0}^{N} f^2(x_i, y_j) \right]^{1/2}$$

and the "distance" of $\overline{f}_1$ from $\overline{f}_2$ is given by the equation

$$||\overline{f}_1 - \overline{f}_2|| = \left\{ \sum_{i=0}^{N} \sum_{j=0}^{M} [f_1(x_i, y_j) - f_2(x_i, y_j)]^2 \right\}^{1/2} \quad (5)$$

Thus, one can formulate the discrete linear approximation problem for functions or vectors $\overline{f}$, which are elements of a finite dimensional normed linear space $\overline{V}$. Note that an approximation to $\overline{f} \in \overline{V}$ is interpreted as an approximation to a family of functions; namely, that family which takes on the values $f(x, y)$ whenever $(x, y) \in D'$. One can now apply the following well-known theorem concerning (least-squares) approximations on normed linear spaces.

Theorem. If $\overline{R}$ is a subspace of a finite dimensional normed linear space $\overline{V}$ and if $\overline{f}$ is any vector in $\overline{V} - \overline{R}$, then there exists a unique vector $\overline{f}_0 \in \overline{R}$ such that

$$||\overline{f}_0 - \overline{f}|| < ||\overline{f} - \overline{g}|| \quad (6)$$

for every vector $\overline{g} \in \overline{R} - [f_0]$. Moreover, if the "norm" on $\overline{V}$ is "induced" by an inner product then

$$\langle \overline{f} - \overline{f}_0, \overline{g} \rangle = 0 \quad (7)$$

for every $\overline{g} \in \overline{R}$.

Relation (7) enables one to determine explicitly that vector $\overline{f}_0$ deviates least from a given $\overline{f}$. For if $\overline{r}_k, k = 0, 1, \cdots K$ is a basis for $\overline{R}$, then since $\overline{f}_0 \in \overline{R}$, there exist constants a_k such that

$$\overline{f}_0(x, y) = \sum_{k=0}^{K} a_k \overline{r}_k(x, y) \quad (8)$$

Moreover, since $\overline{r}_k \in \overline{R}$, it follows from Relation (7) that

$$\langle \overline{f} - f_0, \overline{r}_k \rangle = 0, \qquad k = 0, 1, \cdots K$$

or

$$\langle \overline{f}_0, \overline{r}_k \rangle = \langle \overline{f}, \overline{r}_k \rangle, \qquad k = 0, 1, \cdots K \quad (9)$$

On substituting in Eqs. (9) the value of $\overline{f}_0$ in Eqs. (8),

$$\sum_{t=0}^{K} a_t \langle \overline{r}_t, \overline{r}_k \rangle = \langle \overline{f}, \overline{r}_k \rangle, \qquad k = 0, 1, \cdots K \quad (10)$$

Equations (10) are the "normal" equations.

c. Applications to multidimensional least-squares polynomial approximations. Let R be that linear subspace of V consisting of all polynomials of the form

$$P(x, y) = \sum_{t=0}^{T} \sum_{q=0}^{Q} a_{tq} x^t y^q$$

where $T < N, Q < M$, and $(N + 1)(M + 1)$ is the dimension of the space $\overline{V}$ defined above. Since $T < N$ and $Q < M$, it follows that if $P_1, P_2 \in R$, then $P_1 \sim P_2$, if, and only if, $P_1(x, y) \equiv P_2(x, y), (x, y) \in D$. Thus, in the statement of the above theorem, $\overline{R}$ may be replaced by R, and hence there is only *one* polynomial which deviates the least from a given $\overline{f} \in \overline{V}$.

It is obvious that the functions

$$x^t y^q, t = 0, 1, \cdots T, \qquad q = 0, 1, \cdots Q$$

form a basis for R. Let $\overline{f}$ be a given function in $\overline{V}$ with values

$$f(x_i, y_j), (x_i, y_j) \in D'$$

Then the normal equations corresponding to a least-squares polynomial approximation to $\overline{f}(x, y)$, or equivalently to $f(x, y), (x, y) \in D'$, are by Relation (7) the following:

$$\sum_{t=0}^{T} \sum_{q=0}^{Q} a_{tq} \langle x^t y^q, x^r y^l \rangle = \langle f, x^r y^l \rangle,$$
$$r = 0, 1, \cdots T; l = 0, 1, \cdots T \quad (11)$$

or, using the definition of the inner product, Eqs. (11) take the form

$$\sum_{t=0}^{T}\sum_{q=0}^{Q} a_{tq}\left(\sum_{i=0}^{N}\sum_{j=0}^{M} x_i^{t+r}\, y_j^{q+l}\right) = \sum_{i=0}^{N}\sum_{j=0}^{M} f(x_i, y_j)\, x_i^r\, y_j^l\,, \qquad r = 0, 1, \cdots T;\ l = 0, 1, \cdots Q \tag{12}$$

For the case $T = 2$, $Q = 2$, the normal matrix is given in Table 1.

d. Application to antenna pointing error problem. Star track data consists of local hour angles (LHA) and declination (dec) of a star—measured in station-fixed coordinates. LHA and dec errors are defined as the difference between the observed positions of a star, obtained from antenna angle encoders, and the calculated (refraction-corrected) apparent positions. Least-squares polynomial regression is used to obtain a best estimate of LHA and dec antenna pointing errors.

Star track errors in the local hour angles and declinations are denoted by ΔLHA and Δdec, respectively, and are defined by

$$\Delta LHA = LHA_o - LHA_c$$

$$\Delta dec = dec_o - dec_c$$

where LHA_o, LHA_c (dec_o, dec_c) denote, respectively, the observed and computed values of LHA (dec).

Estimation formulas for ΔLHA and Δdec are assumed in the form

$$\Delta LHA = \sum_{ij} A_{ij}(LHA_o)^i\,(dec_o)^j$$

$$\Delta dec = \sum_{ij} B_{ij}(LHA_o)^i\,(dec_o)^j$$

where A_{ij} and B_{ij} are calculated by means of Eq. (12).

References

1. Halmos, P. R., *Finite Dimensional Vector Spaces.* Princeton University Press, Princeton, New Jersey, 1948.
2. Taylor, A. E., *Introduction to Functional Analysis.* John Wiley & Sons, Inc., New York, 1957.

Table 1. The normal matrix for the case $T = Q = 2$

(r, l)	Matrix								
(0, 0)	$\langle 1, 1\rangle$	$\langle y, 1\rangle$	$\langle y^2, 1\rangle$	$\langle x, 1\rangle$	$\langle xy, 1\rangle$	$\langle xy^2, 1\rangle$	$\langle x^2, 1\rangle$	$\langle x^2y, 1\rangle$	$\langle x^2y^2, 1\rangle$
(0, 1)	$\langle 1, y\rangle$	$\langle y, y\rangle$	$\langle y^2, y\rangle$	$\langle x, y\rangle$	$\langle xy, y\rangle$	$\langle xy^2, y\rangle$	$\langle x^2, y\rangle$	$\langle x^2y, y\rangle$	$\langle x^2y^2, y\rangle$
(0, 2)	$\langle 1, y^2\rangle$	$\langle y, y^2\rangle$	$\langle y^2, y^2\rangle$	$\langle x, y^2\rangle$	$\langle xy, y^2\rangle$	$\langle xy^2, y^2\rangle$	$\langle x^2, y^2\rangle$	$\langle x^2y, y^2\rangle$	$\langle x^2y^2, y^2\rangle$
(1, 0)	$\langle 1, x\rangle$	$\langle y, x\rangle$	$\langle y^2, x\rangle$	$\langle x, x\rangle$	$\langle xy, x\rangle$	$\langle xy^2, x\rangle$	$\langle x^2, x\rangle$	$\langle x^2y, x\rangle$	$\langle x^2y^2, x\rangle$
(1, 1)	$\langle 1, xy\rangle$	$\langle y, xy\rangle$	$\langle y^2, xy\rangle$	$\langle x, xy\rangle$	$\langle xy, xy\rangle$	$\langle xy^2, xy\rangle$	$\langle x^2, xy\rangle$	$\langle x^2y, xy\rangle$	$\langle x^2y^2, xy\rangle$
(1, 2)	$\langle 1, xy^2\rangle$	$\langle y, xy^2\rangle$	$\langle y^2, xy^2\rangle$	$\langle x, xy^2\rangle$	$\langle xy, xy^2\rangle$	$\langle xy^2, xy^2\rangle$	$\langle x^2, xy^2\rangle$	$\langle x^2y, xy^2\rangle$	$\langle x^2y^2, xy^2\rangle$
(2, 0)	$\langle 1, x^2\rangle$	$\langle y, x^2\rangle$	$\langle y^2, x^2\rangle$	$\langle x, x^2\rangle$	$\langle xy, x^2\rangle$	$\langle xy^2, x^2\rangle$	$\langle x^2, x^2\rangle$	$\langle x^2y, x^2\rangle$	$\langle x^2y^2, x^2\rangle$
(2, 1)	$\langle 1, x^2y\rangle$	$\langle y, x^2y\rangle$	$\langle y^2, x^2y\rangle$	$\langle x, x^2y\rangle$	$\langle xy, x^2y\rangle$	$\langle xy^2, x^2y\rangle$	$\langle x^2, x^2y\rangle$	$\langle x^2y, x^2y\rangle$	$\langle x^2y^2, x^2y\rangle$
(2, 2)	$\langle 1, x^2y^2\rangle$	$\langle y, x^2y^2\rangle$	$\langle y^2, x^2y^2\rangle$	$\langle x, x^2y^2\rangle$	$\langle xy, x^2y^2\rangle$	$\langle xy^2, x^2y^2\rangle$	$\langle x^2, x^2y^2\rangle$	$\langle x^2y, x^2y^2\rangle$	$\langle x^2y^2, x^2y^2\rangle$

2. An Improved Method for Range Delay Calibration,

S. C. Ward and F. Borncamp

a. Introduction. Any RF ranging system determines range by measuring propagation (delay) time to the target and back. This propagation time includes delays caused by equipment and cables as well as those caused by the round-trip signal transit time. To make the system accurate, these nonspace-caused delays must be found and subtracted from the range. The JPL range-measuring system converts accumulated phase of a pseudonoise coded phase-modulated carrier to the spacecraft and back into range, effectively measuring range at lunar distances to better than 15-m accuracy.

This article suggests a revised method of measuring the portion of the range measurement caused by delays in the ground station equipment. The new method requires significantly less man-hours to perform the calibration, and it also may be used at all stations, including the Mars DSS. Tests were conducted at the Pioneer DSS to compare the new method with the old, and the results show the two methods to be of equivalent accuracy.

b. The present method. The system presently used by the DSIF is the "big black box" concept (Fig. 1). Basically, it involves ranging over a "known" distance with overall ground equipment, including the tracking antenna defined as a large black box. All delays outside the box are accurately known; thus leaving the difference between measured range and the actual range due only to the box.

Although this method of calibration is effective and reasonably accurate, it has the following faults:

(1) A first-order survey is necessary, and the survey is complicated by the fact that it must be referenced to the RF axis of the tracking antenna—a point that is not readily accessible to the surveyor.

(2) The tracking antenna must be deflected to the collimation tower, thus preventing calibration of the system with the antenna at or near the positions used during spacecraft tracking.

(3) To ensure that the calibration is performed at the same power levels (both uplink and downlink) as those expected during a spacecraft track, a technician must go to the spacecraft simulating equipment at the collimation tower to activate it and to adjust the backside attenuators that control downlink power. This becomes a problem at stations where the collimation tower is difficult to reach. At two DSIF stations, a team of two men must be sent; during inclement weather, the collimation tower cannot be reached at all.

(4) Stations using 210-ft-diam antennas cannot be calibrated because there is no collimation tower. (The

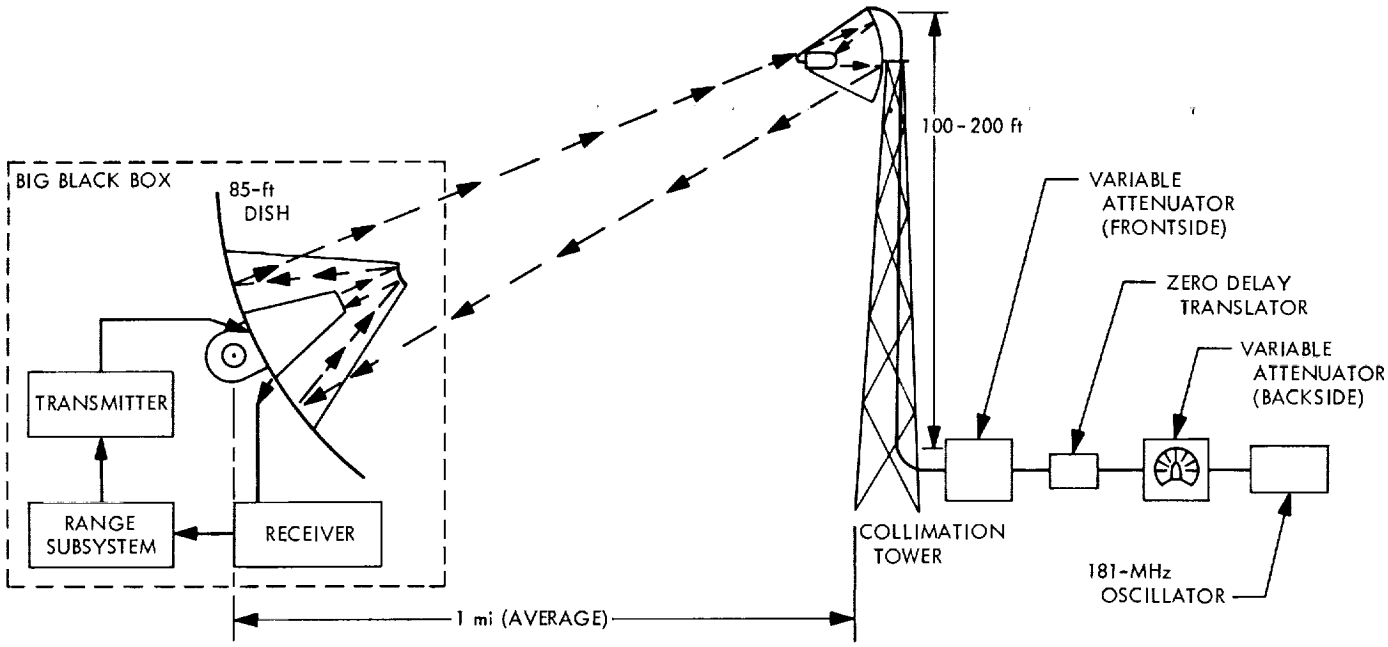

Fig. 1. Present black box method for range delay calibration

required tower would have to be 11 mi in height and located 26 mi away.)

Also contributing to the uncertainties of this method, or limiting the flexibility, are the following conditions:

(1) Because the collimation tower antenna is from 100 to 200 ft above ground, it is difficult to measure accurately its propagation velocity. It, therefore, must be estimated from the manufacturer's specifications.

(2) The propagation velocity calibration of the 100 to 250 ft of coaxial cable varies with temperature, condition of the dielectric (moisture, breaks), and unverified changes in the cable or sections thereof.

(3) To prevent damage to the translator diode, frontside attenuators are required at uplink power above 100 W. The present off-the-shelf attenuators are only good to 10 kW and, therefore, cannot be used for calibrating at 20 kW.

c. New method. The revised method is basically the same as the big black box method, except the turnaround translator is mounted on the edge of the 85-ft-diam dish. The location was chosen to minimize possible multipath effects off the quadripod. In addition, it was desirable to find a mounting point which would not involve using any of the present mesh surface of the dish. The location and suggested method of mounting is shown in Fig. 2.

The station measured the delay, using the same techniques as if they were ranging to the collimation tower. Only a small known figure is necessary to measure back to the reference point at the intersection of the RF axis and the centerline of the declination shaft. For the test, a cable was run from the translator about 100 ft to the variable attenuators and oscillator portion of the translator. Thus, only the antenna and diode were mounted on the dish edge. This permitted the operator to vary the downlink signal level as requested from the control room.

This proposed range-delay calibration technique eliminates the need for a survey and all the uncertainties and man-hours associated with the collimation-tower technique. The off-beam location has sufficient inherent attenuation (72 dB) to negate the need for frontside attenuators. Because the system can be calibrated with the tracking antenna in track position, all the uncertainties due to structural deflections and changes in the cable wrap-up are removed or greatly lessened.

Implementation of the following changes will further lessen required manpower and shorten the calibration procedure:

(1) Use a coherent (181-MHz) frequency for mixing at the diode, thus providing a zero doppler signal to the range subsystem. There are methods which can be used if an RF doppler signal is non-zero, but they can lead to errors and are somewhat inconvenient for the operator. The required signal is

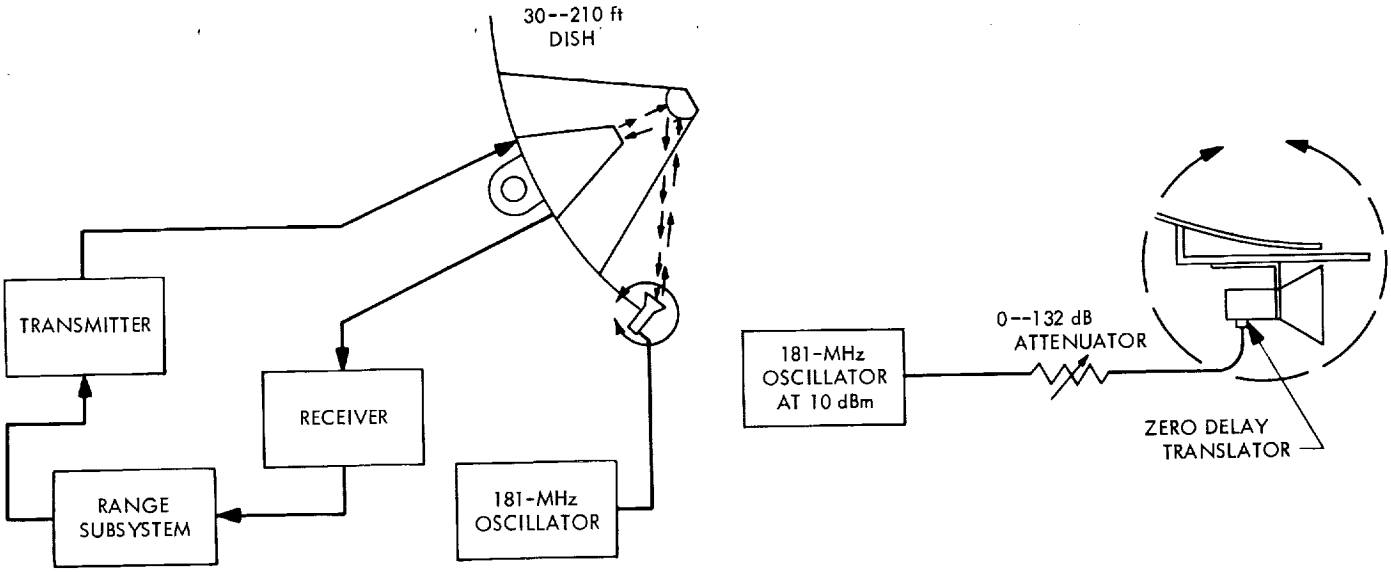

Fig. 2. Proposed method for range delay calibration

available as the exciter–voltage-controlled oscillator × 57/221 × 32 in the DSIF tracking and communications system GSDS 1967 model Block III-C receiver. A possible tie point is just before the test translator, where this signal is available.

(2) Place the variable attenuators located between the source (181 MHz) and the "zero delay" diode, so that the attenuators can be controlled from the receiver position in the control room. This can be achieved by placing an attenuator in the control room and connecting it to the 181-MHz source via a coaxial cable loop, or by using a motor-controlled attenuator at the site of the 181-MHz source.

(3) Use the digital instrumentation subsystem (a digital computer with paper tape, magnetic tape, digital-to-analog converter, multiplexer, input/output devices, etc.) to automate the calibration during countdown and post-tracking. This would reduce a six-step procedure to one step and produce much more accurate results.

d. Test results. The test at the Pioneer DSS was designed to measure the error found for each method of calibration and to compare the calibration results.

Table 2 shows the data as obtained and after it is normalized to a common receiver signal level, transmitted power, and frequency. The first 6 measurements were made on the collimation tower, the second 6 on the dish mount, and the final 10 on the collimation tower.

The sum of the surveyed measurements for correcting the two calibration methods in order to reference them to the intersection of the RF axis and the declination shaft is 1616.65 range units (RU) for the collimation-tower method, and 5.61 RU for the dish-mount method. Thus, the following results are obtained:

Collimation-tower method, RU	1911.35 − 1616.65 = 294.70
Dish mount method, RU	300.80 − 5.61 = 295.19

Table 2. Test results

Transmitter power, kW	Exciter frequency, MHz	Received signal level, dB	Normalized delay[a] (1 kW, 22.046545 MHz, −100 dB), RU
Collimation tower[b]			
1.0	22.046545	−100	1911.6
1.0	22.046545	−110	1911.2
1.0	22.046545	−120	1911.2
1.0	22.046545	−130	1910.8
1.0	22.046545	−140	1911.2
5.0	22.046545	−100	1911.7
Dish mount[c]			
1.0	22.045841	−100	301.38
1.0	22.045841	−110	300.60
1.0	22.045843	−120	300.54
1.0	22.045843	−130	299.96
1.0	22.045843	−140	300.87
5.0	22.045843	−100	301.45
Collimation tower[b]			
1.0	22.045835	−110	1911.1
1.0	22.045827	−120	1911.0
1.0	22.045827	−130	1910.8
1.0	22.045821	−140	1912.0
5.0	22.045817	−100	1911.3
5.0	22.045545	−100	1911.1
1.0	22.045545	−100	1911.3
1.0	22.045545	−140	1912.3
1.0	22.045819	−100	1911.5
1.0	22.045835	−110	1911.0

[a]Normalization factors: frequency = +0.02584 RU/Hz; receiver signal level = −0.375 RU/10 dB; transmitter power = −3.8 RU/5 kW. An RU (range unit) is equivalent to 1.043470103 m.

[b]The mean of the values on the collimation tower is 1911.35 RU with a 1-σ deviation of 0.4 RU.

[c]The mean of the values on the dish mount is 300.80 RU with a 1-σ deviation of 0.5 RU.

The sum of the errors due to survey, cable ringing, etc., is about 0.5 RU. Thus, the results of the two calibration methods agree within the experimental accuracy of the test. A possible additional source of error is the nonlinearity of the phase shifter, which could contribute up to 1 RU. This could be present in both, one, or neither of the above station delay figures.

VI. Technical Facilities

A. Antennas

1. Woomera DSS Antenna Mechanical Upgrade,

W. Kissane and M. Kron

The mechanical upgrade of the Woomera DSS antenna structure and mechanical equipment (SPS 37-51, Vol. II, p. 174) is continuing. The hour-angle and declination gear segments were removed, and stiffening shear plates were welded to the rim of the hour-angle wheel to help maintain the shape of the wheel after the structure was loaded with counterweight. Also, several main members supporting the counterweight box were sequentially replaced with new members whose section properties reflect an increase in strength of 200% to 400%. The combined effects of the shear plates, the stronger members, and an increased number of fasteners at each joint connection have greatly reduced the deflection characteristics of the hour-angle wheel. As an adjunct to the replacement by stronger members, all joint fasteners were replaced with high-strength interference bolts to avoid slippage under cyclic loading conditions.

The entire structure was loaded with all of its operating dead loads, including the feed cone, and all of the gear segments on both the hour-angle and declination wheel were reset. The total indicated runout of the gear teeth was checked and adjusted such that the eccentricity error of the wheel meets specification requirements. The clearance between the wheel rim and the back surface of each gear segment is being filled with molten Kirksite. The new drive skids are being given a final adjustment for gear running clearances.

Installation of the new cable wrapup systems, developed on a prototype basis at the Goldstone DSCC, and associated cable tray runs were completed, as were preliminary measurements of the reflector surface and installation of the primary datum plane targets. Presently the initial data from theodolite readings are being reduced to determine the shim sizes to be used for the final dish setting.

Final detail work on the structure is under way concurrently with a review of the complete upgrade effort.

2. Echo DSS Antenna Mechanical Upgrade,

R. McKee and J. Carlucci

Modifications of the 85-ft-diam HA/dec antenna at the Echo DSS began in early February 1968. Previous reporting on these modifications appeared in SPS 37-51, Vol. II, pp. 171–173.

Rebolting of the pedestal, hour angle wheel, declination wheel, and box girder has been completed. Addition of welded gussets in the box girder area is also complete.

Old surface panels and attachment hardware have been removed, and setting of new panel attachment hardware is nearly complete. Installation of new high-performance S-band surface panels has begun with the installation of the inner row of panels and positioning of panels spanning two main rib trusses to the outer edge of the dish structure.

The upper and lower electronics rooms are nearly complete, with some insulated wall panels yet to be installed.

New hour angle and declination cable wrap-ups have been installed; installation of cable trays has begun on the pedestal structure.

New declination drives have been installed and rough set.

The declination gear has been reset and is ready for the final runout check and pouring of Kirksite (low-temperature metal shim between the gear segments and the wheel flange to create a solid metal shim). Resetting of the hour angle gear is in progress.

B. Buildings

1. SFOF *Mariner* Mars 1969 Mission Support Area, *M. Salem*

The *Mariner* Mars 1969 mission support area in the SFOF has been functionally specified, and a configuration determined. Detail designs for the necessary wall modifications and the electrical distribution system within the mission support area have been completed. As specified in the NASA Support Instrumentation Requirements Document, the *Mariner* Mars 1969 mission support area will contain the following distinct sub-areas: mission director's room, mission control room, observation room, spacecraft performance analysis area, conference room (existing), space science analysis area, principal investigator's area, and flight path analysis area (existing).

The physical arrangement of control and analysis areas is based upon previous *Mariner* Project operations wherein the mission control room was placed contiguous to the spacecraft analysis areas to improve interaction and communication. The mission control room will feature one of the round, six-man conference consoles used very successfully for the *Pioneer VIII* launch operations and the *Surveyor V, VI,* and *VII* mission operations. The mission director and his staff will be positioned such that they can observe all operations when necessary but can remain separated from the operations when desired. An observation room will permit visitors a direct view of all mission operations from outside the immediate analysis areas.

The spacecraft performance analysis area will house the spacecraft performance analysis and command director, an assistant director to head each of the two spacecraft teams, a test director and recorder for each team, and 20 analysts. The data display equipment will be that utilized for all mission operations conducted from the SFOF since the *Mariner IV* mission operations in 1964. Communications within the area, as well as with the remainder of the mission operations team, will be accomplished through the use of the operational voice communications subsystem networks. The television subsystem will be utilized for time display and dissemination of updated sequence-of-events information, as well as display of many individual elements of teletype information.

Analysts will be seated at desks or tables. The area director, his deputy, and an assistant will utilize the area director's consoles, which provide increased capability in both the television and voice communications subsystems. The height of these consoles is being lowered approximately 3 in., and their top is being sloped to provide a significant improvement in forward visibility for the operators.

C. Utilities

1. Goldstone DSCC Communications Switching Center, *B. G. Bridges*

To standardize communications equipment configurations throughout the DSN, it was decided to reconfigure the DSS communications switching centers. The reconfiguration of the center serving the entire Goldstone DSCC (located at the Echo DSS) is expected to be completed in September; that of the centers at the Woomera, Johannesburg, and Cebreros DSSs is scheduled for completion by January. The consolidation of equipment (tactical intercom, teletype, high-speed data, stations communications control group, and microwave) in one centrally located area—the primary goal of the reconfiguration effort—will result in fewer operational personnel being required; i.e., only one technician and one teletype operator will be required each schedule shift.

The interstation microwave switching equipment at the Goldstone DSCC center is shown in Fig. 1a. All communications coming from the Pioneer, Echo, Venus, and Mars DSSs are switched through to JPL. Conversely,

Fig. 1. Goldstone DSCC communications switching center equipment: (a) interstation microwave switching equipment, (b) Western Union microwave and multiplex equipment, (c) stations communications control group, (d) main distributing frame

all communications coming from JPL by Western Union microwave (most telephone communications and voice/data) are switched, or patched, to the appropriate DSS. The microwave and multiplex equipment leased from Western Union is shown in Fig. 1b.

Four bays of equipment, called the stations communications control group (Fig. 1c), handles all routing of voice/data, as well as teletype switching, at the Goldstone DSCC center. The Woomera, Johannesburg, and Cebreros DSS centers will require only three such bays: two for teletype and one for voice/data. High-speed data equipment will be provided at these centers, but the Goldstone DSCC center does not require it.

All land-line communications (e.g., paging, local, telephone, and teletype) are interconnected through a main distributing frame (Fig. 1d). The telephone central-office equipment provides all telephone communications for the Goldstone DSCC and all trunk lines to and from JPL and Barstow. During relocation of the equipment, 200 lines were added, increasing the central-office capability to 500 lines. The central office and all telephone instruments at the Goldstone DSCC are JPL-owned, whereas the Woomera, Johannesburg, and Cebreros DSSs are served by local telephone companies.

2. Air-Conditioner for Venus DSS 400-kW-Transmitter Antenna, *J. Carlucci*

Operation of the modified Venus DSS 85-ft az–el 400-kW-transmitter antenna requires temperatures between 60 and 85°F, with only ±5°F variation from one level over a 24-h period, and humidity of not more than 50% in the electronics room and cassegrain cone area. An inherent problem with chiller compressor design is the sensitivity of such compressors to attitude. Since a unit for this application would have to operate within an attitude of 91 deg from vertical and withstand acceleration rates of 3 deg/s in azimuth and 2 deg/s in elevation, an air-conditioner of special design and construction was required.

The 7.5-ton air-conditioner, as shown in Fig. 2, was designed as three units: two heat exchangers mounted in the dish structure, and one chiller (with compressor) mounted below the alidade in a structural area that rotates in azimuth only. The total load is 53,162 Btu. Installation, checkout, and calibration of the unit have been completed.

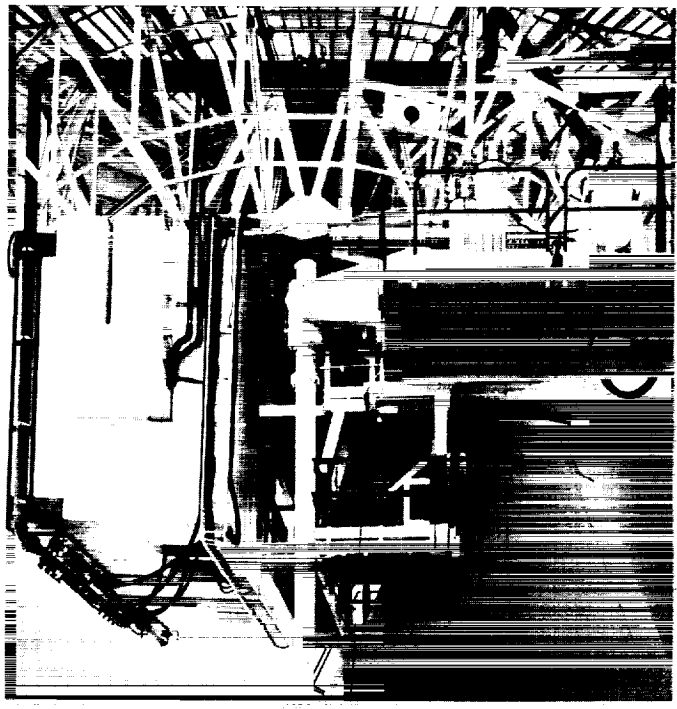

Fig. 2. Air-conditioner for Venus DSS 400-kW-transmitter antenna